THE UNIVERSITY OF QUEENSLAND

AUSTRALIA

Multi-functional and Tunable Microwave Devices and Sub-systems for Wideband Applications

He Zhu

B. Sc., M. Eng.

A thesis submitted for the degree of Doctor of Philosophy at

The University of Queensland in 2017

The School of Information Technology and Electrical Engineering

Abstract

Microwave components and sub-systems have been widely investigated in recent years since they play essential roles in microwave systems. With the rapid development and explosive extension of microwave techniques, high speed, large data volume, and electromagnetic compatibility are not the only issues that concern designers, practitioners, and researchers. Features like multi-functionality, reconfigurability, portability, low energy consumption, miniaturization of circuit size and simple construction have come into focus more and more in recent years. Currently, microwave devices are suffering from several drawbacks: huge losses from a lack of integration of individual components, lack of new functionality, poor adaptability to different environments, low efficiency, flexibility and controllability, high cost and energy consumption, and insufficient miniaturization of circuit size. With these existing challenges and the huge call for innovation in microwave components and sub-systems, new design approaches and structures are extremely in demand and a high point of focus. This thesis aims to solve some of the current challenges mentioned above by making four main contributions.

The first contribution is the development of new design approaches to design microwave devices with multiple functions to replace cascaded devices with a single function. The main target is to reduce the overall number of components used in constructing microwave systems. With a large number of cascaded devices, huge losses will be produced which decrease systems' reliability and overall performance, not to mention the current large circuit volumes, high cost, and energy consumption. Multi-functional componentry is a suitable and proper solution to solve these problems. In wireless microwave systems, power dividers are usually cascaded with bandpass filters, to get rid of unwanted signals and transmit the desired ones. When the number of output terminations is raised, more filters are required, which makes it more difficult for design and implementation. A four-way power divider integrated with filtering characteristics is proposed to replace the cascaded structures. The proposed design shows equal power division, great selection of filtering signals and reduction in device numbers and overall cost.

The second contribution is the development of multiple tunable microwave devices which can be controlled and adapted to different environments. An electrical tuning method is used by loading varactors on microstrip lines. To begin with, tunable bandpass filters were investigated to achieve high tunability of both centre frequency and bandwidth. To that end, several new designs with varactor-loaded coupled-line sections were proposed and verified. Relocatable transmission zero was realised to control the cut-off of the passband at two edges. The concept was applied in the

design of a tunable balanced bandpass filter with a wide tuning range and high common-mode suppression. Wideband power dividers with tunable power division at output terminations were focused on, and new structures have been designed. The tunability of the power division ratio of output signals has been realised with and without integrated filtering characteristics. The achieved results indicate that tunability of power division and filtering response is realised using one compact structure.

The third contribution is the proposal of concepts and structures of multi-port tunable devices with new functions and a compact size. Firstly, tunability of power division in couplers and baluns was investigated. Using tuning elements, one is able to change the amplitude of output signals at different terminations. Apart from the amplitude, the controllability of the differential phase is also targeted. The aim here was to achieve a tunable differential phase of multi-port devices without affecting the equal power division ratio of the amplitude. To that end, a kind of tunable phase shifting unit was adopted to emulate a transmission line with changeable electrical length. A phase-tuned power divider and a phase-tuned hybrid coupler were constructed using the tunable shifting unit. For the power divider, in-phase and out-of-phase states can be converted, maintaining equal output amplitude. For the hybrid coupler, the differential phase can be tuned from orthogonal to another arbitrary angle. All these designs achieve an extremely compact size and the realised functions have not ever been put forward before.

The fourth contribution is the development of tunable beam-forming networks for steerable and reconfigurable antenna arrays. Based on the proposed two-way power with a tunable power division ratio, an eight-way tunable power divider was built for constructing a tunable feeding network for antenna arrays. When an eight-element array is fed by the proposed network, the power distribution at each element can be tuned from equal to unequal states by controlling the tuning elements in the feeding network. By doing so, one is able to make the radiation pattern reconfigurable in terms of many aspects, such as the beamwidth and sidelobe levels. Moreover, wideband tunable phase shifters were designed and cascaded with the tunable feeding network, for the purpose of achieving steerable beam direction. Simulation results reveal that the proposed tunable feeding network can achieve a high level of sidelobe suppression and a wide steering range of beam angle.

Declaration by author

This thesis *is composed of my original work, and contains* no material previously published or written by another person except where due reference has been made in the text. I have clearly stated the contribution by others to jointly-authored works that I have included in my thesis.

I have clearly stated the contribution of others to my thesis as a whole, including statistical assistance, survey design, data analysis, significant technical procedures, professional editorial advice, and any other original research work used or reported in my thesis. The content of my thesis is the result of work I have carried out since the commencement of my research higher degree candidature and does not include a substantial part of work that has been submitted *to qualify for the award of any* other degree or diploma in any university or other tertiary institution. I have clearly stated which parts of my thesis, if any, have been submitted to qualify for another award.

I acknowledge that an electronic copy of my thesis must be lodged with the University Library and, subject to the policy and procedures of The University of Queensland, the thesis be made available for research and study in accordance with the Copyright Act 1968 unless a period of embargo has been approved by the Dean of the Graduate School.

I acknowledge that copyright of all material contained in my thesis resides with the copyright holder(s) of that material. Where appropriate I have obtained copyright permission from the copyright holder to reproduce material in this thesis.

Publications during candidature

Peer-reviewed Journal Papers

1. **H. Zhu**, and A. Abbosh, "Single- and dual-band bandpass filters using coupled stepped-impedance resonators with embedded coupled-lines", *IEEE Microw. Wireless Compon. Lett.*, vol. 26, no. 9, pp. 675-677, Sep. 2016.
2. **H. Zhu**, A. Abbosh, and L. Guo, "Wideband four-way filtering power divider with sharp selectivity and wide stopband using looped coupled-line structures", *IEEE Microw. Wireless Compon. Lett.*, vol. 26, no. 6, pp. 413-416, Jun. 2016.
3. **H. Zhu**, and A. Abbosh, "Modified wideband Marchand balun with tunable power division ratio and constant phase", *IEEE Microw. Wireless Compon. Lett.*, vol. 26, no. 5, pp. 319-321, May. 2016.
4. L. Guo, **H. Zhu**, and A. Abbosh, "Wideband phase shifter with wide phase range using parallel coupled lines and L-shaped networks", *IEEE Microw. Wireless Compon. Lett.*, vol. 26, no. 8, pp. 592-594, Aug. 2016.
5. L. Guo, **H. Zhu**, and A. Abbosh, "Wideband tunable In-phase power divider using three-line coupled structre", *IEEE Microw. Wireless Compon. Lett.*, vol. 26, no. 6, pp. 404-406, Jan. 2016.
6. **H. Zhu**, and A. Abbosh, "Tunable balanced bandpass filter with wide tuning range of center frequency and bandwidth using compact coupled-line resonator", *IEEE Microw. Wireless Compon. Lett.*, vol. 26, no. 1, pp. 7-9, Jan. 2016.
7. **H. Zhu**, and A. Abbosh, "Compact tunable bandpass filter with wide tuning range of centre frequency and bandwidth using coupled lines and short-ended stubs", *IET Microw. Antennas Prop.*, vol. 10, no. 8, pp. 863–870, 2016.
8. **H. Zhu**, and A. Abbosh, "Tunable band-pass filter with wide stopband and high selectivity using centre-loaded coupled structure", *IET Microw. Antennas Prop.*, vol. 9, no. 13, pp. 1371–1375, 2015.
9. **H. Zhu**, and A. Abbosh, "Compact tunable bandpass filter with wide tuning range using ring resonator and short ended coupled lines", *Electron. Lett.*, vol.51, no. 7, pp. 568–570, Apr. 2015.
10. **H. Zhu**, Y. Wang, and A. Abbosh, "Broadband microwave crossover using parallel coupled microstrip lines and short-ended stubs", *IET Microw. Antennas Prop.*, vol. 9, no. 1, pp. 79–85, 2015.
11. **H. Zhu**, A. Abbosh and L. Guo, "Ultra-wideband unequal in-phase power divider using three-line coupled structure", *Electron. Lett.*, vol.50, no. 17, pp. 1081–1082, Jul. 2014.

12. L. Guo, A. Abbosh and **H. Zhu**, "Ultra-wideband in-phase power divider using stepped-impedance three-line coupled structure and microstrip-to-slot line transitions", *Electron. Lett.*, vol.50, no. 5, pp. 383–384, Feb. 2014.

Peer-reviewed Conference Papers

1. **H. Zhu**, E. Ahmed, and A. Abbosh, "Compact dual-band bandpass filters using multi-mode resonator of short-ended and open-ended coupled lines", *Proceedings of Asia-Pacific Microwave Conference (APMC)*, Nanjing, China, 2015.
2. **H. Zhu**, and A. Abbosh, "Directional coupler with two octaves band and high directivity using stepped-impedance coupled structure", *Proceedings of Asia-Pacific Microwave Conference (APMC)*, Nanjing, China, 2015.
3. L. Guo, **H. Zhu**, and A. Abbosh, "Planar UWB phase shifter using parallel coupled lines combined with short-ended stubs and impedance transformer," in *Asia-Pacific Microwave Conference (APMC)*, Nanjing, China, 2015.
4. **H. Zhu**, Y. Wang, and A. Abbosh, "Compact tunable crossover with wide tuning range using coupled lines", *Proceedings of Asia-Pacific Microwave Conference (APMC)*, Sendai, Japan, 2014.
5. **H. Zhu**, and A. Abbosh, "Compact ultra-wideband in-phase power divider using three-line coupled structure", *IEEE Antennas and Propagation Society International Symposium (APSURSI)*, 2014.

Publications included in this thesis

1. **H. Zhu**, and A. Abbosh, "Tunable balanced bandpass filter with wide tuning range of center frequency and bandwidth using compact coupled-line resonator", *IEEE Microw. Wireless Compon. Lett.*, vol. 26, no. 1, pp. 7-9, Jan. 2016. – Partly incorporated as paragraph in Chapter 4.

Contributor	Statement of contribution
He Zhu (Candidate)	Designing and testing (90%) Writing the paper (85%)
A. Abbosh	Designing (10%) Editing the paper (15%)

2. **H. Zhu**, and A. Abbosh, "Compact tunable bandpass filter with wide tuning range using ring resonator and short ended coupled lines", *Electron. Lett.*, vol.51, no. 7, pp. 568–570, Apr. 2015. – Partly incorporated as paragraph in Chapter 4.

Contributor	Statement of contribution
He Zhu (Candidate)	Designing and testing (90%) Writing the paper (85%)
A. Abbosh	Designing (10%) Editing the paper (15%)

3. **H. Zhu**, and A. Abbosh, "Tunable band-pass filter with wide stopband and high selectivity using centre-loaded coupled structure", *IET Microw. Antennas Prop.*, vol. 9, no. 13, pp. 1371–1375, 2015. – Partly incorporated as paragraph in Chapter 4.

Contributor	Statement of contribution
He Zhu (Candidate)	Designing and testing (90%) Writing the paper (85%)
A. Abbosh	Designing (10%) Editing the paper (15%)

4. **H. Zhu**, and A. Abbosh, "Compact tunable bandpass filter with wide tuning range of centre frequency and bandwidth using coupled lines and short-ended stubs", *IET Microw. Antennas Prop.*, vol. 10, no. 8, pp. 863–870, 2016. – Partly incorporated as paragraph in Chapter 4.

Contributor	Statement of contribution
He Zhu (Candidate)	Designing and testing (90%) Writing the paper (85%)
A. Abbosh	Designing (10%) Editing the paper (15%)

5. **H. Zhu**, A. Abbosh, and L. Guo, "Wideband four-way filtering power divider with sharp selectivity and wide stopband using looped coupled-line structures", *IEEE Microw. Wireless Compon. Lett.*, vol.26, no.6, pp. 413-416, Jun.2016. –Partly incorporated as paragraph in Chapter 5.

Contributor	Statement of contribution
He Zhu (Candidate)	Designing and testing (80%) Writing the paper (85%)
A. Abbosh	Designing (10%) Editing the paper (10%)
L. Guo	Designing and testing (10%) Editing the paper (5%)

6. **H. Zhu**, and A. Abbosh, "Modified wideband Marchand balun with tunable power division ratio and constant phase", *IEEE Microw. Wireless Compon. Lett.*, vol. 26, no. 5, pp. 319-321, May. 2016. – Partly incorporated as paragraph in Chapter 6.

Contributor	Statement of contribution
He Zhu (Candidate)	Designing and testing (90%) Writing the paper (85%)
A. Abbosh	Designing (10%) Editing the paper (15%)

Contributions by others to the thesis

Professor Amin Abbosh contributed closely in defining research problem, overall conception and direction of the thesis. Dr. Konstanty Bialkowski provided massive valuable advices and technical support to this work.

Statement of parts of the thesis submitted to qualify for the award of another degree

None

Acknowledgements

I would like to express my sincerest gratitude to my principle supervisor, Professor Amin Abbosh, for his guidance, encouragement, and feedback during my PhD study.

I thank my colleagues at Microwave group, in particular my co-supervisor Dr. Konstanty Bialkowski, for his kind suggestions on this project and support with testing and experiment. I also thank the colleagues at Engineering & Technical Support Group, especially Denis Bill, Richard Newport and John Kohlbach for their kind help on manufacturing the components and devices.

I would like to thank the Chinese Scholarship Council, the School of Information Technology and Electrical Engineering (ITEE) and the Graduate School of the University of Queensland for the scholarship support.

Last but not least, I would like to thank my family for their continuous encouragement and the moral support throughout my PhD study.

Keywords

microwave techniques, tunable devices, multi-functional, wideband, tunable filters, power dividers, multiport devices, phase shifters, antenna arrays, beam-forming networks.

Australian and New Zealand Standard Research Classifications (ANZSRC)

ANZSRC code: 090601, Electrical and Electronic Engineering not elsewhere classified, 100%

Fields of Research (FoR) Classification

FoR code: 0906, Electrical and Electronic Engineering, 100%

Table of Contents

List of Figures

List of Tables

List of Abbreviations

ADS	Advanced Design System
BFN	Beam-Forming Network
BPF	Bandpass Filter
BST	Barium-Strontium-Titanate
BW	Bandwidth
CF	Centre Frequency
CM	Common Mode
DC	Direct Current
DM	Differential Mode
EM	Electromagnetic
FBW	Fractional Bandwidth
FPD	Filtering Power Divider
HTS	High-Temperature Superconductor
HFSS	High Frequency Structural Simulator
IMD	Inter-Modulation Distortion
LAN	Local Area Network
LTCC	Low-Temperature Co-fired Ceramics
MMIC	Monolithic Microwave Integrated Circuit
MEMS	Micro-Electro-Mechanic System
PD	Power Divider
PDR	Power Division Ratio
PS	Phase Shifter
RF	Radio Frequency
RFC	Radio Frequency Choke
RFID	Radio-Frequency Identification
RTPS	Reflection-Type Phase Shifter
SLL	Side-Lobe Level
SPICE	Simulation Program with Integrated Circuit Emphasis
TEM	Transverse-Electromagnetic
TLCS	Three-line Coupled Structure
TP	Transmission Pole
TZ	Transmission Zero
UWB	Ultra-Wideband
YIG	Yttrium Iron Garnet

Chapter 1: Introduction

1.1 Background and Motivation

Any microwave system is constructed with a combination of components used for data transmission using microwave frequency spectrums. Microwave systems have been developed everywhere for numerous kinds of applications, including point-to-point communication, smart phones, wireless local area network (LAN), radar and satellite, navigation, heating and power systems, and medical areas. Due to the overwhelming coverage of microwave systems in our daily life, it is not inappropriate at all to say that no one can live in modern society without getting in touch with microwave systems.

With the rapid development and explosive extension of microwaves, high speed, large data volumes, and electromagnetic compatibility are not the only issues of concern. Features like multi-functionality, reconfigurability, portability, low energy consumption, miniaturization of circuit sizes and simple constructions are more and more in focus in recent years. All of these need innovations not only at the system level, but also at the level of the hardware design of basic microwave components.

Facing crucial changes in public demand and market requirements, it is time to look for new techniques to replace the traditional methods which will never be suitable for the current and future situations. To enhance the overall performance of microwave systems, it is mostly critical to develop a new concept of microwave components and ameliorate current performance. Motivated by the great potential of microwave technology and techniques, especially the immense potential capability of microwave devices, researchers are now pursuing more flexible, functional and controllable devices which are smaller. To that end, great efforts have been made on improving and progressing microwave techniques. Tunable and reconfigurable microwave components, a general concept applicable to a group of devices and circuits, have made massive contributions to make a system “smarter” and thus become a hot focus both in academia and industrial fields.

In reconsidering microwave systems configuration, the main focus of attention has been on their passive components: antennas, filters, phase shifters, power dividers, baluns, and couplers. For each component, new ideas and approaches which involve the concept of tunability and reconfiguration have been presented over the past decade. However, it is time to replace these individual microwave components with a multi-functional and tunable one. In contrast with traditional methods, this thesis

will focus on the development of new design methods as well as structures which have multi-functionality, tunability, and reconfigurability for wideband applications.

1.2 Overview of Multi-functional and Tunable Microwave Components and Sub-systems

Microwave components, or microwave devices, are core compositions of a microwave system. Each device has its own function and all these devices operate together for certain applications. The higher performance of microwave devices can definitely lead to a better capability of a microwave system. In this regard, it is worth investigating deeply into the improvement of the individual components of a system. Though huge efforts have been made in both academic and industrial fields, there is now great scope and the demand for high-performance microwave devices with the capability of multiple functions for different application requirements.

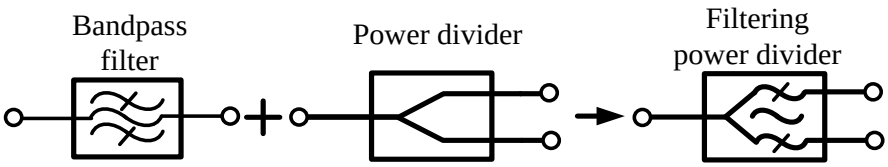

Fig 1. 1 Diagram of a filtering power divider to replace traditional cascaded structure of a bandpass filter and a power divider.

Multi-functional microwave devices, by definition, refer to devices which can operate with multiple functions or have multiple usage potentials in microwave systems. Multi-band filters are an example of such multi-functional microwave devices since they can work at different operating frequencies for different purposes. Another example is filtering power dividers, which integrate the function of power dividers and bandpass filters within one component, as shown in Fig 1.1. Obviously, with multi-functional componentry the number of components within the whole system will be reduced, leading to miniaturization of circuit sizes and system volumes. Meanwhile, since the number of connections between components is reduced, the losses produced by cascading devices are inevitably decreased, which is another benefit. Of course, multi-functionality does not simply mean the combination of several individual elements; it has wider implications in terms of controllability, flexibility, and reliability.

Tunable microwave devices are another type of multi-functional components which have various kinds of controllable or tunable characteristics such as frequency tuning, phase tuning, power tuning, and so on. The concept of tuning in microwave devices has been in existence for a long time and now extends to wider areas and higher levels of research. A tunable filter is a typical kind of tunable microwave device favourable for high tunable/reconfigurable performance, reduced complexity, compact size, and low cost. As illustrated in Fig 1.2, it is always preferable to have one integrated controllable filter that can cover all the filtering banks. In light of critical situations where wireless systems require integration of multi-functionality, multiple band usage, smaller volume and low cost, tunable components become irreplaceable in many scenarios. The advantages of tunable components include integration of multiple functionalities in one single structure; reduced circuit and system size; flexibility in switching working status simultaneously with requirements; high effectiveness of spectrum and power usage; and overall system cost reduction. With all these merits, no one can deny the fact that tunable components are making microwave systems more efficient and reliable.

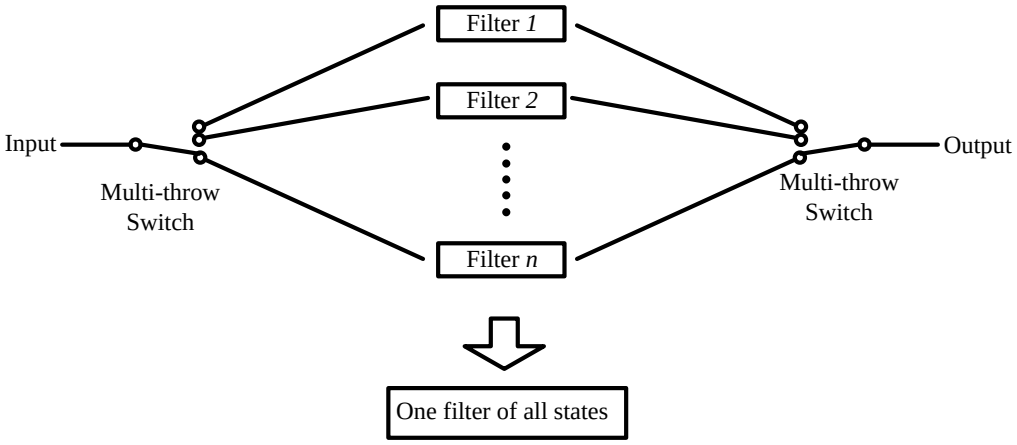

Fig 1. 2 Diagram of tunable filters that represent all states of filtering banks.

Apart from tunable filters, a variety of other kinds of tunable devices has been presented and verified to fulfill the demand of multiple functions, including tunable power dividers, tunable couplers, tunable phase shifters, etc. All of these components play very important roles in different certain kinds of microwave systems since they are able to control the output signals so that they can be adapted for multiple situations. By controlling such kinds of devices, it is easy to have tunability of differential phase, magnitude and signal power at different ports. Generally speaking, the advantages of tunable microwave devices include the following aspects:

- Multiple functions integrated into one structure

- High adaptability to various working conditions
- Efficiency, flexibility, and easy controllability of devices
- Reduction of losses and system complexity
- Improvement in speed and data capacity
- Amelioration of system performance
- Miniaturization of circuit size
- Intelligence by applying software control

This chapter provides a brief introduction of the current research situation and existing techniques of tunable microwave components. A more detailed literature review of each aspect of tunable devices can be found in the next chapter. The rest of this chapter comprises three sections dealing with the following: the objectives of this dissertation, the main contributions that have been achieved in this research project, and the overall organization of the thesis, respectively.

1.3 Aim of the Thesis

As tunable microwave components are in significant demand, and numerous drawbacks exist in the current research, this dissertation is aimed at developing a new concept and ideas about multi-functional tunable microwave devices, as well as improving overall microwave system performance by proposing new structures and configurations. For state-of-the-art technologies in microwave device design, although tremendous progress has been made in reliability and capacity, there are still many issues remaining to be solved. In this section, the main problems and drawbacks are investigated and summarized as follows:

1. Lack of integration of individual components. For a tunable device, the priority is to have changeable characteristics which can satisfy different working conditions using one structure. While it is true that existing tunable microwave devices possess such tunability, most are single-functional. As we all know, a microwave system or sub-system is composed of several components which have different responsibilities for signal transmitting and processing. The connection between two individual components will inevitably result in an additional loss to the system. If it is possible to reduce the number of components in a system without degrading functionality, the overall loss within the system will certainly decrease. Therefore, it is undoubtedly preferable to have one compact component which integrates several functions.

2. Lack of new functionality. Most of the existing designs are capable of a certain degree of tunability, for instance, tunable filters can tune the operating band from one level to another, but the majority of tunable microwave devices have similar functions. In some cases, new functionalities need to be developed to fulfill the requirement of multi-functional systems. This also corresponds to the first point made above, that integration of more functions is required because usually, new functionality comes from the combination and cascade of several individual components. Due to the variety of microwave systems, new functionality can provide new options and more choices to circuit designers in building systems. New functionality means new application, which is always favoured and is the focus of research and industrial areas.

3. Overlooking miniaturization in circuit size. One of the biggest merits of tunable devices is the small volume of their circuit size which contains variable performance and multiple functionalities. However, many designs that have been presented have not taken circuit size into consideration. As mentioned in the first section of this chapter, portable, flexible and multi-functional devices are more and more favoured in the modern world. For example, the smart phone is a typical miniaturized product which combines features of a personal computer operating system and other features for handheld use. Meanwhile, size reduction means lower production cost, more space, and more freedom in the circuit and system design, which is quite critical in microwave componentry development.

In light of these shortcomings, multiple solutions will be provided in this thesis to overcome them to a great extent. Basically, our target is to develop novel tunable microwave designs with a new concept, multiple functionalities, and miniaturization. After investigating previous works presented by other researchers, a new concept and designs have been raised, realised and verified. The challenges in this work and its contributions will be introduced in the next section.

1.4 Original Contributions

This work aims to resolve the problems listed above and is dedicated to providing new approaches for tunable microwave component design. Major original contributions are summarized as:

1. New tunable bandpass filter designs for different applications. The main concerns in tunable filter design include flexible tunability of operating frequency band range and bandwidth. It is also attractive to have a sharp selectivity of the passband, upper-stopband harmonic suppression, and size reduction. A kind of varactor-loaded coupled-line structure is investigated and utilized in

several new filter designs. The proposed designs possess all of the advantages mentioned here, the overall circuit size especially is reduced to a considerable extent. Besides, a four-port differential tunable bandpass filter is presented with full tunability of bandwidth and frequency band, which has never been achieved before.

2. A novel varactor-loaded three-line coupled structure and its application to tunable power divider designs. In microwave systems, power dividers are a crucial component in charge of allocating power to different channels. Although equal and unequal power dividers are common, very few works have focused on making the power division ratio tunable and controllable. This work for the first time presents a tunable wideband power divider with tunable power division at two output ports. Based on this concept, a new kind of tunable power divider with filtering response is introduced which combines the functions of power divider and bandpass filters. This integration significantly reduces overall circuit size and losses in the system and brings more intelligence and convenience to the design. Finally, the filtering response is set to be controllable, which further promotes the functionality of the design.

3. Novel tunable multi-port component designs. Apart from tunable bandpass filters and tunable power dividers, this work is also dedicated to developing a new concept for multi-port component design, involving aspects such as a tunable balun, a tunable quadrature coupler, a phase-tuned power divider and a phase-tuned hybrid. These tunable components provide different functions for different scenarios. For the tunable balun and tunable coupler, the main contribution is that the output power at two output ports is variable while the differential phasing is maintained. For the phase-tuned power divider and phase-tuned hybrid, the purpose is just the opposite: the output power at each output port is unchanged, while the differential phasing can be tuned. In this way, we manage to realise arbitrary output power and arbitrary differential phasing for multi-port microwave devices.

4. Controllable beam-forming network for antenna arrays. Though numerous feeding networks for antenna arrays or phased arrays have been presented before, there is still a gap in tunable or reconfigurable feeding network designs. This original work presents an eight-way feeding network which can achieve tunable output power at each output port. The output power distribution can be easily varied from equal power status to certain kinds of unequal power distribution. By connecting such a network with an antenna array, it is easy to control radiation patterns such as the side-lobe level by controlling the feed power to each element. Meanwhile, tunable phase shifters are connected between each output port and antenna element, so that the main beam direction can be

shifted if a certain differential phase is set. In this way, the side-lobe level and beam direction can be controlled at the same time by the tunable feeding network presented in this research.

1.5 Thesis Organization

Chapter 1 provides a brief introduction to the research background, motivation, and intention, as well as objectives and contributions accomplished in this thesis.

Chapter 2 discusses current research trends and gives a brief literature review on state-of-the-art work on microwave devices and sub-systems. For the microwave devices, passive devices like bandpass filters, power dividers, couplers and phase shifters are reviewed. Tunable bandpass filters, tunable power dividers, and tunable couplers are also described. Lastly, a brief introduction of microwave sub-systems like antenna arrays and phased arrays as well as their feeding networks for beam-forming is outlined. The challenges and problems in existing research are also discussed in this chapter.

Chapter 3 gives design techniques and analysis methods which are used in the development of microwave components. To describe the transmission characteristics of a device, key parameters like scattering parameters and ABCD matrices are used. The principle of the even- and odd-mode analysis method is presented. This method is widely used for deriving the resonance and transmission properties of symmetrical and reciprocal networks. The microstrip technique is described and calculation equations are given since this is the main technique in this thesis for verification of electromagnetic models. Finally, principles of coupled-lines and varactor diodes are illustrated for further reference.

Chapter 4 introduces four novel tunable bandpass filters using different kinds of structures. Firstly a coupled stepped-impedance resonator is proposed and used in single-band and dual-band fixed bandpass filters. Then a varactor-loaded coupled-line structure is utilized for the construction of tunable bandpass filter designs. This structure is extremely compact and significantly contributes to the miniaturization of circuit size. The third design is based on varactor-loaded coupled-line structure, which can relocate the position of the transmission zero at one cut-off edge of the passband. Full controllability of bandwidth, operating frequency, and transmission zeros are achieved in all designs, which enhances their overall performance compared with existing designs. Moreover, a balanced tunable bandpass filter design is built and verified using the varactor-loaded

coupled-line structure, which provides a new option for differential filtering networks with tunability of bandwidth and operating frequency.

Chapter 5 focuses on several power divider designs for wideband applications. The main target is to achieve controllability of the output power division ratio at different output ports. To begin with, a three-line coupled structure is put forward for two power divider designs with equal and unequal power division at two output terminations. It is found that when the three-line coupled structure is loaded with varactors, the equivalent capacitive distribution would be affected, and thus the corresponding output power can be controlled. Based on this concept, a wideband tunable power divider with tunable power division ratio is then constructed. To develop novel multi-functional microwave components, filtering responses with and without a controllable band are integrated with the design mentioned above. Lastly, a multi-port filtering power divider with sharp cut-off is presented and experimentally verified.

Chapter 6 describes a series of tunable multi-port microwave components with multi-functionality. First of all, fixed high-performance directional couplers and crossovers are investigated mainly for building a Butler matrix which is a type of beam-forming network. A wideband tunable balun and a quadrature coupler with a variable power division ratio are firstly investigated for pattern control in antennas and measurement systems, respectively. Although we manage to build tunable multi-port devices with a tunable power ratio and constant phase, it remained to be seen how to have constant power and a controllable phase. To that end, a phase-tuned power divider and a hybrid coupler with arbitrary differential phase are proposed and built. These two devices fill the blank in terms of the controllability of differential phases and exhibit great novelty in the aspect of multi-functioning microwave device design.

Chapter 7 presents a novel concept for construction of tunable beam-forming networks for antenna arrays. Since one of the main components for beam-forming networks is the phase shifter, a new kind of fixed wideband phase shifter and a reflection-type tunable phase shifter are firstly introduced. Based on the tunable wideband power dividers presented in Chapter 5, an eight-way tunable beam-forming network is built. The proposed network is able to realise tunable symmetrical power distribution at eight output ports. To control the beam direction of antenna arrays, eight tunable phase shifters are cascaded at each output termination of the network. A linear array is connected with the proposed feeding networks for verification. Simulations have shown that the proposed beam-forming networks manage to control the side-lobe levels as well as the main beam direction, which has never been achieved before.

Chapter 8 gives the conclusion to the whole thesis, summarizing all the benefits and existing shortcomings in this work. Moreover, future work and plans to operationalise and further develop this research topic are also illustrated.

Chapter 2: Literature Reviews of Microwave Devices and Sub-systems

2.1 Introduction

Microwave devices refer to the components which compose microwave systems by connecting with transmission lines. Generally speaking, microwave devices can be categorized into two types, active devices, and passive devices. In this thesis, the main focus is on passive devices, notably tunable passive devices. Passive devices are of many different types including filters, power dividers, couplers, hybrids, phase shifters, baluns, or even antennas [1]. Correspondingly, tunable microwave devices also comprise many types: tunable filters, tunable power dividers, tunable couplers/hybrids, tunable phase shifters, and so on. Antennas refer to a special component which only has one port, and antenna arrays are a set of antenna elements aligned with specific orders or functionalities [2]. The radiation patterns of antenna arrays can be controlled by beam-forming networks, which operate as the feeding networks to control the signal amplitude and phasing with multiple antennas or radiating elements. Generally speaking, beam-forming networks are a kind of sub-system of microwave systems which consist of several microwave devices such as power dividers, directional couplers, phase shifters, etc. These fundamental components are critical to microwave systems since the performance and integration of microwave devices determine the overall capability of a microwave system. In this chapter, a general introduction of commonly-used passive and tunable devices will be given, and a brief review of the current research and state-of-the-art outcomes will also be elaborated on and discussed.

2.2 Design Technology for Passive Microwave Components

Passive microwave components are critical compositions which can be found in every microwave systems. Microwave filters are able to combine and separate signals based on frequencies, so that they are used to select or limit signal transmission within assigned spectral limits [3]. Filters are an essential part of the cellular base station front-end, since they are able to reject unwanted noise signals and transmit very weak ones received from the antenna. Microwave filters can be categorized into four types according to their functions: low-pass, high-pass, bandpass, and bandstop filters. Among these four types, bandpass filters are the most widely used and focused on for the reason that they can transmit desired signals and confine the rest. Bandpass filters manage to get rid of harmonics and noise signals, which could decrease the SNR and even jeopardize systems.

Such filters' main applications consist of narrowband, wideband, ultra-wideband (UWB), and multi-band filters. Narrowband filters are the most common and popularly used type, for which many advanced fabrication technologies have been developed, including [4]:

- Microstrip technique
- High-temperature superconductor (HTS)
- Monolithic microwave integrated circuit (MMIC)
- Micro-electro-mechanic system (MEMS)
- Low-temperature co-fired ceramics (LTCC)
- Photonic bandgap materials/structures
- Ferrite and ferroelectrics
- Other techniques

Among all these techniques, the microstrip technique has its own advantages due to its ease of fabrication and integration with active components which can be mounted on the top of the board. In this thesis, we will mainly discuss microstrip-based tunable and non-tunable microwave devices.

Resonators are the basic units of a bandpass filter. A resonator could be a transmission line, an open/short stub, a lumped element, a cavity, or any other form. Comb-line and hair-pin resonators are the most commonly used resonators in narrowband filter designs because it is easy to control their coupling coefficients and external factors. Multi-mode resonators [5] are a series of resonators which can produce multiple resonant modes, using an appropriate coupling to form multi-band or ultra-wideband bandpass filters. Typical multi-mode resonators include stepped-impedance resonators [6], multi-stub-loaded resonators [7], ring resonator [8], slot-line/CPW resonators [9]-[10], coupled-line resonators [11], and so on. For multi-band filters, two resonators are coupled together with a decent coupling coefficient, and then fed with tapped feeding lines or spur-lines. For wideband and UWB filters, strong coupling is required and imposed on a multi-mode resonator, so that a flat and constant passband can be achieved. Besides, to achieve strong coupling between resonators, broadside coupled structure was put forward and applied in UWB bandpass filter design, as indicated in Fig 2.1 (a).

Power dividers (PDs) are a kind of passive component used to divide the input power into several smaller amounts of power either equally or unequally, to exit the radiating elements of antenna arrays [12]. Depending on the differential phase at two output ports, they can be categorized into two types, one with the same phase (in-phase PDs) and the other one with a 180° phase difference (out-of-phase PDs). The most well-known in-phase PDs are the Wilkinson [13] and Gysel types

[14], both of which are equal power dividing and narrow-band. For a UWB system, it is favourable to design ultra-wideband PDs to cover the whole band range from 3 GHz to 11 GHz [15]. Many wideband PDs were proposed to fulfill bandwidth requirement using different kinds of techniques, such as the multilayer, multi-mode resonator, coupled structure, and so on. In some cases, unequal output powers at different output ports are required for systems like phased arrays and beam-steering networks. To realise that, different methods are used such as asymmetrical transmission lines [18], microstrip/slotline transition [19], and three-line coupled structures [20]-[21]. It is noted that broadside coupling was adopted in [20] for bandwidth enhancement, as shown in Fig 2.1(b).

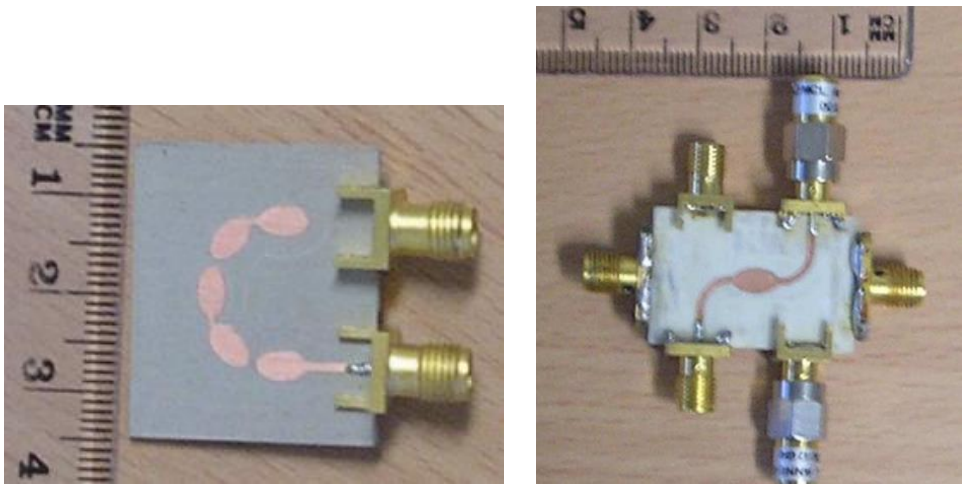

(a) (b)

Fig 2. 1 Broadside coupling technique for (a) bandpass filter design; (b) power divider design [20].

Couplers are passive components that can be used for distributing or combining microwave signals. Usually couplers are four-port networks which have one isolated port and no resistors. There are various types of couplers, including branch-line couplers, directional couplers [22], Lange couplers, rat-race couplers [12], and crossovers. The key parameters and requirements for coupler design include bandwidth, coupling factor, isolation, and output phase difference. Broadside coupling has been proven to have an extremely strong coupling factor and thus is used in directional coupler designs [24]. In other approaches, high isolation up to 35 dB has been realised by employing slotline-based capacitive compensation [25]. An inductor-loading method for directivity enhancement of microstrip directional couplers has been verified in [26]. An inductor-loading method and coupled-line section for directivity enhancement of microstrip directional couplers has been utilized in narrowband applications [27]. Compensation using lumped capacitors and short coupled-line sections were used for directivity improvement in wideband applications [28].

Phase shifters are critical passive components in microwave systems, such as phased arrays, modulators, microwave instrumentation and measurement systems. There are three main types: digital, analogue, and mechanical phase shifters. Here we mainly focus on phase shifters realised by microstrip techniques. Microstrip-based phase shifters have many advantages like easy fabrication, wide operating bandwidth, low cost and easy integration with other circuits. Various techniques are used to build wideband phase shifters, such as the modified Schiffman [29], broadside-coupled structure [30], high/low impedance technique, microstrip-coplanar waveguide, stub-loaded transmission line [31], microstrip-slot transitions, and coupled-line structures. Since bandwidth, frequency shifting range and phase deviation are three main parameters in phase shifter designs, wider bandwidth, wider phase shifting range (more than 90˚ phase shift) and smaller phase variance are required.

2.3 Design Technology for Tunable Microwave Components

2.3.1 Techniques for Tuning

Tunable microwave devices can be realised by different kinds of mechanisms and techniques. Generally popular tuning methods include the following types:

- Mechanical tuning method
- Material tuning method
- Electrical tuning method

The most original method is the mechanical tuning one, which usually uses physical movement of screws to change the internal property of devices. Since it is more desired to have fast response speed, easy controllability and miniaturized circuit size, mechanical or physical tuning is not suitable for realistic applications. Another option of tuning method is to alter the material so as to change resonant current distribution of the structure. This method can be used for tunable antenna designs in which radiation pattern can be made reconfigurable. However, the stability and reliability is a big problem for such kind of tuning method in circuit designs. Besides mechanical tuning and material changing, electrical tuning is more efficient, accurate and easier to control, and thus widely adopted in many designs.

The most common electrical tuning method is to use PIN diodes or varactor diodes which can affect circuit construction to realise tuning. For the PIN diodes, signal would be intercepted when it is

working so that some part of the circuit can be denied working and transmission of the signal will be affected. For the varactor diodes, a proper biasing voltage can change the internal capacitance within the element, and then change the overall capacitive impedance of the circuit. PIN diodes have lower RF losses and smaller signal distortion than varactors, while varactors can provide continuous changing property which PIN diodes can't realise. That's the reason why in reconfigurable devices for different functions PIN diodes are widely used while in tunable devices with gradually tuning performance varactors are more favoured. In a sense, the adoption of tuning elements depends on what kinds of performance one wants to get. In recently years, a new kind of tuning element is widely used based on a capacitance network using Micro-Eletro-Mechanical System (MEMS). It is a kind of technique which combines electrical and mechanical tuning concept by using micro-meter level movement to change internal capacitance driven by DC suppliers. The MEMS-based tuning technique has several advantages like low losses, high linearity, high power handling, and lower power consumption. However, it also suffers from many drawbacks such as high difficulty in packaging, high driven voltage requirement and low reliability.

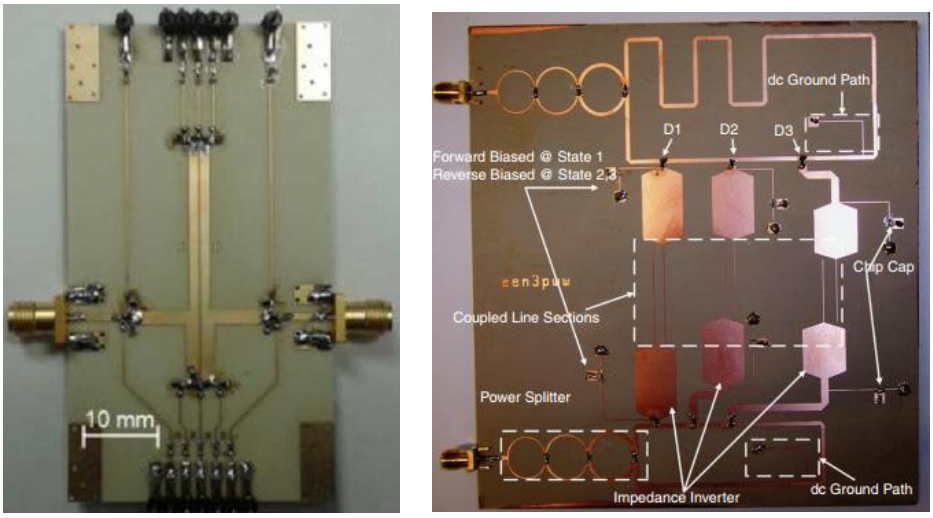

(a) (b)

Fig 2. 2 Developed tunable filters presented in [37] and [38].

2.3.2 Design Methods for Tunable Microwave Devices

Tunable filters have attracted the most attention from researchers since filters are key elements in RF front-ends. For a tunable filter, it is preferable to have high tunable/reconfigurable performance, reduced complexity, compact size, and low cost. Therefore, great efforts have been made and various kinds of tunable filters have been investigated in recent years, including tunable low-pass filters [32], tunable high-pass filters, tunable bandpass filters [33]-[35] and reconfigurable filters

with bandpass-to-bandstop response [36]. Among these filter types, tunable bandpass filters (BPFs) are among the most widely used in multiband or wideband systems. Fig 2.2 shows some typical examples of tunable bandpass filters as presented in [37] and [38].

Many possible designs of tunable BPFs have been investigated using PIN-diode loaded reconfigurable resonators for discrete tuning [39]. Yttrium iron garnet (YIG) filters and Barium-Strontium-Titanate (BST) tunable filters are two types of tunable filters using the electrical tuning method [40]-[41]. However, these two techniques suffer from high power consumption and high loss. RF MEMS switches have low loss and a high power handling capacity and thus have become more and more popular in many designs [42]. However, RF MEMS also have some drawbacks such as difficulty in system integration, low reliability, and they require high driving voltages. Compared with all methods mentioned above, varactor diodes have been more widely used to realise reconfigurable filters [43]-[45].

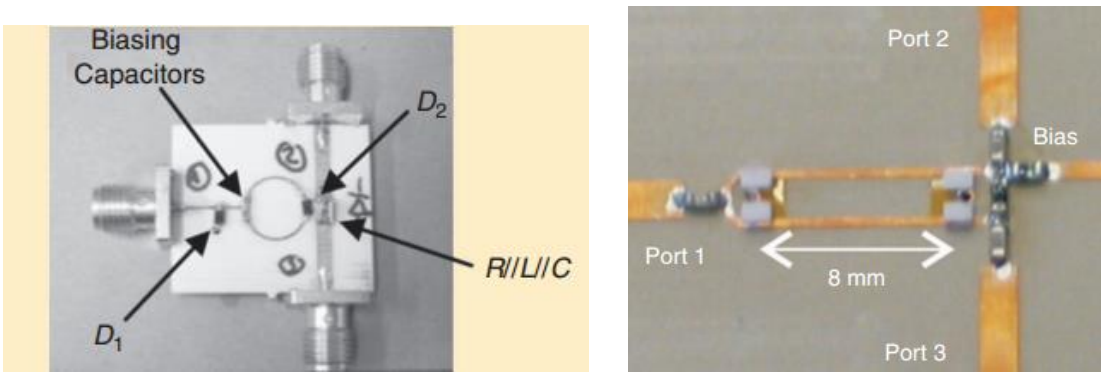

(a) (b)

Fig 2. 3 (a) tunable power divider with 2:1 power division based on a ring structure [57]; (b) frequency agile power divider covering frequency range of 1.7 GHz to 2.4 GHz **[62]**.

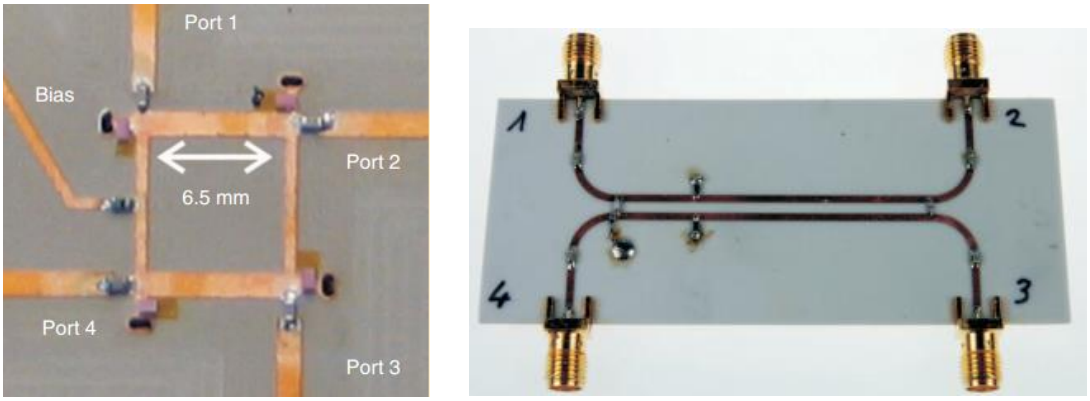

(a) (b)

Fig 2. 4 (a) Freqency agile tunable coupler; (b) tunable coupler with tuning coupling ratio **[62]**.

Usually, tunable bandpass filters can be classified based on their reconfigurability into three main types: tunable bandwidth with fixed centre frequency [46]; tunable centre frequency with constant bandwidth [47]-[48]; and tunable bandwidth and tunable centre frequency [49]-[52]. Among these, the third type is the most needed and widely used due to the flexibility that it can offer when used in wideband or multiband systems, especially if the utilized filters have a wide tuning range for both the centre frequency and bandwidth. To realise that target, different kinds of resonators have been investigated and adopted. Notable examples of these resonators include cascaded structures [15], patches [45], comb-lines [51], multi-mode resonators [52], and loop-shaped resonators [53]. When designing tunable BPFs, creating controllable and adjustable transmission zeros for better selectivity is another important issue of the design. Examples of the structures that have tackled this issue include using varactor loaded dual-mode microstrip open-loop resonator [54], stub-loaded resonators [55] and T-shaped dual-mode resonator [56].

For tunable power divider designs, it is desired to include controllable filtering response for circuit miniaturization purpose. To that end, many researchers have managed to realise tunability of centre frequency [57]-[58] or operating band range [59]-[60]. However, these designs still can't change the amplitude of power at output terminations. In [61], though a planar structure with variable amplitude ratio was presented, it suffered from the obvious drawback of uncontrolled phase performance at three output ports. Fig 2.3(a) shows a design of a tunable power divider with 2:1 power division based on a ring structure [57]. Fig 2.4(b) shows another frequency agile power divider which covers frequency range of 1.7 GHz to 2.4 GHz [62]. However, the tunability of both designs is quite limited. After investigating the state-of-the-art literature, it was found that though some progress have been done in the field of tunable filtering power dividers, tunable power dividers with a variable power division and controllable filtering response are yet to be developed.

Tunable couplers, which are common devices that are widely used in various tunable microwave systems, have the capability to realise multiple functions or working states using one single device. One of the main tunable aspects of couplers is the operational band. Fig 2.5 (a) shows a typical design of a frequency-agile tunable coupler that has achieved a tunability range of 27% [62]. By loading varactor diodes on a branch-line structure, the narrow operating band of a 3-dB coupler can be shifted [63]-[65]. In [66], a tunable directional coupler was implemented in CMOS to achieve a wide operating frequency tuning range, from 2 to 6 GHz. In another approach, a design using MEMS was used to build a quadrature coupler with a tunable band range [67]. In [68], a tunable crossover was realised with controllable operating frequency. In many cases, such as measurement systems or antenna array feeding networks, the tunable coupling coefficient is much more favourable. Fig 2.4(b) shows a tunable coupler with tuning coupling ratios devised by cascading

two directional couplers and shunting two grounded variable capacitors [62]. In [69], a lumped-element-based directional coupler was integrated onto an MMIC to get electronic control over the coupling coefficient from 1.4 to 7.1 dB. Broadside coupled-line sections were connected with varactors in [70] without degrading the directivity, achieving a tunable coupling range from 3 dB to 11 dB. Rat-race couplers with wideband tunable power dividing ratios were realised in [71]-[72] for the first time. Patch hybrid couplers were built by including varactors on the patterned ground plane in [73]. A MEMS-based directional coupler was proposed to achieve two states (10 dB and 18 dB) coupling factors in [74]. Flexible coupling ratio was realised in [75] using a crossover-based structure with 8% bandwidth. Based on this review, it is clear that there is still a great demand for tunable couplers with a wide range of coupling factor tunability across a wide band range.

Moreover, tunable phase shifters are phase shifters are desired for electronically scanned phased-arrays to have steerable beams and controllable radiating direction. In microwave systems, analogue phase shifters have the distinctive merit of being able to generate a continuous phase shift by voltage-controlled tuning elements. In microwave systems, it is preferred to have analogue tunable phase shifters, which will be further described next. Since the most common analogue phase shifters are reflection-type phase shifters, the major focus on tunable phase shifters is also on those of the same type. A four-port network (3-dB quadrature coupler) is used to split the signal into two orthogonal parts, which would reflect back at the reflecting circuits, and, combined together, have a differential phase at the output port. This concept was initially put forward in [76], followed by several further studies using a microstrip [77], and BST substrate [78]. Later the effect of the reflecting circuits on the output termination began to be investigated so as to improve the overall performance of the phase shifters. A small insertion-loss variation was found in [80] by shunting the series resonated varactor with a resistor. To reach full 360˚ relative phase shift, two series resonant loads interconnected with extra transmission lines were adopted [81], resulting in a phase shifting range of more than 400˚.

2. 4 Design Technology for Microwave Sub-systems

2.4.1 Antenna Arrays and Phased Arrays

Antennas are transition devices between a guided wave and a free-space wave which interface circuits and space. An antenna array is a kind of microwave sub-system, which composes of a set of antennas connected together in such a way that they can have specific amplitude and phase relationship. There are numerous applications for antenna arrays, such as broadcasting,

telecommunications, satellite and radar systems, naval or airline usage, weather forecasting, global positioning, radio-frequency identification (RFID), etc. The array's pattern is a product of the element pattern and the array factor, which is related to driven energies and the organization order of antenna elements. In modern microwave systems, steerable antenna arrays have become more and more in favour, especially in moving objects like vehicles or cell phones. There are several kinds of tuning methods for steering, including manually or mechanically steerable antennas, switched-beam arrays, digital tuning arrays, and electrically controlled phased arrays.

Among all these methods, phased arrays are the most widely investigated and used in modern wireless systems, due to their fast transition speed and the easy controllability of their radiation patterns. The principle of phased arrays is to change the radiation pattern to a given angle in free space by allocating a different phase shift (or amplitude) without physical movement [82]. Usually, a phased array is fed by feeding architectures called beam-forming networks which can provide equal interval differential phase distribution. Numerous design analyses and architectures for microwave and millimetre wave phased arrays have been reported in the past decades [83]-[85]. Fig 2.5 illustrates a typical diagram of a transceiver based microwave system using a beam-forming network that provides feeding power for the antenna/phased arrays. Following the sequence from input to output, there are the transceiver, tunable bandpass filters, circulator, beam-forming network and antenna array. The beam-forming network is definitely the most critical part of the system as it is in charge of controlling the phase and magnitude of the radiation pattern. Although at the theoretical and algorithmic level this is quite mature for the optimization of arrays, there still remains a big challenge for designers to have suitably quality feeding networks on the electrical and physical level. There is also a difficulty in building microwave feeding networks, especially controllable feeing ones, to meet fast speed, large data capacity and bandwidth requirements.

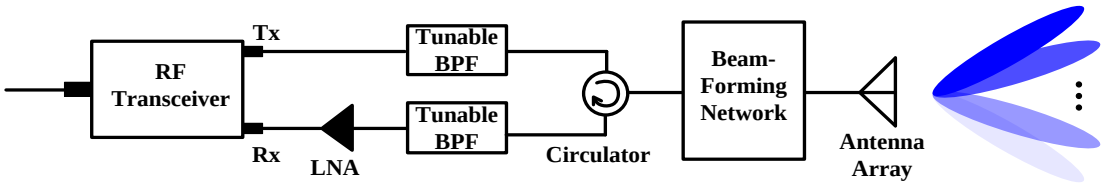

Fig 2. 5 Block diagram of a transceiver based microwave system for beam-forming of antenna arrays.

2.4.2 Beam-forming Networks

It is critical to design appropriate feed architectures for antenna arrays. Array feed architectures, which are usually referred to as beam-forming networks, use RF switches, phase shifters, and

attenuators. Beam-forming is a crucial technique in microwave detection systems, typically used to control signal amplitude and phase with multiple antennas or radiating elements in such applications as phased-array radar systems and biomedical imaging systems. Beam-forming can be used at both the transmitting and receiving ends in order to achieve spatial selectivity. By controlling the amplitude and phase of signals fed to it for each antenna element in an array, a beam-forming network (BFN) can ultimately control the positions of the antenna system's main beam, as well as its side-lobe levels. This means that the BFN to the antennas allows beam steering without having to physically move the antennas.

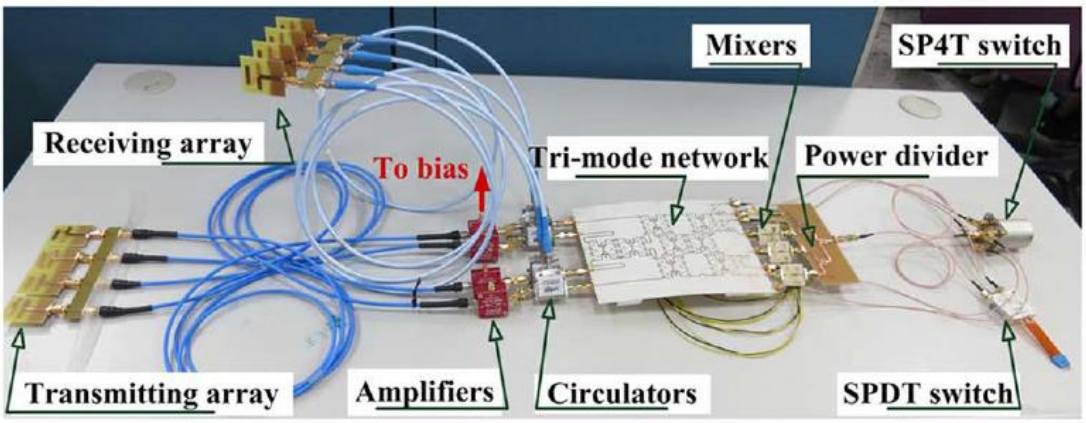

(a)

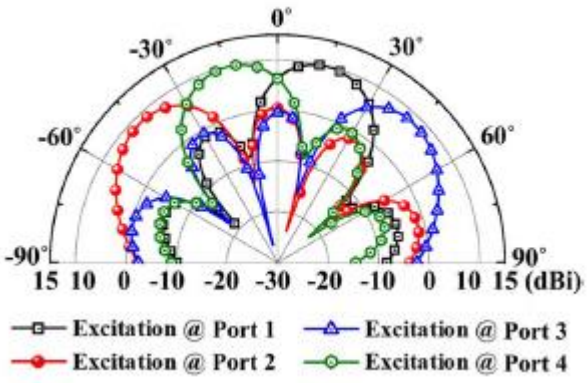

(b)

Fig 2. 6 (a) Design of a beam-switching network presented in [96]; (b) Measured radiation patterns of the phased array at 0.7 GHz.

Some researchers have managed to build feeding networks for antenna arrays to get the desired array patterns [86]-[90]. In all of these works, an unequal power division of multi-port power dividers was designed to allocate a certain amount of power to each port. In this way, it is possible for the feeding power of the array to meet a certain kind of power distribution, so that the desired array beam can be produced. Though beam-width and side-lobe levels can be affected by this means, it is unlikely to change or steer the beam radiation direction. On the other hand, beam-forming can

be realised with advanced RF topologies, among which the Butler matrix is a common way to achieve selectable beams. First presented in [91], the Butler matrix is especially of interest due to its low loss, cost efficiency, and compactness. Typical Butler matrices include 4 × 4, 8 × 8, and 16 × 16 formats, which are usually composed of quadrature hybrid couplers, crossovers, and phase shifters. Although many Butler matrix designs have been presented and applied to BFNs in recent years [92]-[96], they suffering from the drawback of an incapacity to be able to continuously tune the beam angle and multiple input sources.

A more straightforward way is to build a steerable beam-forming network by cascading power dividers with tunable phase shifters, which includes tuning elements in phase shifters to change the phases of the array elements. An electrically steered method was mentioned in some previous works [97], where tunable phase shifters were added to attain continuous tuning. However, the achieved beam angle tuning range was very limited. Improved scanning features with a wider steering angle were reported in [98]. In [99], the design involved a hybrid adaptive antenna array and associated digital beam-forming algorithms for achieving high-speed long-range communications in the millimetre wave frequency bands. Phase shifters with pin-diodes or varactors have been widely adopted in beam-forming networks [100], due to their low cost and compact nature. However, a significant drop of total gain during the steering process remains a big issue. Fig 2.6 shows a design example of a beam-forming network design which is able to switch the beam to certain directions [101]. This idea is quite novel, but the design is unable to tune the beam in a continuous manner. By having reviewed all the work reported above, it is evident that there remains a research gap for tunable beam-forming network designs to have tunable terminal amplitude and phase capability.

2.5 Summary

In this chapter, a thorough literature review has been presented to show the state-of-the-art development of microwave devices, especially tunable devices, and their applications in beam-forming networks for antenna and phased arrays. It has been clearly shown that there is still a great gap in the development of microwave devices to fulfill the requirement of high-speed and multi-functional systems. In the following chapters, various multi-functional microwave devices will be presented, all of which have accomplished flexibility, agility, and reliability, which is the main pursuit of this thesis.

Chapter 3: Design Methodologies

3.1 Introduction

This chapter will provide general design methodologies which will be used for analysis and designing of microwave devices and sub-systems. For the development of microwave devices, transmission characteristics are the main focuses which require proper design procedures and synthesis methods to characterize these parameters. Each device can be regarded as a network with multiple ports. To analyse such kind of networks, related parameters are required to be measured. In this thesis, main parameters of microwave networks investigated include the scattering parameters and ABCD matrix. Due to the reciprocity of a network, structures of microwave components are usually symmetrical, which makes even-/odd-mode analysis method necessary and useful. Coupled-line structures, including two-line and three-line coupled-line structures, are analysed and discussed using the even-/odd-mode analysis method. Moreover, the fabrication technique and tuning elements used for all the designs included in the thesis are microstrip transmission lines and varactor diodes, whose main principles are also discussed in this section.

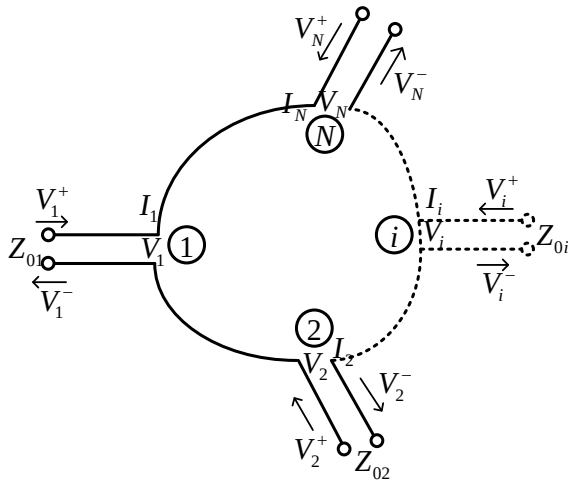

Fig 3. 1 Diagram of an N-port network.

3.2 Fundamental Theoretical Principles

3.2.1 N-port Networks and Scattering Parameters

Before entering the topic of the thesis, to help with understanding of design process, some fundamental principles and design approaches are mentioned in this section. In microwave theory, each device can be considered as an N-port network, which is described by scattering, impedance and transmission parameters. By analysing the related parameters of an N-port network, one is able

to know the details of inner part of the network, which reveal possible functions of the device. Fig 3.1 depicts the diagram of a typical N-port network. It composes of multiple ports (N is the total port number, and *i* refers to the *i*th port, where $i \in 1, 2, \ldots, N$) and each port has an incident wave and a reflected wave which are denoted as V_i^+ and V_i^-, respectively. Correspondingly, at each port there is an incident current I_i^+ and a reflected current I_i^-. For each port, the total voltage and current can be written as

$$V_i = V_i^+ + V_i^- \tag{3.1}$$

$$I_i = I_i^+ + I_i^- \tag{3.2}$$

Therefore, the characteristic impedance at the *i*th port is

$$Z_{0i} = \frac{V_i}{I_i} = \frac{V_i^+ + V_i^-}{I_i^+ + I_i^-} \tag{3.3}$$

For an N-port network, the voltage of each port can be related to the currents and impedances at all ports, and the total voltages can be represented as:

$$\begin{bmatrix} V_1 \\ V_2 \\ \vdots \\ V_N \end{bmatrix} = \begin{bmatrix} Z_{11} & Z_{12} & \cdots & Z_{1N} \\ Z_{21} & Z_{22} & \cdots & Z_{2N} \\ \vdots & \vdots & \ddots & \vdots \\ Z_{N1} & Z_{N2} & \cdots & Z_{NN} \end{bmatrix} \begin{bmatrix} I_1 \\ I_2 \\ \vdots \\ I_N \end{bmatrix} \tag{3.4}$$

Here the N × N matrix is called impedance matrix. On the other hand, if the current at each port is related to the voltages at all ports, one can find the following relation:

$$\begin{bmatrix} I_1 \\ I_2 \\ \vdots \\ I_N \end{bmatrix} = \begin{bmatrix} Y_{11} & Y_{12} & \cdots & Y_{1N} \\ Y_{21} & Y_{22} & \cdots & Y_{2N} \\ \vdots & \vdots & \ddots & \vdots \\ Y_{N1} & Y_{N2} & \cdots & Y_{NN} \end{bmatrix} \begin{bmatrix} V_1 \\ V_2 \\ \vdots \\ V_N \end{bmatrix} \tag{3.5}$$

The N × N matrix is denoted as the admittance matrix. However, both of the impedance matrix and admittance matrix are not suitable for describing transmission characteristics of an N-port network, since measurement of current at microwave frequency band is extremely difficult. Therefore, it is more common and popular to use the scattering parameters, which represent the voltage of the reflected waves with that of all the incident waves, as shown below:

$$\begin{bmatrix} V_1^- \\ V_2^- \\ \vdots \\ V_N^- \end{bmatrix} = \begin{bmatrix} S_{11} & S_{12} & \cdots & S_{1N} \\ S_{21} & S_{22} & \cdots & S_{2N} \\ \vdots & \vdots & \ddots & \vdots \\ S_{N1} & S_{N2} & \cdots & S_{NN} \end{bmatrix} \begin{bmatrix} V_1^+ \\ V_2^+ \\ \vdots \\ V_N^+ \end{bmatrix} \tag{3.6}$$

Each element in the [S] matrix is denoted as $S_{ij} = \left.\frac{V_i^-}{V_j^+}\right|_{V_k^+=0,k\neq j}$, which means that S_{ij} represents the ratio between the voltage of reflected wave at the ith port and that of the incident wave at the *j*th port, while the voltages at other *N*-1 ports are equal to zero. In this way, it is easy to get the transmission characteristics by imposing excitations at the certain ports.

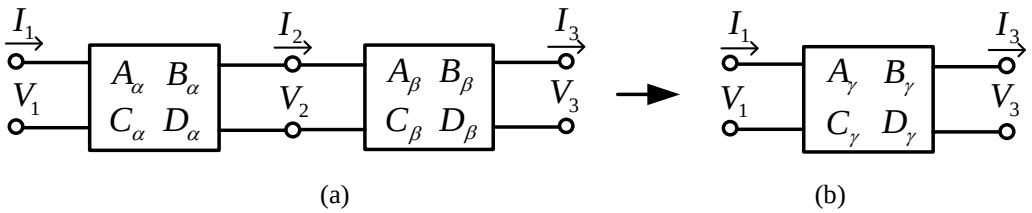

(a) (b)

Fig 3. 2 (a) Cascade of two two-port networks; (b) its equivalent form.

3.2.2 ABCD Matrix and Conversion with Scattering Parameters

In the last section, we have known that the scattering matrix is very convenient in deriving the transmission property of a network. In practice, devices are connected with each other in series to construct a sub-system. In this case, it is much favoured to have transmission parameters which can be multiplied from one to another. A kind of ABCD matrix (or [A] matrix) is able to realise this function, and thus often used for analysis of cascaded structures. Assume two networks that are cascaded in series, as indicated in Fig 3.2 (a). For the two-port network α, the ABCD matrix is defined as:

$$\begin{bmatrix} V_1 \\ I_1 \end{bmatrix} = \begin{bmatrix} A_\alpha & B_\alpha \\ C_\alpha & D_\alpha \end{bmatrix} \begin{bmatrix} V_2 \\ I_2 \end{bmatrix} \tag{3.7}$$

Here A_α, B_α, C_α and D_α represent the element of [A] matrix of the network α. For the second two-port network β, the ABCD-matrix can be expressed as:

$$\begin{bmatrix} V_2 \\ I_2 \end{bmatrix} = \begin{bmatrix} A_\beta & B_\beta \\ C_\beta & D_\beta \end{bmatrix} \begin{bmatrix} V_3 \\ I_3 \end{bmatrix} \tag{3.8}$$

Now substituting V_2 and I_2 from (3.8) into (3.7), one can get

$$\begin{bmatrix} V_1 \\ I_1 \end{bmatrix} = \begin{bmatrix} A_\alpha & B_\alpha \\ C_\alpha & D_\alpha \end{bmatrix} \begin{bmatrix} A_\beta & B_\beta \\ C_\beta & D_\beta \end{bmatrix} \begin{bmatrix} V_3 \\ I_3 \end{bmatrix} \tag{3.9}$$

Therefore, the overall ABCD matrix of two networks from port 1 to port 3 can be represented as a new network γ as seen in Fig 3.2 (b), whose ABCD matrix is:

$$\begin{bmatrix} A_\gamma & B_\gamma \\ C_\gamma & D_\gamma \end{bmatrix} = \begin{bmatrix} A_\alpha & B_\alpha \\ C_\alpha & D_\alpha \end{bmatrix} \begin{bmatrix} A_\beta & B_\beta \\ C_\beta & D_\beta \end{bmatrix} \tag{3.10}$$

In this way, one manages to calculate the product of two cascaded networks. It is the same thing to calculate any cascaded structures with multiple stages. However, similar to the impedance and admittance matrices, the ABCD matrix is also suffering from the difficulty in measuring the current at microwave frequency range. So, it is necessary to build a transformation method to express the scattering parameters using ABCD matrix, as given below:

$$S_{11} = \frac{A + B/Z_0 - CZ_0 - D}{A + B/Z_0 + CZ_0 + D} \tag{3.11}$$

$$S_{12} = \frac{2(AD - BC)}{A + B/Z_0 + CZ_0 + D} \tag{3.12}$$

$$S_{21} = \frac{2}{A + B/Z_0 + CZ_0 + D} \tag{3.13}$$

$$S_{22} = \frac{-A + B/Z_0 - CZ_0 + D}{A + B/Z_0 + CZ_0 + D} \tag{3.14}$$

With the help of (3.11) – (3.14), it is convenient to use ABCD matrix to calculated cascaded structure at first, and then convert the overall ABCE matrix into scattering parameters, so that one can get the overall transmission characteristics of the whole structure.

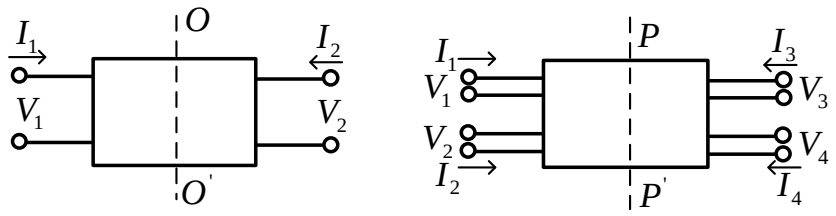

(a) (b)

Fig 3. 3 (a) A symmetrical two-port network; (b) asymmetrical four-port network.

3.3 Even- and Odd-mode Analysis Method

In this section, a popular analysis method for symmetrical networks called even- and odd-mode analysis method will be introduced. The core principle for this method is the symmetry of a network, which enables a complex network downgrade to two or more sub-networks. For instance, the

voltages of a symmetrical two-port network are denoted as V_1 and V_2, as described in Fig 3.3(a). These two voltages can be written as another form as:

$$\begin{bmatrix} V_1 \\ V_2 \end{bmatrix} = \begin{bmatrix} \frac{1}{2}(V_1 + V_2) \\ \frac{1}{2}(V_1 + V_2) \end{bmatrix} + \begin{bmatrix} \frac{1}{2}(V_1 - V_2) \\ -\frac{1}{2}(V_1 - V_2) \end{bmatrix} \tag{3.15}$$

If we define that

$$\begin{bmatrix} V_e \\ V_e \end{bmatrix} = \begin{bmatrix} \frac{1}{2}(V_1 + V_2) \\ \frac{1}{2}(V_1 + V_2) \end{bmatrix} \tag{3.16}$$

$$\begin{bmatrix} V_o \\ -V_o \end{bmatrix} = \begin{bmatrix} \frac{1}{2}(V_1 - V_2) \\ -\frac{1}{2}(V_1 - V_2) \end{bmatrix} \tag{3.17}$$

Here $[V_e \quad V_e]^T$ and $[V_o \quad -V_o]^T$ are called even-mode excitation and odd-mode excitation, respectively. For the even-mode excitation, the magnitude and phase of two signals are identical, which means that it is a kind of symmetrical excitation; for the odd-mode excitation, it has two equal magnitude and out-of-phase sources, which means that it is a kind of anti-symmetrical excitation. Therefore, the symmetric plane (OO') in Fig 3.3(a) can be seen as a perfect magnetic wall (H-wall) when the even-mode excitation is applied and as a perfect electrical wall (E-wall when the odd-mode excitation is applied.

Substituting (3.16) and (3.17) into (3.15), one can re-write the voltage of two sources as

$$\begin{bmatrix} V_1 \\ V_2 \end{bmatrix} = \begin{bmatrix} V_e + V_o \\ V_e - V_o \end{bmatrix} \tag{3.18}$$

Similarly, if the source characteristic impedances is Z_o, for the current it has the following relation:

$$\begin{bmatrix} I_1 \\ I_2 \end{bmatrix} = \begin{bmatrix} I_e + I_o \\ I_e - I_o \end{bmatrix} \tag{3.19}$$

In summary, the algebraic sum of the even-mode excitation and odd-mode excitation is equivalent to the original format, which means that the transmission characteristics can be divided into simpler formats and analysed under even- and odd-mode excitations. In microwave device design, for a two-port network like a filter, usually the even- and odd-mode circuits are used for calculating positions of resonant frequencies and transmission zeros as well as calculating the scattering

parameters. The even-/odd-mode analysis can also be used in symmetrical three-port networks like power dividers. The principle is similar to that of two-port networks.

For four-port networks with reciprocity like couplers, the even- and odd-mode analysis method can help with downgrading the networks to simpler two-port networks, as shown in Fig 2.3 (b). Due to the symmetrical property of the structure, the circuit can be divided into two parts along the symmetrical plane *P-P'*, where the even-mode and odd-mode transmission coefficients and reflection coefficients are denoted as S_{11e}, S_{21e}, S_{11o} and S_{21o}. The general scattering parameters of the whole structure can be expressed as:

$$S_{11} = S_{22} = S_{33} = S_{44} = \frac{S_{11e} + S_{11o}}{2} \tag{3.20}$$

$$S_{21} = S_{21} = S_{43} = S_{34} = \frac{S_{11e} - S_{11o}}{2} \tag{3.21}$$

$$S_{31} = S_{13} = S_{24} = S_{42} = \frac{S_{21e} - S_{21o}}{2} \tag{3.22}$$

$$S_{41} = S_{14} = S_{23} = S_{32} = \frac{S_{21e} + S_{21o}}{2} \tag{3.23}$$

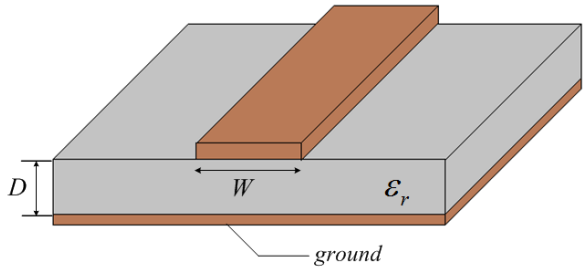

Fig 3. 4 Schematic of microstrip line.

3.4 Microstrip Technique

3.4.1 Microstrip Line

Microstrip is a typical kind of fabrication technique of electrical transmission line that can be fabricated using printed circuit board. It is convenient to use for microwave component designs like filters, power dividers, couplers, antennas, etc. Compared with other fabrication techniques, microstrip has multiple advantages like low volume, easy fabrication, low cost, high reliability, easy integration, wide operating frequency range, and so on. In this thesis, the microstrip technique is adopted for modelling all the designs using electromagnetic simulation.

Microstrip line usually consists of a metal line mounted on a substrate with dielectric constant of ε_r and a metal ground on the bottom, as indicated in Fig 3.4. If the substrate is absent ($\varepsilon_r = 1$), there is only air in between the conductor and ground plane, leading to propagation of pure TEM (transverse-electromagnetic) wave. However, due to the existence of the substrate ($\varepsilon_r > 1$) and the region of air above the substrate, it is impossible to realise the phase matching alone the interface between the air region and the substrate, because the propagation speed of TEM wave in the air is c, while it is c/ε_r in the substrate. Due to this reason, microstrip technique does not support propagation of pure TEM wave. In reality, however, the thickness of the substrate is much smaller than the wave-length of the propagating wave ($D \ll \lambda$), and thus the microstrip technique can support such kind of quasi-TEM wave field distribution, which is very similar to the TEM wave. The phase velocity v_p and propagation constant β can be expressed as:

$$v_p = \frac{c}{\varepsilon_e} \tag{3.24}$$

$$\beta = k_0\sqrt{\varepsilon_e} \tag{3.25}$$

where c is the speed of light, k_0 is the propagation constant for the free space ($\omega\sqrt{\mu_0\varepsilon_0}$), and ε_e refers to the effective dielectric constant of the substrate, which satisfies the relation of $1 < \varepsilon_e < \varepsilon_r$ and relied on the thickness of the substrate D and width of the conductor W. The effective dielectric constant can be explained as a dielectric constant of an average medium, which can be calculated by the following formula:

$$\varepsilon_e = \frac{\varepsilon_r + 1}{2} + \frac{\varepsilon_r - 1}{2} \cdot \frac{1}{\sqrt{1 + 12\,D/W}} \tag{3.26}$$

Given the dimensions of a microstrip line, its characteristic impedance can be calculated by:

$$Z_0 = \begin{cases} \dfrac{60}{\sqrt{\varepsilon_e}} \ln\left(\dfrac{8d}{W} + \dfrac{W}{4d}\right), & W/D \le 1 \\ \dfrac{120\pi}{\sqrt{\varepsilon_e}[W/D + 1.393 + 0.667\ln(W/D + 1.444)]}, & W/D \ge 1 \end{cases} \tag{3.27}$$

With the given value of Z_0 and the dielectric constant of ε_r, the ratio of W/D can be obtained by:

$$\frac{W}{D} = \begin{cases} \dfrac{8e^A}{e^{2A} - 2}, & W/D < 2 \\ \dfrac{2}{\pi}\left[B - 1 - \ln(2B - 1) + \dfrac{\varepsilon_r - 1}{2\varepsilon_r}\left\{\ln(B - 1) + 0.39 - \dfrac{0.61}{\varepsilon_r}\right\}\right], & W/D > 2 \end{cases} \tag{3.28}$$

where

$$A = \frac{Z_0}{60}\sqrt{\frac{\varepsilon_r + 1}{2}} + \frac{\varepsilon_r - 1}{\varepsilon_r + 1}\left(0.23 + \frac{0.11}{\varepsilon_r}\right)$$

$$B = \frac{377}{2Z_0\sqrt{\varepsilon_e}}$$

On the other hand, the length of a microstrip line with electrical length of ϕ at the frequency of f can be calculated from the following equation:

$$l = \frac{\phi}{\beta} = \frac{\phi \cdot c}{2\pi f \cdot \sqrt{\varepsilon_e}} \tag{3.29}$$

These equations and related equations were derived by Hammerstad and Edward in [102] and [103]. Therefore, in design of microwave components using microwave technique, it is convenient to calculate the dimensions of the structure when the electrical parameters are prescribed. In the following chapters, microstrip technique is widely used and the related dimensions are obtained using the mentioned equations.

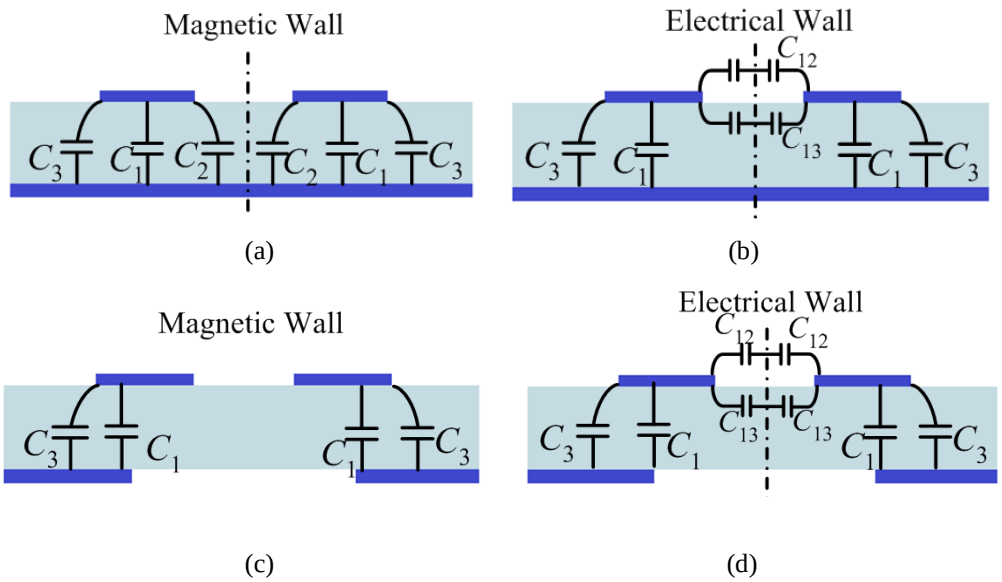

Fig 3. 5 Model of a coupled-line operating in (a) even-mode; (b) odd-mode; coulpled-line with defected ground structure operating in: (c) even-mode; (d) odd-mode.

3.4.2 Microstrip Coupled-line

When two signals travelling along different transmission lines which are near enough to each other, there will be a component between two signals that is common to each other. This phenomenon is

called coupling. These two transmission lines are a pair of coupled-line. Microstrip coupled-lines are very common in microwave components, since they are able to transmit signals from one transmission line to another with direct current (DC) isolation. When we apply a voltage on one microstrip line of a pair of coupled-line, there will be voltage difference between two lines and between lines with the ground, which lead to a charge distribution on metals. This distribution of charges can be modelled with equivalent capacitances, as shown in Figs 3.5 (a) and (b), where even-mode and odd-mode models are given with the grounded capacitances and mutual capacitances.

Since the coupled-line for per length can be modelled with equivalent capacitances, it is possible to estimate the transmission characteristics of a coupled-line by computing these capacitances. This can be done using the even-mode and odd-mode separately, where the magnetic wall and electrical wall are applied along the symmetric line. Assume that the gap between two lines is *s*, The values for the grounded capacitances C_1, C_2 and C_3 are given in [12] as:

$$C_1 = \frac{\varepsilon_r \varepsilon_0 W}{D} \tag{3.30}$$

$$C_2 = \frac{\sqrt{\varepsilon_e}}{2(cZ_0)} - \frac{C_1}{2} \tag{3.31}$$

$$C_3 = \frac{C_2}{1 + A(D/s)\tanh(8s/D)} \sqrt{\frac{\varepsilon_r}{\varepsilon_e}} \tag{3.32}$$

where

$$A = \exp\{-0.1\exp[2.33 - 2.53(W/D)]\} \tag{3.33}$$

For the mutual capacitance C_{12} and C_{13} in the odd-mode model, a term of *k* is defined as

$$k = \frac{s/D}{s/D + 2(W/D)}$$

If $0 \leq k^2 \leq 0.5$, another term of K is defined as

$$K = \frac{1}{\pi} \ln\{2 \frac{1 + (1 - k^2)^{1/4}}{1 - (1 - k^2)^{1/4}}\}$$

else if $0.5 < k^2 \leq 1$,

$$K = \frac{\pi}{\ln\{2(1+\sqrt{k})/(1-\sqrt{k})\}}$$

The mutual capacitance in the air and in the substrate can be expressed as:

$$C_{12} = \varepsilon_0 K \tag{3.34}$$

$$C_{13} = \frac{\varepsilon_0 \varepsilon_r}{\pi} \ln \coth(\frac{\pi s}{4D}) + 0.65 C_f \left(\frac{0.02D}{s}\sqrt{\varepsilon_r} + 1 - \varepsilon_r^{-2}\right) \tag{3.35}$$

Therefore, the even- and odd-mode equivalent capacitances are

$$C_{even} = C_1 + C_2 + C_3 \tag{3.36}$$

$$C_{odd} = C_1 + C_3 + C_{12} + C_{13} \tag{3.37}$$

The even and odd mode characteristic impedances are related to the even and odd mode capacitances C_{even} and C_{odd}:

$$Z_{oe} = \frac{1}{c\sqrt{C_{even} C_{eair}}} \tag{3.38}$$

$$Z_{oo} = \frac{1}{c\sqrt{C_{odd} C_{oair}}} \tag{3.39}$$

where C_{eair} and C_{oair} are the even- and odd-mode capacitances when the dielectric is replaced by air. Using Equations (3.30) – (3.39), one can solve the required W and D for any coupled-line structure using the given type of substrate.

Sometimes a defected ground on the backside of the coupled-line is desired to enhance the coupling between the coupled-line. Since the structure is symmetrical, it is still possible to estimate the transmission characteristics of a coupled-line by computing the modelled equivalent capacitances per length using even- and odd-mode circuit of the structure, as shown in Figs 3.5 (c) and (d). In this case, the even- and odd-mode equivalent capacitances are expressed as

$$C_{even} = C_1 + C_3 \tag{3.40}$$

$$C_{odd} = C_1 + C_3 + 2C_{12} + 2C_{13} \tag{3.41}$$

The values of these capacitances can be used to calculate the physical dimension of the structure using the conformal mapping technique and the Schwartz–Christoffel method. If the coupled-line width, gap, and the ground width are assumed as w_c, s and w_s, the conformal mapping relations between the equivalent capacitances and dimensions of the structure are listed in the following equations [104]:

$$C_{even} = \varepsilon_0 \left[\varepsilon_r \frac{K'(k_1)}{K(k_1)} + \frac{K'(k_2)}{K(k_2)} \right] \tag{3.42}$$

$$C_{odd} = \varepsilon_0 \left[\frac{K'(k_3)}{K(k_3)} + \varepsilon_r \{ \frac{K'(k_1)}{K(k_1)} + \frac{K'(k_4)}{K(k_4)} \} \right] \tag{3.43}$$

where

$$k_1 = \sqrt{\frac{1 + \exp(-\pi \frac{w_s - s}{2D})}{1 + \exp(-\pi \frac{w_s - s - 2w_c}{2D})}} \tag{3.44}$$

$$k_2 = \tanh(\frac{\pi w_s}{4(D + d)}) \tanh(\frac{\pi(w_s + s)}{4(D + d)}) \tag{3.45}$$

$$k_3 = \frac{w_s - 2s}{w_s} \tag{3.46}$$

$$k_4 = \frac{\tanh(\frac{\pi s}{4D})}{\tanh(\frac{\pi(s + 2w_c)}{4D})} \tag{3.47}$$

$$d = \begin{cases} w_c, & w_c > (w_s - s)/2 \\ \frac{w_s - s}{2}, & w_c < (w_s - s)/2 \end{cases} \tag{3.48}$$

3.4.3 Microstrip Three-line Coupled-line

Last section introduced the principle of two-line coupled-line. Sometimes, the transmitted signal needs to be coupled to two different paths. In this case, a kind of three-line coupled-line structure is required. It is composed of three transmission lines which are parallel to each other. The distance between the centreline and sidelines is set to be equal to *s*, and widths of the centre conductor and two side conductors are w_c and w_s, respectively. The structure can be analysed using a three fundamental modes method: even-even, odd-odd and odd-even modes [105]. The per-unit length capacitance distribution of the three-line coupled-line is given in Fig 3.6 (a), while the capacitance distributions of even-even, odd-odd and odd-even mode are shown in Figs 3.6 (b)-(d). For the even-even mode, a magnetic wall is applied at the central plane between the centreline and two sidelines, and only three grounded capacitances exist between each line and the ground. For the odd-odd mode, two sidelines are out-of-phase with respect to the centreline, and central planes between the centreline and two sidelines behave as electrical walls. For the odd-even mode, the two

sidelines are excited with opposite polarity with the centreline grounded. Under all these conditions, the equivalent capacitance for each of three lines can be calculated as:

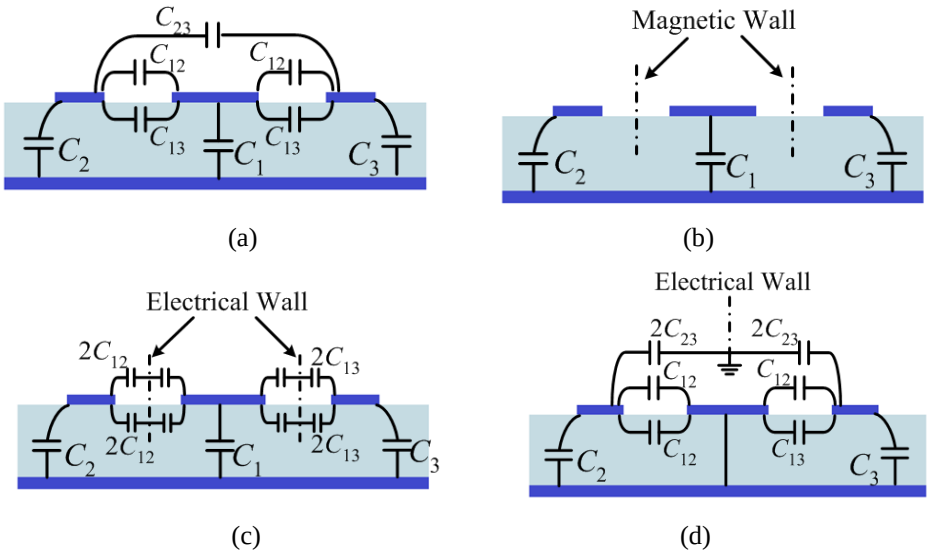

Fig 3. 6 (a) Per-unit length capacitances of the used capacitor-loaded three-line coupled structure and equivalent circuits using three fundamental mode analysis method: (b) even-even mode; (c) odd-odd mode, and (d) odd-even mode.

$$\text{Even-even mode:} \quad C_{1ee} = C_1,\ C_{2ee} = C_2,\ C_{3ee} = C_3 \tag{3.49}$$

$$\text{Odd-odd mode:} \quad \begin{cases} C_{1oo} = C_1 + 2(C_{12} + C_{13}) \\ C_{2oo} = C_2 + 2C_{12} \\ C_{3oo} = C_3 + 2C_{13} \end{cases} \tag{3.50}$$

$$\text{Odd-even mode:} \quad \begin{cases} C_{1oe} = \infty \\ C_{2oe} = C_2 + C_{12} + 2C_{23} \\ C_{3oe} = C_3 + C_{13} + 2C_{23} \end{cases} \tag{3.51}$$

where C_m (m = 1, 2, 3) refers to the capacitance per unit length between the transmission line and the ground, and C_{mn} is defined as the mutual capacitances per unit length between any two lines (m, n = 1, 2, 3). Here one can regard C_{23} equal to 0 since the mutual coupling between two sidelines is tiny and negligible. C_{v1} and C_{v2} are the capacitances of the added varactors between the centreline and sidelines. The characteristic impedance of each of three lines at any of three modes can be found using the relation in [105]:

$$Z_{xij} = \frac{1}{v_{ij} C_{xij}} \tag{3.52}$$

where x is the line number, ij refers to the mode (can be *ee*, *oo* or *oe*), v_{ij} is the phase velocity of the ij mode and its value can be calculated from the formula in [12]:

$$v_{ij} = \frac{c}{\sqrt{\varepsilon_{ij}}} \tag{3.53}$$

Here c is the velocity of light in free space and ε_{ij} is the effective dielectric constant of propagation at the mode of ij. The dielectric constant of even-even mode (ε_{ee}) can be considered as the same of that of the substrate (ε_r), whereas for the odd-odd mode (ε_{oo}) and odd-even mode (ε_{oe}), the effective dielectric constant is regarded as $(1+ \varepsilon_r)/2$. Since for the odd-even (OE) mode, the central line (line I) is grounded, thus the coupling only occurred between the two side lines which is negligible. Therefore, the OE mode can be considered have no effect on the coupling of the entire structure and the proposed structure can be regarded as a pair of two lines coupled line (the first pair of two lines coupled line is line I and line II, the second pair of two lines coupled line is line I and line III).

The Z matrix of the two lines asymmetric coupled line can be expressed using the characteristic mode impedance as

$$Z = \begin{bmatrix} \frac{Z_e^a + Z_e^a}{2s} & \frac{Z_e^a - Z_e^a}{2s} & \frac{(Z_e^a - Z_o^a)\sqrt{1-s^2}}{2s} & \frac{(Z_e^a + Z_o^a)\sqrt{1-s^2}}{2s} \\ \frac{Z_e^b - Z_e^b}{2s} & \frac{Z_e^b + Z_e^b}{2s} & \frac{(Z_e^b + Z_o^b)\sqrt{1-s^2}}{2s} & \frac{(Z_e^b - Z_o^b)\sqrt{1-s^2}}{2s} \\ \frac{(Z_e^b - Z_e^b)\sqrt{1-s^2}}{2s} & \frac{(Z_e^b + Z_e^b)\sqrt{1-s^2}}{2s} & \frac{Z_e^b + Z_o^b}{2s} & \frac{Z_e^b - Z_o^b}{2s} \\ \frac{(Z_e^a + Z_e^a)\sqrt{1-s^2}}{2s} & \frac{(Z_e^a - Z_e^a)\sqrt{1-s^2}}{2s} & \frac{Z_e^a - Z_o^a}{2s} & \frac{Z_e^a + Z_o^a}{2s} \end{bmatrix} \tag{3.54}$$

where $s = j\tan\theta$ and for the quarter-wavelength coupled line, $s = j$, a and b are the line number. Based on (3.45), the coupling factor between the two coupled lines is:

$$K = \frac{Z_e^{a,b} - Z_e^{a,b}}{\sqrt{(Z_o^{a,b} + Z_e^{a,b})(Z_o^{b,a} + Z_e^{b,a})}} \tag{3.55}$$

From Fig 2.6, it can be seen that the even mode and odd mode of the two coupled lines structure correspond to the odd-odd (OO) mode and even-even (EE) mode of the proposed structure. Therefore, the coupling factors between line I and line II (K_{12}) and line I and line III (K_{13}) can be expressed as:

$$K_{12} = \frac{Z_{2ee} - Z_{2oo}}{\sqrt{(Z_{1ee} + Z_{1oo})(Z_{2ee} + Z_{2oo})}} \tag{3.56}$$

$$K_{13} = \frac{Z_{3ee} - Z_{3oo}}{\sqrt{(Z_{1ee} + Z_{1oo})(Z_{3ee} + Z_{3oo})}} \tag{3.57}$$

Combining (3.47)-(3.50) with (3.54) and (3.55), and considering the effect of C_{v1} and C_{v2} on the structure, the coupling factors can be modified and expressed with the equivalent capacitances and varactors as

$$K_{12} = \frac{C_{2oo} - C_{2ee} + 2C_{v1}}{\sqrt{(C_{1ee} + C_{1oo} + 2C_{v1} + 2C_{v2})(C_{2ee} + C_{2oo} + 2C_{v1})}} \tag{3.58}$$

$$K_{12} = \frac{C_{3oo} - C_{3ee} + 2C_{v2}}{\sqrt{(C_{1ee} + C_{1oo} + 2C_{v1} + 2C_{v2})(C_{3ee} + C_{3oo} + 2C_{v2})}} \tag{3.59}$$

Based on the symmetric feature of the proposed structure, it can be stated that

$$C_2 = C_3, \;\; C_{12} = C_{13} \tag{3.60}$$

Using the conformal mapping technique and following the procedure used in [12], one can get:

$$C_1 = 2\varepsilon_0 \varepsilon_r \frac{K'(k_1)}{K(k_1)} \tag{3.61}$$

$$C_2 = C_3 = 2\varepsilon_0 \varepsilon_r \frac{K'(k_2)}{K(k_2)} \tag{3.62}$$

$$C_{12} = C_{13} = \varepsilon_0 \{1 + 0.5(1 + \varepsilon_0)\} \frac{K'(k_3)}{K(k_3)} \tag{3.63}$$

where

$$k_1 = \sqrt{\frac{1 + \exp(\frac{\pi w_s}{2D})}{1 + \exp(\pi \frac{w_c}{2D})}} \tag{3.64}$$

$$k_2 = \sqrt{\frac{1 + \exp(\pi \frac{w_c + 2s}{2D})}{1 + \exp(\pi \frac{w_c + 2s + 2w_s}{2D})}} \tag{3.65}$$

$$k_3 = \sqrt{\frac{s(\frac{w_c}{2} + w_s + s)}{(\frac{w_c}{2} + s)(w + s)}} \tag{3.66}$$

$K(k)$ and $K'(k)$: the first kind elliptical integral and its complementary. By using Equations (3.61) – (3.66), one can find the required dimensions for any kind of three-line coupled-line structure.

3.5 Varactor-Diode-Based Techniques

3.5.1 Basic model of Varactor Diodes

As mentioned in Chapter 1, tunable microwave devices are extremely demanded for improving the flexibility and controllability of a system. For a variety of microwave systems, it is desirable to have high tuning speed which is beyond 1 GHz/μs. To obtain the target, varactor diodes are quite excellent for realizing electronic tuning characteristics. As one knows, varactor diodes mainly consist of p-n junction operated in a reverse-biased condition. When the reverse voltage is raised, a certain region inside the diode will increase accordingly, which leads to a decreased capacitance and vice versa. In this way, a possible controllability of the capacitance can be realised by changing the supplied voltage.

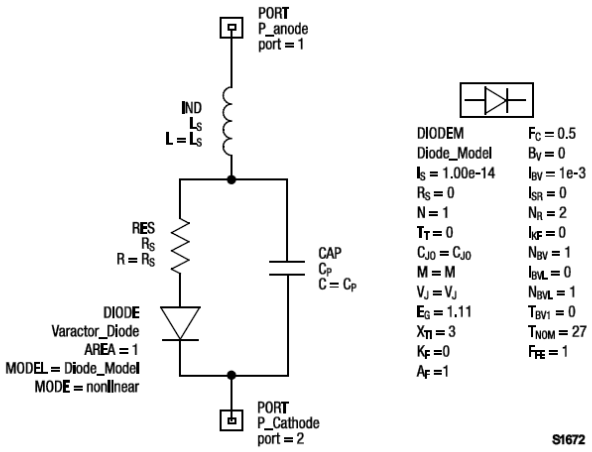

Part Number	CJO (pF)	VJ (V)	M	CP (pF)	RS (Ω)	LS (nH)
SMV1281-011LF SMV1281-079LF	13	14	6	0.62	1.7	1.2

(a)

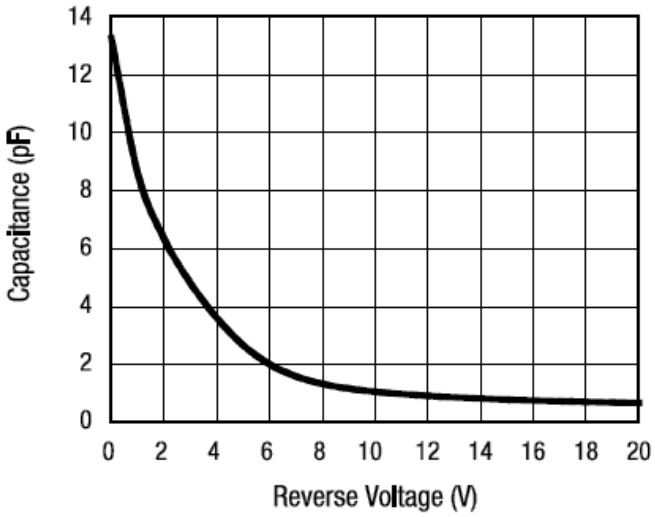

(b)

Fig 3. 7 (a) Equivalent circuit and parameters of the SPICE model of SMV1281 varactors; (b) the capacitance versus reverse voltage.

To depict the characteristics of a varactor diode, a more specific and detailed circuit model is required. Therefore, a kind of simulation program with integrated circuit emphasis (SPICE) model is built to check the behaviour of a varactor diode. This technique is based on the varactor model extraction procedure from *S*-parameter data. Here let's take the Skyworks SMV1281 as an example. Fig 3.7(a) shows the SPICE model equivalent circuit and related parameters for SMV1281 varactors. In this circuit, R_s is the parasitic resistance of the diode; L_s and C_p are the parasitic inductance and capacitance depending on the package.

To predict the performance of the varactor, there is a characteristic curve of the junction capacitance C_j versus the reverse biasing voltage, which can be synthesized by the following equation:

$$C_j = \frac{C_{j0}}{(1 + V/V_j)^{\gamma}} \tag{3.67}$$

where C_j and C_{j0} are the reverse biased variable junction capacitance and junction capacitance without external biasing, respectively; $V$and V_j refer to the applied reverse biasing voltage and built-in junction potential voltage, and γ is a coefficient which is related to C_j and V and depended on the junction doping profile. Based on the given relation between the junction capacitance and biasing voltage, a characteristic curve of tuning capacitance can be plotted, as shown in Fig 3.7(b). In this way, when a certain value of capacitance is needed in a circuit, one can easily find the required biasing voltage based on the characteristic curve.

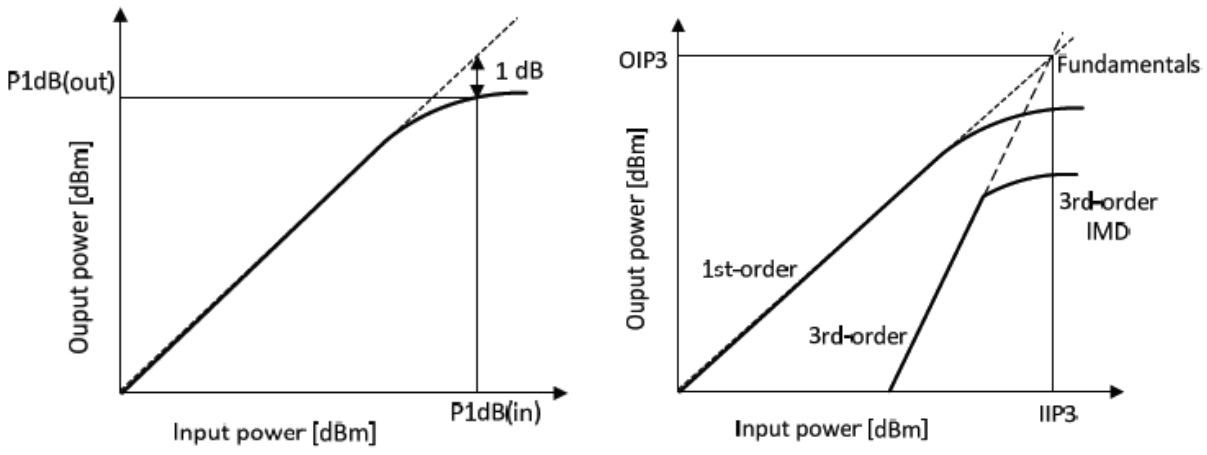

(a) (b)

Fig 3. 8 Illustration of (a) 1-dB compression point (P1dB); (b) the third order intercept point (IP_3).

3.5.2 Non-linearity Characteristics

As one knows, linearity is defined as the power range where a circuit output power remains proportional to its input power. Because of the existence of active components such as pin diodes or varactors, the circuit suffers from non-linearity which results in disproportional of the output signals to the input one. Due to this reason, large signal performance of the circuit needs to be measured. The two most importance parameters are the 1-dB compression point and the third-order intercept point, as illustrated in Figs 3.8 (a) and (b).

The 1-dB compression point (P1dB) defined as the input power level at which the output power of the device is 1 dB below its linear characteristics. Therefore the useful operation area should be in the linear region which is below this point. It is important to know at what point compression begins to occur so input levels can be restricted to prevent distortion. The other parameter is defined by inter-modulation distortions (IMDs) that occur when more than one signal is present at the input of a nonlinear device simultaneously. If the signals are close together in frequency, some of the sum and difference frequencies called intermodulation products produced can occur. The third-order intercept point (IP_3) is expressed in dBm and it refers to the linear (non-saturated) input/output power levels for which the third order IMDs would reach the level of the fundamental components. Third-order products are the most troublesome of the intermodulation effects caused by non-linear operation. The IP_3 value is an imaginary point that indicates when the amplitude of the third-order products equals the input signals. For a varactor diode, both the 1-dB compression point and the third-order intercept point are good indicators of its linearity, which need to be considered and measured during design process.

3.6 Summary

In this chapter, some principal parameters are investigated for measuring the transmission property of multi-port microwave networks. The principles of a popular method called even- and odd-mode analysis method have been introduced. In the following chapters, the proposed microwave devices are usually analysed by the even- and odd-mode method for determining the related parameters. Then, the fabrication technique of microstrip lines is adopted for building EM models, and design equations have been listed for calculating dimensions. Equations for the coupled-line structures are derived, and varactor diodes and non-linear characteristics are discussed.

Chapter 4: Development of Novel Tunable Bandpass Filters

4.1 Introduction

Microwave tunable devices are becoming more and more essential in microwave systems like RF-front ends that require multiple operating bands or functions. To achieve better agility and flexibility of a system, it is favoured to have tunable bandpass filters (BPFs) to control the bandwidth and frequency range of transmitting and rejecting signals. As illustrated in Chapter 2, tunable filters are able to combine several working states within one structure, resulting in great miniaturization of size of circuits and whole systems. As illustrated in Fig 4.1, design of a tunable BPF is typically focused on the reconfigurability of magnitude response with tunable bandwidth (BW) and centre frequency (CF). A desired design is supposed to have tunable bandwidth (from BW_1 to BW_2) at any centre frequency between f_1 and f_2. In a transceiver-based microwave system, different centre frequencies are required for generating stepped frequency in continuous wave. Meanwhile, it is also favoured to have sharp selectivity and stopband rejection for harmonics. To that end, independently controlled transmission zeros (TZs) are also a critical issue to pay attention to during the design process.

In this chapter, new design approaches and several novel structures aimed at multi-functionality and full tunability have been realised. The proposed designs are based on varactor-loaded resonators, including coupled-line resonators, short-ended resonators, and short-stub loaded ring resonators. Electrically tuning is adopted to realise tunable value of capacitance using varactor diodes. To be specific, first of all, a wideband tunable BPF with wide stopband and high selectivity is presented by using a coupled-line structure tapped at its centre with a coupled stub loaded with a short-ended varactor. Then two prototypes of second-order BPF designs are investigated are constructed by utilizing coupled-line resonators and ring resonators with short-ended stubs, respectively. These two designs are able to achieve wide tuning range of both of BW and CF. Last but not the least, a tunable balanced BPF with wide tuning range of CF and BW using coupled-line resonator is developed. All of these designs are built based on theoretical analysis and simulated via full-wave simulation tools. Moreover, experimental verifications are conducted for all designs which confirm the proposed design approaches.

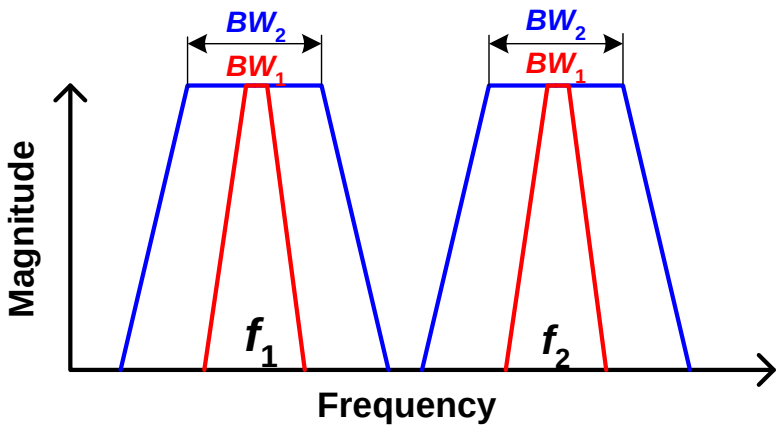

Fig 4. 1 Reconfigurable magnitude of a tunable bandpass filter

4.2 Tunable BPF with Wide Stopband and High Selectivity

This section will present a wideband tunable bandpass filter with controllable TZs and wide spurious-free stopband using a single-layer structure. The goal of this design is to have controllable bandwidth with high level of cut-off selectivity [106] and stopband-rejecting performance [107]-[108]. Generally speaking, to increase the degree of freedom in the bandwidth tunability, the passband of some of the recently investigated filters is defined by two independently adjustable transmission zeros (TZs). In [45], a tunable dual-mode triangular patch filter was proposed to achieve an independent control of the centre frequency and bandwidth. In [109], sharp skirt selectivity and wide bandwidth tuning range were achieved by cascading a tunable BPF and lowpass filter. However, the multilayer structure used in [109] might add some degree of difficulty in the fabrication and circuit integration. Therefore, the following design approach is able to fill up the blank of single-layer tunable BPF with controllable BW, wide upper-stopband rejection and high selectivity.

The proposed design is based on a coupled-line structure tapped at its centre with a coupled stub loaded with a short-ended varactor. The design is aimed at wideband reconfigurable applications requiring more than 40% fractional bandwidth. By tuning the varactors located at the centre of the coupled-line sections, a wide bandwidth tuning range can be extended to more than 100%. This design includes a shunted stub using short-ended coupled-line structure for two reconfigurable TZs that can be independently tuned. Besides, multiple TZs are created within the stopband by the coupled-line sections as well as the shunted stub, to suppress any spurious harmonics across a wide upper-stopband.

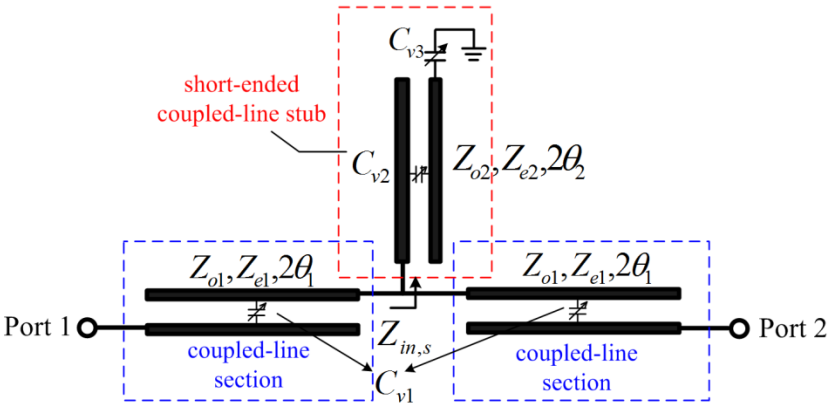

Fig 4. 2 Configuration of the proposed tunable filter.

4.2.1 Analysis of the Proposed Structure

Fig 4.2 depicts the configuration of the proposed filter. It is composed of two coupled-line sections tapped at their connection with a coupled stub. A varactor, C_{v1}, is added at the centre of each of the coupled-line sections to tune the performance within the selected passband. The stub is loaded at its centre by a varactor (C_{v2}) and at its end using a short-ended varactor (C_{v3}). Those two varactors are used to independently tune the transmission zeros (TZs), which define the two edges of the filter's passband and thus the band of the whole design.

The proposed structure can be analyzed using the ABCD-matrix approach. To that end, it is possible to show that the ABCD matrix for any of the coupled-line sections or the coupled stub can be calculated using:

$$[ABCD]_i = \begin{bmatrix} A & B \\ C & D \end{bmatrix}_i = \begin{bmatrix} Z_{11}/Z_{21} & (Z_{11}^2 - Z_{21}^2)/Z_{21} \\ 1/Z_{21} & Z_{11}/Z_{21} \end{bmatrix}_i \tag{4.1}$$

where,

$$Z_{11} = -\frac{jZ_{oi}[1 - \tan\theta_i\,(2Z_{oi}\omega C_{vi} + \tan\theta_i)]}{4(Z_{oi}\omega C_{vi} + \tan\theta_i)} - 0.5jZ_{ei}\cot(2\theta_i) \tag{4.2}$$

$$Z_{21} = \frac{jZ_{oi}[1 - \tan\theta_i\,(2Z_{oi}\omega C_{vi} + \tan\theta_i)]}{4(Z_{oi}\omega C_{vi} + \tan\theta_i)(\cos 2\theta_i - Z_{oi}\omega C_{vi}\sin 2\theta_i)} - 0.5\,jZ_{ei}/\sin(2\theta_i) \tag{4.3}$$

Here, $2\theta_i, Z_{ei}, Z_{oi}$ represent the electrical length, even- and odd-mode impedances of the coupled-line sections or the coupled stub. To that end, i=1 for any of the coupled-line sections and i=2 for the coupled short-ended stub. The input impedance of the loaded stub $Z_{in,s}$ can be calculated using its ABCD parameters.

$$Z_{in,s} = \frac{A_2 Z_l + B_2}{C_2 Z_l + D_2} = \frac{A_2/(j\omega C_{v3}) + B_2}{C_2/(j\omega C_{v3}) + D_2} \tag{4.4}$$

Thus, the ABCD matrix of the whole structure depicted in Fig 4. 2 can be found as:

$$[ABCD]_f = [ABCD]_1 \times [ABCD]_s \times [ABCD]_1 \tag{4.5}$$

where,

$$[ABCD]_s = \begin{bmatrix} 1 & 0 \\ 1/Z_{in,s} & 1 \end{bmatrix} \tag{4.6}$$

Once the ABCD Matrix is obtained, one can derive the S-parameters of the design using the well-known ABCD-to-S-parameters transformation tables shown below

$$S_{11} = \frac{A_f + B_f/Z_0 - C_f Z_0 - D_f}{A_f + B_f/Z_0 + C_f Z_0 + D_f} \tag{4.7}$$

$$S_{21} = \frac{2}{A_f + B_f/Z_0 + C_f Z_0 + D_f} \tag{4.8}$$

Using the aforementioned analysis in Matlab, the performance of the filter for different values of the design parameters can be calculated as shown in Fig 4.3. Based on the iterative solution of (4.1)-(4.8), it was found that the electrical lengths θ_1 and θ_2 depicted in Fig 4.2 should be 45° at the centre frequency 1.8 GHz. It was also noted that the mode impedance of the coupled-line sections and stub have an impact on the minimum band that can be realised. Increasing the values of the even-mode impedance and reducing the values of the odd-mode impedance enable increasing the minimum achievable width of the passband. In the current design in this paper, which aims at wideband applications, the impedances of Z_{e1}, Z_{o1}, Z_{e2} and Z_{o2} are found to be 130, 70, 120, and 68 Ω, respectively, for a minimum fractional band of 45%.

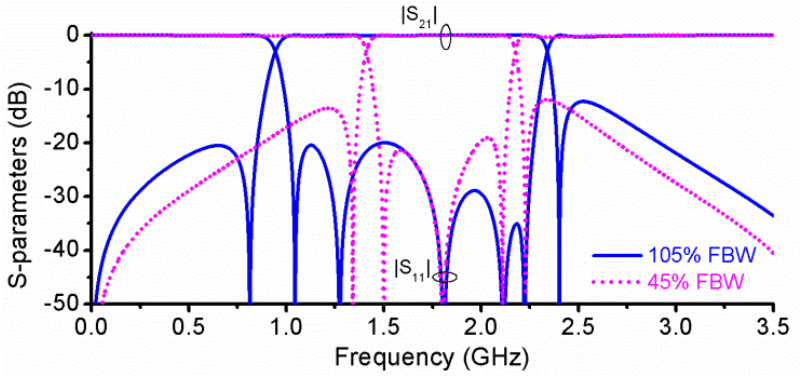

Fig 4. 3 Calculated results at fractional bandwidth of 45% (C_{v1}=0.25, C_{v2}=0.45, C_{v3}=20) and 105% (C_{v1}=1, C_{v2}=6, C_{v3}=5.5). Unit: pF.

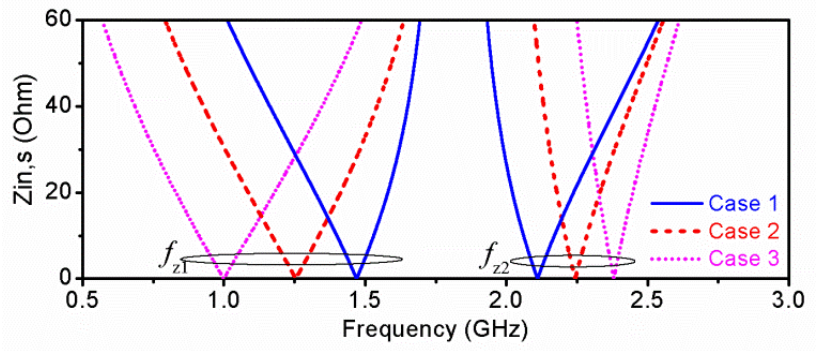

Fig 4. 4 Variation of Zin,s with frequency at different varactor capacitances. (Case 1: C_{v1}=1, C_{v2}=0.1, C_{v3}=20; Case 2: C_{v1}=1, C_{v2}=1, C_{v3}=3; Case 3: C_{v1}=1, C_{v2}=10, C_{v3}=1.5; Unit: pF.)

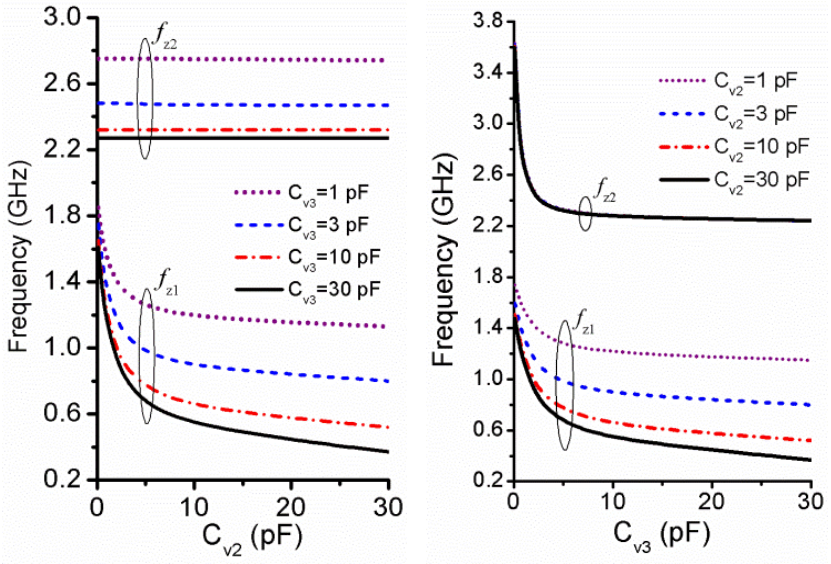

(a) (b)

Fig 4. 5 The relationship between two TZs and C_{v2}, C_{v3}: (a) C_{v2} is variable, and (b) C_{v2} is variable.

4.2.2 Filtering Performance

A snapshot of the calculated results shown in Fig 4.3 indicates a reconfigurable fractional bandwidth (FBW) that can be tuned from 45% to 105%. It is seen that when the bandwidth increases, the value of C_{v1} needs to be increased to keep the performance acceptable within the passband. Since C_{v1} is located at the centre of the coupled-line section, it contributes significantly to the coupling strength of the coupled-line, and thus a requirement to increase C_{v1} indicates the need for a larger effective coupling factor for the coupled structure. The performance of the filter indicates a Chebyshev response with 0.2 dB maximum ripple within the passband. It is observed that additional resonant poles of S_{11} appear within the passband when the FBW is increased from 45% to 105%, as shown in Fig 4. 3.

To verify that the two TZs are actually generated and controlled by the central stub, the input impedance of that stub ($Z_{in,s}$) is calculated and plotted in Fig 4.4, for different values of C_{v2} and C_{v3}. It can be seen that $Z_{in,s}$ has two zero roots that satisfy the condition $Z_{in,s} = 0$, which eventually defines the two TZs (f_{z1} and f_{z2}) of the whole structure of the filter. Based on Fig 4.4 and further calculation depicted in Fig 4.5, the positions of the two TZs are found only related to C_{v2} and C_{v3}. When C_{v2} is increased while C_{v3} is fixed, the first TZ (f_{z1}) moves towards lower frequencies, whereas the second TZ (f_{z2}) remains unchanged, as shown in Fig 4.5 (a). Thus, the lower edge of the passband can be independently reconfigurable by tuning C_{v2}. On the other hand, when C_{v3} is increased while C_{v2} is fixed, both of f_{z1} and f_{z2} move to lower frequencies at the same time as shown in Fig 4.5 (b). This indicates that the upper edge of the passband is also independently reconfigurable by changing both C_{v2} and C_{v3} at the same time. Of course, the tuning of the two TZs is also in accordance with the tunability of bandwidth of the filter.

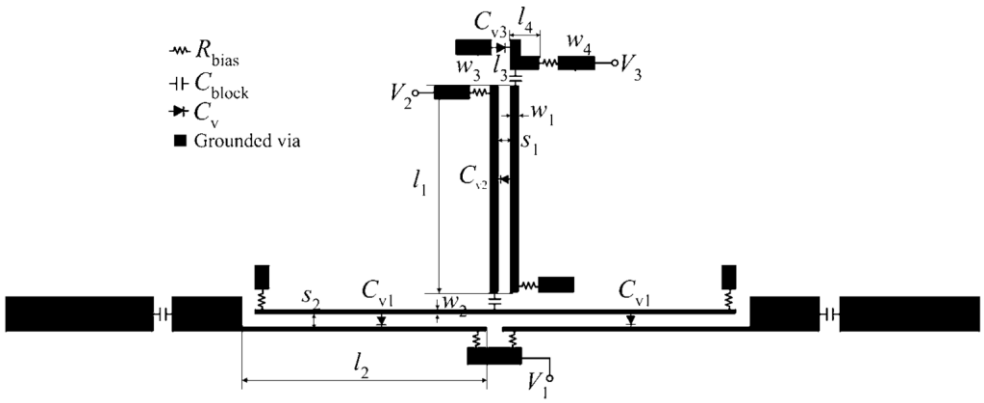

Fig 4. 6 The layout of the proposed tunable filter with biasing circuit.

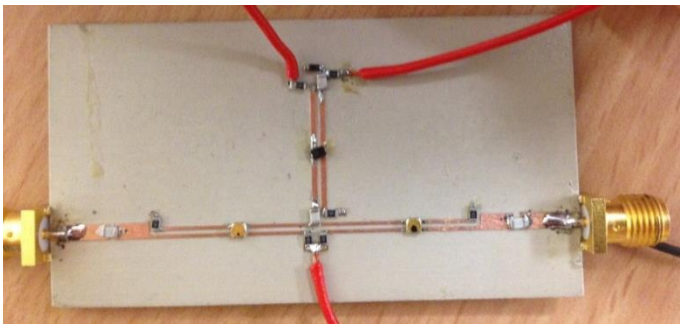

Fig 4. 7 Photograph of the fabricated tunable bandpass filter.

4.2.3 Design and Experimental Verification

To validate the proposed design procedure, a tunable BPF which has a centre frequency around 1.6 GHz and tunable fractional bandwidth (FBW) from 45% to 105% is designed, built and tested. The substrate used in the design is RT/Duriod 6006 with ε_r = 6.15 and h = 1.27 mm. Using the design

Equations (4.1)-(4.8), it is possible to find that the required ranges of values for the varactor capacitances are: C_{v1}=0.2-2 pF, C_{v2}=0.5-15 pF, C_{v3}=2-30 pF. To realise those ranges of values, the hyper abrupt junction tuning varactors SMV2019-219 (0.16-2.25 pF, 0-20 V, R_s=4.8 Ω), SMV1283-011LF (0.52-14.2 pF, 0-26 V, R_s=2.4 Ω), and SMV1213-079LF (1.9-30 pF, 0-8 V, R_s=1.4 Ω) are used for C_{v1}, C_{v2}, and C_{v3}, respectively. The mode impedances (Z_{e1}, Z_{o1}, Z_{e2} and Z_{o2}) are the same as those found in the previous calculations. The EM simulator High Frequency Structural Simulator (HFSS) is used to verify the theoretical calculations. To that end, SPICE models of the aforementioned varactors as provided in [110] are used in the co-simulation within HFSS and Advanced Design System (ADS). Fig 4.6 depicts the configuration of the simulated filter with its biasing circuits. R_{bias} and C_{block} refer to the DC biasing resistor and DC block capacitor, which are Panasonic resistor 100 kΩ and Murata 0402 GRM 100 pF, respectively. The optimized design parameters in (mm) of the filter are found to be: l_1=14.5, l_2=19.5, l_3=1.5, l_4=1.5, w_1=0.72, w_2=0.36, w_3=0.6, w_4=1.0, s_1=0.4, s_2=0.54. The optimized design was then fabricated and tested. A photo of the fabricated structure is shown in Fig 4.7.

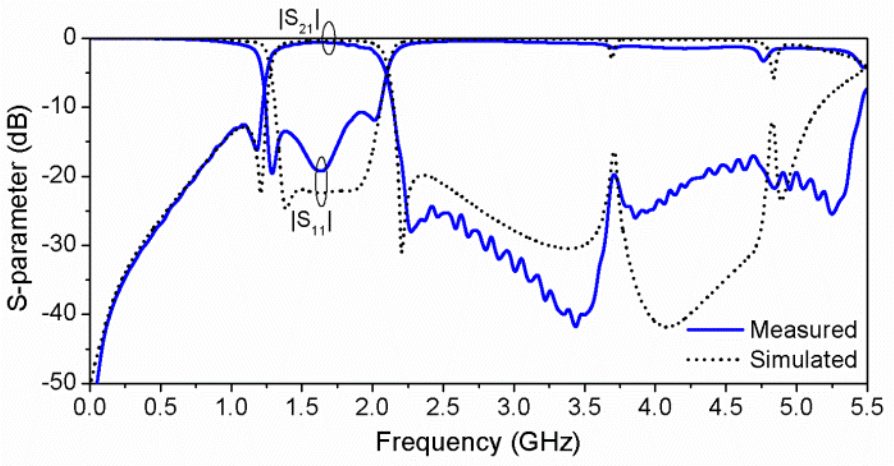

(a)

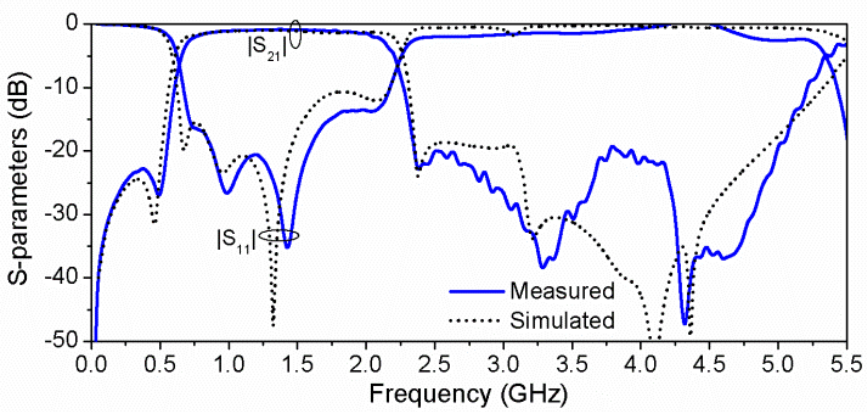

(b)

Fig 4. 8 Performance of the proposed filter: (a) 45% fractional band: V_1=20, V_2=26, V_3=6; (b) 105% fractional band: V_1=0, V_2=0, V_3=1.5. Unit: V.

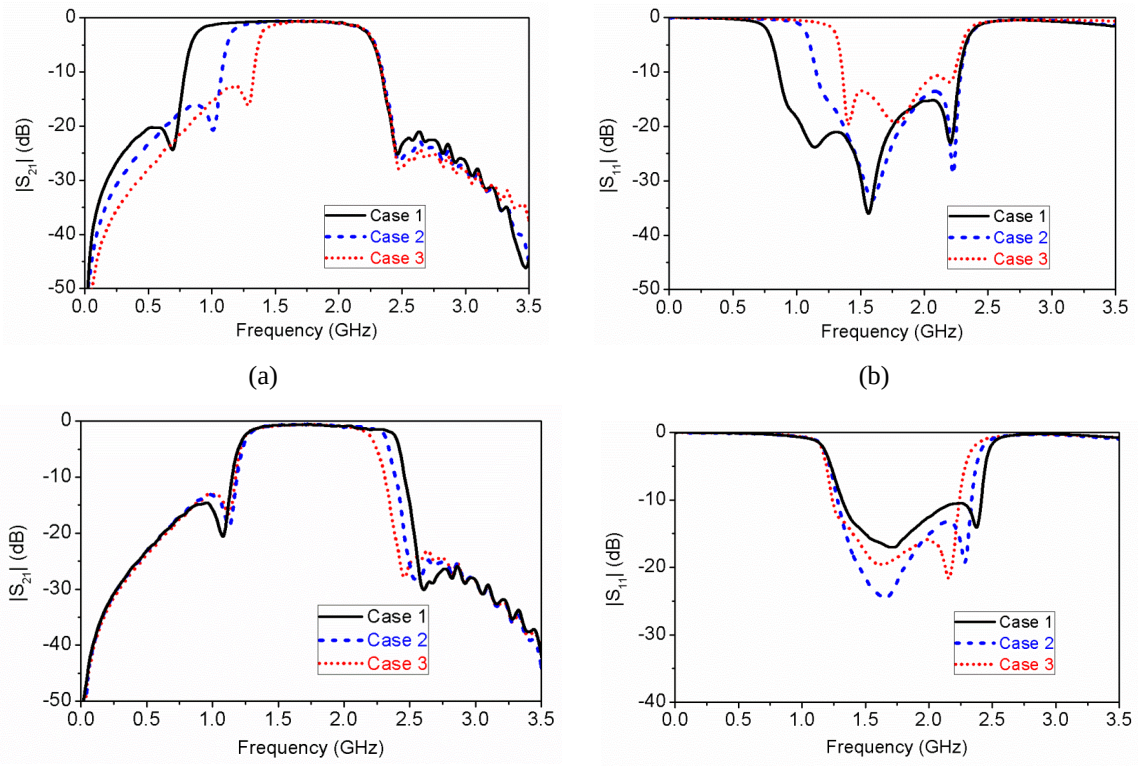

Fig 4. 9 Measured results of the independently controlled TZs: S-parameters of lower-edge f_{tz1} (a) $|S_{21}|$, and (b) $|S_{11}|$ (Case 1: V_1=20, V_2=26, V_3=6; Case 2: V_1=16, V_2=14, V_3=6; Case 3: V_1=12, V_2=2, V_3=6); S-parameters of upper-edge f_{tz2} (c) $|S_{21}|$, and (d) $|S_{11}|$ (Case 1: V_1=10, V_2=4, V_3=8; Case 2: V_1=12, V_2=13, V_3=4.5; Case 3: V_1=14, V_2=21, V_3=0). Unit: V.

The simulated and measured results are shown in Fig 4.8 for both 45% and 105% FBWs. The developed filter has a 3-dB tunable FBW from 47.8% to 105.7%. The in-band insertion loss for the 45% FBW is less than 1.4 dB, while the return loss is more than 12 dB across the frequency range from 1.29 GHz to 2.08 GHz. The attenuation at the upper stopband is more than 18 dB up to the frequency 5.35 GHz. For the 105% FBW state, the in-band insertion loss is less than 1.2 dB, while the return loss is more than 15.2 dB across the frequency range from 0.67 GHz to 2.17 GHz. The measured upper stopband extends up to 5.05 GHz with 20 dB suppression. There is some slight difference between the simulated and measured performances due to the expected minor difference between the used SPICE models and realistic performance of the varactors as well as the manufacturing tolerances. The independent controllability of the two TZs of the proposed design is also verified via measurements as depicted in Fig 4.9, which shows those TZs although not as strong as those observed in the simulations. That feature enables realizing an excellent selectivity and controllability at the edges of the passband.

The group delay of the proposed BPF is calculated and shown in Fig 4.10 for the narrowband and wideband designs. The group delay within the passband is flat with a maximum peak-to-peak deviation of 0.5 ns. The nonlinear characteristics of the filter are mostly determined by the used nonlinear elements (varactors in the designed filter). To calculate the third-order intercept points (IP_3) of the filter, two input signals are used with a separation Δf = 1 MHz. It is found that IP_3 is 18.4 dBm at the centre frequency of 1.8 GHz, whereas the input 1-dB gain compression point (P_{1dB}) is found to be 20.8 dBm. If a certain application requires larger values for IIP_3 and P_{1dB}, different varactors should be used.

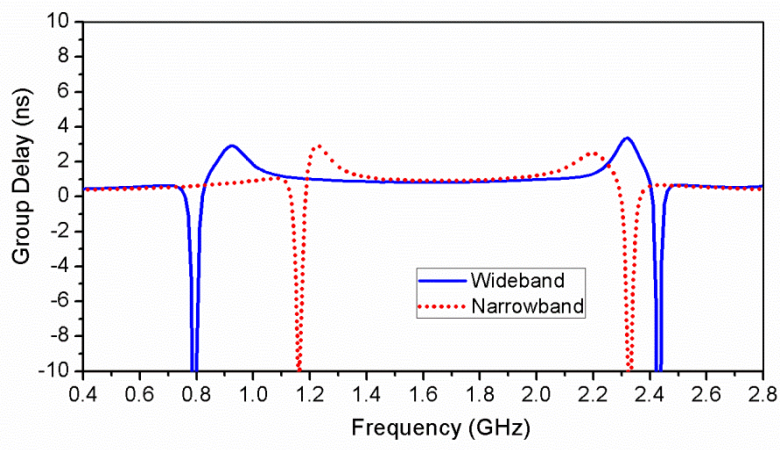

Fig 4. 10 Group delay within the passband for narrowband and wideband designs.

Compared with other existing works, the presented results prove that this design approach possesses the following merits: (1) wide bandwidth tuning range extending to more than 100% fractional bandwidth; (2) transmission zeros located at the edges of the passband contributing to a sharp skirt selectivity, and relocatable transmission zeros; (3) multiple transmission zeros that are generated in the upper-stopband for harmonics suppression extending to around four times the centre frequency; and (4) a structure that is based on single-layer print circuit board, which is easy to fabricate and integrate with other circuits.

4.3 Design of Compact Tunable BPF with Wide Tuning Range of CF and BW (I)

In the last section, we presented a design approach for wideband tunable BPF with 40% to 100% bandwidth. In some microwave systems, wide bandwidth is not always necessary especially for those with narrow operating band range. It is more preferred to have relocatable centre frequency

and adjustable bandwidth, just as indicated in Fig 4.1. It is also required that at any unwanted frequency band, upper-stopband rejection is highly demanded in order to avoid harmonics. To that end, comb-line resonators were widely used in tunable bandpass filter designs [111]-[112] due to their easy controllability of resonant characteristics. Split-ring resonators based on a multilayer structure was adopted in [113] achieving a wide bandwidth tuning range. Independently adjustable transmission zeros were employed in [114] to obtain good selectivity of the passband.

In the following sections, new design methods will be given for pursuing high performance tunable BPF with wide tuning range for both the centre frequency and bandwidth. Firstly, a new kind of ring resonator loaded with short-ended stubs is presented and utilized for BPF design. The bandwidth and resonant frequencies is easily controlled by several tapped and grounded varactors. A complete design method is given for guidance of build a design model in full-wave simulation environment, and then a prototype is fabricated and tested for validating the proposed design.

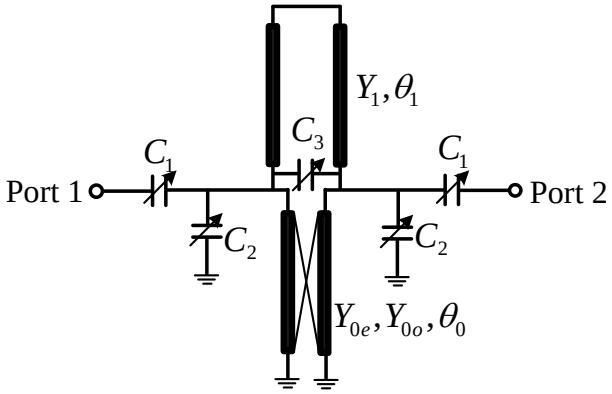

(a)

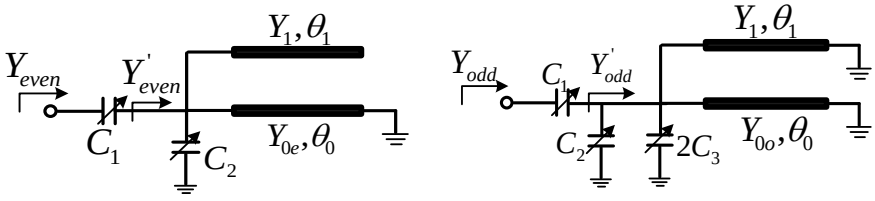

(b) (c)

Fig 4. 11 Proposed tunable BPF: (a) equivalent transmission line circuit of the proposed BPF; (b) even-mode equivalent circuit; (c) odd-mode equivalent circuit.

4.3.1 Analysis of the Ring Resonator and Short-ended Coupled-lines

Fig 4.11 (a) shows the basic transmission line equivalent circuit of the proposed tunable bandpass filter (BPF). It is composed of a ring resonator, which has a total electrical length of $2\theta_1$ and admittance Y_1, connected with a short-ended coupled-line section (θ_0, Y_{0e}, Y_{0o}). Two varactors with

capacitance C_1 are placed between the feedlines and the resonators. The two connected ends of the ring resonator and coupled-line section are connected to the ground using two varactors of capacitance C_2. Another varactor with capacitance C_3 is used to connect the two ends of the resonator. Since the structure is fully symmetric, it can be analysed by the even- and odd-mode method. The even- and odd-mode equivalent circuits are depicted in Fig 4.11 (b) and (c). When the even- and odd-mode excitations are applied respectively, the input admittances in both cases are

$$Y'_{even} = j\omega C_2 + jY_1 \tan\theta_1 - jY_{0e} \cot\theta_0 \tag{4.9}$$

$$Y_{even} = jwC_1 \cdot Y'_{even}/(jwC_1 + Y'_{even}) \tag{4.10}$$

$$Y'_{odd} = j\omega C_2 + j2\omega C_3 - jY_1 \cot\theta_1 - jY_{0o} \cot\theta_0 \tag{4.11}$$

$$Y_{odd} = jwC_1 \cdot Y'_{odd}/(jwC_1 + Y'_{odd}) \tag{4.12}$$

The S-parameters of the filter can thus be found via

$$S_{11} = \frac{Y_L^2 - Y_{odd}Y_{even}}{(Y_L + Y_{odd})(Y_L + Y_{even})} \tag{4.13}$$

$$S_{21} = \frac{Y_L(Y_{odd} - Y_{even})}{(Y_L + Y_{odd})(Y_L + Y_{even})} \tag{4.14}$$

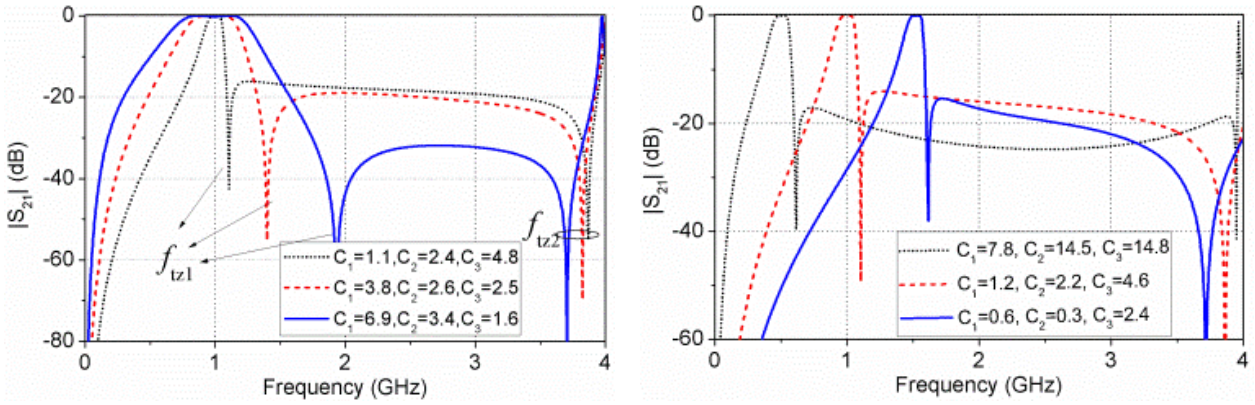

(a) (b)

Fig 4. 12 Theoretically calculated tunability of: (a) bandwidth; (b) centre frequency.

Y_L refers to the load characteristic admittance. The iterative solution of Equations (4.9) - (4.14) can calculate the required design parameters for any desired performance. For example, if the filter is designed for a centre frequency tuning range of 0.5-1.5 GHz and bandwidth tuning range of 100-300 MHz, the iterative solution of Equations (4.9) - (4.14) gives the following design values: θ_0=11.8°, θ_1=20.2°, Y_1=1.16×10^{-3} S, Y_{0e}=5.65×10^{-3} S, Y_{0o}=1.35×10^{-2} S, at the centre frequency 1

GHz. The calculated results using those values and different varactors' capacitance values (shown in pF in the legend of Fig 4.11) in Matlab demonstrate the wide tunability of bandwidth and centre frequency of the proposed BPF as depicted in Fig 4.12. In summary, Fig 4.12 (a) indicates that to fix the centre frequency and increase the bandwidth, C_1 and C_2 should be increased, while C_3 should be decreased. On the other hand, Fig 4.12 (b) shows that to move the centre frequency to higher values while maintaining the bandwidth unchanged, the capacitances C_1, C_2 and C_3 should be decreased.

It is observed that two transmission zeros (f_{tz1} and f_{tz2}, shown in Fig 4.12) appear in the upper-stopband. f_{tz1} is very close to the passband resulting in a sharp-skirt passband selectivity, whereas f_{tz2} enables realizing wide upper stopband. To theoretically predict the positions of those zeros from (4.10) and (4.12), the following conditions should be met:

$$Y_{odd}(\omega_{TZ}) - Y_{even}(\omega_{TZ}) = 0 \tag{4.15}$$

The iterative solution of (4.15) for different values of design parameters indicate that the positions of f_{tz1} and f_{tz2} are defined mainly by C_3. When C_3 increases, f_{tz1} moves to lower frequencies, while f_{tz2} moves to higher frequencies.

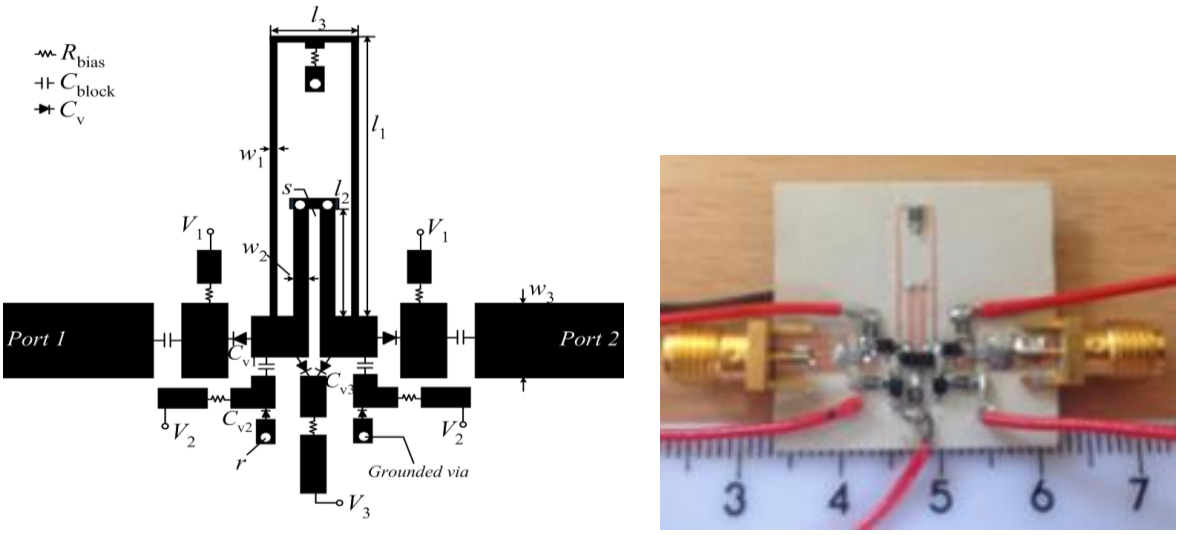

Fig 4. 13 Layout and photo of the proposed filter

4.3.2 Design and Results

A prototype is designed using microstrip technology with centre frequency tuning range from 0.5 GHz to 1.5 GHz, and bandwidth tuning range from 100 MHz to 300 MHz. The substrate used in the design is Rogers RO3003 with dielectric constant ε_r = 3 and thickness h = 1.52 mm. Using the aforementioned calculated design parameters, the initial dimensions assuming the use of microstrip

technology can be calculated using the well-known microstrip design equations. The EM simulation software Advanced Design System (ADS) is then used to get the following optimized dimensions (mm) shown in Fig 4.13: l_1=13.4, l_2=5.5, l_3=3.6, w_1=0.3, w_2=0.62, w_3=1.1, s=0.5, r=0.15. Fig 4.13 displays a photograph of the fabricated filter, which has the compact overall size of 25 mm × 28 mm (0.07 λ_g × 0.08 λ_g, λ_g is the guided wavelength at the centre frequency 1 GHz).

The biasing circuit of the tunable BPF shown in Fig 4.13 includes an RF choke with a DC biasing resistor of 10 kΩ, and DC block capacitors of 100 pF. The varactors used in the filter are hyper abrupt junction tuning elements SMV1281 with tuning range from 0.6 to 14.2 pF and parasitic resistor R_s of 2.4 Ω. To enable proper DC biasing of the varactor C_3, it is replaced by cascading two varactors C_{v3} that have the same effective value of C_3 with one common ground. To get accurate results in ADS simulations, SPICE models of the tuning elements are utilized.

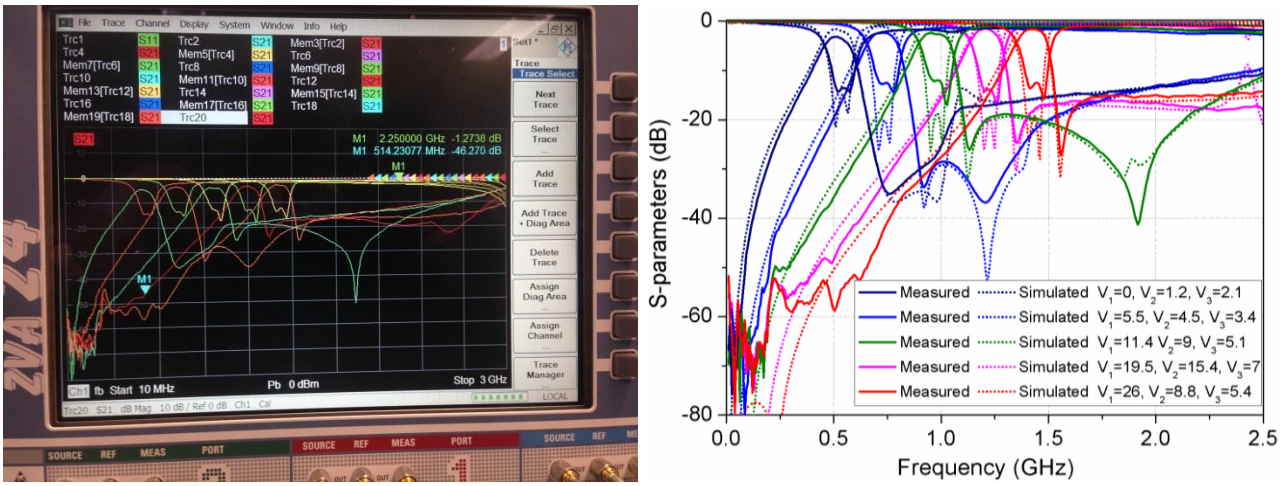

(a)

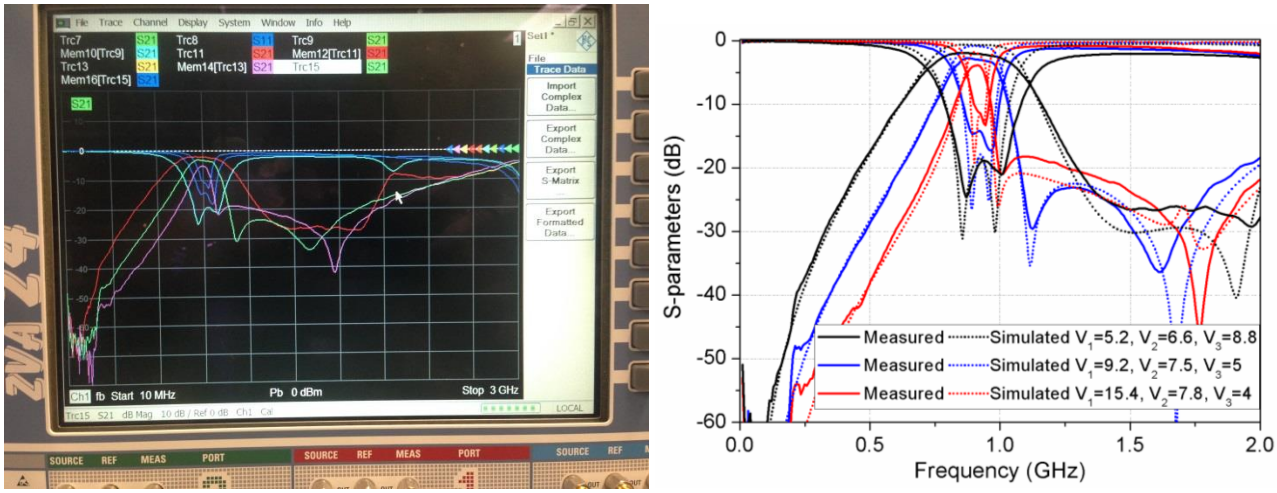

(b)

Fig 4. 14 Simulated and measured results of the proposed BPF: (a) Centre frequency; (b) Bandwidth.

Fig 4.14 shows the simulated and measured results at different varactors' biasing voltages. A wide tuning range of the centre frequency from 0.52 GHz to 1.42 GHz (tuning ratio of 92.8%, which is larger than the recently published results [115], [116]) with certain bandwidth of 150 MHz is depicted in Fig 4.14 (a). As depicted in Fig 4.14 (b), the bandwidth tunability at 1 GHz is from 90 MHz to 320 MHz (tuning range ratio is 3.56). The insertion loss for all the investigated cases is between 1.6 dB and 3.9 dB. Those results agree well with the theory and indicate the very wide tuning range of both centre frequency and bandwidth. The slight difference between the theoretical, simulated and measured results might be due to the differences between the actual diodes and their SPICE models as well as the manufacturing tolerance.

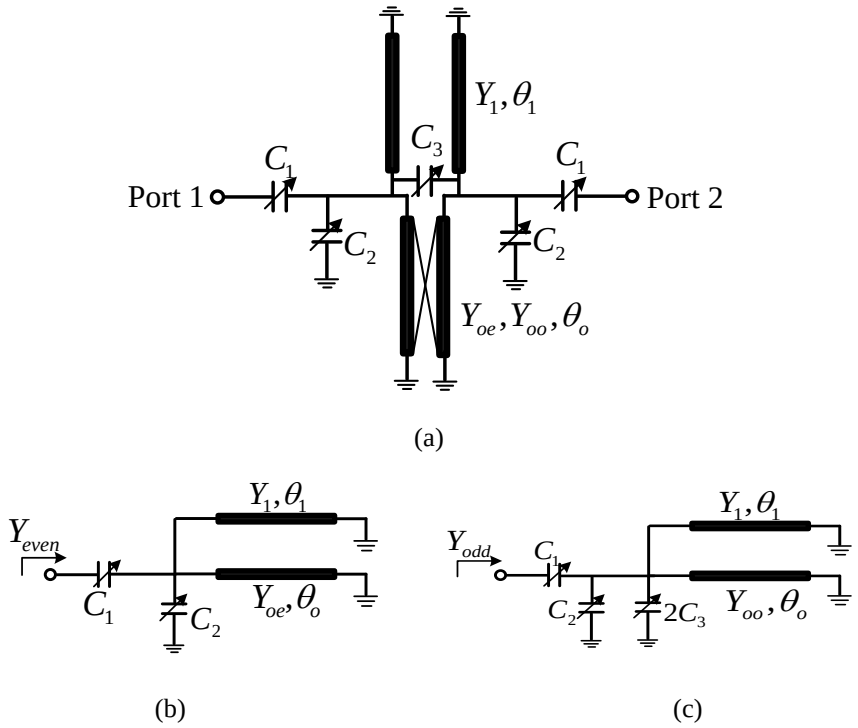

Fig 4. 15 (a) Transmission line schematic of the proposed filter, (b) even-mode equivalent circuit, and (c) odd-mode equivalent circuit.

4.4 Design of Compact Tunable BPF with Wide Tuning Range of CF and BW (II)

In this section, we will continue the investigation on design approach for tunable BPF design with wide tuning range of centre frequency and bandwidth. Moreover, the controllability of transmission zeros and selectivity of passband is also considered. The position of a transmission zero is designed to be located at either side of the passband. Instead of using ring resonator, this section will present a second-order tunable BPF using varactor-loaded coupled-lines and short-ended stubs. A thorough

theoretical analysis is given to find the initial values of the filter's design parameters and estimate its performance. To validate the proposed design and its theoretical analysis, two prototype filters are fabricated and tested.

4.4.1 Varactor-loaded Coupled-lines and Short-ended Stubs

Fig 4.15 shows a schematic diagram of the proposed tunable bandpass filter. It is composed of a short-ended coupled-line section, which has even- and odd-mode admittances of Y_{oe}, Y_{oo} and electrical length of θ_o, calculated at the centre frequency f_c, connected in parallel with a pair of short-ended stubs, which have an admittance of Y_1 and electrical length of θ_1, calculated at f_c. Several varactors that have the following capacitances are added to the structure at different locations to control the filtering performance: Two pairs of varactors with capacitances C_1 and C_2 forming two inverted L-sections that connect the input and output ports to the resonator; and a varactor with a capacitance C_3 connected between the coupled-line section and stubs.

Since the proposed structure in Fig 4.15 is symmetric, the even-/odd-mode analysis method can be adopted for analysis of the circuit. To that end, the even- and odd-mode equivalent circuits of the proposed filter are given in Fig 4.15 (b) and (c). For the even-mode case, the input admittance is

$$Y_{even} = \frac{j\omega C_1 \cdot (j\omega C_2 - jY_1 \cot\theta_1 - jY_{oe} \cot\theta_0)}{j\omega C_1 + j\omega C_2 - jY_1 \cot\theta_1 - jY_{oe} \cot\theta_0} \tag{4.16}$$

The odd-mode input admittance is

$$Y_{odd} = \frac{j\omega C_1 \cdot (j\omega C_2 + j2\omega C_3 - jY_1 \cot\theta_1 - jY_{oo} \cot\theta_0)}{j\omega C_1 + j\omega C_2 + j2\omega C_3 - jY_1 \cot\theta_1 - jY_{oo} \cot\theta_0} \tag{4.17}$$

Assuming that the device is connected to ports that have a characteristic admittance (Y_o), the scattering parameters of the structure in Fig 4.15 can be calculated from the admittance parameters. The overall performance of the BPF can thus be calculated using Equations (4.13) and (4.14). Based on the targeted FBW and centre frequency f_c, a tunable BPF can be constructed when the resonant frequencies f_{even} and f_{odd} are known. It is known that the even- and odd-mode resonant frequencies of the structure can be found from the following conditions:

$$\mathrm{Im}[Y_{even}] = 0 \tag{4.18}$$

$$\mathrm{Im}[Y_{odd}] = 0 \tag{4.19}$$

Solving (4.18) and (4.19) and using (4.16) and (4.17), the relation between the resonant frequencies (f_{even} and f_{odd}) and the design parameters of the filter can be expressed as

$$f_{even} = \frac{Y_1 \cot\theta_1 + Y_{0e} \cot\theta_0}{2\pi \cdot \left(C_2 + \frac{C_1}{1 + (\omega C_1 / Y_0)^2}\right)} \tag{4.20}$$

$$f_{odd} = \frac{Y_1 \cot\theta_1 + Y_{0o} \cot\theta_0}{2\pi \cdot (C_2 + 2C_3 + \frac{C_1}{1 + (\omega C_1 / Y_0)^2})} \tag{4.21}$$

From Equations (4.20) and (4.21), it is observed that f_{even} depends on C_1, C_2, and has nothing to do with C_3, while f_{odd} is related to C_1, C_2 and C_3 at the same time. Since f_{even} and f_{odd} defines the tuning range for both of the band and centre frequency, it is possible to conclude from (4.20) and (4.21) that the varactor capacitances C_1, C_2 and C_3 can be used to tune the centre frequency and band of the filter. The criteria of selecting these capacitances are given in the following sections.

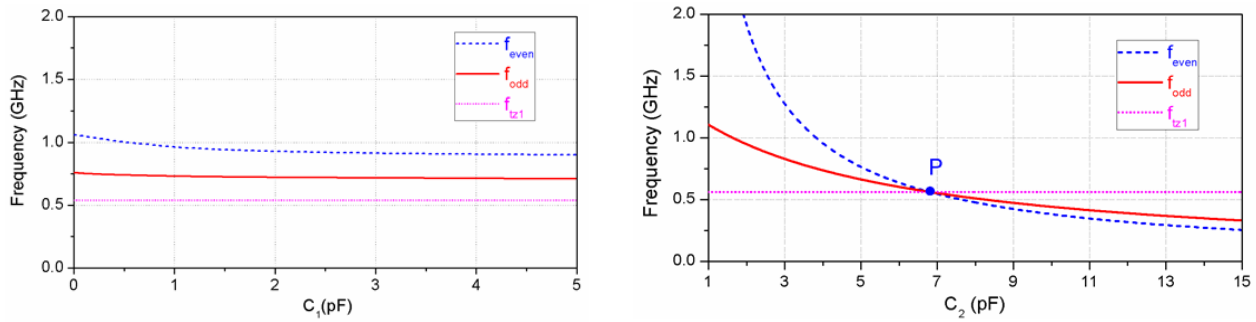

(a) (b)

Fig 4. 16 Relationship between (a) C_1, (b) C_2, and the resonant frequencies f_{even}, f_{odd} and transmission zero f_{tz1}.

4.4.2 Relocatable Transmission zeros

To achieve sharp selectivity of the passband, the transmission zeros of the filter are to be properly located. To find the location of those transmission zeros, the condition $|S_{21}| = 0$ is to be solved. It is possible to conclude that the aforementioned condition can be met with the following cases.

$$Y_{odd} - Y_{even} = 0 \tag{4.22}$$

$$\begin{cases} |Y_{even}| = \infty \\ |Y_{odd}| = \infty \end{cases} \tag{4.23}$$

The solution of Equation (4.22) gives the location of the transmission zero f_{tz1}, which can be made very close to the passband for better selectivity.

$$f_{tz1} \cdot \tan(\theta_0 \frac{f_{tz1}}{f_0}) = \frac{(Y_{oo} - Y_{oe})}{4\pi C_3} \tag{4.24}$$

From (4.24) one can find that the position of f_{tz1} is determined by the properties of the coupled-line section (Y_{oe}, Y_{oo}, and θ_0) and the capacitance C_3. It is observed that when $f_{even}>f_{odd}$, f_{tz1} appears at the upper side of the passband, but when $f_{even}<f_{odd}$, f_{tz1} appears at the lower side of the passband. Those two cases are fully controlled using C_3, as proven in (4.24), enabling the reconfigurability of this effective transmission zero in line with the centre and band tunability as required by the design. The other transmission zeros, which can be found by solving (4.23), are expressed as:

$$f_{tz2} = \frac{n\pi f_c}{\theta_0}, \;\; n = 0,1,2 \ldots \tag{4.25}$$

$$f_{tz3} = \frac{n\pi f_c}{\theta_1}, \;\; n = 0,1,2 \ldots \tag{4.26}$$

Obviously, a transmission zero appears at DC when n equals to zero. The first two non-zero TZs occur when *n* equals 1. As observed from (4.25) and (4.26), the smaller θ_o and θ_1 are, the larger f_{tz2} and f_{tz3} will be. Therefore, with the aim of achieving a compact structure and thus using small values for θ_o and θ_1, these two transmission zeros will be located at higher frequencies, resulting in good suppression of harmonics in the upper-stopband at selected locations as per (4.25) and (4.26). Besides, these two transmission zeros are not affected by the varactor capacitances, indicating the possibility for the designer to locate them appropriately to suppress any harmonics irrespective of the tuning requirement.

4.4.3 Study of the Filter's Tunability

To judge the required values of the design parameters needed for a certain tunability range of the filter concerning its centre frequency and bandwidth, let us assume that a filter with the following requirements are needed. Centre frequency tuning range is from 0.5 GHz to 1.5 GHz, and bandwidth range is from 50 MHz to 250 MHz. Using the iterative solution of the previous theory, it is possible to find that the following values of the design parameters are needed: $\theta_0=\theta_1=30^\circ$, $Z_{oe}=1/Y_{oe}$ =160 Ω, $Z_{oo}=1/Y_{oo}$ =65 Ω, and $Z_1=1/Y_1$ =100 Ω. Using parametric analysis for other design requirements, it was found that the values of Z_{oe}, Z_{oo} and Z_1 should meet the following conditions.

$$\sqrt{Z_{oe}Z_{oo}} = 2Z_o = 100\Omega \tag{4.27}$$

$$Z_1 = 2Z_o = 100\Omega \tag{4.28}$$

Using those calculated values in (4.20), (4.21) and (4.24), variation of the resonant frequencies (f_{even} and f_{odd}) and transmission zero f_{tz1} for different values of the varactor capacitances are calculated

and shown in Fig 4.16. It can be easily concluded from the results that two resonant modes are utilized in the filter design. From Fig 4.16 (a), one can find that C_1 has no effect on f_{tz1}, as previously expected, and has a slight effect on f_{odd} and f_{even}. From Fig 4.16 (b), it is also possible to conclude that when C_2 is increased, both of f_{odd} and f_{even} decrease, while the transmission zero f_{tz1} remains constant. It is well known that the even- and odd-mode resonant frequencies have the following relation with the filter's centre frequency

$$f_c = \frac{f_{even} + f_{odd}}{2} \tag{4.29}$$

Thus, it is possible to conclude that the intersection points P in Fig 4.16 actually indicate the case of locating the TZ at the position of the centre frequency. Thus, this case represents an all-reject filter and it is a transitional case that marks the values of the varactor capacitance that cause a shift in the position of f_{tz1} from the upper to the lower side of the passband. This case is important in the design in the sense that it represents the possibility of the transmission zero relocation.

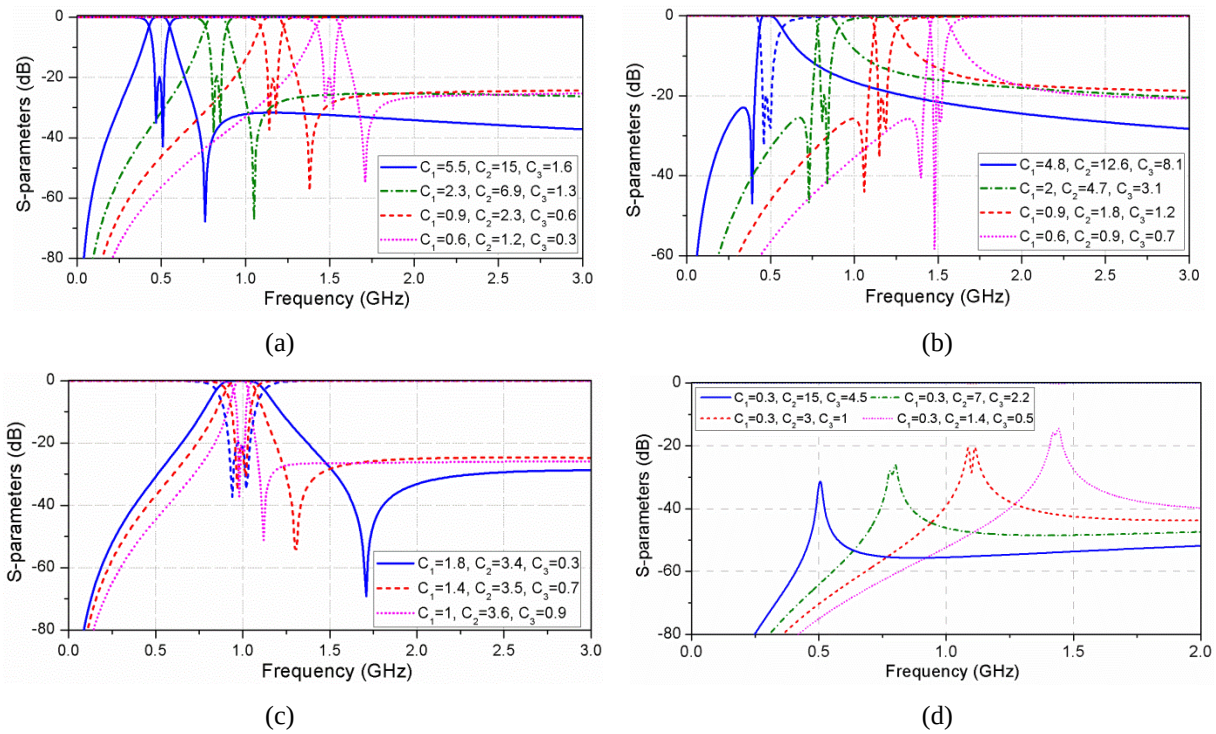

Fig 4. 17 Calculated performance for (a) tunable centre frequency with upper side transmission zero, (b) tunable centre frequency with lower side transmission zero, (c) tunable bandwidth, and (d) zero-bandwidth situation. (Unit: pF).

Using the selected circuit parameters in Equations (4.20) and (4.21) with varactor capacitance that changes within the reasonable range (eg. 0.3 pF to 15pF), the scattering parameters of the filter can be calculated as depicted in Figs 4.17 (a)-(c). In Fig 4.17 (a), the centre frequency of the operating band can be shifted from 0.5 GHz to 1.5 GHz, with fixed bandwidth and f_{tz1} located at the upper

side of the passband; while from Fig 4.17 (b), same performance is achieved except the TZ is located at the lower side of the passband. Bandwidth tunability is shown in Fig 4.17 (c) demonstrating a tunable 3-dB bandwidth from 50 MHz to 300 MHz at certain frequency. The value range of capacitance used in all cases is from 0.3 pF to 15 pF, which can be realised by RF varactors. These results reveal the potential of the proposed structure to realise a wide range of tunability for the centre frequency and bandwidth as well as a relocatable transmission zero.It is also noted that by appropriately selecting the values of C_1, C_2 and C_3 to meet the aforementioned situation $f_{even} = f_{odd} = f_{tz1}$, the passband is suppressed by the transmission zero, resulting in zero bandwidth of the passband as shown in Fig 4.17 (d).

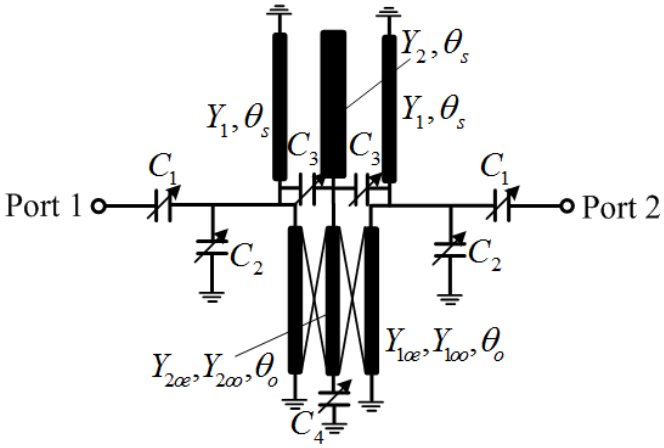

Fig 4. 18 Schematic of a three-order tunable bandpass filter.

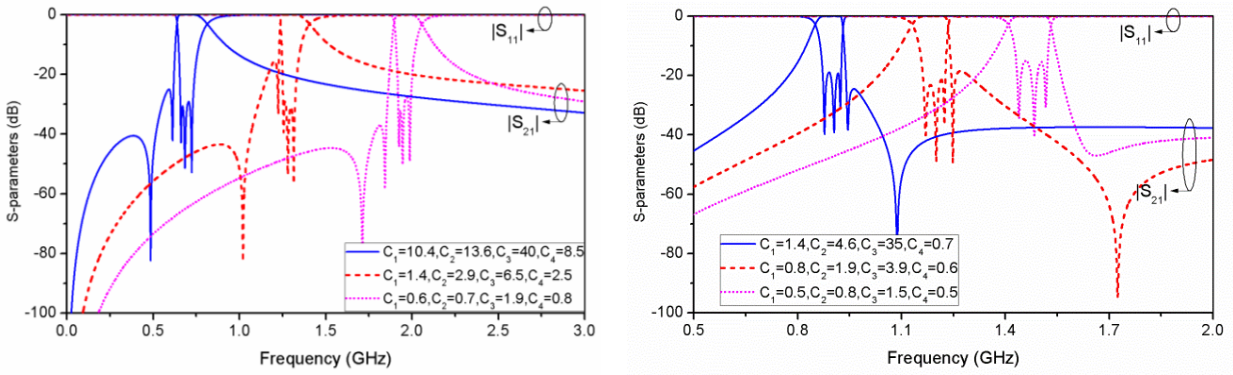

(a) (b)

Fig 4. 19 Tunable filtering response of a three-pole structure with transmission zeros at (a) left side; (b) right side.

4.4.4 Simulation of Third-order BPF

To further improve the selectivity of passband, the proposed structure can be extrapolated to higher order. For an n-order filter, there are n-1 transmission zeros appearing at the edges and n transmission poles within the passband. To increase the order of the presented basic structure,

additional short-ended stubs with equal length can be added to the coupled-line section. Also, an additional varactor is connected between any two adjacent stubs, such as, while C_1 and C_2 remain the same for the two-order filter. Meanwhile, an additional varactor is needed at the end of the stubs which are not the first or the last one. This is because more controllability of the resonant mode is required when tuning the position of passband. In this way, the external quality factor and coupling coefficients can be easily controlled. By upgrading the proposed structure to higher order (n≥3), more transmission zeros and poles can be achieved, which is favourable for sharper passband selectivity and better stopband rejection. Here, a three-pole structure, which has full tunability of bandwidth and operating frequency, is included as an example, as shown in Fig 4.18.

It is observed from Fig 4.18 that three-pole structure is composed of a three-line coupled-line section, two short-ended stubs and an open-ended stub in the middle. All the stubs have the same length of θ_s, while the coupled-line section's length is θ_0. To control the filtering performance, two pairs of varactors with capacitances C_1 and C_2 forming two inverted L-sections that connect the input and output ports to the resonator, and a varactor with a capacitance C_3 connected between the coupled-line section and stubs are used. An additional varactor C_4 is added at the end of the middle-line. Fig 4.19 shows the tunability of the three-pole bandpass filter. By increasing the capacitance of C_1, C_2, C_3, and C_4, the operating frequency moves to higher frequencies. Two transmission zeros are created at one side of the passband, and can be shifted to the other side of the passband. Due to the existence of C_2, C_3, and C_4, all the three resonant modes can be fully controlled. Meanwhile, the external quality factor is controlled by C_1, and thus the operating bandwidth can be increased or reduced as needed. Compared with the performance of the two-pole structure (Fig 4.16), the three-pole design has sharper cut-off and thus better selectivity as depicted in Fig 4.19.

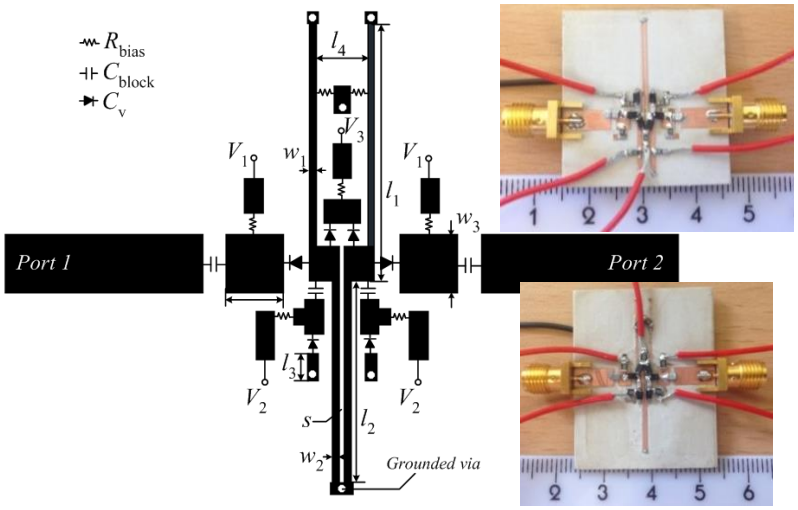

Fig 4. 20 Layout of the proposed tunable bandpass filter.

Table 4. 1 Values of design parameters (dimensions in mm).

Design #1				Design #2			
Name	value	Name	value	Name	value	Name	Value
l_1	17.2	w_1	0.3	l_1	10.6	w_1	0.8
l_2	13.7	w_2	0.32	l_2	17.5	w_2	0.36
l_3	1.0	w_3	3.6	l_3	1.0	w_3	3.6
l_4	2.6	s	0.2	l_4	1.6	s	0.2

4.4.5 Experiential Results and Discussions

To validate the proposed design procedure, two tunable filter prototypes are designed with centre frequency tunability from 0.5 GHz to 1.5 GHz, and bandwidth from 50 MHz to 150 MHz. Two prototypes are designed and built. Design #1 has the transmission zero f_{tz1} at upper side of the passband, whereas Design #2 has f_{tz1} at the lower side of the passband. The selected substrate for the designs is Rogers RO3003 with dielectric constant of 3 and thickness of 1.52 mm. The varactors used in the design are hyper abrupt junction tuning elements SMV1281 with tuning range from 0.6 to 14.2 pF and parasitic resistor R_s of 2.4 Ω. The simulation software Advanced Design System (ADS) is used in both schematic and layout design. After following the aforementioned design procedure, the optimized values of the design parameters are found to be: Design #1; θ_o=24.6˚, Z_{oe} = 166.8 Ω, Z_{oo}=70.5 Ω, θ_1=26.2˚, and Z_1=100 Ω; Design #2, θ_o=28.7˚, Z_{oe}=172.4 Ω, Z_{oo}=63.2 Ω, θ_1=12.2˚, and Z_1=100 Ω. All the electrical lengths are calculated at the centre frequency of 1 GHz. The initial capacitance values in pF for C_1, C_2 and C_3 are: 1.3, 1.4, and 0.9, for Design #1; and 1.2, 3.0, and 4.2, for Design #2, respectively.

The configuration of the proposed tunable BPF is shown in Fig 4.20. Six varactors and three different voltage suppliers are required to control the performance of the filter. For easy design of the biasing circuit, two cascaded varactors C_{v3} with one common ground are used to represent C_3. Thus, the used value of C_{v3} is twice the calculated value of C_3. The biasing circuit is realised by DC biasing resistor R_{bias} with the value of 10 kΩ, and DC block capacitors C_{block} of 100 pF to block the DC signal. Once the initial dimensions are calculated assuming the use of a single-layer microstrip technique and using the well-known microstrip design equations [32], the simulation process is started with building the layout for the structure in ADS. To get accurate optimized results, SPICE models of the varactor diodes [33] are included using co-simulation method in both schematic and layout simulation in ADS. The final dimensions of two designs are listed in Table 4.1. Fig 4.20 also presents photographs of the fabricated filters, which have overall sizes of 0.06 λ_g × 0.14λ_g and 0.06 λ_g × 0.16λ_g (λ_g is the guided- wavelength at the centre frequency 1 GHz), indicating that they are both compact designs. Besides, it is noted that in order to solder the tuning elements and biasing circuits properly, some extra microstrip patches are needed that could possibly work as transmission

line with small electrical lengths are included in the layout, resulting in some effects on deteriorating the overall performance of the devices.

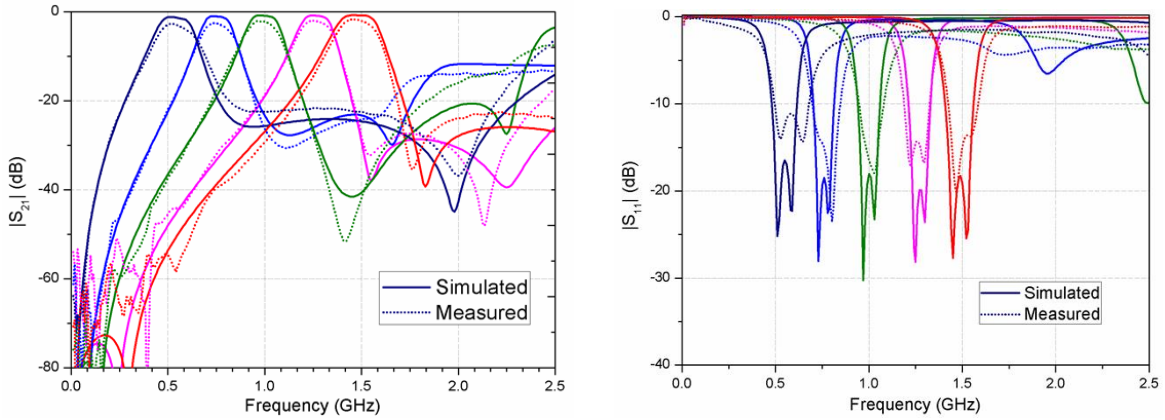

(a) (b)

Fig 4. 21 Centre frequency tunability of Design #1: (a) $|S_{21}|$; (b) $|S_{11}|$. (From low to high frequency, values of V_1, V_2 are V_3 are: 0.6,1.4,1.8; 3.8,6.5,3.2; 6.6,12.6,6.8; 10.2,20.4,10.2; 26,26,15.6, Unit:V.)

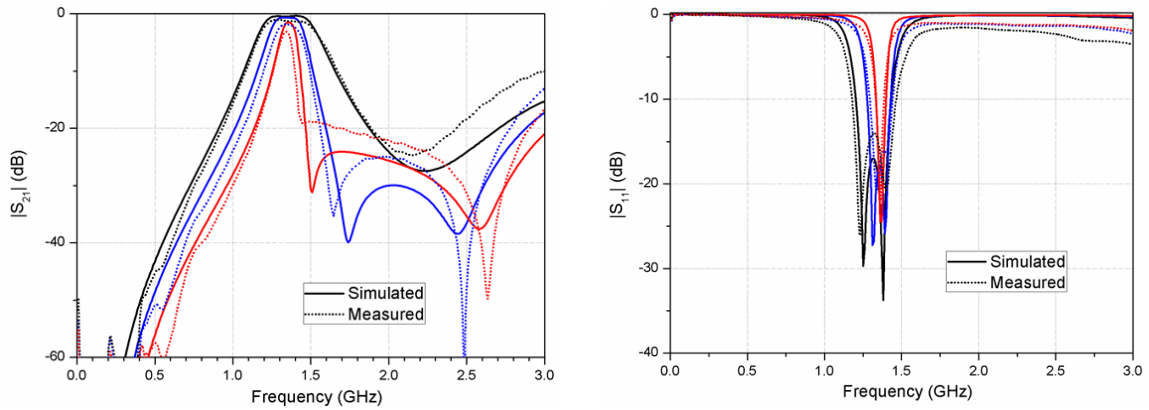

(a) (b)

Fig 4. 22 Bandwidth tunability of Design #1: (a) $|S_{21}|$; (b) $|S_{11}|$. (From narrow to wide band, values of V_1, V_2 are V_3 are: 26,26,10.2; 16.8,24.5,12.8; 9.6,20.4,26, Unit: V.)

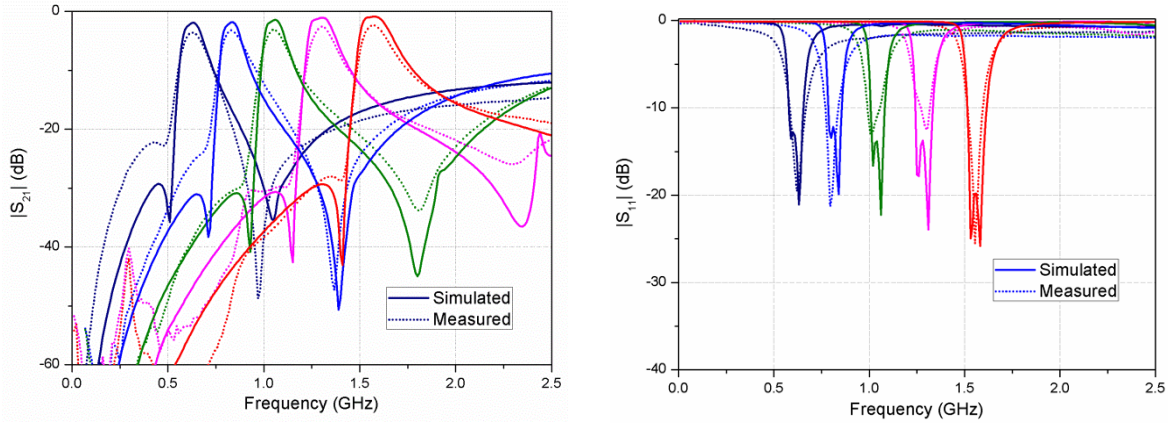

(a) (b)

Fig 4. 23 Centre frequency tunability of Design #2: (a) $|S_{21}|$; (b) $|S_{11}|$. (From low frequency to high frequency, values of V_1, V_2 are V_3 are: 4.6,2.9,1.1; 9.4,5.7,3.4; 15,8.8,5.6; 21.2,14.6,8.4; 26,26,12.4, Unit: V.)

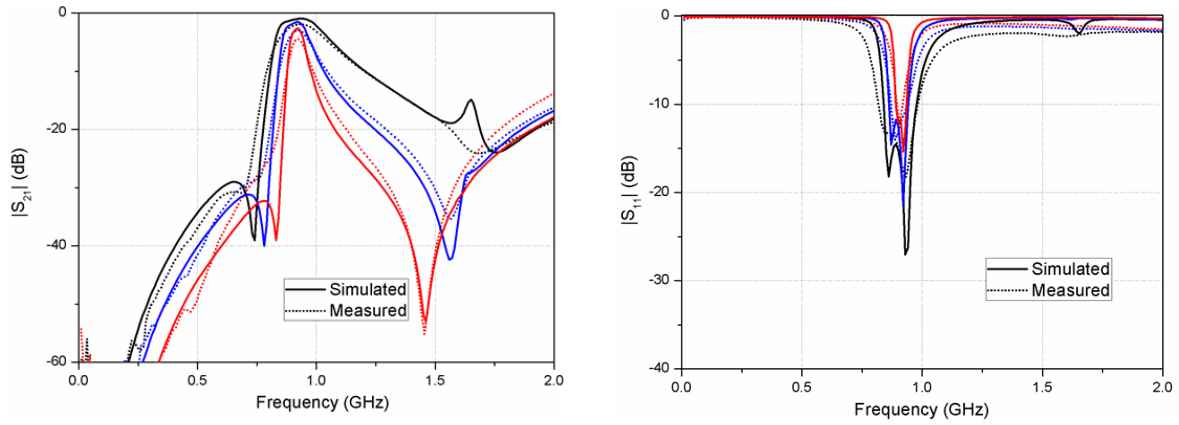

(a) (b)

Fig 4. 24 Bandwidth tunability of Design #2: (a) $|S_{21}|$; (b) $|S_{11}|$. (From narrow to wide band, values of V_1, V_2 are V_3 are: 14.8, 6.4, 4.5; 10.2, 6.9, 4.2; 7.8, 7.4, 3.6, Unit: V.)

The simulated and measured results of the filter are shown in Figs 4.21 – 4.24, for Design #1 and Design #2 respectively. A comparison between the results of Design #1 with those for Design #2 clearly indicates the relocation of the transmission zero from the upper to the lower side of the passband. The measured results, which are in well agreement with the simulated, indicate that Design # 1 and #2 have a wide tuning range for the centre frequency of 0.52-1.48 GHz (tuning ratio = 2.85) and 0.6-1.58 GHz (tuning ratio = 2.63), respectively. The results also show that Design #1 and #2 have a wide 3 dB bandwidth tunability of 55-285 MHz (tuning ratio = 5.2), and 45-190 MHz (tuning ratio = 4.2), respectively. These results meet the design objectives of the filter. The insertion loss for the two designs is between 1.2 dB and 3.5 dB for Design #1 and 1.8 dB to 4.3 dB for Design #2. Those results indicate that similar centre frequency tunability is achieved in the two designs. To verify the non-linear performance of the filters, the third-order intercept points are calculated by using two input signals with 1 MHz separation. The IIP_3 points for Design # 1 and #2 are 6.8 and 8.4 dBm at 0.6 GHz, and 17.8 and 19.6 dBm at 1.4 GHz, respectively, when the bandwidth is fixed at 100 MHz for all the investigated cases. It is found that the IP_3 increases when the operating centre frequency or bandwidth is increased due to the limited linearity of the diodes.

In general, good agreement between the measured and simulated results in the passband, cut-off band and locations of the transmission zeros can be observed. The slight differences, especially in the insertion losses where the measured are generally more than the simulated values, are thought to be due to the difference between the used SPICE models and realistic performance of the varactors, as well as the manufacturing tolerances. Some parasitic harmonics in the performance are caused by the added small patches for biasing circuit, the soldering process of the fabricated circuits and other manufacturing errors. Compared with other existing designs, the proposed structure has the widest

centre frequency tuning range with a very decent bandwidth tuning range. Besides, the proposed design is more compact in size (only about $0.01\lambda_g^2$). It is verified that the proposed design is suitable for various multiband wireless communication transceivers and microwave systems.

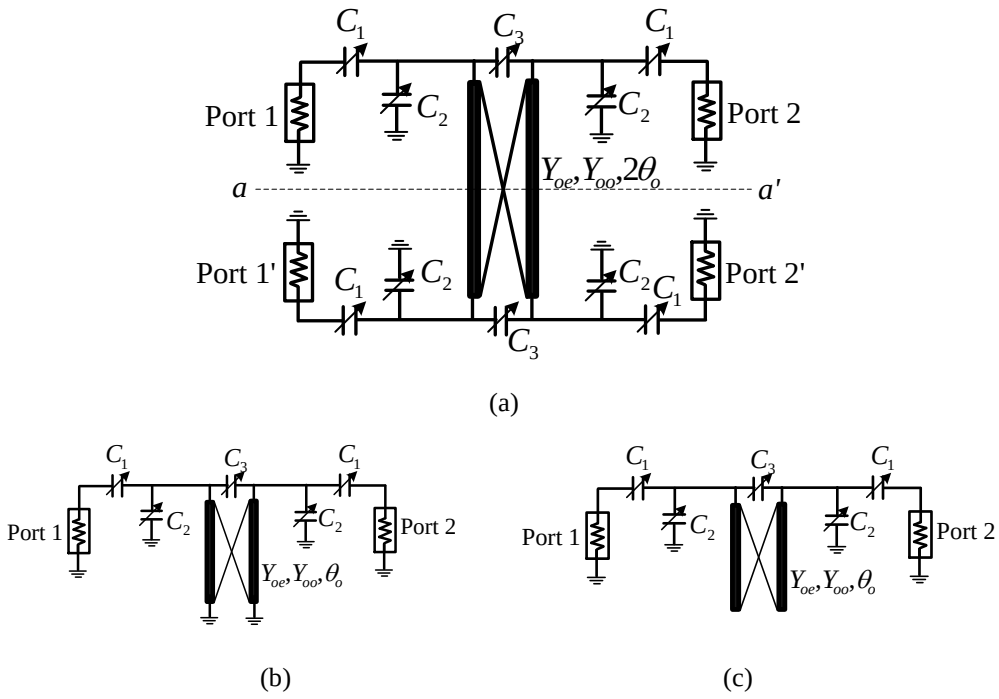

Fig 4. 25 Configuration of the proposed tunable balanced BPF.

4.5 Design of Tunable Balanced BPF

Due to the capability of providing high immunity to environment noise and suppressing common-mode signals, differential bandpass filters (BPFs) have become popular in communication systems. For miniaturization purpose, tunable balanced BPFs have been built using structures with reconfigurable passband and stopband [117]-[118]. An analysis based on the external quality factor and inter-stage coupling coefficients are used to investigate the band control in [117], which utilizes half-wavelength resonators loaded with varactors. A wide differential-mode operating centre frequency range was obtained in [118] with constant fractional bandwidth (FBW) using step-impedance resonators.

Despite the good performance of the previously designed filters, the tunability of both the bandwidth and centre frequency of a compact balanced filter are yet to be achieved. In this section, a compact balanced BPF with tunability of both the centre frequency and bandwidth is presented. The design uses one resonator in the form of a short-section of parallel-coupled lines loaded with varactors. The proposed filter is able to realise a wide tuning range in the differential-mode (DM) of

both the centre frequency and bandwidth accompanied by high common-mode (CM) suppression. The analysis of equivalent circuits is firstly given to verify the resonant modes of the filter; following by a design of differential BPF prototype with experimental verification.

4.5.1 Equivalent Circuit

The basic transmission line equivalent circuit of the proposed balanced BPF is shown in Fig 4.25 (a). It is composed of a coupled-line structure with even- and odd-mode impedances of Z_{oe} and Z_{oo} and electrical length of θ_o at the centre frequency f_o, two pairs of tapping varactors with capacitance C_1, two pairs of grounded varactors with capacitance C_2 and a pair of varactors with capacitance C_3 connected between the two ends of the coupled-line structure. Since the structure is symmetric along the line a-a'. In the DM excitation, the symmetric line appears as a perfect electrical wall (short circuit), whereas at CM excitation, that line appears as a perfect magnetic wall (open circuit). Thus, the equivalent circuits of the two modes of operation are as shown in Figs 4.25 (b) and (c).

Using the mode analysis method, the DM even- and odd-mode resonant frequencies can be found from the input admittances of the DM circuits, which are given as

$$Y_{even}^{dd} = \frac{j\omega C_1 \cdot (j\omega C_2 - jY_{oe}\cot\theta_0)}{j\omega C_1 + j\omega C_2 - jY_{oe}\cot\theta_0} \tag{4.30}$$

$$Y_{odd}^{dd} = \frac{j\omega C_1 \cdot (j\omega C_2 + j2\omega C_3 - jY_{oo}\cot\theta_0)}{j\omega C_1 + j\omega C_2 + j2\omega C_3 - jY_{oo}\cot\theta_0} \tag{4.31}$$

Here, $Y_{oe} = 1/Z_{oe}$ and $Y_{oo} = 1/Z_{oo}$. The even- and odd-mode DM resonant frequencies can be found when the conditions $\mathrm{Im}[Y_{even}^{dd}] = 0$ and $\mathrm{Im}[Y_{odd}^{dd}] = 0$ are satisfied.

Similarly, the resonant-mode analysis of the CM circuit gives the following even- and odd-mode input admittances

$$Y_{even}^{cc} = \frac{j\omega C_1 \cdot (j\omega C_2 + jY_{oe}\tan\theta_0)}{j\omega C_1 + j\omega C_2 + jY_{oe}\tan\theta_0)} \tag{4.32}$$

$$Y_{odd}^{cc} = \frac{j\omega C_1 \cdot (j\omega C_2 + j2\omega C_3 + jY_{oo}\tan\theta_0)}{j\omega C_1 + j\omega C_2 + j2\omega C_3 + jY_{oo}\tan\theta_0} \tag{4.33}$$

The even- and odd-mode CM resonant frequencies can be found by solving $\mathrm{Im}[Y_{even}^{cc}] = 0$ and $\mathrm{Im}[Y_{odd}^{cc}] = 0$.

4.5.2 Analysis of Resonant Modes and Calculation of S-parameters

The transmission zeros (TZs) of the DM circuit are also of interest in tunable BPF design as they define the selectivity of the filter. The TZs can be calculated when the condition $Y_{even}^{dd} - Y_{odd}^{dd} = 0$ is met giving the solution:

$$f_{tz} \cdot \tan(\theta_0 \cdot \frac{f_{tz}}{f_o}) = \frac{(Y_{oo} - Y_{oe})}{4\pi C_3} \tag{4.34}$$

The location of the transmission zero f_{tz} depends on C_3; if f_{tz} is selected to be very close to the passband, the performance will have excellent selectivity. As an example of the achievable resonant frequencies, Fig 4.26 shows the positions of the DM even- and odd-mode resonant frequencies (f_{even}^{dd}, f_{odd}^{dd}) and the CM even- and odd-mode resonant frequencies (f_{even}^{cc}, f_{odd}^{cc}) using (4.29) - (4.34) when $Z_{oe} = 120\Omega$, $Z_{oo} = 70\Omega$, $\theta_o = 25°$, and $f_o = 900$ MHz. It is observed that f_{even}^{dd} and f_{odd}^{dd} appear around the centre frequency f_o while f_{even}^{cc} and f_{odd}^{cc} appear at much higher frequencies (higher than $4f_o$). This result means that an excellent CM suppression is guaranteed across the desired DM operating band and beyond.

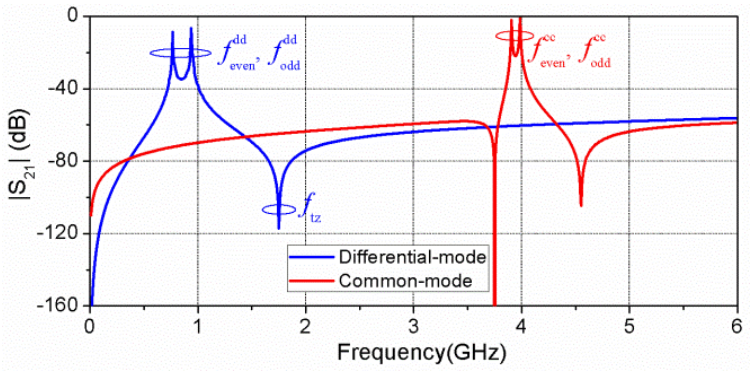

Fig 4. 26 DM and CM resonant modes when: C_1=0.3 pF, C_2=5 pF, and C_3=0.5 pF.

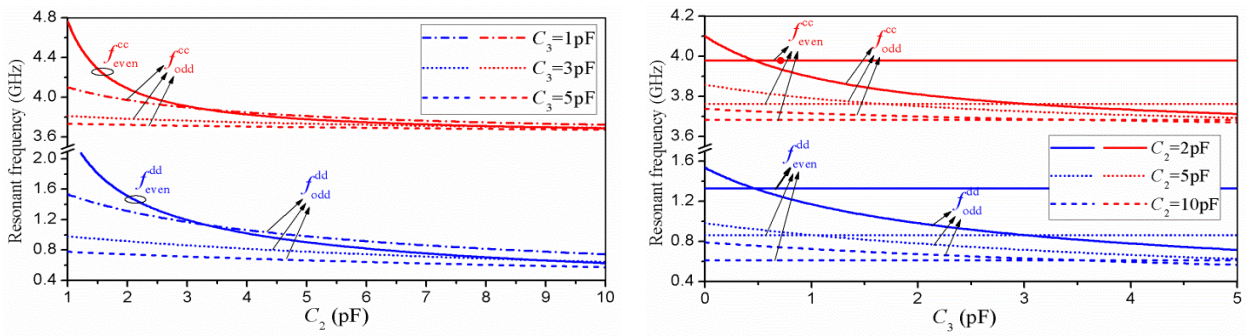

(a) (b)

Fig 4. 27 DM and CM resonant modes with variance of: (a) C_2 and (b) C_3 when C_1=0.01 pF.

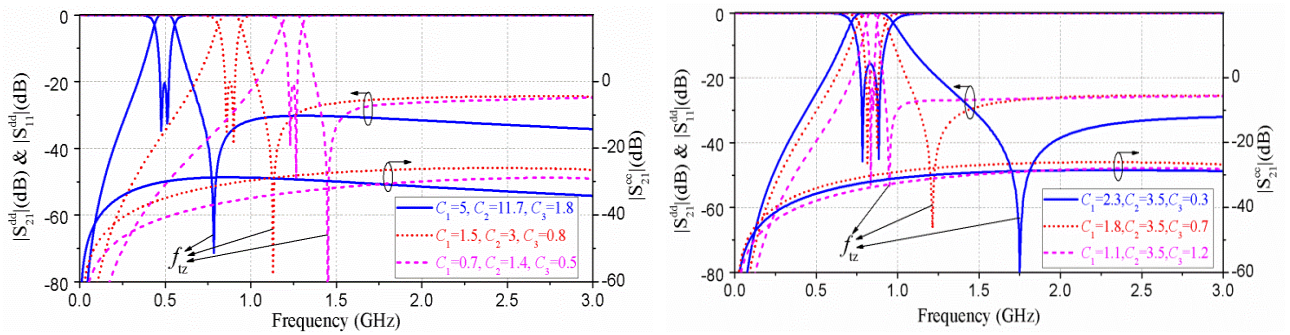

(a) (b)

Fig 4. 28 Calculated results on tunability of (a) centre frequency and (b) bandwidth, with the given values of C_1, C_2 and C_3 (Unit: pF).

If the capacitances C_1, C_2 and C_3 are tuned, the DM and CM resonant modes are changed according to Equations (4.29) to (4.32). It is noted that the effect of C_1 on the resonant frequencies is not significant but it affects the DM external quality factor, whereas C_2 and C_3 mainly define the resonant modes. Fig 4.26 shows the relation between DM, CM resonant modes and C_2, C_3, for given values of the other parameters. From Fig 4.27 (a), one can observe that all the DM and CM resonant modes decrease when C_2 is increased. From Fig 4.27 (b), it is seen that f_{even}^{dd} and f_{even}^{cc} do not depend on C_3; however, f_{odd}^{dd} and f_{odd}^{cc} decrease when C_3 is increased. Using the given parameters, all the DM resonant modes are controllable across the range from 0.5 GHz to 2 GHz, while CM resonant modes vary from 3.6 GHz to 4.8 GHz, indicating no CM modes appearing within the DM frequency range. Once the values of capacitance C_1, C_2 and C_3 are determined, the S-parameters under differential-mode excitation can be calculated using following equations:

$$S_{11}^{dd} = \frac{Y_o^2 - Y_{odd}^{dd} Y_{even}^{dd}}{(Y_o + Y_{odd}^{dd})(Y_o + Y_{even}^{dd})} \tag{4.35}$$

$$S_{21}^{dd} = \frac{Y_o (Y_{odd}^{dd} - Y_{even}^{dd})}{(Y_o + Y_{odd}^{dd})(Y_o + Y_{even}^{dd})} \tag{4.36}$$

Similarly, common-mode excited S-parameters can also be calculated by replacing Y_{even}^{dd} and Y_{odd}^{dd} with Y_{even}^{cc} and Y_{odd}^{cc}. Fig 4.28 (a) and (b) show the Calculated S-parameters based on Equations (4.29) to (4.36), which demonstrate wide tunability of both centre frequency and bandwidth. To get Fig 4.27, the initial values for C_1, C_2 and C_3 are initially estimated from Fig 4.26. Then, an iterative Matlab algorithm is used to get final values of C_1, C_2 and C_3 to meet the desired centre frequency f_c and bandwidth. It is noticed from Fig 4.27 that in all the cases, $|S_{21}^{cc}|$ is smaller than -25 dB from DC up to more than 3 GHz, indicating an excellent CM suppression under any circumstance.

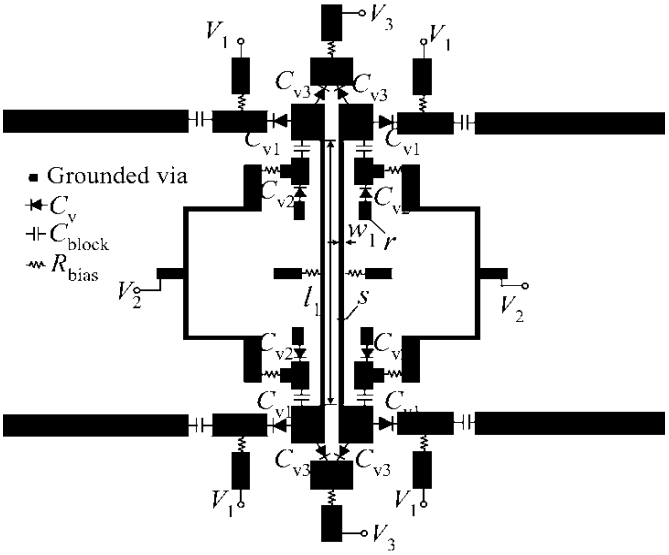

Fig 4. 29 Layout of the proposed tunable balanced BPF.

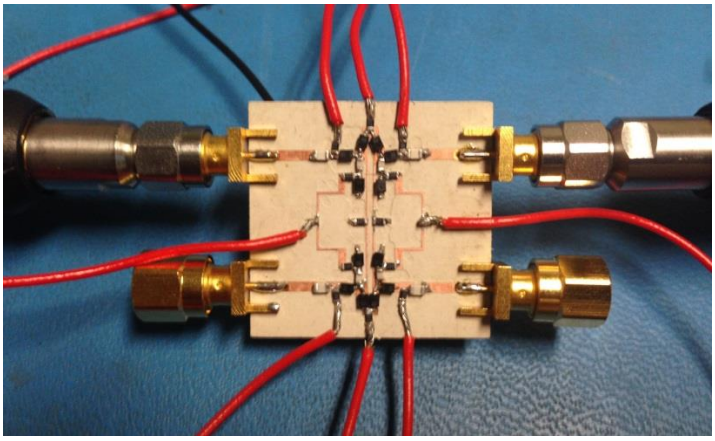

Fig 4. 30 Photograph of the proposed tunable balanced BPF.

4.5.3 Simulation and Experiment

To validate the proposed filter, a prototype with DM centre frequency tunability from 0.6 GHz to 1.2 GHz, and bandwidth tunability from 60 MHz to 200 MHz is designed, built and tested. Figs 4.29 and 4.30 show the configuration and photograph of the filter. The substrate used in the design is RT/Duriod 6010 with dielectric constant of 10.2 and thickness of 1.27 mm. Following the design procedure, the optimized values of the design parameters are found using the simulator ADS to be: $Z_{oe} = 125.6\Omega$, $Z_{oo} = 74.5\Omega$, and $\theta_0 = 25.8°$, whereas the dimensions in (mm) are found to be: $l_1 = 14.4$, $w_1 = 0.2$, $s = 0.62$. The utilized varactors are the hyper abrupt junction SMV1281 with capacitance tuning range from 0.6 to 14.2 pF and parasitic resistor R_s of 2.4 Ω. The technical datasheets of those varactors are used as a guide to find their required biasing voltages based on the needed capacitances. A biasing circuit is realised using the biasing resistor R_{bias} of 2.2 kΩ and DC

block capacitors C_{block} of 100 pF. The prototyped filter has an extremely small size, which is $0.12\lambda_g \times 0.08\lambda_g$, where λ_g is the guided-wavelength at f_o.

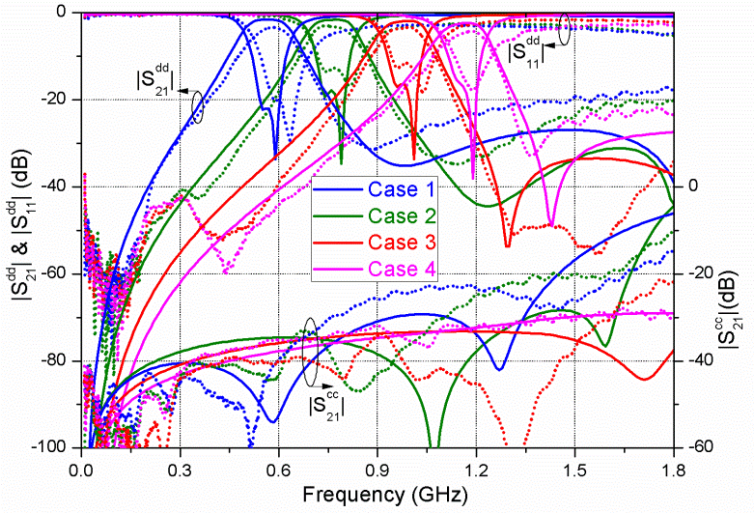

(a)

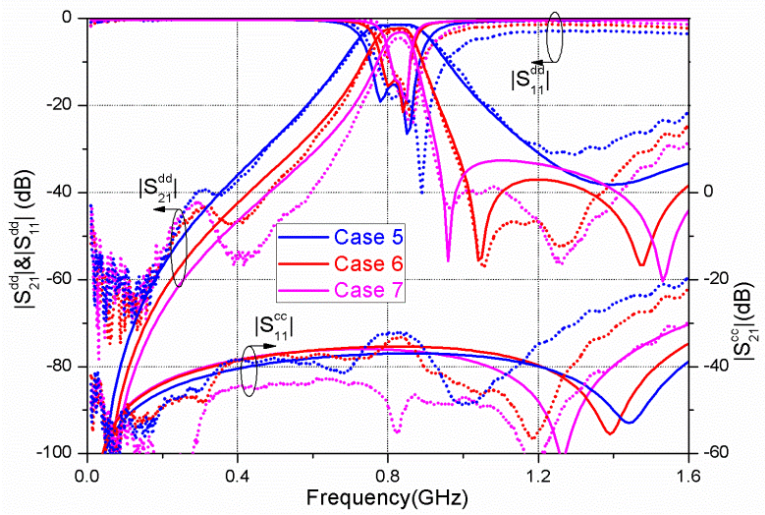

(b)

Fig 4. 31 Simulated (solid lines) and measured (dotted lines) tunability of (a) centre frequency: V_1, V_2 and V_3 of Case 1 to Case 4 are: 4.3/2.7/23, 9.4/6.5/11.7, 16.3/12.5/13.8, and 25.2/26/17.2, and (b) bandwidth: V_1, V_2 and V_3 of Case 5 to Case 7 are: 10/7.6/17.5, 13.5/7.7/9.3, and 16.7/7.8/8.1. Unit: V.

The simulated and measured results are shown in Figs 4.31 (a) and (b). A wide measured DM operating frequency tuning range from 0.58 GHz to 1.22 GHz, and wide measured 3 dB bandwidth tuning range from 65 MHz to 180 MHz are realised. The DM insertion loss across the whole tuning ranges varies between 1.8 dB and 4.5 dB, whereas the CM insertion loss is more than 30 dB across the DM operating passband and more than 20 dB across the wider range (from DC up to the frequency 1.6 GHz) in all those cases. There is some slight difference between the simulated and measured performances due to the expected minor difference between the used SPICE models and realistic performance of the varactors as well as the manufacturing tolerances. The nonlinear

characteristics of the filter are also tested. It is found that the measured third-order intercept points (IIP_3) is 17.6 dBm, whereas the input 1-dB gain compression point ($P_{1\,dB}$) is 20.4 dBm at 900 MHz. It is noted that the presented tunable BPF has the most compact size with widest tuning range for both the centre frequency and bandwidth with competitive insertion loss compared to other existing designs, which indicates great application potential of the proposed device.

4.6 Summary

In this chapter, several new types of tunable bandpass filters have been presented. The design objective is to have more flexibility in tuning of bandwidth and operating frequency band. In addition, stopband rejection and selectivity of passband are also considered, mainly realised by generating and controlling transmission zeros. Various kinds of resonators have been proposed for filter construction, including stub-loaded ring resonator, coupled-line resonator, short-ended resonator, etc. Varactors are widely used mainly for controlling resonant modes, coupling coefficients and external factors. The modelling and simulations are done in full-wave electromagnetic environment. Data from experiment have indicated that the tuning range for bandwidth and operating band can reach 0.52-1.48 (95%) and 55 – 285 MHz.

Moreover, a tunable differential BPF has been developed with sufficient tunability as well as great common-mode suppression. The even-odd mode analysis theory is used to verify the design and find the initial values of the design parameters. The performance of a prototype indicate a wide differential-mode operating range from 0.58 to 1.22 GHz, and 3 dB bandwidth tuning range from 65 to 180 MHz with more than 30 dB of common-mode suppression at all DM operating passband. The circuit is extremely compact in size, indicating huge potential in modern reconfigurable communication systems.

Chapter 5: Development of Wideband Power Divider with Tunable Power Division Ratio

5.1 Introduction

Power dividers (PDs) are key components in microwave wireless communication systems, especially in constructing feeding networks for antennas arrays. The most common power divider designs are Wilkinson and Gysel power dividers, which have been modified and applied in various kinds of systems. Both of two designs have equal power division for broadband applications. In some specific cases, unequal output power at different output ports is required and important, for systems like phased arrays and beam-steering networks. To realise unequal or arbitrary output power division, different methods were used: asymmetrical transmission lines [119]-[120], microstrip/slotline transition [121], double-sided parallel strip-lines [122], branch-line structure [123], and three-line coupled structure [105].

In microwave wireless systems, power dividers are usually connected with bandpass filters to get rid of undesired signals. The cascaded devices lead to bulky overall circuit size and large insertion loss. To avoid these shortcomings, it is favourable to have power dividers with filtering responses, in other words, to integrate filters with power dividers. Different features and merits were displayed in many filtering power dividers before: single- or dual-band filtering power dividers were presented in [124]-[126] with good in-band isolation; wideband filtering responses were realised using ring resonator [127]; four-way filtering power dividers with sharp selectivity were achieved in [128]. To introduce arbitrary power division in filtering power dividers, a kind of modified Gysel power divider was proposed in [129] by replacing transmission lines with coupling structures.

Moreover, for further circuit miniaturization and multi-function purposes, tunable microwave devices are extremely demanded to use one reconfigurable component instead of several fixed ones. Last chapter has introduced the concept of tunable bandpass filters and several new designs with different functions. In this chapter, we aim to integrate the tunable functions within the development of power dividers. To that end, a wideband power divider with tunable power division ratio is firstly realised, based on varactor-loaded three-line coupled structure. Compared with the traditional power dividers, this structure is able to control the magnitude of signals at two output ports, as indicated in Fig 5.1 (a). Moreover, two novel concepts are proposed for the first time. Based on such kind of tunable power divider with tunable power division ratio, it is favourable to introduce a filtering response (Type-II) as indicated in Fig 5.1 (b). The overall size of the system can be reduced by integrating a wideband bandpass filter within the tunable power divider. Moreover, if

one can integrate a tunable bandpass filter [130]-[133] within the Type-I PD with tunable power ratio, there would be multiple functions of such kind of devices and great miniaturization of the microwave systems, as shown in Fig 5.1 (c).

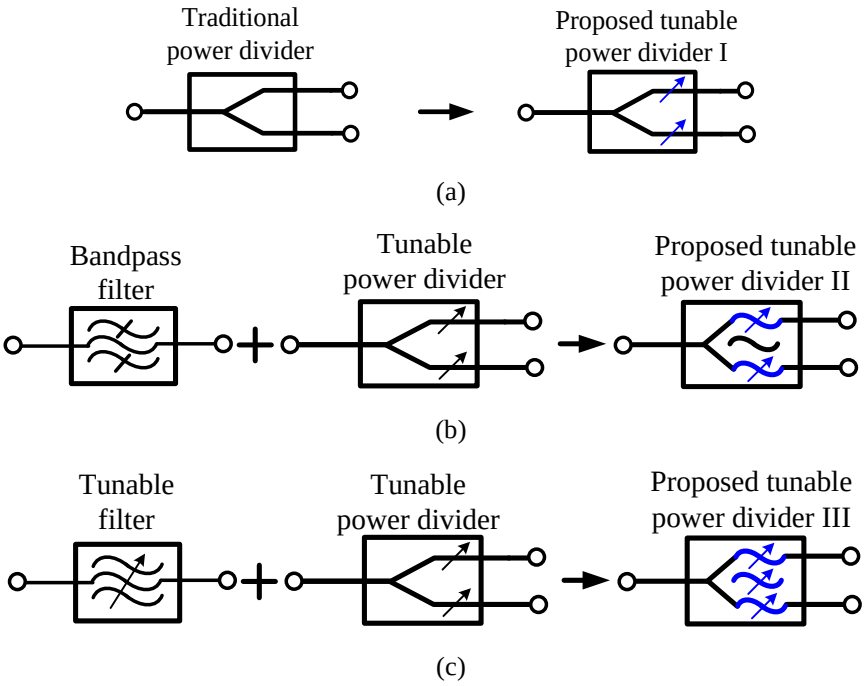

Fig 5. 1 Proposed concept of (a) Type-I; (b) Type-II; and (c) Type-III

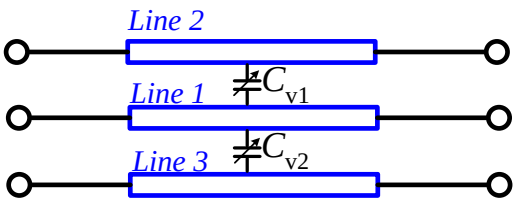

Fig 5. 2 Transmission line model of the three-line coupled structure with two loaded capacitors between the centre-line and two sidelines.

In this chapter, three different power dividers designs have been developed, to meet the functioning requirement of Type-I, Type-II and Type-III power dividers. All of these designs are based on a novel varactor-loaded coupled structure. In the following sections, the varactor-loaded coupled structure is firstly analysed, followed by three prototypes with experimental verifications. In the end, a kind of four-way filtering power divider with sharp selectivity and high upper-stopband rejection is also presented.

5.2 Varactor-loaded Three-line Coupled Structure (TLCS)

5.2.1 Configuration

In Chapter 3, we have discussed about the three-line coupled-line. In this section, a kind of three-line coupled structure with loaded capacitance will be discussed and adopted, as shown in Fig 5.2. Two varactors with tuning capacitance C_{v1} and C_{v2} are loaded in between the centreline and two sidelines. Since we have known the coupling factors of a three-line coupled structure, the modified coupling factors between the centreline and two sidelines can be expressed as:

$$K_{12} = \frac{C_{2oo} - C_{2ee} + 2C_{v1}}{\sqrt{(C_{1ee} + C_{1oo} + 2C_{v1} + 2C_{v2})(C_{2ee} + C_{2oo} + 2C_{v1})}} \tag{5.1}$$

$$K_{12} = \frac{C_{3oo} - C_{3ee} + 2C_{v2}}{\sqrt{(C_{1ee} + C_{1oo} + 2C_{v1} + 2C_{v2})(C_{3ee} + C_{3oo} + 2C_{v2})}} \tag{5.2}$$

On the other hand, if the centreline is fed with an input signal, and two sidelines are connected to two terminations, one can build a one-to-two power divider. For such kind one-to-two PD, the output power at two output ports can be regarded as P_2 and P_3. The required coupling factors of each sideline connected to two output ports and the power division ratio (PDR) between two output ports can be defined using the coupling factors as:

$$K_{12} = \sqrt{\frac{P_2}{P_2 + P_3}} = \frac{k}{\sqrt{k^2 + 1}} \tag{5.3}$$

$$K_{13} = \sqrt{\frac{P_3}{P_2 + P_3}} = \frac{1}{\sqrt{k^2 + 1}} \tag{5.4}$$

$$PDR = k^2 = \frac{P_2}{P_3} = \frac{K_{12}^2}{K_{13}^2} \tag{5.5}$$

Here k refers to the amplitude ratio of $|S_{21}|$ and $|S_{31}|$, and also the square root of the PDR. Substituting (5.1) and (5.2) in (5.5), the power division ratio can be expressed as

$$PDR = \frac{C_{3ee} + C_{3oo} + 2C_{v2}}{C_{2ee} + C_{2oo} + 2C_{v1}} \cdot \left(\frac{C_{2oo} - C_{2ee} + 2C_{v1}}{C_{3oo} - C_{3ee} + 2C_{v2}}\right)^2 \tag{5.6}$$

It is seen from (5.6) that the power division ratio can be changed by controlling and varying the added capacitances of C_{v1} and C_{v2}. The following section will show the numerical relation between the PDR and value of the loaded capacitance.

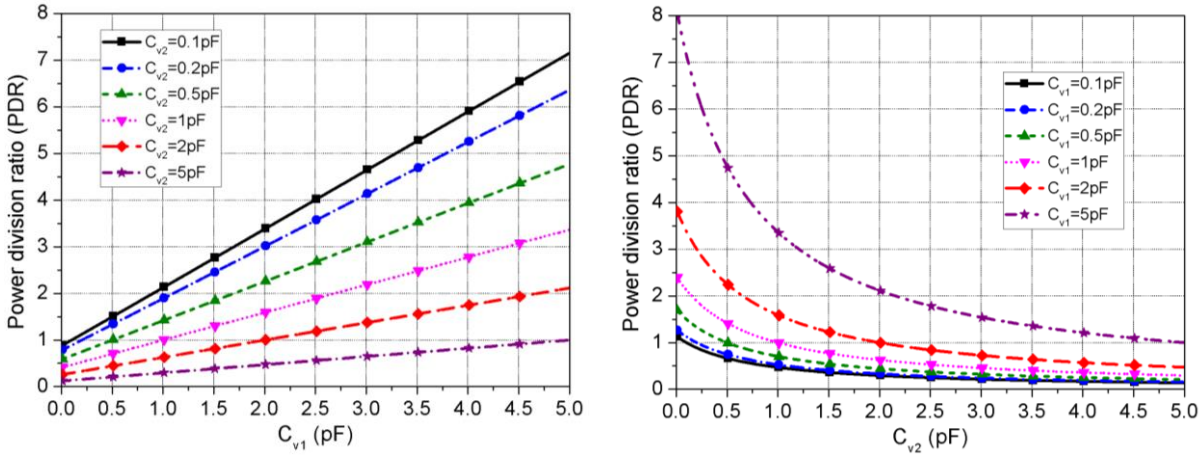

(a) (b)

Fig 5. 3 Achievable power division ratio against (a) C_{v1} and (b) C_{v2}.

5.2.2 Power Division Ratio (PDR)

Equation (5.6) defines the achievable PDR with regard to the mode-impedance of the TLCS as well as the value of the loaded capacitance. Once the mode-impedance (equivalently C_{xij}) and loaded varactors are defined, the PDR can be found and controlled easily. It is obvious that when the coupling coefficient of the TLCS is varied, the achievable PDR will also be changed. Following the discussion in [134], in this design, the mode-impedance for the TLCS is set to be: $Z_{1ee} = 157.3\ \Omega$, $Z_{1oo} = 15.9\ \Omega$, $Z_{2ee} = Z_{3ee} = 120.7\ \Omega$, and $Z_{2oo} = Z_{3oo} = 20.7\ \Omega$.

Using Equation (5.6), the realizable PDR against the added varactors C_{v1} and C_{v2} are depicted in Figs 5.3 (a) and (b). It can be observed that the theoretical results in Fig 5.3 indicate a wide tuning range of tunable PDRs using two tuning elements. When C_{v2} is fixed, a larger PDR can be obtained using a larger value of C_{v1}, and the PDR is proportional to the value of C_{v1}. It is the same for C_{v2} if C_{v1} is fixed. It is worth mentioning that the achievable PDR can be realised at all frequencies, which means this structure can achieve wideband tunable performance. This can be explained by the frequency-independent effect of the loaded capacitance on the energy distribution on each sideline.

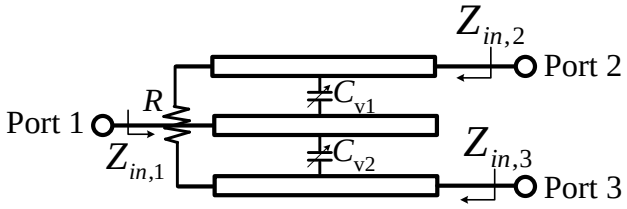

Fig 5. 4 Configuration of the tunable power divider with tuning power division ratio

5.3 Design of Wideband Tunable Power Divider with Tuning Power Division Ratio

5.3.1 Configuration

In this section, a tunable power divider is proposed based on the presented varactor-loaded three-line coupled structure. The tunability of PDR is implemented by utilizing tuning elements like varactors. Fig 5.4 shows the configuration of the initial power divider with tunable PDR. The input port is located at one side of the centreline, whereas the output ports are at the end of two sidelines. The other ends of two sidelines are connected together with an isolation resistor *R* in the middle. The electrical length of the TLCS is always equal to quarter-wavelength at centre frequency, which is a similar to two-line coupled-line that can generate transmission zeros due to the cancellation of magnitude at certain frequency points.

5.3.2 Matching and Isolations

For a power divider, it is very critical to investigate the matching property at each port and the isolation between all output ports. In this design, it is possible to prove that perfect matching at all ports and perfect isolation between output ports can be achieved while the PDR is changed. Here the impedance matrix of the six-port network shown in Fig 5.2 is studied for finding the input impedance of each port [135]. The input impedance of port 1 can be written as:

$$Z_{in,1} = -j\frac{(Z_{1ee} + Z_{1oo} + 2Z_{1oe})}{4}\cot\theta + \frac{(Z_{1ee} - Z_{1oo})^2\csc^2\theta}{4Z_0 - j(Z_{1ee} + Z_{1oo} + 2Z_{1oe})\cot\theta} \tag{5.7}$$

Since the overall electrical length of TLCS is selected as quarter-wavelength at the centre frequency f_0, and thus the input impedance of the input port can be reduced as

$$Z_{in,1} = \frac{(Z_{1ee} - Z_{1oo})^2}{4Z_0} = Z_0 \tag{5.8}$$

Meanwhile, the coupling of two sidelines is minimal and negligible when the following equation is satisfied

$$\sqrt{Z_{1ee}Z_{1oo}} = \sqrt{Z_{2ee}Z_{2oo}} = \sqrt{Z_{3ee}Z_{oo}} = Z_0 \tag{5.9}$$

From (5.6) and (5.9), one can solve that the value of Z_{1ee} and Z_{1oo} are: $Z_{1ee} = 120.7\ \Omega$, $Z_{1oo} = 20.7\ \Omega$. These values are the basic requirement which the three-line coupled structure should satisfy.

On the other hand, it is also critical to find the matching property of two output ports. Under the even-even and odd-odd mode conditions, the excitations at two output ports (Port 2 and Port 3) are in-phase, which means that there is no current flowing through the resistor. Whereas for the odd-even mode, the resistor has some effect on the output impedances $Z_{in,2}$ and $Z_{in,3}$, which can be expressed as

$$Z_{in,2} = Z_{2oe}\frac{R + j2Z_{2oe}\tan\theta}{2Z_{2oe} + jR\tan\theta} \tag{5.10}$$

$$Z_{in,3} = Z_{3oe}\frac{R + j2Z_{3oe}\tan\theta}{2Z_{3oe} + jR\tan\theta} \tag{5.11}$$

where Z_{2oe} and Z_{3oe} can be found from the following equations [136]:

$$Z_{2oe} = \frac{Z_{2ee}Z_{2oo}\varepsilon_{oe}}{Z_{2oo}\varepsilon_{ee} + Z_{2ee}\varepsilon_{oo}} \tag{5.12}$$

$$Z_{3oe} = \frac{Z_{3ee}Z_{3oo}\varepsilon_{oe}}{Z_{3oo}\varepsilon_{ee} + Z_{3ee}\varepsilon_{oo}} \tag{5.13}$$

To achieve perfect matching at output ports, it is required to have

$$Z_{in,2} = Z_{in,3} = Z_o \tag{5.14}$$

To determine the value of *R*, we consider the case of equal power division without adding varactors between lines, for simplicity. Under such circumstance, it is obvious to have $Z_{2oe} = Z_{3oe}$. To achieve perfect matching at the centre frequency f_0, the resistor *R* can be found from the following equation

$$R = \frac{2Z_{2oe}^2}{Z_0} \tag{5.15}$$

5.3.3 Predicted S-parameters

From the analysis above, the input impedances at all ports are varied when the PDR is changed, because they are all related to C_{v1} and C_{v2}. However, the influence of C_{v1} and C_{v2} is minor, which means the matching properties are not greatly affected, resulting in acceptable return loss at all ports. Fig 5.5 gives the variation of input impedance of Port 1 across a wideband frequency range from 0.8 GHz to 2.2 GHz. It can be observed that the deviation range of $Z_{in,1}$ is from 30 Ω to 60 Ω, which is quite stable at Z_0 and leading to a satisfactory return loss (more than 10 dB). The matching property will deteriorate when the operating frequency moves away from f_0 to higher or lower frequencies, as shown in Fig 5.5 (a).

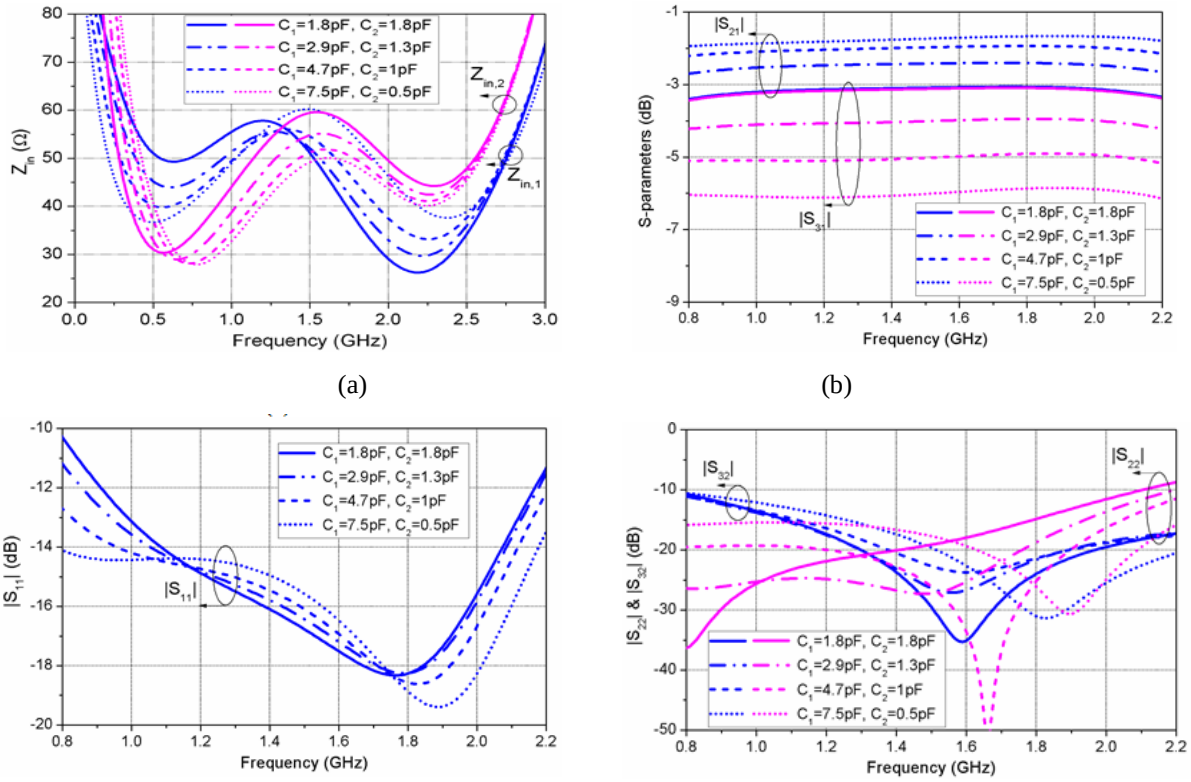

(a) (b)

(a) (b)

Fig 5. 5 Calculated results of (a) characteristic impedance at port 1 and port 2; (b) $|S_{21}|$ and $|S_{31}|$; (c) $|S_{11}|$; (d) $|S_{22}|$ and $|S_{32}|$.

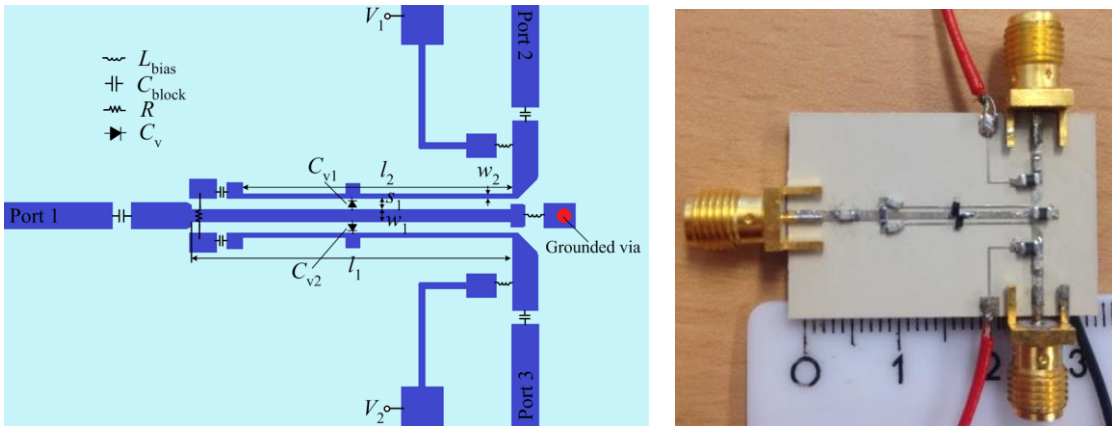

(a) (b)

Fig 5. 6 (a) Layout and (b) photograph of the fabricated prototype.

A wide range of power division ratio (PDR) can be realised by varying the values of two varactors across a very wideband frequency range. Fig 5.5 displays the variation of output power against capacitance C_{v1} and C_{v2}, as well as the return loss at all ports and isolation between two output ports. Fig 5.5 (b) shows different output power of four cases with different PDRs of 1:1, 1.5:1, 2:1 and 3:1. The operating frequency band is up to more than 80% from 0.8 GHz to 2.2 GHz with very small deviation. In Figs 5.6 (c) and (d), good matching at all ports and isolation between Port 2 and Port 3 are predicted. It is noted that the power division of Port 2 and Port 3 can be reversed. In other words,

when the value of C_{v2} is larger than C_{v1}, smaller PDRs such as 0.7:1, 0.5:1 and 0.3:1 can also be realised by reversing values of C_{v1} and C_{v2} in Fig 5.5.

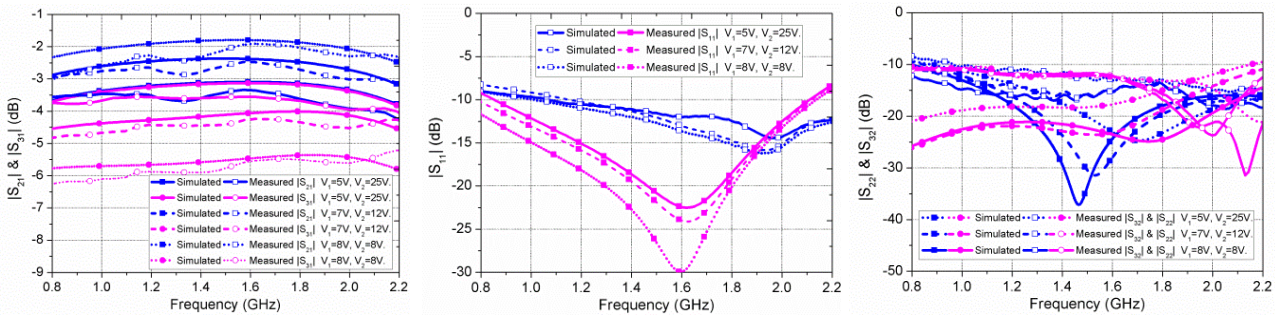

(a) (b) (c)

Fig 5. 7 Simulated and measured results: (a) $|S_{21}|$ and $|S_{31}|$; (b) $|S_{11}|$; and (c) $|S_{22}|$ and $|S_{32}|$.

5.3.4 Experimental Verifications

Following the analysis above, a 3D electromagnetic model is built in EM simulation tool ADS, and full-wave simulation has been done to validate the idea of wideband PDR tunability. The proposed tunable PD based on TLCS is designed on the substrate with dielectric constant of 10.2 and thickness of 1.27 mm. The layout of the structure is shown in Fig 5.6. Two varactors, which are connected between the centreline and sidelines, are realised by Skyworks SMV-1283. The value of the isolation resistor R is set to be 100 Ω. To build a biasing circuit for the varactors and block the DC current, a RF choke of 10 μH inductors and 100 pF capacitors are added.

Figs 5.7 (a), (b) and (c) show the simulated and measured S-parameters of the fabricated prototype of the tunable PD. Power division ratio of 1:1, 1.5:1, and 2:1 are realised, with more than 10 dB return loss at Port 1, Port 2 and Port 3. The measured insertion loss at Port 2 and Port 3 are 2.4 dB/2.9 dB/3.6 dB and 5.8 dB/4.6 dB/3.8 dB, compared with simulated ones of 2.0 dB/2.6 dB/3.2 dB and 5.5 dB/4.4 dB/3.2 dB. The isolation between Port 2 and Port 3 is better than 11 dB. The operating band range is from 1.06 GHz to 2.1 GHz (65.8% bandwidth), which is slightly shifted to higher frequencies compared with the design objective. Some differences between the experimental results with the predicted ones are due to some errors during the fabrication and testing process.

5.4 Design Filtering Power Divider with Tunable Power Division Ratio

This section will present a filtering power divider with tunable power division ratio. As we all know, the cascaded structure of devices lead to bulky circuit size and large insertion loss. To avoid these shortcomings, it is favourable to have power dividers with filtering responses, in other words, to integrate filtering response with power dividers as shown in Fig 5.1 (b). Therefore, a pair of stepped-impedance open stubs is loaded with the proposed tunable power divider based on TLCS, to fulfil the design objective.

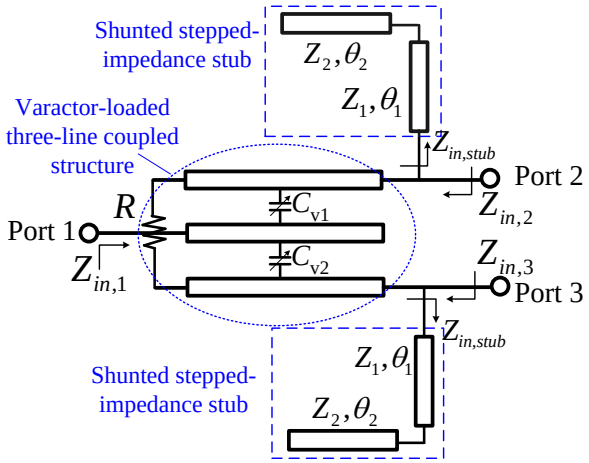

Fig 5. 8 Configuration of the tunable power divider with tuning power division ratio and filtering response.

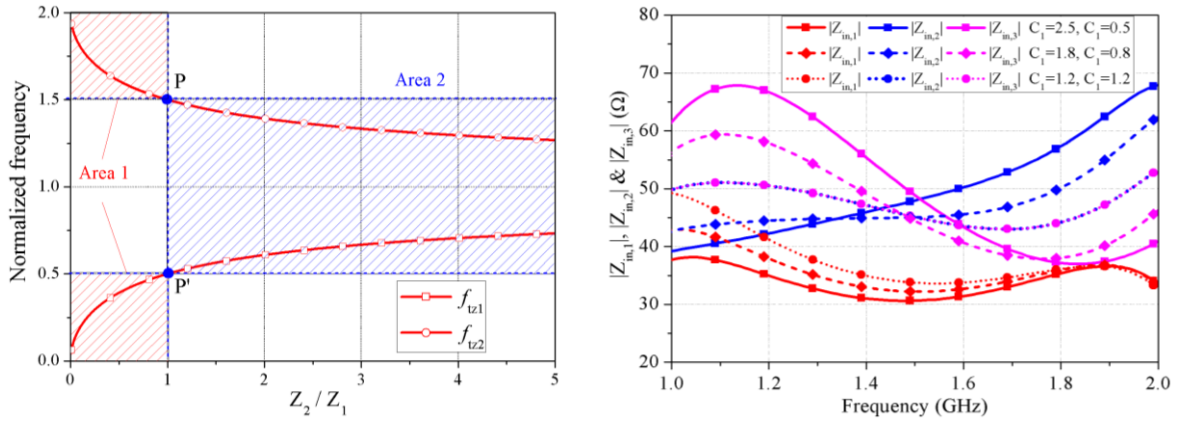

(a) (b)

Fig 5. 9 (a) Position of f_{tz1} and f_{tz2} against impedance ratio of Z_2 and Z_1; (b) The input impedance at the input/output ports with different values of C_{v1} and C_{v2} (Unit: pF).

5.4.1 Configuration and Analysis

Fig 5.8 displays the configuration of the proposed filtering tunable power divider. It consists of a varactor-loaded three-line structure and two shunted stepped-impedance stubs. Two varactors C_{v1} and C_{v2} are located at the central position of the structure between the centreline and two sidelines. The terminations of the two sidelines are connected together with a resistor R between them. The stepped-impedance stubs have two sets of transmission lines of Z_1, θ_1 and Z_2, θ_2.

The design is also able to achieve a tunable power division ratio. Since the electrical parameters are selected as the same as the last design presented in Section 5.3, the achievable PDR also follows the distribution displayed in Fig 5.3. The matching properties are also the same with the last design, for the reason that the shunted stubs have infinite impedance at the operating band, which can be seen as open circuit and thus have no effect on $Z_{\text{in},2}$ and $Z_{\text{in},3}$. Meanwhile, the shunted stepped-impedance stubs help to generate two transmission zeros (f_{tz1} and f_{tz2}) at the edges of the passband. The input impedance of the shunted stubs can be expressed as

$$Z_{in,stub} = jZ_1 \frac{Z_1 \tan\theta_1 - Z_2 \cot\theta_2}{Z_1 + Z_2 \tan\theta_1 \cot\theta_2} \tag{5.16}$$

To obtain symmetric locations of the zeros at f_o and flat response within the passband range, the electrical lengths of the stub is fixed as $\theta_1 = \theta_2 = 90°$ at f_o. In this case, the locations of the normalized f_{tz1} and f_{tz2} are determined by the impedance ratio of Z_2 and Z_1, as indicated in the following equations:

$$\begin{aligned} f_{tz1} &= arctan\sqrt{Z_2/Z_1} \\ f_{tz2} &= 2 - arctan\sqrt{Z_2/Z_1} \end{aligned} \tag{5.17}$$

Fig 5.9 (a) depicts the variance trend of θ_{tz1} and θ_{tz2} against Z_2/Z_1. When Z_2/Z_1 is equal to 1, f_{tz1} and f_{tz2} are located at $0.5f_o$ and $1.5f_o$ (point P and P' in Fig 5.9[a]). Due to the discontinuity of the step, f_{tz1} and f_{tz2} will move away from f_o or move close to f_o when Z_2/Z_1 is smaller or larger than 1, as indicated as Area 1 and Area 2 in Fig 5.9 (a), respectively. In this design, the impedance of Z_1 and Z_2 are chosen as 105 Ω and 42 Ω, and thus f_{tz1} and f_{tz2} are located at $0.38f_o$ and $1.62f_o$.

The input impedance at all three ports are studied with the selected parameters above. It is noted that the $Z_{in,stub}$ equals to infinity at f_o, which means the shunted stubs have no effect on $Z_{in,1}$, $Z_{in,2}$ and $Z_{in,3}$. As revealed in Fig 5.9 (b), when different values of C_{v1} and C_{v2} are used and the power division ratio varies from 1:1 to 1.5:1 and 2:1, $Z_{in,1}$, $Z_{in,2}$ and $Z_{in,3}$ are all constant within the range from 30 Ω to 68 Ω, indicating satisfactory matching properties at two output ports with better than

10 dB return loss regardless of the value of PDR. Therefore, it is possible to achieve ideal matching, isolation, and continuous tunability of power division ratio.

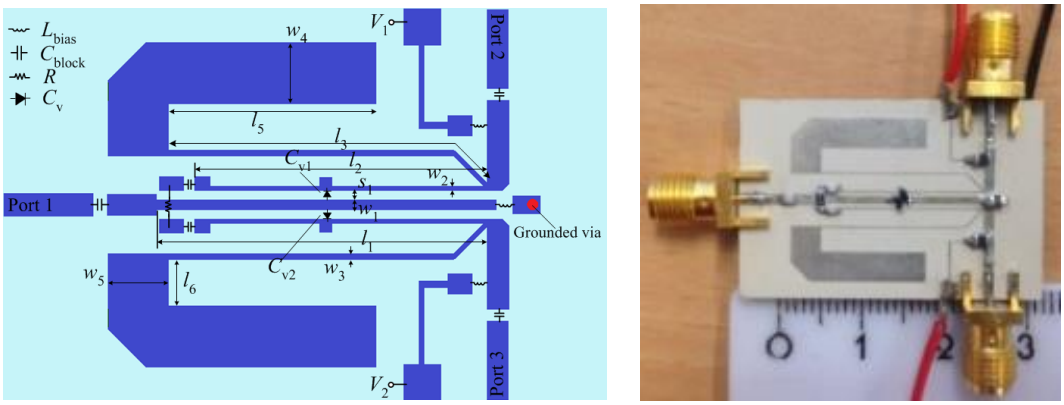

(a) (b)

Fig 5. 10 (a) Layout and (b) photograph of the fabricated prototype.

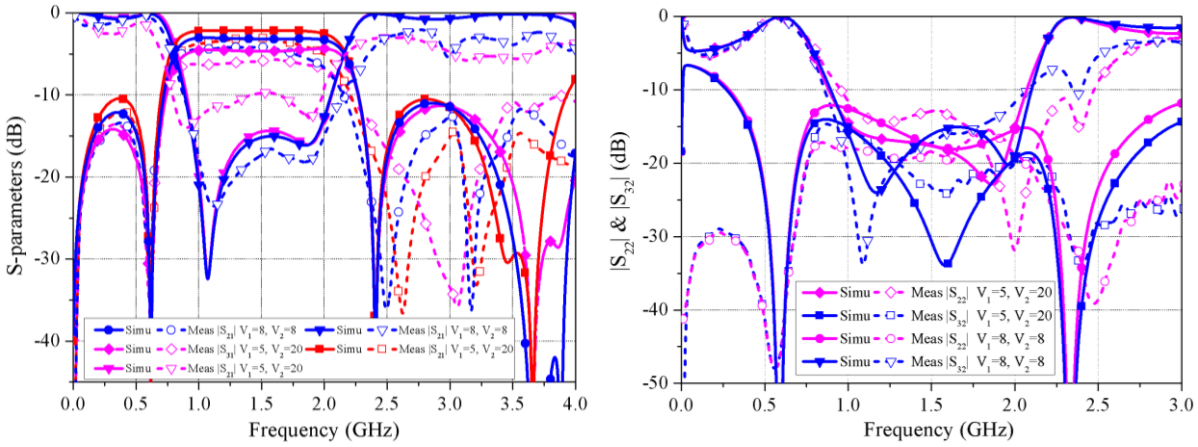

(a) (b)

Fig 5. 11 Simulated and measured results of the proposed device (Unit: V): (a) $|S_{11}|$, $|S_{21}|$ and $|S_{31}|$; (b) $|S_{22}|$ and $|S_{32}|$.

5.4.2 Simulation and Measurement

To verify the design approach, a prototype model is built and simulated with SPICE model of varactors in Agilent's Advanced Design System (ADS). The layout of the proposed design is shown in Fig 5.10. The substrate used here has dielectric constant of 10.2 and thickness of 1.27 mm. The varactors are adopted as Skyworks SMV2019-219. To provide decent power to the varactors, a biasing network composed of 10 μH RF choke and 100 pF DC block capacitors is built. The isolating resistor is selected as 100 Ω. The related electrical parameters of the three-line structure and stepped-impedance stubs are the same as discussed above. The final dimensions of the structure are (all in mm): l_1=19.4, l_2=16.6, l_3=19.8, l_4=12.2, l_5=2.8, w_1=0.9, w_2=0.2, w_3=0.15, w_4=3.5, w_5=3.5 and s_1=0.4.

Figs 5.11 (a) and (b) show the simulated and measured results of the fabricated prototype of the proposed tunable power divider. Two different states are displayed in Fig 5.11 with different power divisions of 1:1 and 2:1. Filtering responses are realised due to the existence of transmission zeros created by the shunted stubs. Compared with the simulated S_{21} and S_{31} of 3.2 dB and 3.2 dB (PDR = 1:1), 2.2 dB and 5 dB (PDR = 2:1), the measured S_{21} and S_{31} are found to be 3.8 dB (PDR = 1:1), 3 dB and 6 dB (PDR = 2:1), as given in Fig 5.11 (a). Two poles are located within the passband, and acceptable input return loss (more than 10 dB) across a wide band range from 0.8 GHz to 2.05 GHz. Besides, the upper- and lower-stopband have more than 10 dB rejections. Fig 5.11 (b) demonstrates the proposed design has excellent matching (better than 12 dB) at Port 2 and 3, and perfect wideband isolation (better than 15 dB) between Port 2 and Port 3. The operating passband range is from 1.02 GHz to 1.96 GHz (63% bandwidth). The measured differential phase between Port 2 and Port 3 is 2.5˚ and 7.5˚ when PDR equals to 1:1 and 2:1, compared with the simulated ones of 1˚ and 4.5˚. The proposed device has a compact size of 0.26 λ_g × 0.24 λ_g, which is favoured in miniaturization of circuit and systems.

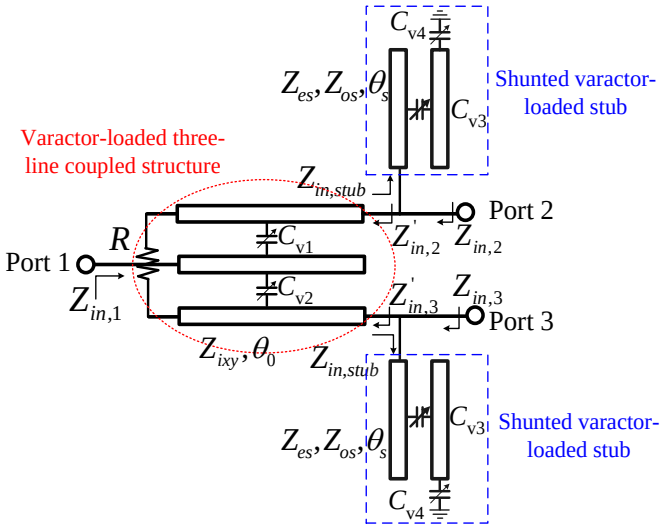

Fig 5. 12 Configuration of the tunable power divider with tuning power division ratio and controllable filtering response.

5.5 Design of Tunable Power Divider with Controllable Filtering Response

Last section presented a tunable power divider with integrated characteristics of bandpass filters. To make the filtering response controllable, a new design of tunable power divider is presented in this section, which has the function shown in Fig 5.1 (c). The detailed theoretical analysis and a design procedure are given. For verification of the proposed concept, a prototype is simulated, fabricated and successfully tested.

5.5.1 Design Configuration

In this design, a kind of three-line coupled structure with tunable coupling factor is adopted in the proposed design, so as to achieve the desired power division across wideband frequency range. To integrate a controllable filtering feature, varactor-loaded short-ended stubs are shunted at the output ports, leading to a controllable filtering response. Multiple transmission zeros are created by the stubs at both edges of the passband as well as in the upper-stopband resulting in sharp cut-off selectivity of the filtering band and wide harmonic suppressions.

The configuration of the proposed tunable power divider is shown in Fig 5.12. It is composed of a varactor-loaded three-line coupled structure (as marked in dotted circle) and two shunted varactor-loaded stubs (as marked in dashed block) in the form of coupled lines. The input port is located at one side of the centreline of the three-line coupled structure, whereas the output ports are at the far ends of the two sidelines. The other ends of the two sidelines are connected together with an isolation resistor *R*. Two varactors with capacitance values of C_{v1} and C_{v2} are connected between the centreline and the two sidelines at the centre position to control the coupling factor and thus output power division ratio. Two short-ended stubs, which are in the form of coupled lines loaded with varactors of capacitances C_{v3} and C_{v4}, are shunted to the output ports.

5.5.2 Controllable Filtering Response

To investigate the filtering property of the proposed device, the loaded varactors C_{v1} and C_{v2} are fixed at equal values (1 pF) so that equal power division can be obtained. The shunted varactor-loaded stub is shown in the blue dashed boxes in Fig 5.13. Here, two varactors with variable capacitance C_{v3} and C_{v4} are added at middle as well as the end of the coupled-line section (Z_{es}, Z_{os}, θ_s). In this example, the electrical lengths of coupled-line section θ_0 and stubs θ_s are set equal to quarter wave-length at the centre operating frequency f_o.

The *ABCD*-matrix approach is used for analysis to depict the filtering performance of the stub. For the shunted varactor-loaded stub, the coupled-line section with can be calculated using

$$[A]_{sc} = \begin{bmatrix} A_2 & B_2 \\ C_2 & D_2 \end{bmatrix} = \begin{bmatrix} Z_{11}/Z_{21} & (Z_{11}^2 - Z_{21}^2)/Z_{21} \\ 1/Z_{21} & Z_{11}/Z_{21} \end{bmatrix} \tag{5.18}$$

where

$$Z_{11} = -\frac{jZ_{os}[1-\tan\theta_s(2Z_{os}\omega C_{v3}+\tan\theta_s)]}{4(Z_{os}\omega C_{v3}+\tan\theta_s)} - j\frac{Z_{es}\cot(2\theta_s)}{2} \tag{5.19}$$

$$Z_{21} = \frac{jZ_{os}[1-\tan\theta_s(2Z_{os}\omega C_{v3}+\tan\theta_s)]}{4(Z_{os}\omega C_{v3}+\tan\theta_s)(\cos 2\theta_s - Z_{os}\omega C_{v3}\sin 2\theta_s)} - j\frac{Z_{es}/\sin(2\theta_s)}{2} \quad (5.20)$$

The input impedance of the loaded stub can be written as

$$Z_{in,stub} = \frac{A_2/(j\omega C_{v4}) + B_2}{C_2/(j\omega C_{v4}) + D_2} \quad (5.21)$$

where A_2, B_2, C_2 and D_2 can be found from (5.18)-(5.20). The *ABCD*-matrix of the shunted stub can be written as

$$[A]_s = \begin{bmatrix} 1 & 0 \\ 1/Z_{in,stub} & 1 \end{bmatrix} \quad (5.22)$$

Due to the shunted stubs, multiple transmission zeros are produced when the following equation is satisfied

$$Z_{in,stub} = 0 \quad (5.23)$$

Considering that the microstrip technique is adopted for verification in this design, the impedance should be selected within the range of 140 Ω to 180 Ω and 60 Ω to 80 Ω for Z_{es} and Z_{os}, respectively. In this design as an example, the related parameters of the shunted stubs are selected as Z_{es} = 168 Ω and Z_{os} = 74 Ω in the calculations.

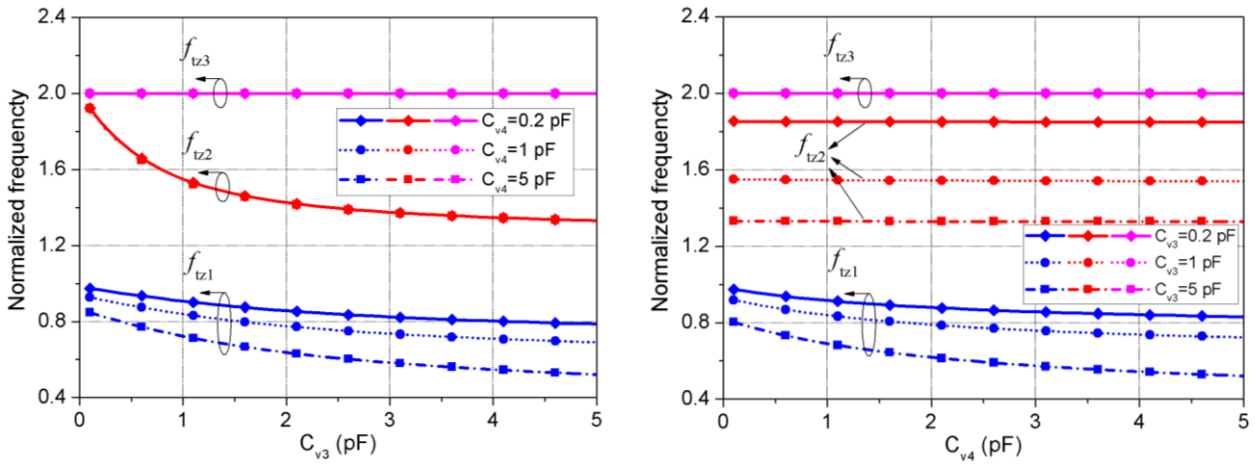

(a) (b)

Fig 5. 13 Position of first three transmission zeros (f_{tz1}, f_{tz2} and f_{tz3}) with (a) C_{v3}; (b) C_{v4}.

A series transmission zeros located at $2f_o$, $4f_o$, …, $2nf_o$ are created due to the three-line coupled structure. On the other hand, by solving Equation (5.23), multiple transmission zeros are produced by the loaded short-ended stubs. In the frequency range of 0 to $4f_o$, six transmission zeros are created, among which two are generated by the three-line coupled structure at $2f_o$ and $4f_o$ (named

f_{tz3} and f_{tz6}), while the other four TZs (named f_{tz1}, f_{tz2}, f_{tz4} and f_{tz5}) are produced by the loaded short-ended stubs. Since f_{tz1} and f_{tz2} are located at the two edges of the filtering band, sharp cut-off skirts of the passband can be obtained.

Fig 5.13 shows the changing tendency of the first three multiple transmission zeros (f_{tz1}, f_{tz2}, f_{tz3}) against C_{v3} and C_{v4}, since f_{tz1} and f_{tz2} are located at the lower- and upper-edge of the passband, contributing to a sharp passband cut-offs selectivity. As mentioned above, f_{tz3} is produced by the three-line coupled structure, which is not affected by C_{v3} and C_{v4}. It is observed that f_{tz1} and f_{tz2} are affected by C_{v3}, while f_{tz1} is affected only by C_{v4}. Therefore, f_{tz1} can be adjusted by tuning C_{v3} and C_{v4} at the same time, while f_{tz2} can be controlled independently by tuning C_{v3}. In this way, the lower- and upper-edge of the passband can be controlled to be relocated independently by selecting appropriate C_{v3} and C_{v4}.

Since the fractional bandwidth (FBW) and centre frequency of the tunable filtering band are closely related to the position of TZs, it can be easily predicted that the FBW and centre can be varied using C_{v3} and C_{v4}. The FBW is calculated here using the two side frequencies (f_L and f_H) at which there is a 3-dB drop compared to the maximum value of S_{21}.

$$FBW = \frac{2(f_H - f_L)}{(f_H + f_L)} \tag{5.24}$$

Fig 5.14 shows the effect of C_{v3} and C_{v4} on the FBW and centre frequency of the filtering band. It is observed that the FBW can be varied from 0.25 to 0.75, while the normalized operating centre frequency can be shifted from 0.9 to 1.2. When C_{v3} increases and C_{v4} is fixed, larger FBW can be obtained and the centre frequency of the band moves to lower frequencies. Similar phenomenon can be found when C_{v3} and C_{v4} are reversed: when C_{v4} increases and C_{v3} is fixed, larger FBW can be obtained and the centre frequency of the band moves to lower frequencies. To sum up, the value of C_{v3} and C_{v4} can be chosen according to the desired target of FBW and centre frequency according to Fig 5.15.

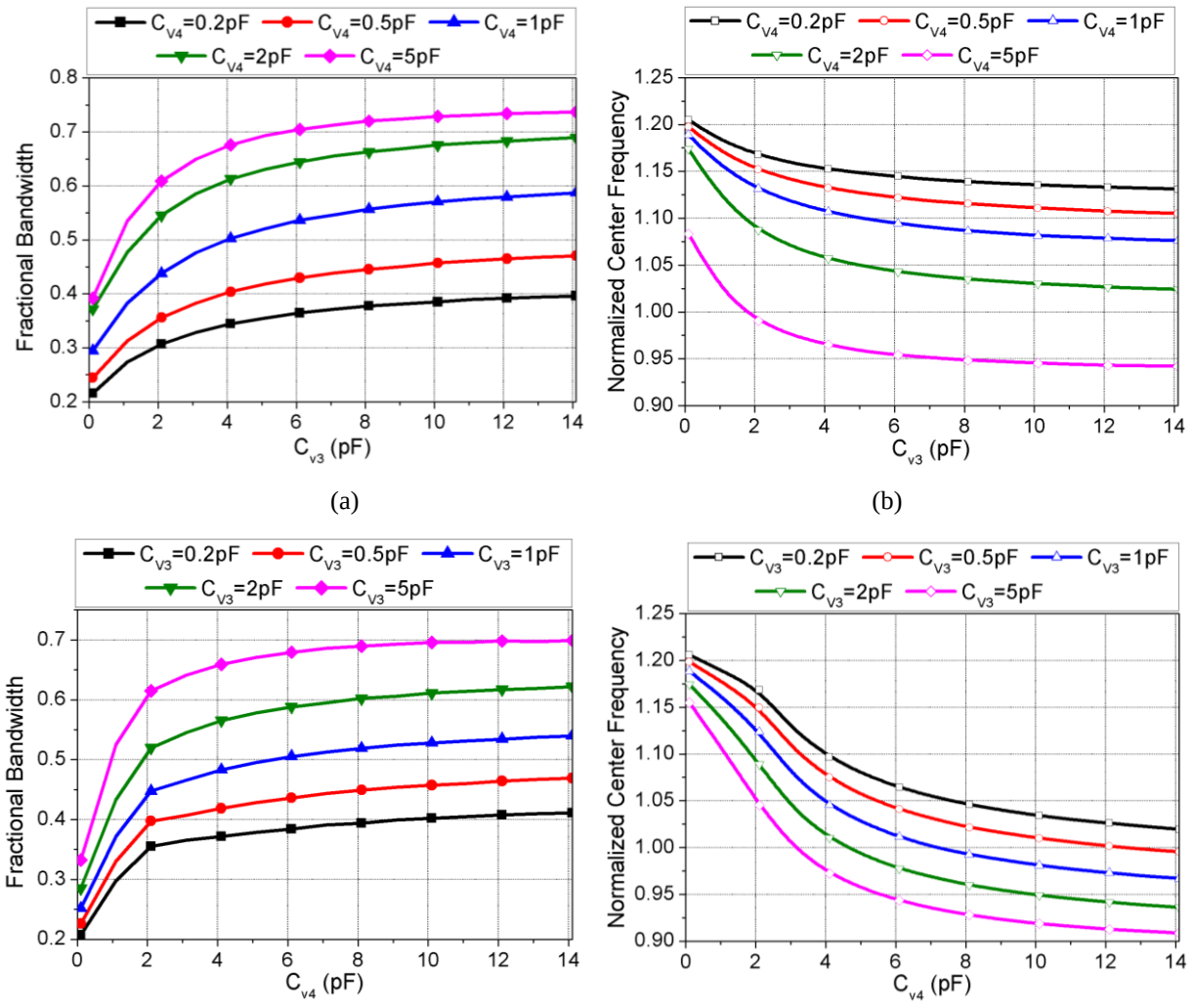

Fig 5. 14 Effect of C_{v3} and C_{v4} on the filtering response of the proposed tunable power divider: Effect of C_{v3} on the tunability of (a) FBW and (b) normalized centre frequency. Effect of C_{v4} on the tunability of the (c) FBW, and (d) normalized centre frequency.

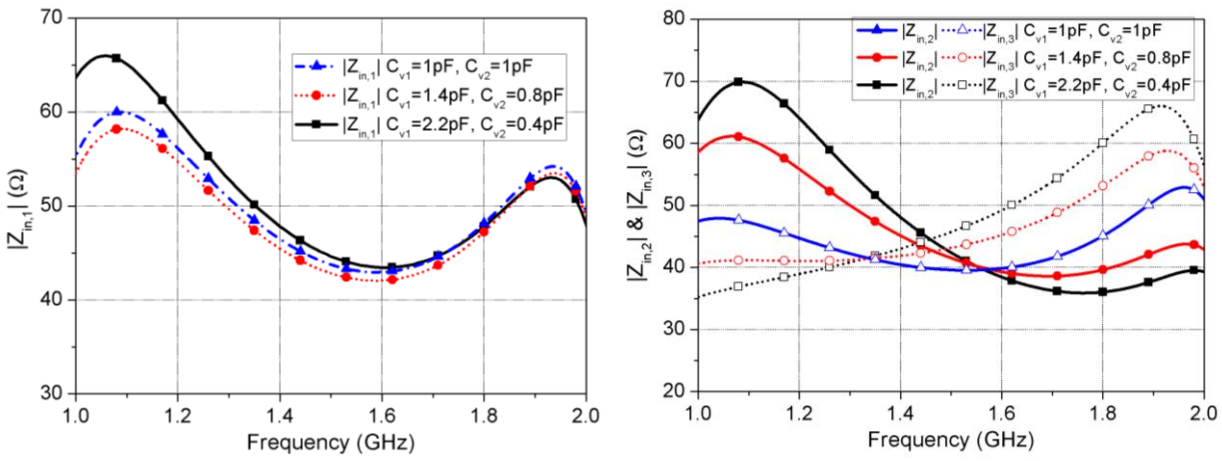

Fig 5. 15 The input impedance with varied C_{v1} and C_{v2} at (a) input port (Port 1), and (b) output ports (Port 2 and Port 3).

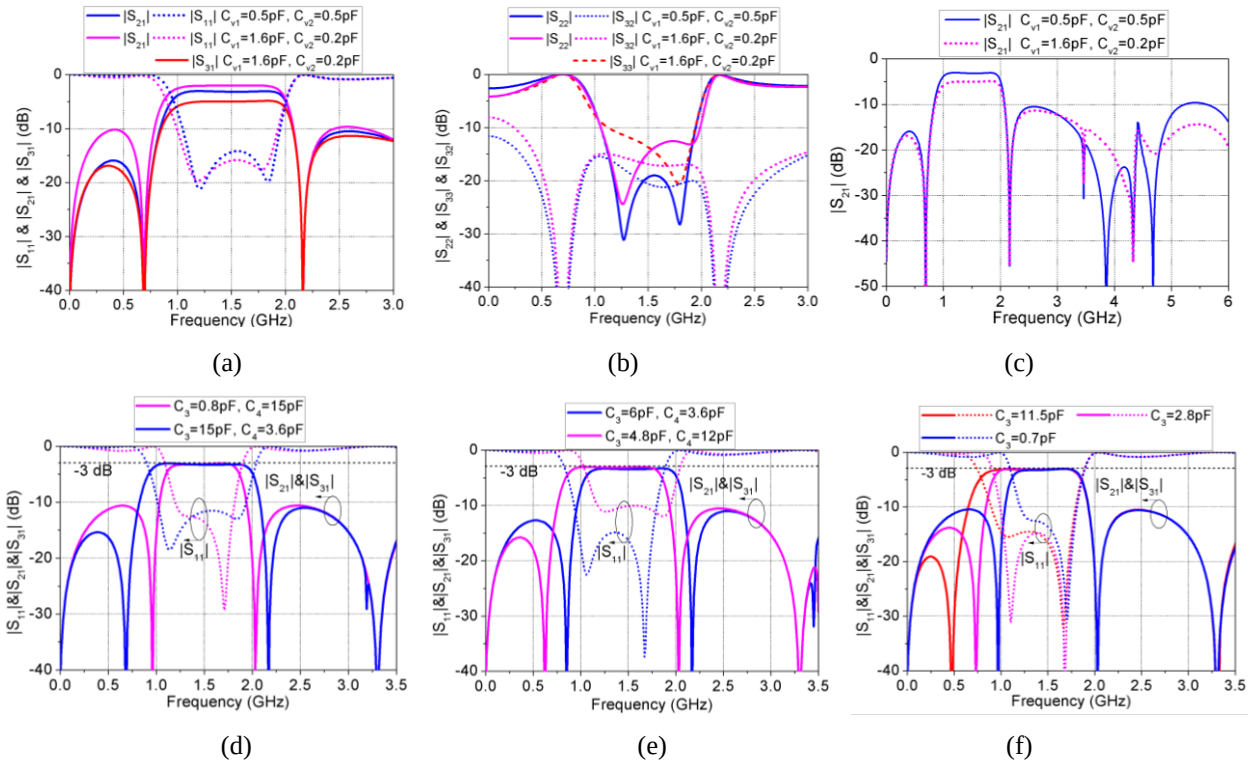

Fig 5. 16 Circuit simulation of S-parameters of the device: (a) $|S_{11}|$, $|S_{21}|$ and $|S_{31}|$; (b) $|S_{22}|$, $|S_{33}|$ and $|S_{32}|$; (c) $|S_{21}|$; and controllability of (d) bandwidth; (e) centre frequency, and (f) cut-off edge.

5.5.3 Matching Property

From Fig 5.12 one can find that the input impedance can be expressed as

$$Z_{in,2} = Z'_{in,2} // Z_{in,stub},\ Z_{in,3} = Z'_{in,3} // Z_{in,stub} \tag{5.25}$$

Since the input impedance of the stub is extremely high, and thus can be assumed to be open circuit at the centre frequency ($Z_{in,stub} = \infty$), we can assume that

$$Z'_{in,2} = Z_{in,2},\ Z'_{in,3} = Z_{in,3} \tag{5.26}$$

The expression of $Z_{in,2}$ and $Z_{in,3}$ are given in Equations (5.10) and (5.11). To achieve perfect matching at output ports, it is required to have

$$Z_{in,2} = Z_{in,3} = Z_o \tag{5.27}$$

From the analysis above, one can find that the input impedances at all ports are varied when the PDR is changed because they are all related to C_{v1} and C_{v2}. The question here is whether that variation is significant to cause degraded matching. Figs 5.15 (a) and (b) depict the variation of the input impedances of Port 1, Port 2 and Port 3 across a wideband frequency range from 0.8 GHz to 2.0 GHz. For the input port, the characteristic impedance is stable around 50 Ω (42 Ω to 66 Ω) with limited effect from C_{v1} and C_{v2}. Similarly, it can be observed from Fig 5.15 (b) that the range of

variation of $Z_{in,2}$ and $Z_{in,3}$ is from 35 Ω to 70 Ω, which is quite stable around Z_o across the wide frequency range. These features indicate that excellent wideband impedance matching can be achieved at all the ports.

5.5.4 Tunability Analysis of Tunable Power Divider with Controllable Band

Based on the previous analysis and discussion, it is possible to predict the performance of the proposed tunable power divider presented in Fig 5.12. The centre frequency f_o in this design is selected as 1.5 GHz. Let us assume the design objectives as: (1) tunable power division ratios of 1:1, 2:1, and 3:1; (2) controllable bandwidth from 50% to 70%, and centre frequency tunability from $0.9f_o$ to $1.1f_o$; (3) sharp selectivity and relocatable cut-offs at edges of the passband and harmonic-suppression in the upper-stopband to $4f_o$; (4) equal phase at the two output ports within the operating band.

Fig 5.16 shows all the investigated cases of the tunable power division as well as tunable filtering feature of the proposed power divider using circuit simulation in Agilent's Advanced Design System (ADS). For the first goal, Figs 5.16 (a)-(c) show the tunability of the power division ratio with fixed filtering response. Since the power division is controlled by C_{v1} and C_{v2}, whereas C_{v3} and C_{v4} are fixed as 5 pF and 12 pF, the shaping of the filtering passband is flat and stable. Different PDRs of 1:1, 2:1 and 3:1 (the ideal insertion loss of S_{21} and S_{31} are 3.01 and 3.01 dB, 1.76 and 4.77 dB, and 1.25 and 6.02 dB, respectively) are investigated with around 60% bandwidth at centre frequency of 1.5 GHz. The isolation and output port matching are also excellent across a wideband frequency range as indicated in Fig 5.16 (b). When changing the value of C_{v1} and C_{v2}, tunable power division is realised with flat insertion loss. The return loss at the input port is more than 15 dB, while the isolation and output return losses are more than 12 dB. Fig 5.16 (c) indicates wide range of upper-stopband with more than 10-dB rejection is achieved under different power division ratios.

Meanwhile, to investigate the tunability of the filtering band, C_{v3} and C_{v4} are now varied while C_{v1} and C_{v2} are fixed at 1.2 pF, as shown in Figs 5.16 (d) - (f). The achievable bandwidth in this example can be tuned from 50% to around 75%. Besides, the centre frequency can be shifted by around 200 MHz without affecting the bandwidth, as shown in Fig 5.16 (e). Two edges of the passband can be shifted independently by controlling C_{v3} and C_{v4}. Fig 5.16 (f) shows the reconfigurability of the lower-edge of the passband. It is notable that when C_{v1} and C_{v2} are changed (from equal to unequal power division), the tunability of the band is still the same, which indicates independent tunability of the power division ratio and filtering response. There is some slight variation in $|S_{11}|$ as can be found in Fig 5.16 (e) due to the influence of the loaded varactor on the

input impedance of Port 1. However, a satisfactory return loss of more than 10 dB across filtering bandwidth is maintained.

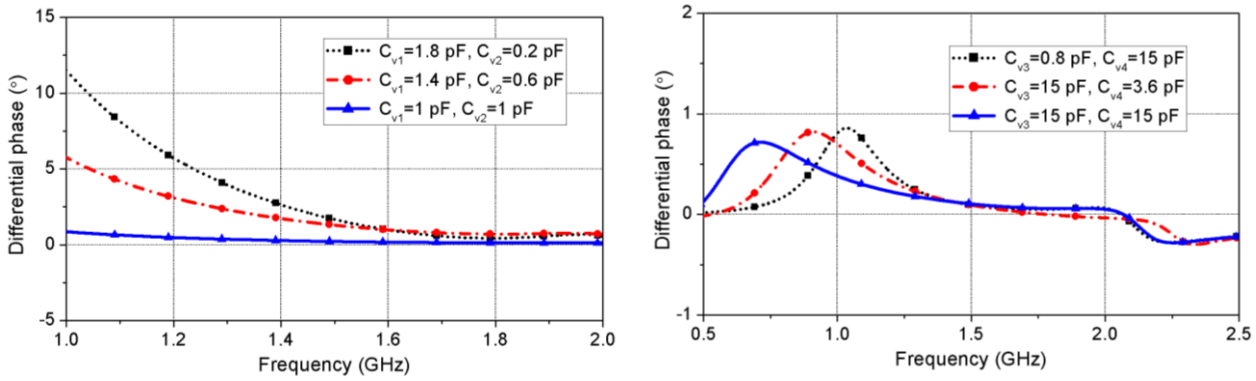

(a) (b)

Fig 5. 17 The differential phase for different (a) PDRs (variable C_{v1} and C_{v2} & constant C_{v3} and C_{v4}), and (b) filtering response (variable C_{v3} and C_{v4} & constant C_{v1} and C_{v2}).

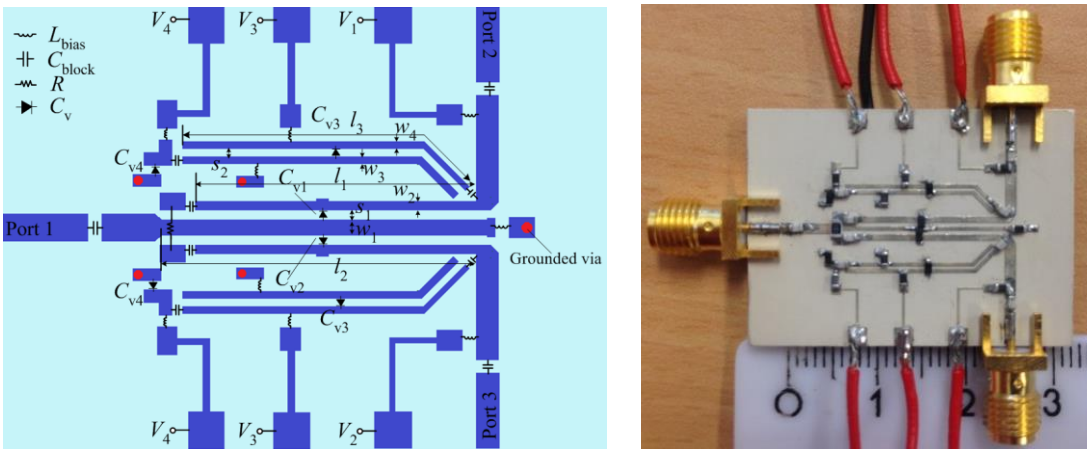

(a) (b)

Fig 5. 18 (a) Layout the proposed device; (b) Photograph of the device.

Moreover, the differential phase between the two output ports is critical to maintain the linearity of systems using the proposed power divider. Here, the effect of the utilized varactors on the differential phase ($\angle S_{21} - \angle S_{31}$) is investigated and shown in Fig 5.17 under two different scenarios. Firstly, Fig 5.17 (a) shows that when the PDR is changed from 1:1 (blue line) to 2:1 (red line) and 3:1 (black line) by changing C_{v1} and C_{v2}, the differential phase slightly increases due to the effect of C_{v1} and C_{v2} on the slope of S_{21} and S_{31}. For the second scenario shown in Fig 5.17 (b), when C_{v3} and C_{v4} are changed while C_{v1} and C_{v2} are fixed, the differential phase only changes slightly as the varactors only changes the filtering response and have no effect on the amplitude or phase performance of the power divider within the passband. To sum up, although some fluctuation may be introduced by C_{v1} and C_{v2} at some frequencies, the differential phase between the two output

ports is still very small and the device can be regarded as an in-phase power divider operating at a wideband range.

5.5.5 Design Procedure

To make the design approach more practical, a general design procedure is given below. Assuming that it is required to design a tunable power divider with certain centre frequency, PDR and desired filtering bandwidth and frequency range, the designer can proceed with the following steps:

1. Find the mode impedances of the three-line coupled structure under *ee*-mode, *oe*-mode and *oo*-mod: $Z_{1ee} = 157.3\ \Omega$, $Z_{1oo} = 15.9\ \Omega$, $Z_{2ee} = 120.7\ \Omega$, $Z_{2oo} = 20.7\ \Omega$, and $Z_{2oe} = Z_{3oe} = Z_o$; and then find the corresponding physical dimensions after selecting a suitable substrate; find the value of resistor *R* using (5.15);

2. Select the electrical lengths of the three-line coupled structure and shunted stubs as quarter-wavelength at f_o. relative parameters of the stub can be selected within the range of 140 Ω to 180 Ω and 60 Ω to 80 Ω for Z_{es} and Z_{os} (Z_{es} = 168 Ω and Z_{os} = 74 Ω in this design);

3. Once the initial physical dimensions of the structure are fixed, find the required values for C_{v1} and C_{v2} from Fig 5.3 based on the desired PDR; select appropriate values for C_{v3} and C_{v4} from Fig 5.14 to get the objective FBW, centre frequency and position of cut-off zeros.

4. Build the electromagnetic model in full-wave simulation tool with biasing circuit and SPICE models of tuning elements, and do the simulation. The selection voltages should be based on the analysed results from Sections 5.5.3 and 5.5.4. Finally, tuning and optimization the whole structure is required.

5.5.6 Experimental Results and Discussions

To verify the proposed design, full-wave simulation is used with SPICE model of varactors in Agilent's Advanced Design System (ADS). Fig 5.18 (a) shows the layout and the biasing circuit of the prototype. The adopted substrate for fabrication is Rogers RO3010, which has a dielectric constant of 10.2 and height of 1.27 mm. Two varactors C_{v1} and C_{v2}, which are connected between the centreline and each sideline, are realised by Skyworks SMV2019-219 (L_s=0.7 nH, R_s=4.8 Ω, capacitance tuning range from 0.16 pF to 2.25 pF). Meanwhile, another two varactors are loaded on each stub: C_{v3} is laid across the coupled-line at centre position of the stub, and C_{v4} is loaded between the end of the coupled conductor and ground. The type of the varactors of C_{v3} and C_{v4} is adopted as Skyworks SMV1283-011LF (L_s=1.7 nH, R_s=2.4 Ω, capacitance tuning range from 0.52 pF to 14.2 pF). Due to the existence of several active elements, a biasing network which is

composed of 10 μH RF choke and 100 pF DC block capacitors is used. The dimensions (in mm) are optimized to be: l_1=16.8, l_2=18.7, l_3=17.8, w_1=0.35, w_2=0.7, w_3=0.45, w_4=0.45, w_5=3.5, s_2=0.45 and s_2=0.25. The overall size of the proposed power divider design is 0.3 λ_g × 0.21 λ_g (λ_g is the guided-wavelength at the centre frequency 1.5 GHz).

A prototype of the tunable power divider is fabricated (a photo is shown in Fig 5.18[b]) and tested. To verify the tunability, different voltages of the biasing sources are used. The selection of voltages is based on the required value of the capacitance first using the data sheet of the varactors [110]. The detailed testing procedure is described as follows: Firstly, the power division ratio is studied by controlling the voltage of V_1 and V_2. Here V_3 and V_4 are fixed as 5 V and 0 V in all the cases with different PDRs. Figs 5.19 (a) and (b) depict the simulated and measured results for this case. Two different states are tested and given in Fig 5.19 with different power divisions of 1:1 and 2:1 within the passband range. Compared with the simulated S_{21} and S_{31} of 3.2 dB and 3.2 dB (PDR = 1:1), 2.2 dB and 5 dB (PDR = 2:1), the measured S_{21} and S_{31} are 3.8 dB (PDR = 1:1), and 2.8 dB and 5.8 dB (PDR = 2:1), respectively, as given in Fig 5.19 (a). Two resonant poles are located within the passband, indicating good return loss at the input port across a wide band range from 1.05 GHz to 1.9 GHz. Besides, the upper- and lower-stopband have more than 10 dB rejections. Fig 5.19 (b) demonstrates satisfactory matching (more than 11 dB) at the output ports, and perfect wideband output ports isolation which is more than 15 dB. The operating passband range is from 1.02 GHz to 1.85 GHz (58% FBW) compared with design objective from 1.05 GHz to 1.95 GHz (60% FBW).

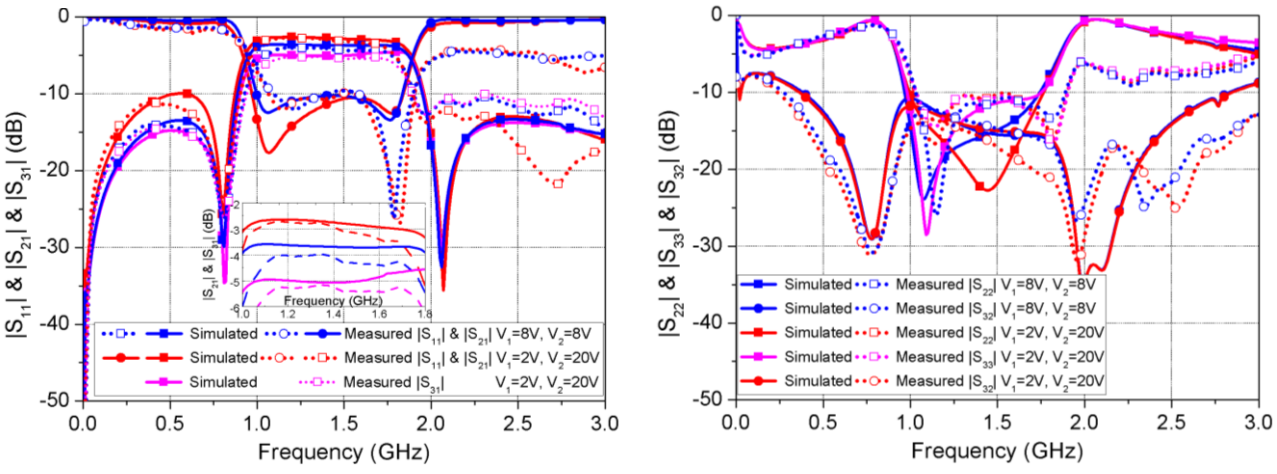

(a) (b)

Fig 5. 19 Simulated and measured results of the proposed tunable power divider with different PDRs: (a) $|S_{11}|$, $|S_{21}|$ and $|S_{31}|$; (b) $|S_{22}|$ and $|S_{32}|$;

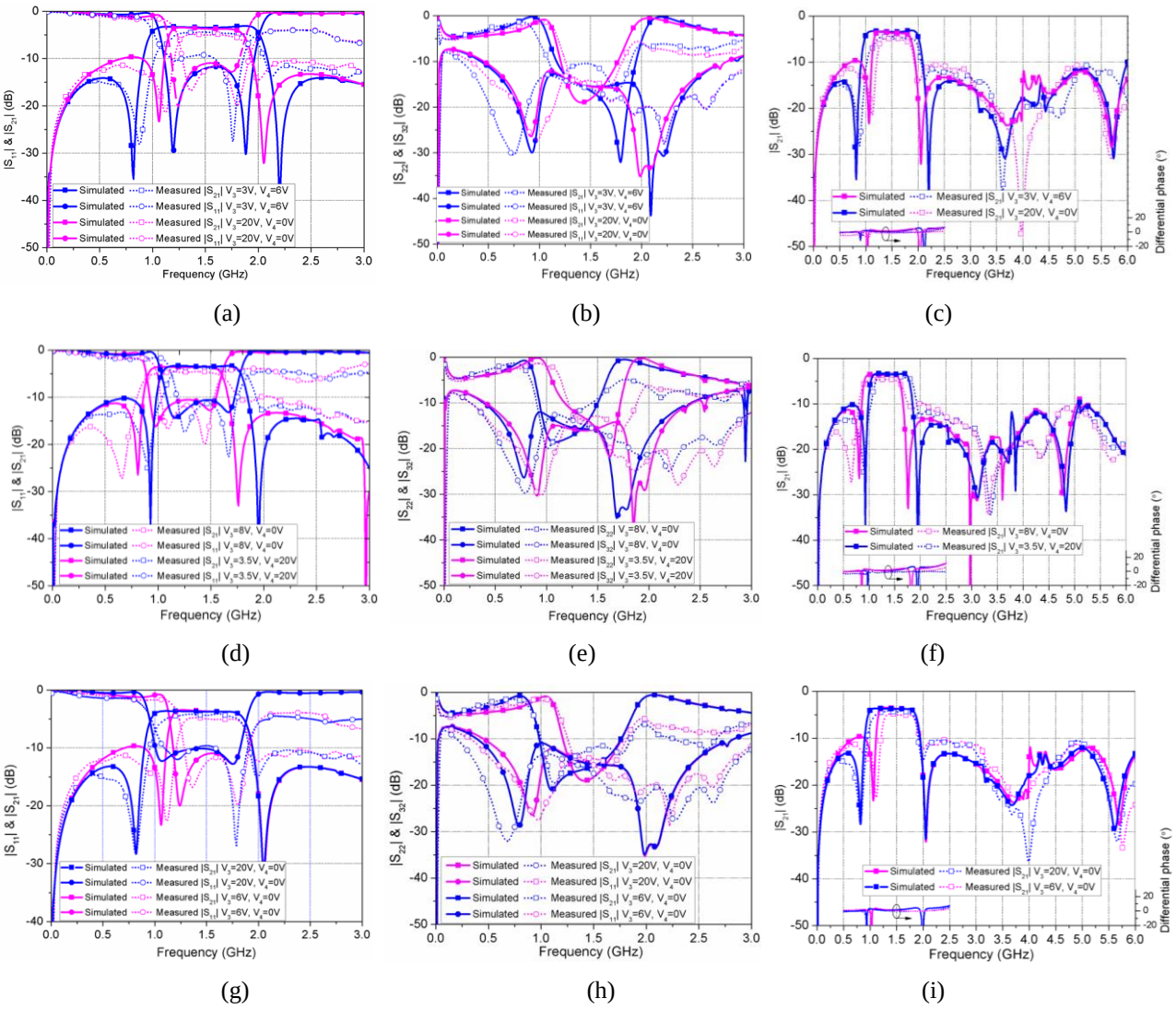

Fig 5. 20 Simulated and measured results of the proposed tunable power divider with (1) Bandwidth tunability of (a) $|S_{11}|$, $|S_{21}|$ and $|S_{31}|$; (b) $|S_{22}|$ and $|S_{32}|$, and (c) $|S_{21}|$ from 0 to 6 GHz, and in-band differential phase; (2) centre frequency tunability of (d) $|S_{11}|$, $|S_{21}|$ and $|S_{31}|$; (e) $|S_{22}|$ and $|S_{32}|$, and (f) $|S_{21}|$ from 0 to 6 GHz, and in-band differential phase; and (3) cut-off edge tunability of (g) $|S_{11}|$, $|S_{21}|$ and $|S_{31}|$; (h) $|S_{22}|$ and $|S_{32}|$, and (i) $|S_{21}|$ from 0 to 6 GHz, and in-band differential phase.

On the other hand, for the tunability of filtering response, the voltages of V_3 and V_4 are tuned while V_1 and V_2 are set as 8V in all cases. Fig 5.20 shows all the investigated cases of the design revealing that the proposed design has the tunability of bandwidth, centre frequency, and cut-off edge. In Figs 5.20 (a), (b) and (c), the bandwidth of the filtering response is varied from 35% (1.25 GHz to 1.78 GHz) to 63.2% (1.05 GHz-2.02 GHz), compared with the simulated band from 48% (1.22 GHz to 2.0 GHz) 70.6% (0.98 GHz-2.05 GHz). Figs 5.20 (d), (e) and (f) illustrate the shifting feature of passband. The measured centre operating frequency is shifted from 1.3 GHz to 1.48 GHz, with fixed 60% fractional bandwidth, compared with the simulated shifting range from 1.28 GHz to 1.45 GHz. Figs 5.20 (g), (h) and (i) depict the tunability of the cut-off edge, since the cut-off

selectivity of filtering passband are very critical. The lower-edge transmission zero can be tuned from 0.8 GHz to 1.08 GHz, without affecting the upper-edge zero. Similarly, the upper-edge zero can also be controlled without affecting the lower-edge of the passband. The measured in-band insertion loss for all cases is from 4.2 dB to 4.8 dB, compared with the simulation values (3.5 dB to 3.8 dB). Moreover, multiple transmission zeros are located in the upper-stopband, and thus wide stopband frequency range (from upper-edge of the passband up to 6 GHz) of more than 10 dB harmonic rejection can be observed. Besides, as seen from Figs 5.20 (b), (e) and (h), excellent matching (more than 12 dB) at Port 2 and Port 3 as well as perfect wideband isolation (more than 14 dB) are observed in all investigated cases. Lastly, the differential phase between the two output ports is maintained to be less than ±4.5˚ within specific filtering band ranges in all of the investigated cases. This verifies that the differential phase is not affected when the filtering response is tuned. This feature ensures the linearity of the proposed device.

The experimental performance is slightly different from the simulated one due to the nonlinearity of the tuning elements, as well as some losses in the fabrication process and the testing environment. Better results can be obtained if other kinds of varactors with smaller resistance and wider achievable capacitance range are used. It is worthy to note that although several works have previously been reported on tunable power dividers with filtering responses, it is the first time to present a filtering power divider with controllable operating band and centre frequency. Compared with other recently presented works, the proposed design has obtained the tunability of power division ratio, bandwidth, centre frequency, relocation of cut-off, and harmonic suppression. Moreover, compared with the cascading of tunable wideband filtering response with a power divider, the proposed design has much smaller insertion loss and reduced circuit size, which is favourable in miniaturized microwave systems.

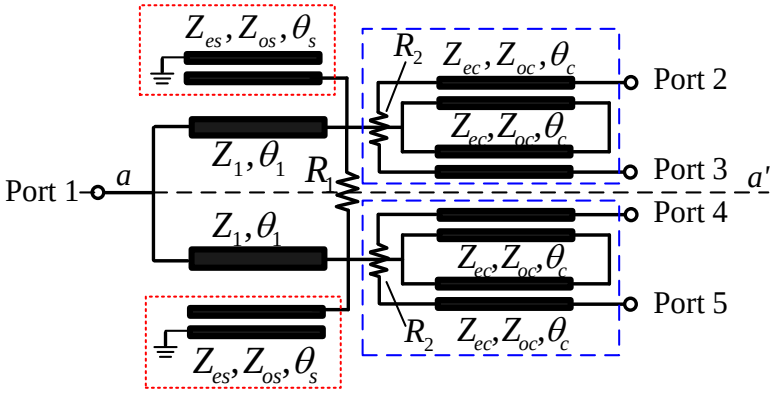

Fig 5. 21 Schematic diagrams of the proposed four-way filtering power divider.

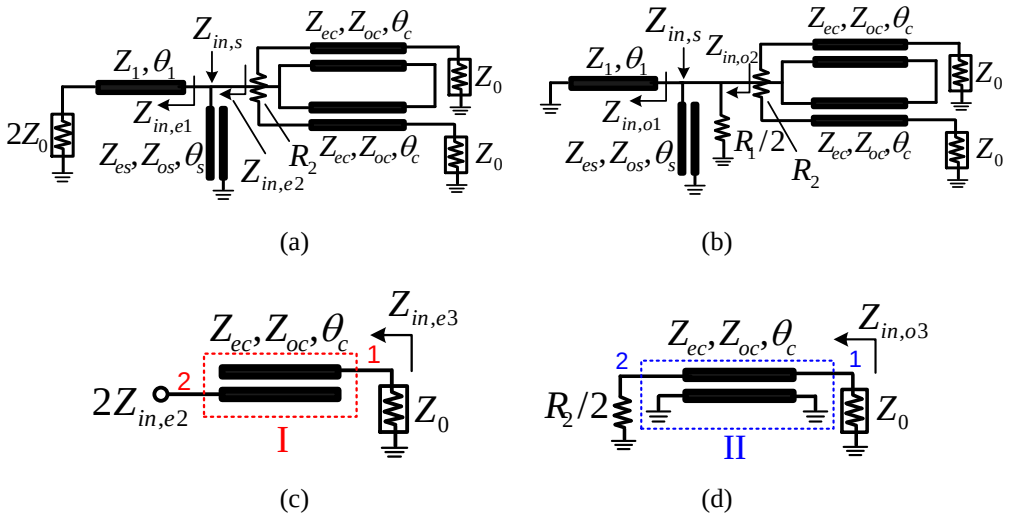

Fig 5. 22 (a) Even- and (b) odd-mode equivalent circuit of the filtering PD; (c) even- and (d) odd-mode circuit of the looped coupled-line structure.

5.6 Design of Wideband Four-way Filtering Power Divider

In the last few sections, tunable power division ratios and filtering responses were realised. In some cases, it is demanded to have multiple output ports for power dividers for feeding antenna arrays with multiple elements. Therefore, the target of this section is to introduce a four-way wideband filtering power divider (FPD) with wide bandwidth, sharp passband skirt selectivity and wide upper-stopband rejection with high attenuation. The power division into four output ports with wideband performance is realised using two looped coupled-line structures. Moreover, short-ended coupled-line stubs are loaded on the input of the looped coupled lines to introduce multiple transmission zeros for stopband rejection. The structure is analysed using even- and odd-mode methods. A detailed design procedure is introduced, followed by verification of the design using both simulation and experiment.

5.6.1 Configuration and Analysis

Fig 5.21 gives the basic configuration of the proposed four-way FPD. It is composed of two short-ended coupled-lines stubs (Z_{es}, Z_{os}, θ_s), two looped coupled-line structures (Z_{ec}, Z_{oc}, θ_c), and two connecting lines (Z_1, θ_1). An isolation resistor R_1 is loaded between the two connecting lines, whereas another two resistors R_2 connect the open-ends of the looped coupled-line sections. The short-ended coupled-line stubs (shown in dotted boxes) work as multi-mode resonators and generates multiple transmission poles as well as transmission zeros. The looped coupled-line sections (shown in dashed boxes) are utilized to divide the power to four output ports with the required matching and isolation.

Since the proposed structure is fully symmetric, it can be synthesized by using even-/odd-mode analysis method. Figs 5.22 (a) and (b) depict the even-mode and odd-mode equivalent circuits. When the even-mode excitation is applied, the termination at port two is characterized as $2Z_0$, and the corresponding input impedance of $Z_{in,e1}$, $Z_{in,s}$ and $Z_{in,e2}$ can be expressed as

$$Z_{in,e1} = Z_1 \frac{2Z_0 + jZ_1 tan\theta_1}{Z_1 + j2Z_0 tan\theta_1} \tag{5.28}$$

$$Z_{in,s} = \frac{j}{2} \cdot \frac{(Z_{es} - Z_{os})^2 - (Z_{es} + Z_{os})^2 cos^2\theta_s}{(Z_{es} + Z_{os}) sin\theta_s cos\theta_s} \tag{5.29}$$

$$Z_{in,e2} = \frac{Z_{in,e1} Z_{in,s}}{Z_{in,e1} + Z_{in,s}} \tag{5.30}$$

Similarly, when the odd-mode excitation is applied, the corresponding input impedance of $Z_{in,o1}$ and $Z_{in,o2}$ can be expressed as

$$Z_{in,o1} = jZ_1 tan\theta_1 \tag{5.31}$$

$$Z_{in,o2} = \frac{Z_{in,e2} Z_{in,s} R_1}{2Z_{in,e2} Z_{in,s} + Z_{in,s} R_1 + Z_{in,s} R_1} \tag{5.32}$$

To achieve perfect matching at Port 1 and isolation between Port 2 (or Port 3) and Port 4 (or Port 5), the following relation should be satisfied:

$$Z_{in,e2} = Z_{in,o2} \tag{5.33}$$

Then, the value of R_1 can be found from Equations (5.30) and (5.32) in (5.33)

$$R_1 = \frac{2Z_{in,e1} Z_{in,o1}}{Z_{in,o1} - Z_{in,e1}} \tag{5.34}$$

To prevent producing harmonics, the electrical lengths of the connecting lines of the coupled-lines are fixed as quarter-wavelength at the centre frequency, which is 1.5 GHz in this design. Combining Equations (5.28) to (5.34), it can be found that $Z_{in,s}$ equals to infinite, $Z_1 = Z_0/\sqrt{2}$, and $R_1 = Z_0$ at the centre frequency, regardless of the values of Z_{es} and Z_{os}.

To achieve perfect matching at all output ports and high isolation between Port 2 and Port 3 (or Port 4 and Port 5), a second-order even- and odd-mode analysis is applied on all the looped coupled-line

sections, as shown in Figs 5.22 (c) and (d). Then the input impedance of the output terminations under even- and odd-mode excitations can be characterized and equated to Z_0:

$$Z_{in,e3} = \frac{A_1 2Z_{in,e2} + B_1}{C_1 2Z_{in,e2} + D_1} = Z_0 \tag{5.35}$$

$$Z_{in,o3} = \frac{A_2 R_2 + 2B_2}{C_2 R_2 + 2D_2} = Z_0 \tag{5.36}$$

Here, A_1, B_1, C_1 and D_1 are the elements of ABCD-matrix for the two-port network I shown in Fig 5.23 (c), and A_2, B_2, C_2 and D_2 are the elements of ABCD-matrix for the two-port network II shown in Fig 5.22 (d). Then, the value of R_2 is found to be

$$R_2 = \frac{2(D_2 Z_0 - B_2)}{A_2 - C_2 Z_0} \tag{5.37}$$

It is found from equation (5.37) that $R_2 = 4Z_0$ is required for output matching regardless of the values of Z_{ec} and Z_{oc}.

5.6.2 Transmission Zeros and Matching Properties

Once the matching and isolation requirements of the power divider are satisfied, the filtering response can be characterized by determining the positions of transmission zeros (TZs) and transmission poles (TPs), which are produced by the loaded short-ended coupled-line stubs. By Equating (5.36) to zero, the positions of four TZs (f_{tz1}, f_{tz2}, f_{tz3} and f_{tz4}) can be found at:

$$\begin{aligned} &\theta_{TZ1} = arccos\frac{Z_{es} - Z_{os}}{Z_{es} + Z_{os}}, \quad && \theta_{TZ2} = \pi - \theta_{TZ1}, \\ &\theta_{TZ3} = \pi + \theta_{TZ1}, && \theta_{TZ4} = \pi, \end{aligned} \tag{5.38}$$

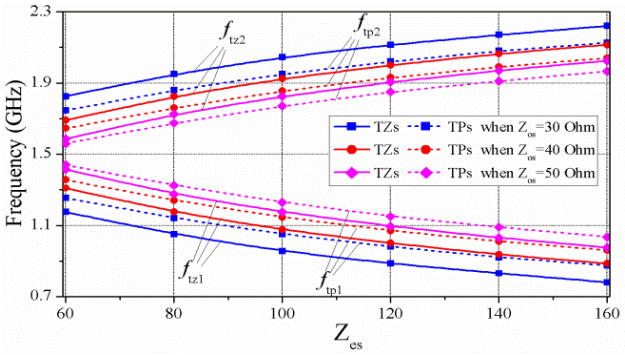

(a)

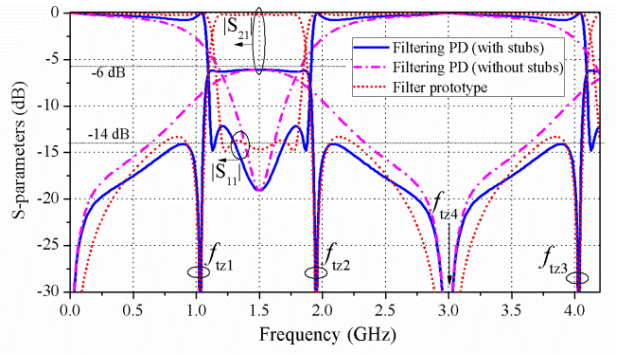

(b)

Fig 5. 23 (a) Variations of transmission poles (TPs) and zeros (TZs) with Zes and Zos; (b) S-parameters with and without short-ended coupled-line stubs.

The positions of TPs (f_{tp1} and f_{tp2}) defined by the short-ended coupled-lines stubs and connecting lines can be found at:

$$\theta_{TP1} = arcsin\sqrt{\frac{4Z_{es}Z_{os}}{(Z_{es}+Z_{os})(Z_{es}+Z_{os}+Z_1)}}\ ,$$
$$\theta_{TP2} = \pi - arcsin\sqrt{\frac{4Z_{es}Z_{os}}{(Z_{es}+Z_{os})(Z_{es}+Z_{os}+Z_1)}} \quad (5.39)$$

The locations of two TZs (f_{tz1} and f_{tz2}) and TPs (f_{tp1} and f_{tp2}) as a function of the characteristic impedance of Z_{es} and Z_{os} are shown in Fig 5.23 (a) using Equations (5.38) and (5.39). As a design example, f_{tp1} and f_{tp2} are selected at 1.0 GHz, 2.0 GHz, 1.03 GHz, and 1.97 GHz, respectively, to obtain around 60% bandwidth, and therefore Z_{es} and Z_{os} are selected as 108 Ω and 35 Ω. To provide a sufficient coupling at all output ports, the coupling coefficient of the looed-coupled structure is selected as 0.75 ($Z_{ec} = 120$ Ω and $Z_{oc} = 33.6$ Ω). Fig 5.23 (b) depicts the S-parameters of the proposed filtering divider (with and without the loaded short-ended coupled-line stubs) as well as the S-parameters of the bandpass filter prototype composed of coupled-line and a shunted short-ended coupled-lines stub. It is observed that compared with the case without loaded short-ended coupled-line stubs, multiple TZs appear at the upper-stopband resulting in sharp selectivity of the passband and wide upper-stopband rejection.

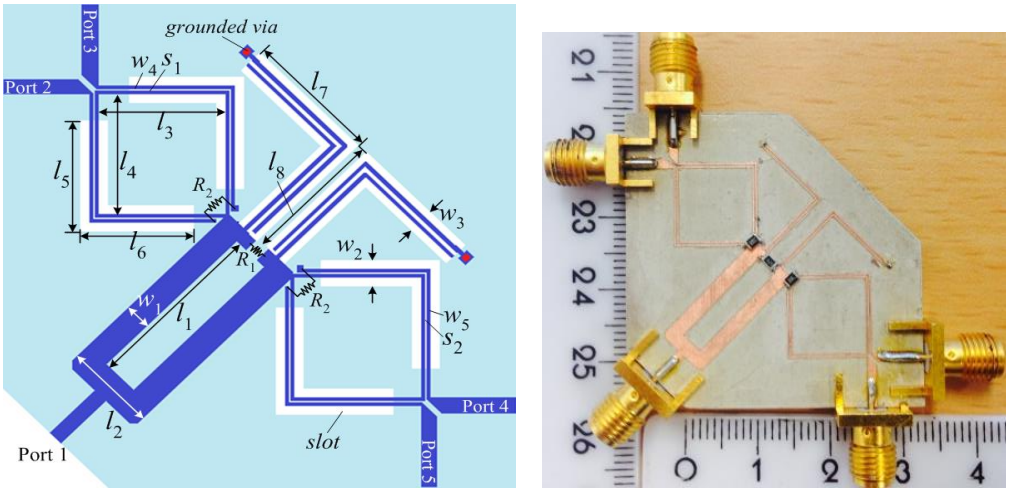

(a) (b)

Fig 5. 24 (a) Layout of the fabricated filtering PD; (b) Photograph.

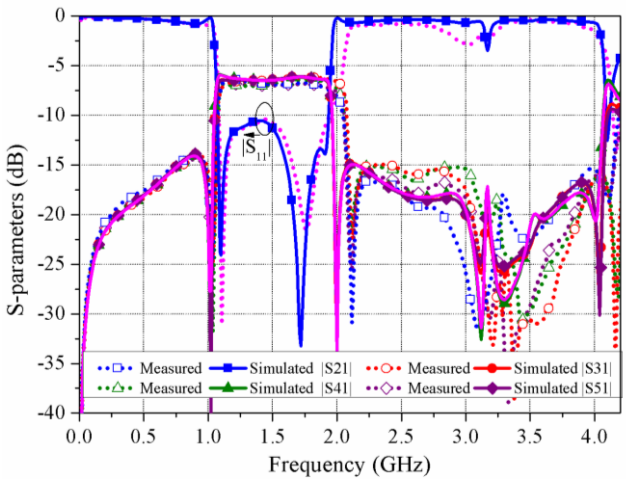

(a)

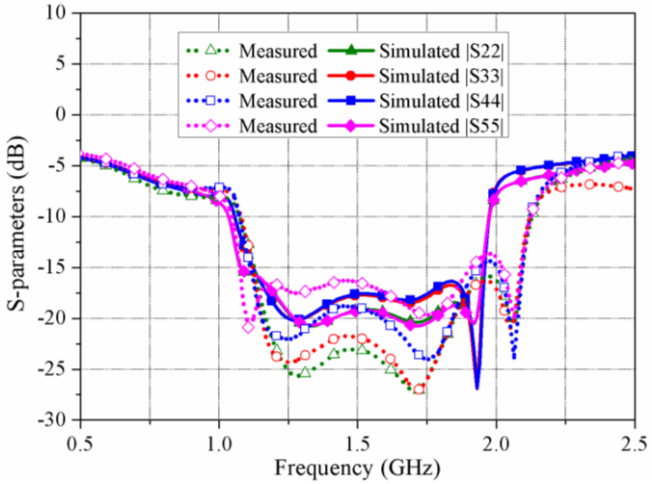

(b)

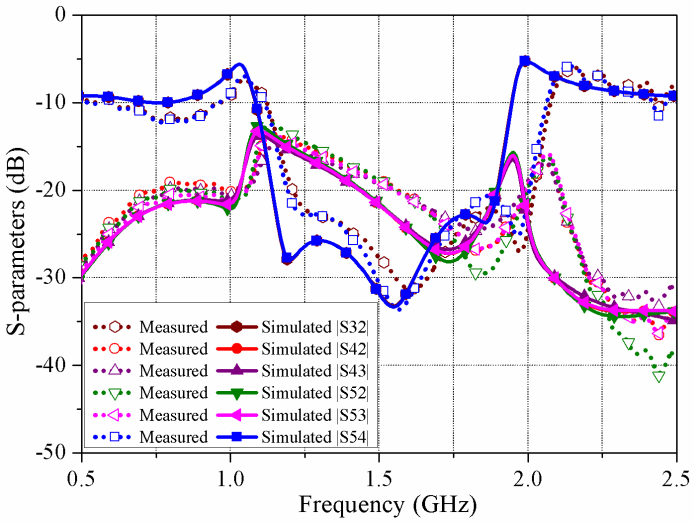

(c)

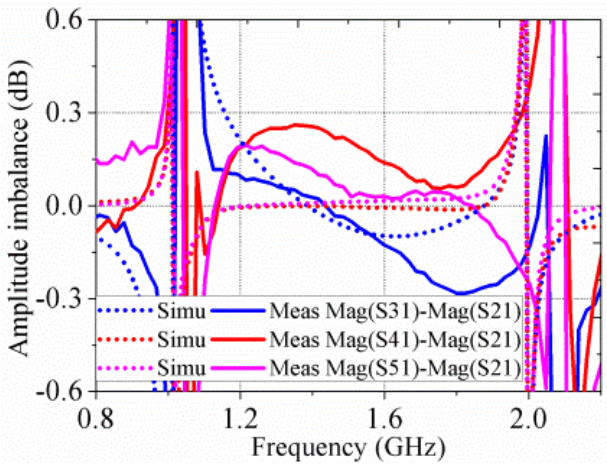

(d)

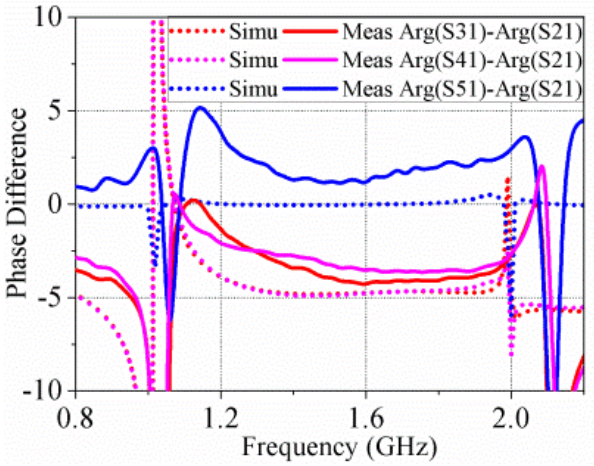

(e)

Fig 5. 25 Simulated and measured S-parameters of the proposed FPD: (a) insertion loss and input port return loss; (b) output ports return loss; (c) isolation; (d) magnitude imbalance, and (e) phase difference between all output ports.

5.6.3 Results and Discussions

To validate the proposed method, an example design with about 60% target fractional bandwidth centred at 1.5 GHz is simulated, fabricated and tested. The layout of the device is shown in Fig 5.25 (a). The initial electrical parameters used are derived from the analysis above, which are: $\theta_1 = \theta_s = \theta_c = 90^\circ$, $Z_1 = 35\ \Omega$, $Z_{es} = 108\ \Omega$, $Z_{os} = 35\ \Omega$, $Z_{ec} = 120\ \Omega$, $Z_{oc} = 33.6\ \Omega$, $R_1 = 50\ \Omega$, and $R_1 = 200\ \Omega$. Grounded slots on the ground layer shown in Fig 5.24 are used to realise the required mode impedances without using narrow gaps or thin lines in the coupled-line structure. The full-wave simulator HFSS v.14 is used to verify the theoretical results. The substrate used in the design is Rogers RT6010 (dielectric = 10.2, h = 1.27 mm). The theoretical parameters are optimized using HFSS and the final design dimensions (in mm) are: l_1=14.5, l_2=7.1, l_3=10, l_4=10, l_5 =9.2, l_6 =9.2, l_7 =10.9, l_8 =11.3, w_1 =2.0, w_2 =2.4, w_3 =2.2, w_4 =0.2, w_5 =0.2, s_1 =0.2, s_2 =0.2, $R_1 = 60\ \Omega$, and $R_1 = 200\ \Omega$.

A photograph of the fabricated prototype is given in Fig 5.24 (b). Figs 5.25 (a) - (c) show the simulated and measured S-parameters of the fabricated FPD. From Fig 5.25 (a), one can observe that the measured reflection coefficient at the input port is less than -10 dB across the band from 1.08 to 1.93 GHz, whereas the transmission coefficients for all the output ports ($|S_{21}|$, $|S_{31}|$, $|S_{41}|$, and $|S_{51}|$) are larger than -6.4 dB in the simulations and -6.8 dB in the measurements (the ideal value for four-way power divider should be -6 dB) across the same band range, indicating that a fractional bandwidth of 56.5% is achieved. Due to multiple transmission zeros, sharp skirt selectivity and more than 15 dB upper-stopband rejection up to 4.15 GHz are achieved. From Figs 5.25 (b) and (c), it is seen that the reflection coefficients at all output ports are less than -15 dB and the isolation between any two output ports is larger than 13 dB, demonstrating that excellent output matching and isolation are satisfied. The measured amplitude and phase imbalance of all the output ports are less than 0.3 dB and 4˚ respectively, as shown in Figs 5.25 (e) and (f). Some slight differences between the simulation and measurement are due to errors in the fabrication process.

5.7 Summary

In this chapter, a new concept of tunable power divider which can tune the output power division has been presented. The function is based on a kind of varactor-loaded three-line coupled structure. When the loaded capacitance is varied, the power distribution on the sidelines can be easily changed. Therefore, when two sidelines are connected with output terminations, tunable power division ratio can be realised. Moreover, the proposed tunable power dividers have wide operating bandwidth,

and the tunable power division ratio is constant across the same bandwidth, due to the frequency-independent characteristics of the three-line coupled structure.

To satisfy the design objectives of circuit miniaturization and multi-functionality, filtering responses have been integrated in the proposed tunable power dividers. As a result, two designs of tunable power divider with integrated filtering response have been proposed. One design have fixed filtering characteristics with around more than 60% bandwidth and multiple transmission zeros. The other design has the tunability of the power division ratio and controllability of the filtering band, which is realised by varactor-loaded shunted stubs. The testing results have demonstrated that the presented design has the tunability of power division ratio from 0.5:1 to 2:1, controllable filtering bandwidth from 48% to 71%, tunable centre frequency from 1.3 GHz to 1.48 GHz, sharp cut-off with transmission zeros, and upper-stopband harmonic suppressions up to more than 6 GHz.

Besides, to feed a four-element antenna array with filtering response, a four-way filtering power divider with high selectivity and upper-stopband rejection has been reported. The proposed design uses two short-ended coupled-line stubs and two looped coupled-line structures. To verify the theory and design procedure, a filtering power divider prototype has been fabricated and tested. The tested results indicate that 56.5% bandwidth filtering response centred at 1.5 GHz with sharp passband selectivity and wide upper-stopband rejection has been achieved. Compared with other existing designs, the proposed design is the most compact one with the widest bandwidth, sharpest skirt selectivity and greatest upper-stopband suppression with excellent output matching and isolation, indicating that it has great potential to be used in wireless microwave communication systems.

Chapter 6 Development of Multi-port Tunable Microwave Devices

6.1 Introduction

The last two chapters have introduced the importance of tunable microwave devices in RF front-ends, and presented a few of novel ideas and designs of tunable filters, tunable power dividers and filtering power dividers [137]. In addition to power dividers, there are other kinds of multi-port microwave devices which are also critical and commonly used for constructing microwave systems, such as directional couplers, hybrids, baluns, and crossovers. It is also extremely demanded to have tunable characteristics and multi-functionality within one component. Tunable power dividers with tunable power division ratio have been investigated in the last chapter. For other multi-port devices like couplers and baluns, it is also favourable to have tunable power division at output terminations. Therefore, a new design of tunable balun and tunable quadrature coupler will be presented in this chapter.

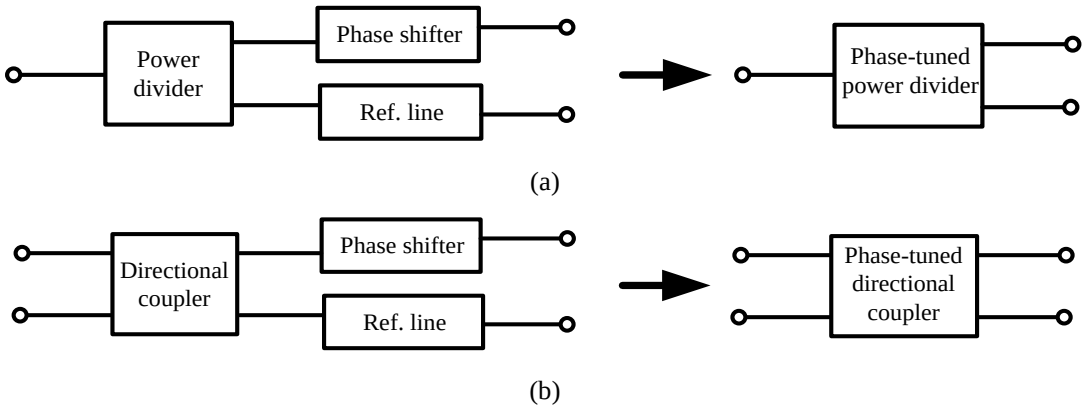

Fig 6. 1 Concept of the proposed structures: (a) phase-tuned power divider; (b) phased-tuned directional coupler.

On the other hand, in some cases, the differential phase is more concerned about than the amplitude. Under such circumstances, it is desired to achieve variable or arbitrary differential phase rather than the fixed one. For example, multi-port microwave devices are usually connected with phase shifters in many cases especially for development of feeding network of phased arrays. In this case, to introduce a differential phase between two elements, a phase shifter and a reference line are required to be connected with the output of a power divider using traditional method. This kind of configuration will definitely result in bulky size and large loss. To overcome these shortcomings, a kind of phase-tuned power divider is presented here, which is able to have controlled output phase at two output ports. In this case, the functions of power dividing and phase shifting can be

integrated into one component as indicated in Fig 6.1 (a). Similarly, a certain differential phase is also wanted between two output ports of directional couplers. In traditional configurations, the through port and coupling port are required to connect with a phase shifter and a reference line. In this chapter, a new kind of directional coupler with tunable differential phase will be presented. As shown in Fig 6.1 (b), this design is able to have the functionality of a directional coupler and phase shifters. Thorough theoretical analysis will be given, followed by full-wave simulation and experimental verifications.

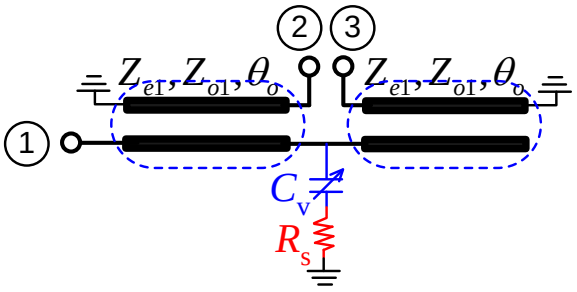

Fig 6. 2 Configuration of the proposed tunable balun.

6.2 Design of Wideband Marchand Balun with Tunable Power Division Ratio

Baluns are crucial passive microwave components which is able to transform balanced signals to the unbalanced ones. Therefore, baluns are widely used as antennas' feeders to avoid pattern degradation due to unbalanced signals from the feedline. In wireless communication systems, broadband baluns are used to feed dual-polarized antennas for better isolation and cross-polarization suppression. The most well-known and widely used design is Marchand balun due to its simplicity and wide bandwidth performance.

In many antenna systems, especially dipole-based or dual-polarized antennas, different feeding power levels with constant phase difference of 180˚ are required to control the direction of the radiation pattern. In such cases, tunable baluns with tunable power division and constant differential phase at 180˚ are necessary. In this case, a tunable balun based on a modified Marchand balun is proposed in this paper, for the first time, to realise the function of continuous tunability of power division at two output ports with constant differential phase across a wide band.

6.2.1 Configuration and Analysis

Fig 6.2 shows the configuration of the proposed tunable balun. It is based on the traditional Marchand balun, in which two coupled-line sections that are short-ended on one side and open-

ended on the other side are used. The even- and odd-mode impedances and electrical length of each coupled-line section are Z_{oe}, Z_{oo} and θ_o, respectively. The electrical length θ_o is quarter-wavelength at the centre frequency f_o, which is chosen here as 2 GHz. Different from the varactor-loaded three-line coupled structure [136], a centrally loaded structure is used to get tunable output signals: a varactor with capacitance of C_v and a series resistor R_s are loaded at the central point of the two coupled-line sections. The coupled-line sections that are enclosed by dashed line in Fig 6.2 can be considered as two four-port backward couplers with one terminal short-ended and the other one open-ended, while the rest two terminals are connected together.

To determine the parameters of coupled-line sections, we initially assume the structure without the shunt loading of the series varactor and resistor, and odd-even mode analysis of the balun can be used to find the transmission (S_{21} and S_{31}) and reflection (S_{11}) coefficients of the balun [139]:

$$S_{21} = -S_{31} = (j2K\sqrt{1-K^2})/(1+K^2) \tag{6.1}$$

$$S_{11} = (1-3K^2)/(1+K^2) \tag{6.2}$$

where K is the coupling factor K, which is expressed as

$$K = (Z_{oe} - Z_{oo})/(Z_{oe} + Z_{oo}) \tag{6.3}$$

The even- and odd-mode impedances Z_{oe}, Z_{oo} are related to the characteristic impedance Z_o (50 Ω) as follows

$$Z_{oe}Z_{oo} = Z_o^2 \tag{6.4}$$

Fig 6.3 shows the calculated transmission coefficients of the circuit for different values of K using Equations (6.1) – (6.4). To achieve more than 80% fractional bandwidth with regard to both the transmission and reflection coefficients, K is selected to be 0.67. Hence, based on this fact and using (6.3) and (6.4), the mode impedances of the coupled sections should be Z_{oe} = 112.4 Ω, and Z_{oo} = 22.2 Ω in this design.

After Z_{oe} and Z_{oo} are determined, a shunt load composed of a series combination of a varactor with capacitance C_v and a resistor R_s is then attached between the centre point of the two coupled-line sections and ground, as depicted in Fig 6.2. Following the procedure explained in [140], it is possible to prove that the power division ratio (*PDR*) between two output ports has the following relation with design parameters:

$$PDR = 1 + K^4 Z_o^4 \omega_o^2 C_v^2 / [(K^2 + \omega_o^2 C_v^2 + 1/R_s^2 + 1)R_s^2] \tag{6.5}$$

Meanwhile, the differential phase of two output ports Δφ can be expressed using the same procedure as

$$\Delta\varphi = \pi + K^2 Z_o \omega_o C_v/(K^2 + 1/R_s + 1) \approx \pi \tag{6.6}$$

It is clear from (6.5) that the cases C_v = 0 and $R_s \rightarrow \infty$ result in *PDR* = 1, which is the equal power division achieved using the traditional design. Other values for C_v and R_s can be used to realise different *PDR*. However, it is to be noted from Equation (6.5) that the tuning element C_v is multiplied by the radian frequency, and thus the *PDR* might not be stable across a wide band especially if a wide *PDR* tuning range is required. Therefore, C_v and R_s need to be selected properly for a stable *PDR* with wide tuning range values across wide frequency bandwidth.

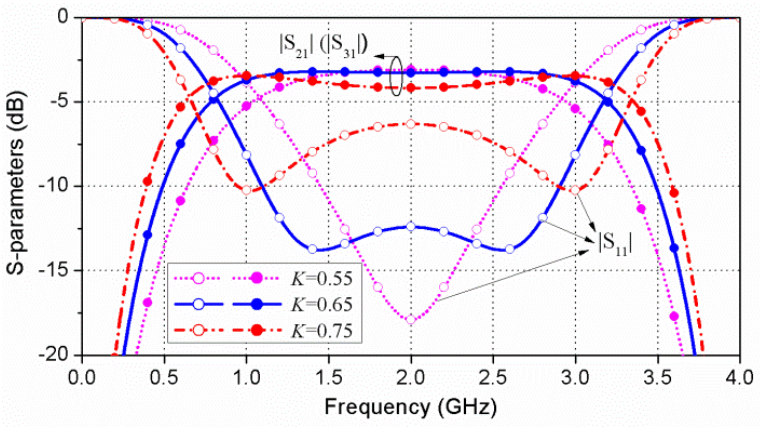

Fig 6. 3 S-parameters for different values of the coupling factor *K*.

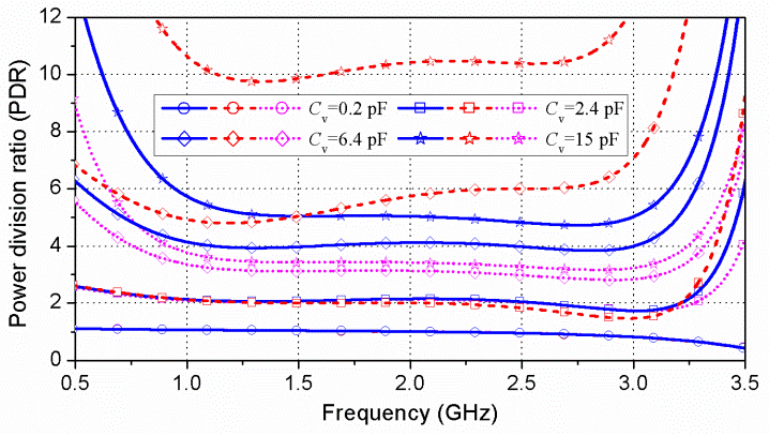

Fig 6. 4 Power division ratio for the indicated values of C_v and following values of R_s: 10 Ω (dashed lines); 20 Ω (solid lines); 30 Ω (dotted lines).

Based on (6.5) with *K* = 0.67, the variation of *PDR* for different values of C_v and R_s are shown in Fig 6.4. When R_s equals 10 Ω, 20 Ω, or 30 Ω and C_v is changed across the reasonable values from 0.2 to 15 pF, the maximum range for the achievable *PDR* at the centre frequency f_o are 10:1, 5:1 and

3.3:1, respectively. While using small values for R_s enables realizing wide tunable range for the *PDR* (in this case *PDR* = 10.5 when R_s = 10 Ω), the covered frequency band is limited, as depicted in Fig 6.4. On the other hand, using large values for R_s allows tuning the *PDR* across a limited range (maximum *PDR* is only 3.3 when R_s = 30 Ω) even if large range of values for C_v is used, but the fractional operating bandwidth can be up to 100%. Thus a compromise is needed between the desired tuning range of *PDR* and operating frequency band when selecting the loaded elements.

The introduction of the series resistance R_s results in some power loss. To explore that effect, Fig 6.5 (a) shows the relation between value of R_s (10 Ω and 20 Ω) and additional loss compared with zero power loss cases, including no series resistance and equal power division cases. The maximum loss in total within the band 1.2-2.8 GHz is 0.75 dB.

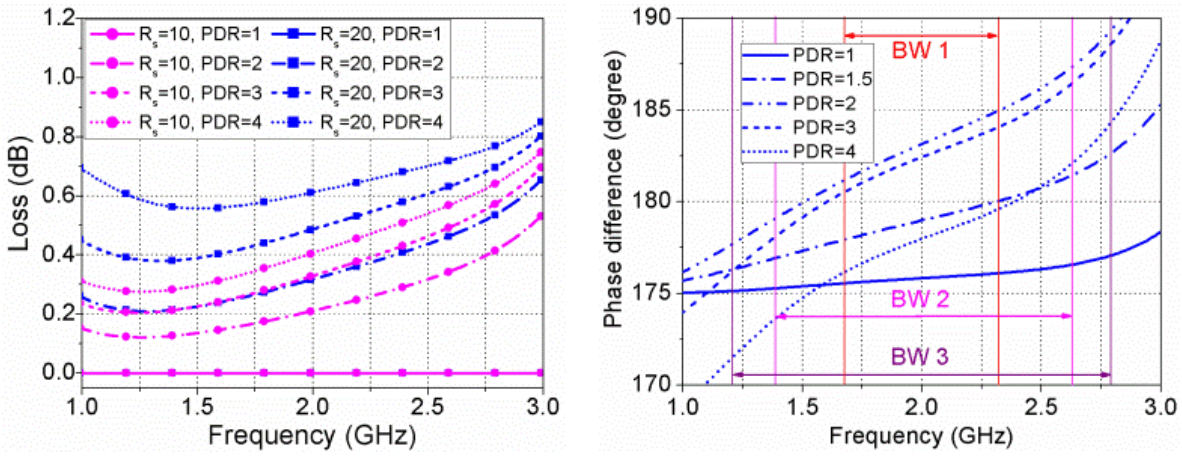

(a) (b)

Fig 6. 5 (a) Power consumption by R_s for different power division ratios, and (b) phase difference with different bandwidths and power ratios.

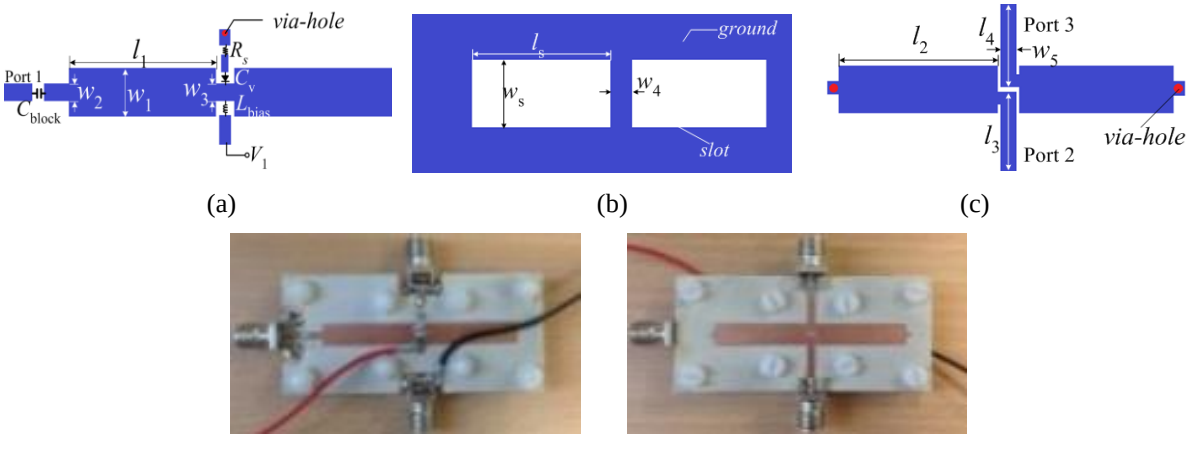

(a) (b) (c)

(d) (e)

Fig 6. 6 Layout of the proposed balun: (a) top layer; (b) middle layer; (c) bottom layer; photograph of the fabricated prototype: (d) top layer; (e) bottom layer.

For all the investigated cases, Δφ can be verified using Equation (6.6), which is almost stable at 180˚ and has a second term with small value. Fig 6.5 (b) depicts the phase difference between the two output ports. It can be seen that the phase imbalance is only ±5˚ for 35% fractional bandwidth (BW 1 in Fig 6.5[b]), whereas it is ±7˚ and ±9˚ for 60% and 80% bandwidth (BW 2 and BW 3 in Fig 6.5 [b]).

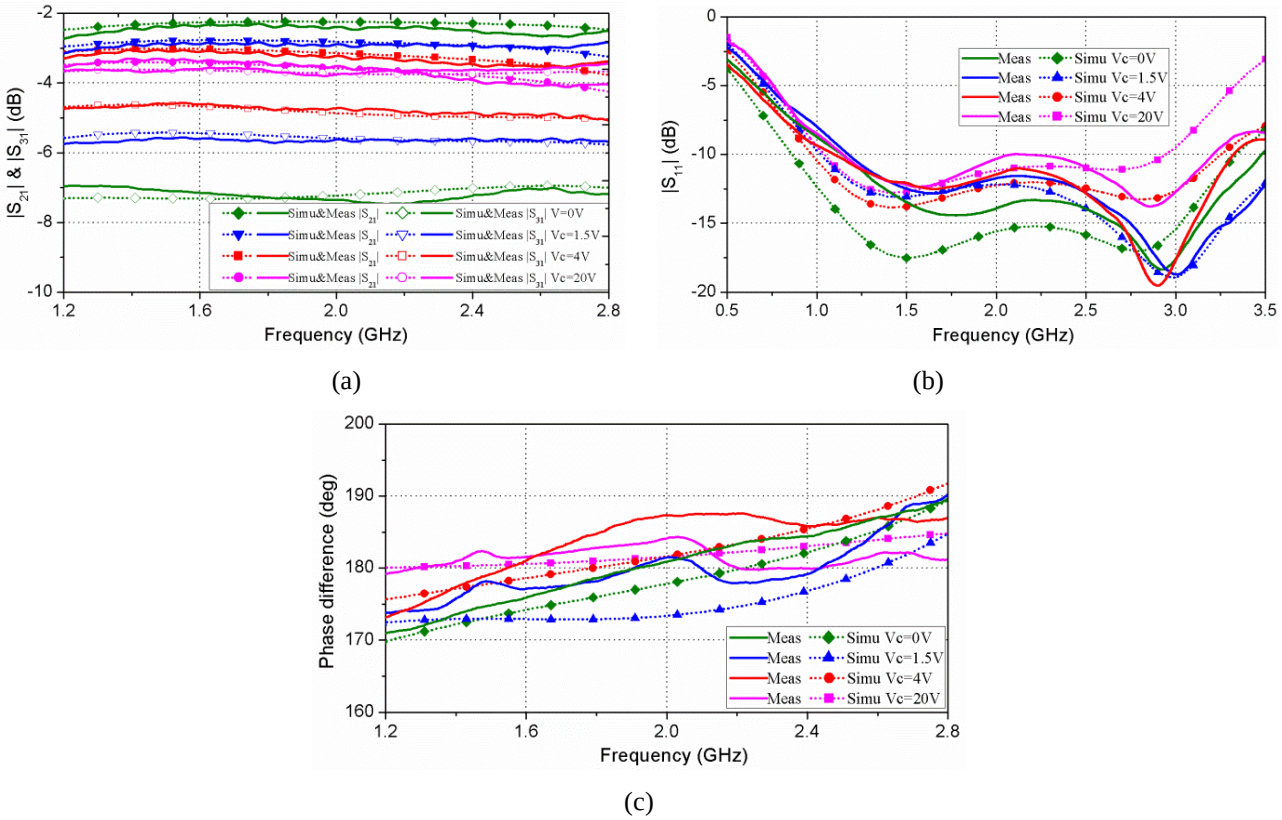

Fig 6. 7 Experimental and simulated performance of the proposed tunable balun: (a) $|S_{21}|$ and $|S_{31}|$; (b) $|S_{11}|$; and (c) differential phase

6.2.2 Design and Results

To verify the proposed design approach, an electromagnetic (EM) model is built in the full-wave electromagnetic simulator HFSS and co-simulated in ADS using SPICE model of varactors. To achieve the required tight coupling (K = 0.67) for the balun across a wide band, a multilayer structure is utilized. The input port is located at the top layer, which is coupled to the two output ports at the bottom layer via a slot on the middle layer. Figs 6.6 (a)-(c) show the layout of the three layers of the proposed tunable balun. Substrate with dielectric constant of 3 and thickness of 0.76 mm is used here. The initial dimensions are found based on the aforementioned design parameter values (K = 0.67, R_s = 20) using the method presented in [141]. The utilized varactor in the design is the hyper abrupt junction SMV2202 with capacitance tuning range from 0.3 to 3.2 pF and parasitic

resistor of 3 Ω. The biasing circuit for the varactor diode is realised using an inductor L_{bias} of 1 μH and DC block capacitor C_{block} of 100 pF. After optimizations in HFSS, the final dimensions (in mm) are determined as follows: $L_1 = L_2 = L_s = 21.5$, $L_3 = 12.8$, $L_4 = 10.2$, $W_1 = 5.4$, $W_2 = W_3 = 1.9$, $W_4 = 2.3$, $W_5 = 1.9$, $W_6 = 5.4$, and $W_s = 10.2$. The optimized value for the series resistor R_s is found to be 22 Ω, which is used in the form of a chip resistor.

A prototype, which is shown in Figs 6.6 (d) and (e), is fabricated and tested. The simulated and measured results are displayed in Fig 6.7 for the output power division tunability, input port matching and output ports phase variation. When the biasing voltage V_c is decreased from 20 V to 0, the measured S_{21} are -3.6 dB, -3.4 dB, -3.1 dB and -2.6 dB, compared with the simulated ones of -3.5 dB, -3.3 dB, -2.9 dB and -2.3 dB. Correspondingly, the measured S_{31} are -3.5 dB, -4.7 dB, -5.8 dB, and -7.2 dB. Thus, the achieved power division ratios are1:1, 1.4:1, 2:1, and 3.5:1, respectively. Under such *PDR*s, the measured amplitude imbalances are 0.6 dB, 0.4 dB, 0.3 dB, and 0.8 dB, respectively. More than 10 dB input port return loss is achieved in all the cases across the band from 1.2 GHz to 2.8 GHz. The differential phase of the output ports is nearly constant with a deviation of 7˚ within 60% bandwidth, and about 9˚ within 80% bandwidth, as shown in Fig 6.7 (c). The proposed design can work across wide band of 80%, with *PDR* up to 3.5:1 (or 5.5 dB) and relatively stable 180˚ differential phase between two output ports.

In using the proposed device within systems, it is important to verify the packaging and temperature effect issues. To that end, the device is simulated in HFSS and ADS by including the metallic enclosure, which is the cavity needed to suspend the multilayer structure of the device, and the temperature coefficient of the varactors. It was found that for a temperature range of -55 C˚ to 125 C˚ and cavity clearance of 1.5 cm or more, the performance is quite stable with only less than 5% variations in the power division ratio.

Since the literature doesn't include any paper on baluns with tunable power ratio, the comparison is performed with tunable couplers, power dividers and phase-tuned baluns. The proposed design can work across much wider band of 80%, with *PDR* of 5.5 dB and 180˚ ± 9˚ differential phase. For low phase imbalance applications, the device can still achieve wider band and better return loss with larger power ratio range compared with recent works.

6.3 Design of Tunable Quadrature Coupler with Wide Range of Controlled Coupling Coefficient

Couplers are common devices that are widely used in various microwave systems, such as mixers, phase shifters, balanced power amplifiers, feeding networks for antennas, and soft-defined radars to name a few. Tunable couplers have the capability to realise multiple functions or working states using one single device. One of the main tunable aspects of couplers is the operational band. By loading varactor diodes on branch-line structure, the narrow operating band of a 3-dB coupler can be shifted [142]-[145]. In [146], a tunable directional coupler was implemented in CMOS to achieve a wide operating frequency tuning range from 2 to 6 GHz. In many cases, such as measurement systems or antenna array feeding networks, tunable coupling coefficient is much more favourable. In [147], a lumped-element-based directional coupler was integrated onto a MMIC to get electronic control over the coupling coefficient from 1.4 to 7.1 dB. Broadside coupled-line sections were connected with varactors in [148] without degrading the directivity, achieving tunable coupling range from 3 dB to 11 dB. Based on the aforementioned review, it is clear that there is still a great demand for tunable couplers with wide range of coupling factor tunability across a wide band.

In this section, a tunable quadrature coupler aiming at full tuning range of coupling coefficient is presented. The structure is based on two sets of coupled-line sections loaded with varactors. The analysis of the structure is given to enable selecting the circuit design parameters. The design is validated via full-wave electromagnetic simulations and experiments.

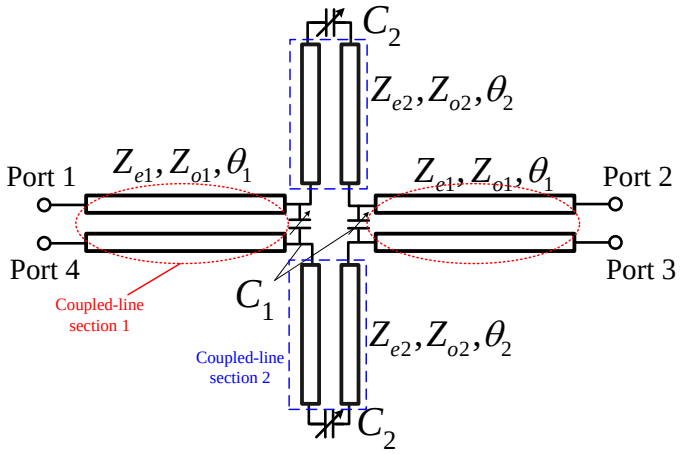

Fig 6. 8 Configuration of the proposed tunable quadrature coupler.

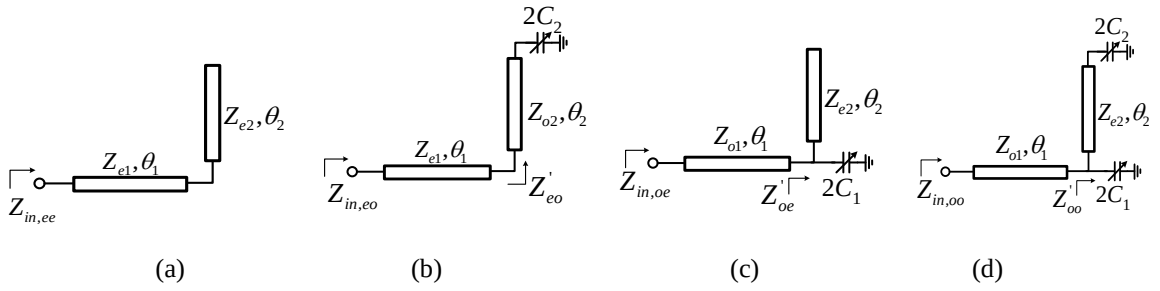

(a) (b) (c) (d)

Fig 6. 9 Equivalent circuit of the proposed structure using even-/odd –mode analysis: (a) even-even mode; (b) even-odd mode; (c) odd-even mode; (d) odd-odd mode.

6.3.1 Proposed Structure and Analysis

The objective of this work is to build a quadrature coupler with a tunable coupling coefficient *k* as well as stable quadrature differential phase between the two output ports. Fig 6.8 shows the configuration of the proposed device. It is composed of two pairs of coupled-line sections, indicated as section 1 in dashed blocks (Z_{e1}, Z_{o1}, θ_1) and section 2 in dotted blocks (Z_{e2}, Z_{o2}, θ_2). Section 1 includes the four ports of the device, whereas section 2 is used to load section 1 at the connection point of the two parts of that section. The even- and odd-mode electrical lengths of all of the coupled-line sections are assumed to be equal. Two sets of varactors (C_1 and C_2) are used to load section 1 at the connection point of its two parts and section 2 at its two open ends, respectively. By controlling the capacitances of C_1 and C_2, the coupling factor can be tuned.

Due to the symmetry along the plane OO' and PP', the proposed structure can be analysed using twofold even- and odd-mode analysis. By applying electrical wall (E-wall) or magnetic wall (H-wall) on plane OO' and PP', four different combinations appear as even-even (*ee*), even-odd (*eo*), odd-even (*oe*), and odd-odd (*oo*) mode conditions. Fig 6.9 shows the equivalent circuits under *ee*-, *eo*-, *oe*-, and *oo*-mode excitations. For the *ee*-mode, the input impedance $Z_{in,ee}$ can be expressed as

$$Z_{in,ee} = Z_{e1}\frac{jZ_{e1}\tan\theta_1 - jZ_{e2}\cot\theta_2}{Z_{e1} + j(-jZ_{e2}\cot\theta_2)\tan\theta_1} \tag{6.7}$$

For the *eo*-mode, the input impedance $Z_{in,eo}$ can be expressed as

$$Z_{in,eo} = Z_{e1}\frac{Z'_{eo} + jZ_{e1}\tan\theta_1}{Z_{e1} + jZ'_{eo}\tan\theta_1} \tag{6.8}$$

where

$$Z'_{eo} = \frac{\frac{1}{j2\omega C_2} + jZ_{o2}\tan\theta_2}{Z_{o2} + j(\frac{1}{j2\omega C_2})\tan\theta_2} \tag{6.9}$$

For the *oe*-mode, the input impedance $Z_{in,oe}$ is written as

$$Z_{in,oe} = Z_{o1}\frac{Z'_{oe} + jZ_{o1}\tan\theta_1}{Z_{o1} + jZ'_{oe}\tan\theta_1} \tag{6.10}$$

where

$$Z'_{oe} = \frac{\frac{1}{j2\omega C_1}\cdot(-jZ_{e2}\cot\theta_2)}{\frac{1}{j2\omega C_1} + (-jZ_{e2}\cot\theta_2)} \tag{6.11}$$

Similarly, for the *oo*-mode, the input impedance $Z_{in,oo}$ is

$$Z_{in,oo} = Z_{o1}\frac{Z'_{oo} + jZ_{o1}\tan\theta_1}{Z_{o1} + jZ'_{oo}\tan\theta_1} \tag{6.12}$$

where

$$Z'_{oo} = \frac{\frac{1}{j2\omega C_1}\cdot Z''_{oo}}{\frac{1}{j2\omega C_1} + Z''_{oo}} = \frac{\frac{1}{j2\omega C_1}\cdot Z'_{eo}}{\frac{1}{j2\omega C_1} + Z'_{eo}} \tag{6.13}$$

$$Z''_{oo} = Z'_{eo} \tag{6.14}$$

To calculate the S-parameters of the structure, the following equations [150] are adopted:

$$S_{11} = \frac{\Gamma_{ee} + \Gamma_{eo} + \Gamma_{oe} + \Gamma_{oo}}{4} \tag{6.15}$$

$$S_{21} = \frac{\Gamma_{ee} - \Gamma_{eo} + \Gamma_{oe} - \Gamma_{oo}}{4} \tag{6.16}$$

$$S_{31} = \frac{\Gamma_{ee} - \Gamma_{eo} - \Gamma_{oe} + \Gamma_{oo}}{4} \tag{6.17}$$

$$S_{41} = \frac{\Gamma_{ee} + \Gamma_{eo} - \Gamma_{oe} - \Gamma_{oo}}{4} \tag{6.18}$$

Here, Γ_{ee}, Γ_{eo}, Γ_{oe}, and Γ_{oo} are the corresponding reflection coefficients under the four modes, which have the following relations with the one-port input impedances:

$$\Gamma_{ee} = \frac{Z_{in,ee} - Z_o}{Z_{in,ee} + Z_o} \tag{6.19}$$

$$\Gamma_{eo} = \frac{Z_{in,eo} - Z_o}{Z_{in,eo} + Z_o} \tag{6.20}$$

$$\Gamma_{oe} = \frac{Z_{in,oe} - Z_o}{Z_{in,oe} + Z_o} \tag{6.21}$$

$$\Gamma_{oo} = \frac{Z_{in,oo} - Z_o}{Z_{in,oo} + Z_o} \tag{6.22}$$

For a quadrature coupler, ideal matching and isolation are required so that the following equation should be satisfied:

$$S_{11} = S_{41} = 0 \tag{6.23}$$

Combing (6.23) with (6.15)-(6.22), it is possible to find that

$$\begin{cases} \Gamma_{ee} + \Gamma_{eo} = 0 \\ \Gamma_{oe} + \Gamma_{oo} = 0 \end{cases} \tag{6.24}$$

To investigate the relations between Z_{o1}, Z_{o2}, Z_{e1} and Z_{e2}, the electrical lengths and capacitances can be prescribed with specific values. Assuming C_1 is open-circuited (to emulate no varactor), C_2 is short-circuited (to emulate short-ended coupled lines) and $\theta_1 = \theta_2 = 45°$ at the centre frequency f_o, equation (6.23) is satisfied, if the following equations are met:

$$Z_{e2} = \frac{(Z_{o1}^2 - Z_o^2)}{Z_o^2} Z_{e1} \tag{6.25}$$

$$r = \frac{Z_{e2}}{Z_{e1}} = \frac{Z_{o1}^2 - Z_o^2}{Z_o^2} \tag{6.26}$$

$$Z_{o2} = \frac{Z_{e1} + Z_{e2}}{Z_{e1} Z_{e2}} Z_o^2 \tag{6.27}$$

Based on the relations between Z_{o1}, Z_{o2}, Z_{e1} and Z_{e2} listed in (6.25)-(6.27), Fig 6.10 is plotted to help finding the mentioned design parameters. On the other hand, to investigate the coupling coefficient k (defined as $k = |S_{31}|/|S_{21}|$) between the coupling port and the through port, the following equations can be derived from (6.24)

$$Z_{in,ee} Z_{in,eo} = Z_o^2 \tag{6.28}$$

$$Z_{in,oe} Z_{in,oo} = Z_o^2 \tag{6.29}$$

Combining (6.23) and (6.28)-(6.29), one can find that the coupling coefficient k and one-port mode-impedance have following relations:

$$Z_{in,ee} Z_o - Z_{in,oe} Z_o = -jk(Z_{in,ee} Z_{in,oe} - Z_o^2) \tag{6.30}$$

$$Z_{in,eo} Z_o - Z_{in,oo} Z_o = -jk(Z_{in,eo} Z_{in,oo} - Z_o^2) \tag{6.31}$$

$$k = \frac{j(Z_{in,ee} - Z_{in,oe}) Z_o}{Z_{in,ee} Z_{in,oe} - Z_o^2} \tag{6.32}$$

$$k = \frac{j(Z_{in,eo} - Z_{in,oo}) Z_o}{Z_{in,eo} Z_{in,oo} - Z_o^2} \tag{6.33}$$

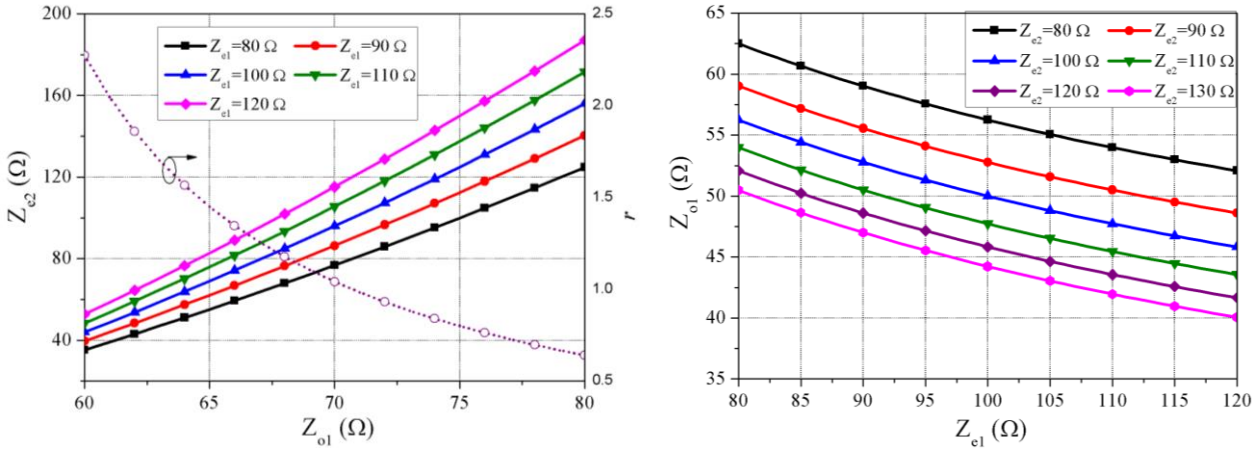

(a) (b)

Fig 6. 10 (a) Z_{e2} against Z_{o1} and impedance ratio R with different Z_{e1}; (b) Z_{o1} against Z_{e1} with different values of Z_{e2}.

It is found that when the electrical lengths of all of the coupled-line sections are selected as 45˚ at f_o, the coupling coefficient k can be varied from 0 to infinite by changing C_1 and C_2. In this design electrical lengths of all coupled-line sections are set as 45 ˚ at f_o. Therefore, C_1 and C_2 can be expressed in terms of the characteristic impedances of all coupled-line sections and k. In this case, the expressions of $Z_{in,ee}$ and $Z_{in,oe}$ can be modified as

$$Z_{in,ee} = jZ_{e1}\frac{Z_{e1} - Z_{e2}}{Z_{e1} + Z_{e2}} \tag{6.34}$$

$$Z_{in,oe} = jZ_{o1}\frac{Z_{o1}(Z_{e2} \cdot 2\omega C_1 + 1) - Z_{e2}}{Z_{o1}(Z_{e2} \cdot 2\omega C_1 + 1) + Z_{e2}} \tag{6.35}$$

$$Z_{in,oe} = \frac{kZ_o^2 - jkZ_oZ_{in,ee}}{kZ_{in,ee} - jZ_o} \tag{6.36}$$

Substituting Equations (28)-(30) into (26), one can find that the expression of C_1 can be given as:

$$C_1 = \left(\frac{1+m}{1-m} \cdot \frac{Z_{e2}}{Z_{o1}} - 1\right) \cdot \frac{1}{2\omega \cdot Z_{e2}} \tag{6.37}$$

where

$$m = \frac{k \cdot Z_o^2(Z_{e1} + Z_{e2}) - Z_oZ_{e1}(Z_{e1} - Z_{e2})}{k \cdot Z_{o1}Z_{e1}(Z_{e1} + Z_{e2}) - Z_oZ_{o1}(Z_{e1} + Z_{e2})} \tag{6.38}$$

Similarly, the input impedance of $Z_{in,eo}$ and $Z_{in,oo}$ can be rewritten with $\theta_1 = \theta_2 = 45°$ as

$$Z_{in,eo} = jZ_{e1}\frac{Z_{e1} \cdot n + n - 2}{Z_{e1} \cdot n - n + 2} \tag{6.39}$$

$$Z_{in,oo} = jZ_{o1}\frac{Z_{o1}n - 2\omega C_1 \cdot Z_{o1}(n-2) + n - 2}{Z_{o1}n - 2\omega C_1 \cdot Z_{o1}(n-2) - n + 2} \tag{6.40}$$

where

$$n = Z_{o2} \cdot 2\omega C_2 + 1 \tag{6.41}$$

Substituting (33)-(35) into (27), one can solve for C_2 as

$$C_2 = \frac{(2\omega C_1 Z_{o1}+1)\left(kZ_o^2+Z_oZ_{e1}\right)-(2\omega C_1 Z_{o1}-1)(Z_oZ_{o1}-kZ_{o1}Z_{e1})}{\omega\cdot Z_{o1}Z_{o2}(1-2\omega C_1)\left(k\cdot Z_o^2+Z_oZ_{e1}\right)+\omega\cdot Z_{o2}Z_{o1}(1-2\omega C_1)(Z_oZ_{o1}-kZ_{o1}Z_{e1})} - \frac{1}{2\omega\cdot Z_{o2}} \tag{6.42}$$

From (6.37) and (6.42), one can find C_1 and C_2 after f_o and k are selected with the given design parameters of the coupled-line sections from Fig 6.10.

6.3.2 Calculated S-parameters

Based on the analysis above, the S-parameters for different coupling coefficients can be found with selected C_1 and C_2. The centre frequency f_o is fixed at 1 GHz in this design. Figs 6.11 (a)-(e) show the amplitude and phase responses of all the investigated cases. Fig 6.11 (a) shows the coupling power at Port 3, where seven different coupling coefficients are plotted. The coupling coefficient moves gradually from 3 dB to 20 dB. Since the analysis is done on a narrow-band basis, some deviations appear when the operating frequency extends away from the centre frequency. The previous analysis guarantees achieving ideal performance at the centre frequency f_o. Outside that frequency, $|S_{21}|$ and $|S_{31}|$ show some deviations from the ideal values. When the coupling coefficient varies from -6 dB to -20 dB, the deviation is ±1 dB, which is still acceptable, for both of $|S_{21}|$ and $|S_{31}|$ across 20% fractional bandwidth. However, when the coupling coefficient is 3 dB, the simulated fractional bandwidth is reduced to 14% for ±1 dB deviation.

For the matching and isolation issues, quasi-perfect matching and isolation can be observed from Figs 6.11 (c) and (d). The return loss is larger than 12 dB while the isolation is larger than 15 dB across a relatively wide bandwidth (from 0.9 GHz to 1.1 GHz, bandwidth = 20%). For a quadrature coupler, the differential phase is quite important. As shown in Fig 6.11 (e), within the operating band range from 0.9 GHz to 1.1 GHz, the differential phase is between 85˚ to 97˚ (phase deviation = ±7˚), which is satisfactory for the wide tunable coupling coefficient and wideband usage. It is noted that the phase deviation increases when the coupling coefficient decreases at the upper and lower edges of the band.

In some cases, no coupled signal is required at Port 3 leading to an all-through state. Under such circumstance, all the power goes to Port 2, and thus the power division ratio is 1:0. The S-parameters for this case are shown in Fig 6.11 (f). A transmission zero with 70 dB attenuation appears at Port 3 at f_o, which can be assumed that no signal is coupled at this port. Meanwhile, perfect matching and isolation are remained at Port 1 and Port 4.

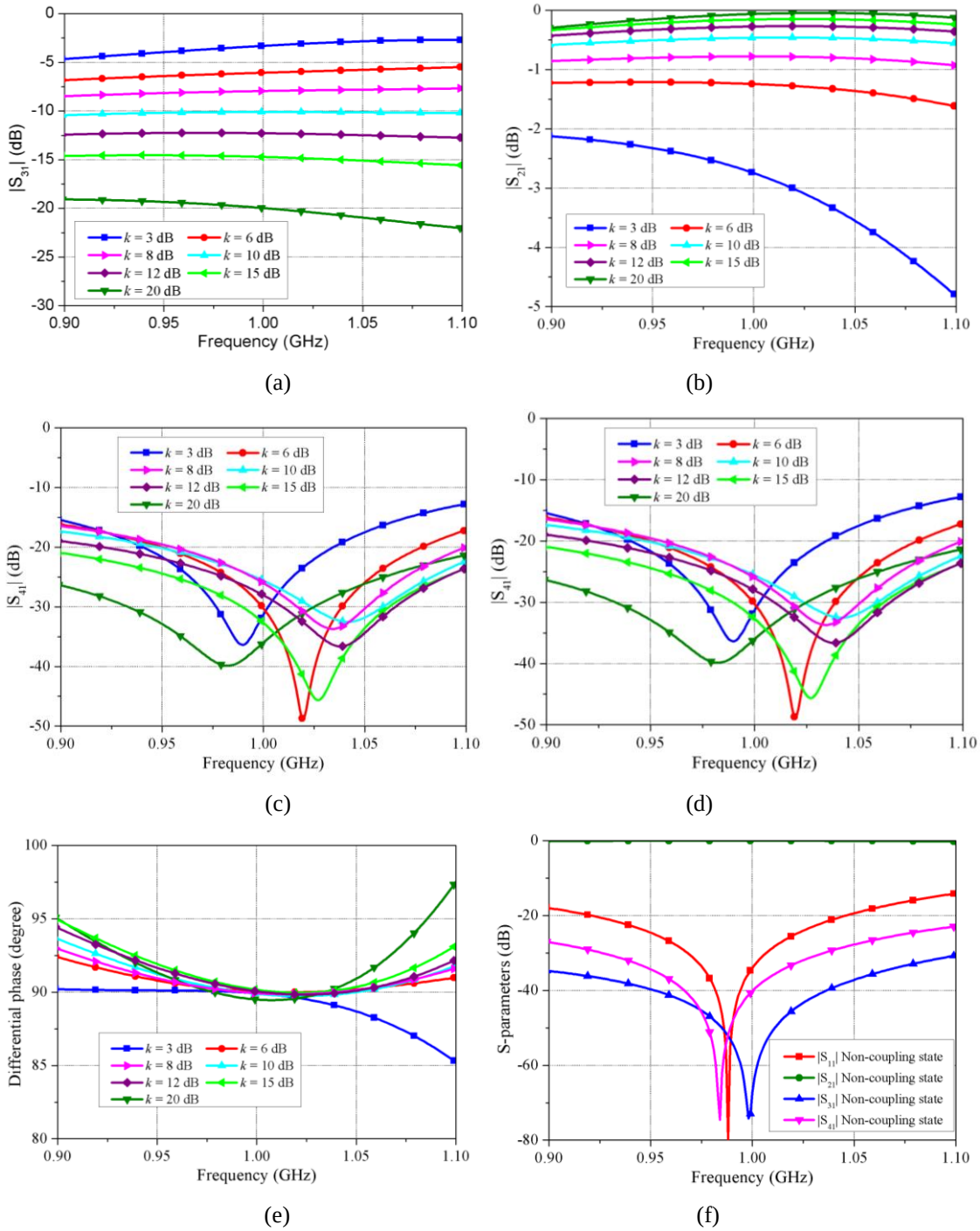

Fig 6. 11 Calculated S-parameters with different coupling coefficient (k): (a) $|S_{31}|$; and (b) $|S_{21}|$; (c) $|S_{11}|$; and (d) $|S_{41}|$; (e) differential phase; (f) non-coupling state.

To make the design approach more practical and useful, a general design procedure is given below. Select the electrical lengths of each coupled-line section as 45° at f_o; appropriate values of characteristic impedance of Z_{o1}, Z_{o2}, Z_{e1} and Z_{e2} can be found from Fig 6.10; For any k, use (6.37) and (6.42) to find C_1 and C_2; Use (6.15) to (6.18) to depict the S-parameters of the proposed coupler with certain coupling coefficient k; Build the electromagnetic model in full-wave simulator with biasing circuit, simulate the structure with tuning elements, and then optimize the whole structure. Finally, experimental test is required, which is discussed in the following section.

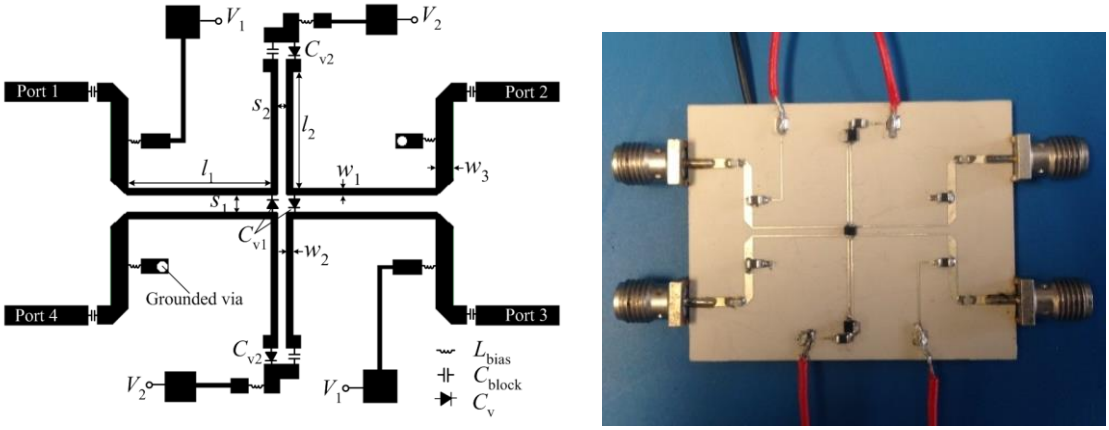

Fig 6. 12 Layout and photograph of the proposed device.

6.3.3 Experimental Results and Discussions

To verify the proposed design, full-wave simulation is used with SPICE model of varactors in Agilent's Advanced Design System (ADS). Fig 6.12 shows the layout and biasing circuit. Two pairs of varactors C_{v1} and C_{v2}, which are connected between the centreline and each sideline, are realised by Skyworks SMV2019-219 (capacitance range from 0.16 pF to 2.25 pF, with parasitic resistance of 4.8 Ω) and SMV1702-011LF (capacitance range from 12.58 pF to 103.3 pF, with parasitic resistance of 0.5 Ω), respectively. The controlling voltages of C_{v1} and C_{v2} are V_1 and V_2. The RF chokes and DC block capacitors for biasing are chosen as 10 μH and 100 pF. In this design as an example, the characteristic impedance of coupled-line sections are selected as $Z_{o1} = 70\ \Omega$, Z_{o2}=54 Ω, $Z_{e1} = 90\ \Omega$, and $Z_{e2} = 102\ \Omega$. Accordingly, the optimized dimensions of the structure are listed as: l_1=13.6, l_2=12, w_1=0.2, w_2=0.2, w_3=1.18, s_1=0.95 and s_2=0.3. The overall size of the proposed design is $0.24\lambda_g \times 0.2\lambda_g$ (λ_g is the guided-wavelength at the centre frequency 1 GHz).

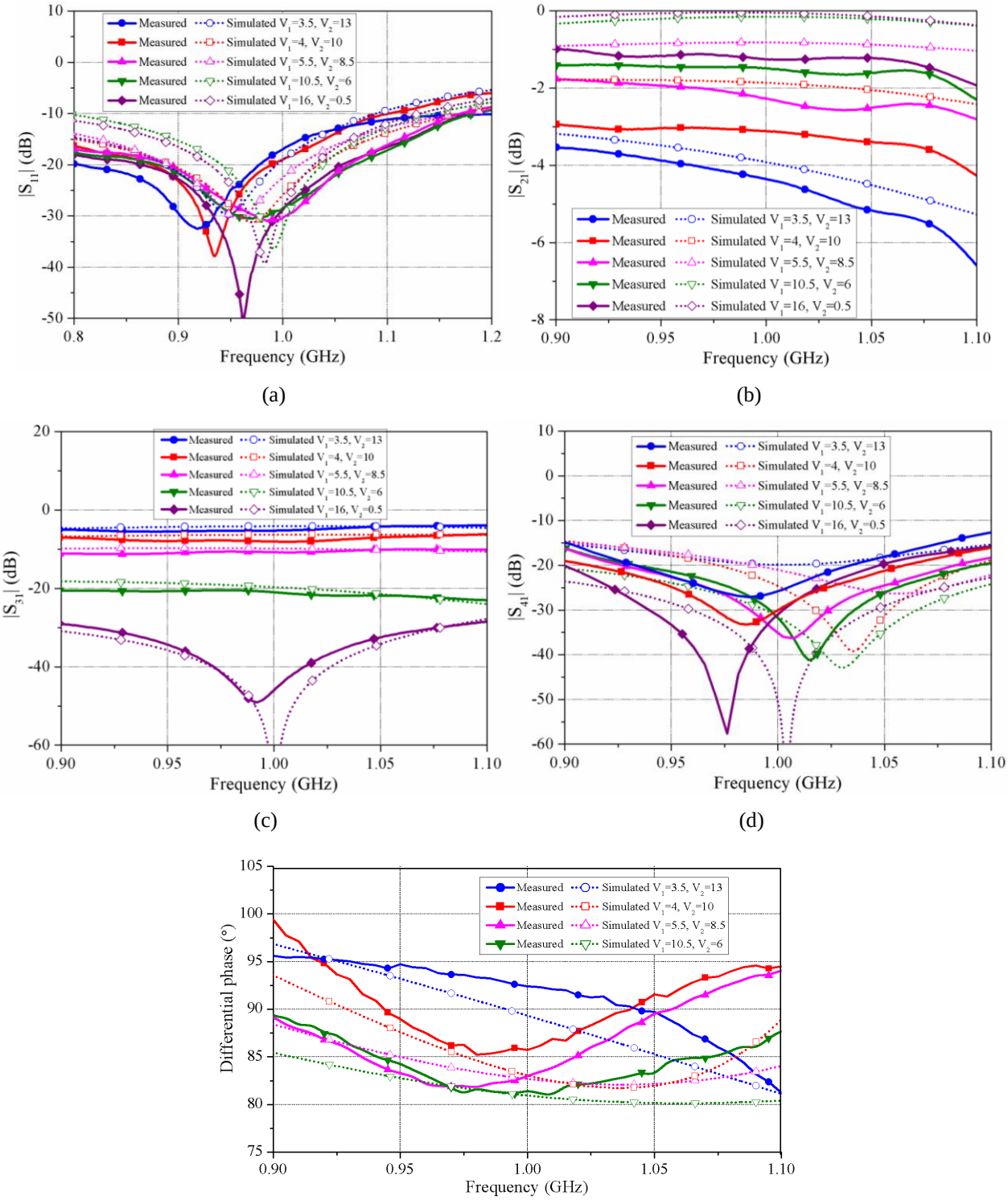

Fig 6. 13 Simulated and measured results of the fabricated prototype: (a) $|S_{31}|$; and (b) $|S_{21}|$; (c) $|S_{11}|$; and (d) $|S_{41}|$; (e) Differential phase.

A prototype of the proposed tunable coupler is built and tested for verification. Fig 6.13 (a) shows the accomplished coupling signals at Port 3 from simulation and measurement. It can be seen that the coupling coefficient of the coupler can be varied from 3 dB to 6 dB, 10 dB, 20 dB, and 0, which is non-coupling state. The responses are quite stable with small deviation (smaller than 1.5 dB)

across a wide band range from 0.9 GHz to 1.1 GHz. Correspondingly, the signals at the through port are shown in Fig 6.13 (b). The measured through signals at 1 GHz are around 1.2 dB, 1.5 dB, 2.4 dB, 3 dB, and 4.4 dB, compared with the simulated ones of 0.2 dB, 0.3 dB, 1.2 dB, 2 dB and 3.2 dB, across the same band range. At 3-dB coupling, the measured deviation is larger than other coupling coefficients, and thus the band in this specific case is reduced to 16% (0.9 GHz to 1.06 GHz).

Figs 6.13 (c) and (d) depict the return loss at any port (due to the fully symmetrical property, only Port 1 is shown here) and isolation between the input port and isolated one. The measured return loss is larger than 10 dB across the band range from 0.9 GHz to 1.1 GHz. The reflection poles in the measurement shift slightly to lower frequencies compared with the simulated ones, which might be caused by some errors in fabrication. From Fig 6.13(d) one can find that perfect isolation between Port 1 and Port 4 existing regardless of the coupling coefficient. The measured isolation is always larger than 15 dB in the band from 0.9 GHz to 1.1 GHz.

The phase performance is displayed in Fig 6.13 (e) for different coupling coefficients. The overall differential phase varies between from 82° and 98° (±8°) in the measurements and from 81° to 97° in the simulations. Considering that the proposed design operates at 20% bandwidth, the overall phase difference is acceptable. It is to be noted that for the non-coupling state, the differential phase is not applicable and thus not given here. The experimental performance is slightly different from the simulated one due to the nonlinearity of the tuning elements, errors in the fabrication process and losses in the testing environment.

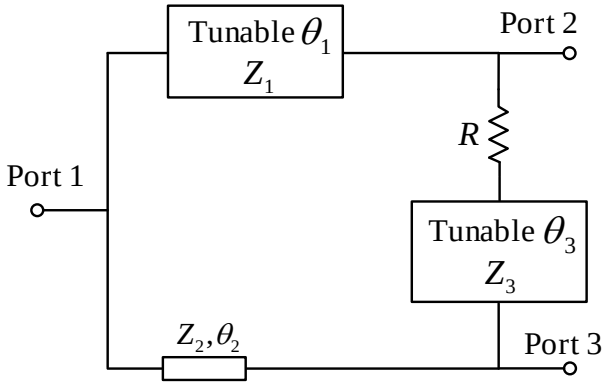

Fig 6. 14 Configuration of the proposed reconfigurable power divider.

6.4 Design of Power Divider with Reconfigurable Phase

Last chapter and previous sections of this chapter have introduced several novel ideas on tunable power division ratio in development of multi-port devices such as power dividers, couplers and

balun [149]. However, in some cases, it is more demanded to have reconfigurable differential phase between two output signals. The thorough review of the literature indicates that although the in-phase and out-of-phase PDs were heavily investigated as individual devices, the combination of these two types of PDs in a single structure has never been researched. In this chapter, a reconfigurable power divider which can be reconfigured to be either an in-phase or out-of-phase is proposed. The theory, simulations and measurements will be presented, indicating that two states can be achieved from the proposed design with in-phase and out-of-phase reconfiguration.

6.4.1 Configuration and Theoretical Analysis

Fig 6.14 illustrates the configuration of the proposed reconfigurable power divider. The structure includes two variable-length TLs, with variable electrical length θ_1 and θ_3 and fixed characteristic impedance Z_1 and Z_3, one fixed transmission line with length θ_2 and impedance Z_2, and one isolation resistor R. The port impedances of the device are Z_o. The output power division ratio is expressed as $k^2 = P_2/P_3$, assuming Ports 2 and 3 are the output ports. The analysis aims to satisfy the following conditions:

$$S_{11} = S_{22} = S_{33} = S_{32} = 0, S_{21} = kS_{31} \tag{6.43}$$

Using the even-odd mode analysis method, four conditions with regard to the structure parameters can be derived:

$$\begin{cases} Z_1 = Z_2 = Z_3 = \sqrt{2}Z_o & (6.44) \\ R = 2Z_o & (6.45) \\ \theta_1 = \dfrac{\pi}{2} + \theta_3 & (6.46) \\ \theta_2 = \dfrac{\pi}{2} & (6.47) \end{cases}$$

Another important property of the power divider is the phase difference at the two output ports (Port 2 and Port 3). The phase difference between the two output ports can be expressed as:

$$\Delta\emptyset = tan^{-1}\left(\frac{\sqrt{2}}{tan\,\theta_3}\right) - tan^{-1}\left(\sqrt{2}\,tan\,\theta_1\right) \tag{6.48}$$

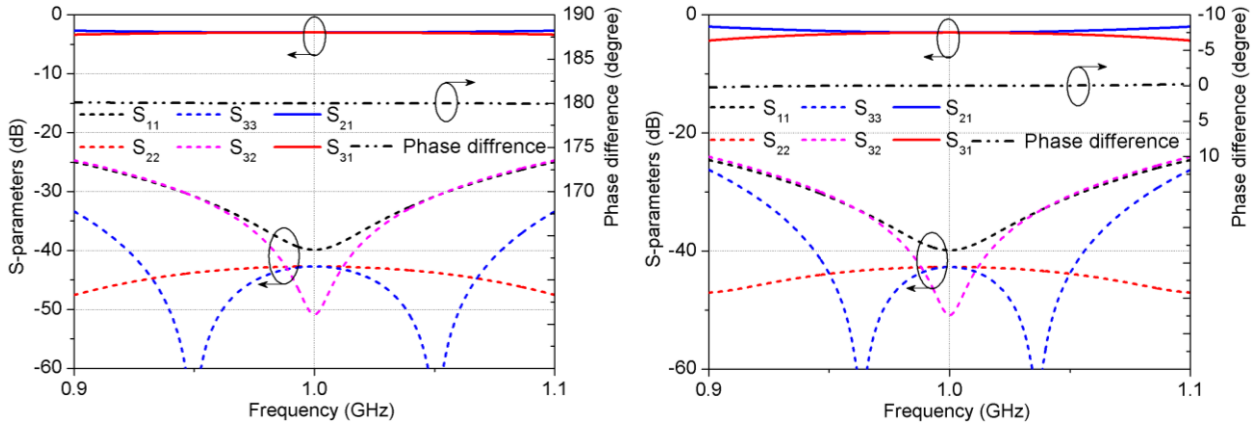

(a) (b)

Fig 6. 15 S-parameters and phase difference between the two output ports for the (a) 180° (out-of-phase) case when $Z_1 = Z_2 = Z_3 = 70.7\ \Omega, R = 100\ \Omega, \theta_1 = 270°$, and $\theta_3 = 180°$, and (b) 0° (in-phase) case when $Z_1 = Z_2 = Z_3 = 70.7\Omega, R = 100\Omega, \theta_1 = 450°$, and $\theta_3 = 360°$.

Combining the conditions (6.44)-(6.47) and (6.48), two important scenarios can be realised:

(1) When $\theta_1 = 270°$ and $\theta_3 = 180°$, 180° phase difference at the two output ports can be achieved with equal power division ratio (k=1).

(2) When $\theta_1 = 450°$ and $\theta_3 = 360°$, a 0° phase difference at two output ports can be achieved with equal power division ratio (k=1).

These two scenarios are simulated and the results are shown in Fig 6.15. It can be seen from Fig 6.15 that the two states (out-of-phase and in-phase) with satisfied S-parameters and phase differences can be achieved over the band 0.9-1.1 GHz by using different lengths for θ_1 and θ_3 when $Z_1 = Z_2 = Z_3 = 70.7\ \Omega$, $R = 100\ \Omega$ and $\theta_1 - \theta_3 = 90°$. These conclusions imply that a reconfigurable PD with these two states can be constructed by tuning the values of θ_1 and θ_3. To realise that target, tunable phase shifters (PS) are used to emulate variable length transmission lines. The PS should fulfil the need of achieving different lengths (180°, 270°, 360° and 450°) with acceptable return and insertion losses and characteristic impedance of 70.7 Ω.

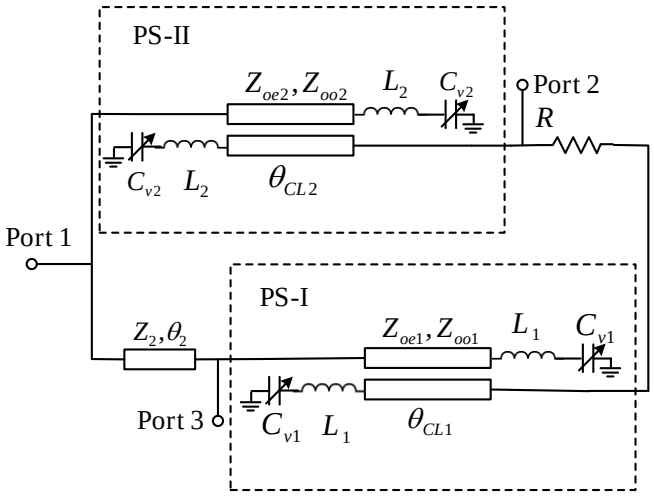

Fig 6. 16 Schematic diagram of the reconfigurable PD.

6.4.2 Tunable Phase Shifting Unit and Modified Circuit

The schematic diagram of utilizing two tunable phase shifting (PS) units to emulate the two variable-length transmission lines is shown in Fig 6.16. The tunable PSs are reflection type phase shifters using one section of loaded coupled line and a pair of varactors and inductors at the end of the coupled line. To analyze the possibility of using tunable phase shifting units to approximate the transmission lines with different lengths, the PS unit is analyzed using ABCD matrix:

$$\begin{bmatrix} A_{PS} & B_{PS} \\ C_{PS} & D_{PS} \end{bmatrix} = \begin{bmatrix} A' - \dfrac{B'}{Z_L} & B' \\ C' - \dfrac{2A'}{Z_L} + \dfrac{B'}{Z_L^2} & A' - \dfrac{B'}{Z_L} \end{bmatrix} \tag{6.49}$$

where

$$Z_{in}^{e} = \frac{Z_L Z_{oe}(Z_L + jZ_{oe}\tan\theta)}{2Z_{oe}Z_L + j(Z_{oe}^2 + Z_L^2)\tan\theta} \tag{6.50}$$

$$Z_{in}^{o} = \frac{Z_L Z_{oo}(Z_L + jZ_{oo}\tan\theta)}{2Z_{oo}Z_L + j(Z_{oo}^2 + Z_L^2)\tan\theta} \tag{6.51}$$

$$A_e = \cos\theta + \frac{jZ_{oe}\sin\theta}{Z_L} \tag{6.52}$$

$$A_o = \cos\theta + \frac{jZ_{oo}\sin\theta}{Z_L} \tag{6.53}$$

$$A' = D' = \frac{A_e A_o (Z_{in}^{e} + Z_{in}^{o})}{A_o Z_{in}^{e} - A_e Z_{in}^{o}} \tag{6.54}$$

$$B' = \frac{(Z_{in}^{e} + Z_{in}^{o})^2 - \left(\frac{Z_{in}^{e}}{A_e} - \frac{Z_{in}^{o}}{A_o}\right)^2}{2\left(\frac{Z_{in}^{e}}{A_e} - \frac{Z_{in}^{o}}{A_o}\right)} \tag{6.55}$$

$$C' = \frac{2A_eA_o}{A_oZ_{in}^{e} - A_eZ_{in}^{o}} \tag{6.56}$$

In Equations (6.50)-(6.53), Z_L is the load impedance of the coupled line and from Fig 6.16, it can be expressed as $Z_L = j\omega L + \frac{1}{j\omega C_v}$. It is well known that the ABCD matrix of a section of transmission line is:

$$\begin{bmatrix} A_{TL} & B_{TL} \\ C_{TL} & D_{TL} \end{bmatrix} = \begin{bmatrix} \cos\theta_{TL} & jZ_{TL}\sin\theta_{TL} \\ jY_{TL}\sin\theta_{TL} & \cos\theta_{TL} \end{bmatrix} \tag{6.57}$$

where $Z_{TL} = 70.7\ \Omega$ is the characteristic impedance of the transmission line, Y_{TL} is the admittance, and θ_{TL} is the electrical length. Thus, to design the PS, which can emulate a section of transmission line, the expression in (6.49) should be equated to (6.57). Since the maximum phase tuning range for one section of PS is less than 270°, two PSs with different parameters need to be designed to cover different range of phase (equivalent to different lengths of the transmission line). In this paper, PS-I is used to cover the phase range from 180° to 360° which can be used to emulate the transmission line with length θ_3, whereas PS-II is used to cover the phase range from 270° to 450° which can be used to emulate the transmission line with length θ_1.

By equating (6.49) to (6.57), several conditions for PS-I and PS-II need to be satisfied as shown in Table 6.1. Combining (6.50)-(5.56) with the conditions shown in Table I, the required parameters for PS-I and-II can be iteratively solved using MATLAB. The calculated parameters for PS-I and II are shown in Table 6.2 and the required values of capacitor C_v for different length of transmission lines are shown in Table 6.3. The values of $Z_{oe1}, Z_{oo1}, Z_{oe2}, Z_{oo2}, \theta_{CL1}, \theta_{CL2}, L_1$, and L_2 are determined based on Table II. The sets of values for C_{v1} and C_{v2} under the two states (in-phase and out-of-phase) are optimized and have the following values: For the in-phase state, $C_{v1} = 10.6\ pF, C_{v2} = 14.8\ pF$ and for the out-of-phase state, $C_{v1} = 1.06\ pF, C_{v2} = 1.02\ pF$.

Table 6. 1 CONDITIONS TO BE SATISFIED FOR PS-I AND II

		A'	B'	C'	D'
PS-I	180°	-1	0	$-\frac{2}{Z_L}$	-1
	270°	$-j\frac{Z_{TL}}{Z_L}$	$-jZ_{TL}$	$-j\frac{Z_{TL}}{Z_L^2} - j\frac{1}{Z_{TL}}$	$-j\frac{Z_{TL}}{Z_L}$
	360°	1	0	$\frac{2}{Z_L}$	1

PS-II	270°	$-j\frac{Z_{TL}}{Z_L}$	$-jZ_{TL}$	$-j\frac{Z_{TL}}{Z_L^2}-j\frac{1}{Z_{TL}}$	$-j\frac{Z_{TL}}{Z_L}$
	360°	1	0	$\frac{2}{Z_L}$	1
	450°	$j\frac{Z_{TL}}{Z_L}$	jZ_{TL}	$j\frac{Z_{TL}}{Z_L^2}+j\frac{1}{Z_{TL}}$	$j\frac{Z_{TL}}{Z_L}$

Table 6. 2 THE CALCULATED PARAMETERS FOR THE TWO TUNABLE PHASE SHIFTERS

	Z_{oe} (Ω)	Z_{oo} (Ω)	θ_{CL}	L (nH)
PS-I	180	31	90°	13
PS-II	225	27	126°	20

Table 6. 3 THE REQUIRED VALUES OF C_v (PF) TO EMULATE DIFFERENT LENGTHS OF TRANSMISSION LINES

	180°	270°	360°	450°
PS-I	1.02	1.954	20	N/A
PS-II	N/A	1	1.614	20

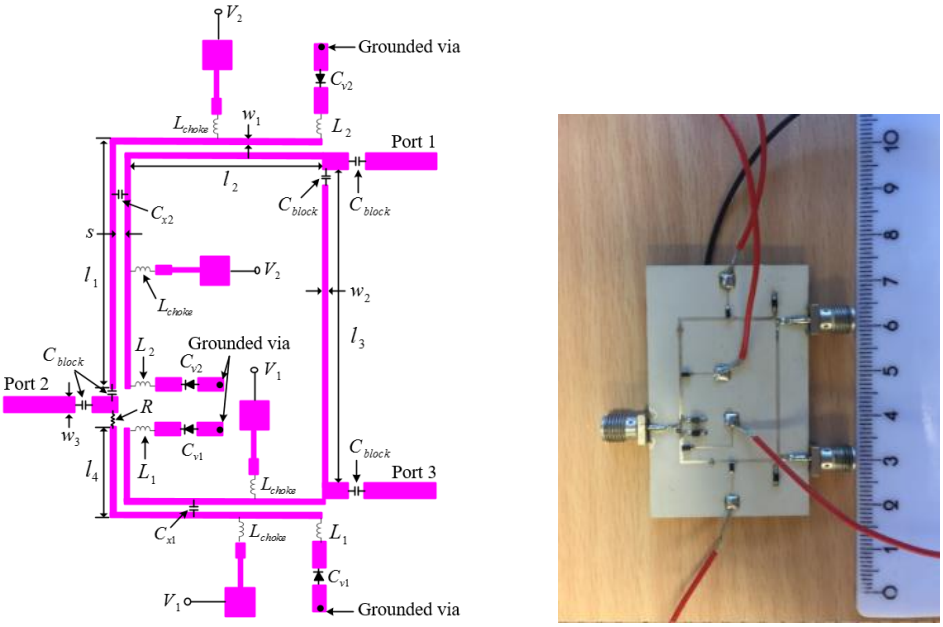

(a) (b)

Fig 6. 17 (a) Layout of the proposed reconfigurable power divider, and (b) the manufactured device.

6.4.3 Experimental Results and Discussions

To validate the proposed theory, a reconfigurable power divider is designed and built using microstrip line technology based on the layout shown in Fig 6.17 (a). Since a low odd-mode impedance of the coupled lines is required in the design, two chip capacitors are connected between the middle point of the coupled lines to increase the equivalent odd-mode capacitance of the coupled line and thus decrease the odd-mode impedance. Four SMV1283-011LF varactor diodes are used to realise the variable capacitors (C_{v1} and C_{v2}). Four chip inductors of 50 μH are used as the radio frequency chokes (RFC) and four chip capacitors of 100 pF are used as the DC blocks.

The substrate used in the design is Rogers 3010 with dielectric constant of 10.2 and thickness of 1.27 mm. The optimum dimensions for the structure after using HFSS are: $w_1 = 0.28\,mm$, $w_2 = 0.57\,mm$, $w_3 = 1.18\,mm$, $l_1 = 22.77\,mm$, $l_2 = 20.62\,mm$, $l_3 = 28.92\,mm$, $l_4 = 7.09\,mm$ and $s = 0.1\,mm$. The values of the used capacitors (C_{x1} and C_{x2}) and inductors (L_1 and L_2) after the optimization are: $C_{x1} = 5\,pF$, $C_{x2} = 1\,pF$, $L_1 = 7\,nH$ and $L_2 = 4\,nH$.

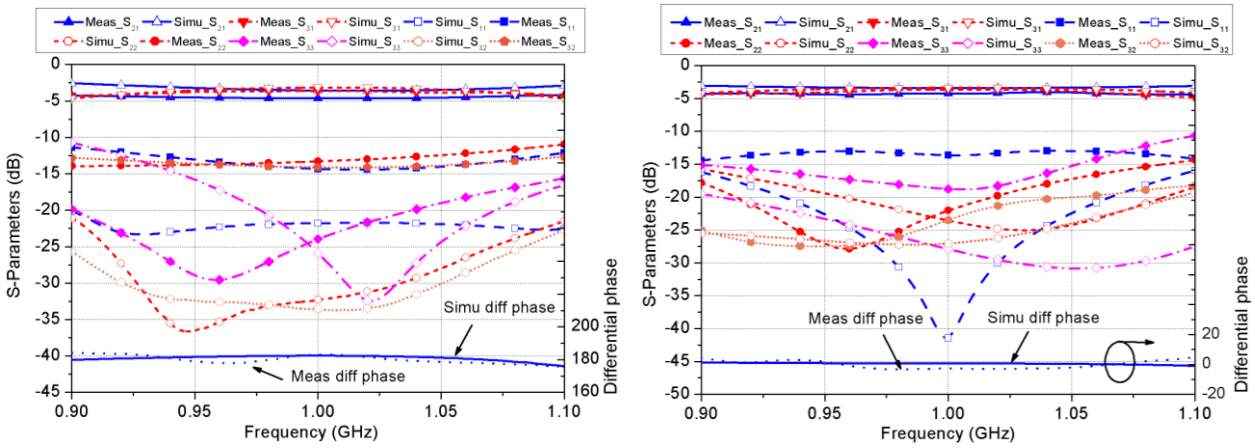

(a) (b)

Fig 6. 18 S-parameters and differential phase for the (a) out-of-phase state, and (b) in-phase state. For in-phase state: $V_1 = 2.1\,V$ and $V_2 = 1\,V$, for out-of-phase state: $V_1 = 13\,V$ and $V_2 = 20\,V$.

The final device is manufactured as shown in Fig 6.17 (b), and the full-wave simulation and measurement results of the two different states are shown in Fig 6.18. It can be that when the biasing voltage is $V_1 = 13\,V$ and $V_2 = 20\,V$, the out-of-phase state can be achieved with return loss at all of the three ports and the isolation between the two output ports are more than 12 dB across the frequency range from 0.9 to 1.1 GHz. A stable phase difference with 180°±5° between the two output ports can be achieved with 3.7±0.6 dB transmission coefficient. When the biasing voltage is $V_1 = 2.1\,V$ and $V_2 = 1\,V$, the in-phase state can be achieved with more than 12 dB return losses at the three ports and more than 15 dB isolation between the two output ports. A stable phase difference of $0° \pm 5°$ between the two output ports can also be achieved with 3.6±0.4 dB transmission coefficient. In this case, it is verified that the proposed design is able to realise reconfiguration of in-phase and out-of-phase states, which has great potential in microwave wireless communication systems.

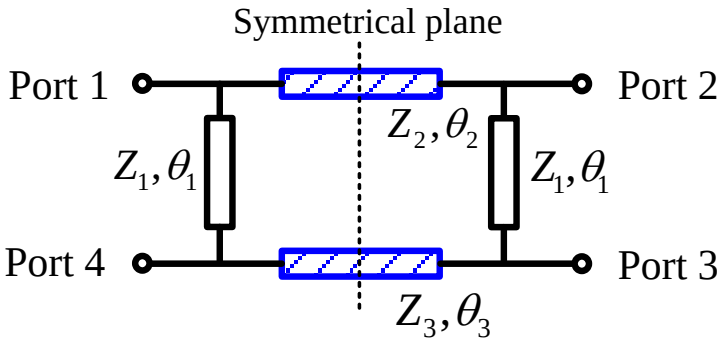

Fig 6. 19 Configuration of the proposed structure.

6.5 Design of Tunable Hybrid Coupler with Variable Phase-Difference

Directional couplers are commonly used in microwave wireless systems due to their ability to equal provide power division and constant phase. In some cases, arbitrary differential phase between two output ports is more favoured than constant one, which leads to new designs presented in [151] - [154]. However, fixed couplers are not able to be adapted in multi-functional systems which require variable differential phase. This section will present a new design of tunable hybrid coupler with variable phase difference.

6.5.1 Configuration and Theoretical Analysis

Fig 6.19 shows the proposed structure which is composed of two transmission lines with electrical length of θ_2 and θ_3 and characteristic impedance of Z_2 and Z_3, and two fixed transmission line with length and impedance θ_1 and Z_1. For a hybrid coupler with arbitrary phase, the general S-parameters can be expressed as

$$[S] = -\frac{j}{\sqrt{2}}\begin{bmatrix} 0 & e^{j\varphi} & 1 & 0 \\ e^{j\varphi} & 0 & 0 & 1 \\ 1 & 0 & 0 & e^{j\phi} \\ 0 & 1 & e^{j\phi} & 0 \end{bmatrix} \tag{6.58}$$

Where φ and ϕ represent the phase differences at two output terminations respectively. Due to the hybrid characteristics, the following equation is always satisfied

$$\varphi + \phi = 180° \tag{6.59}$$

Normally if $\varphi = \phi = 90°$, the structure turns to be a quadrature couple; while if φ (or ϕ) equals to $180°$, it will work as a Rat-Race coupler. In this work, the objective is to realise arbitrary

differential phase using tuning elements. To that end, the even- and odd-mode analysis approach is adopted to investigate the transmission characteristics of the network. Due to the symmetrical property of the structure, the circuit can be divided into two parts along the symmetrical plane indicated in Fig 6.19. For the even-mode/odd-mode circuit, the transmission coefficient and reflection coefficient are noted as S_{11e}, S_{21e}, S_{11o} and S_{21o}. Therefore, the general S-parameters of the whole structure can be expressed as follows [155]:

$$S_{11} = \frac{S_{11e} + S_{11o}}{2} \tag{6.60}$$

$$S_{21} = \frac{S_{11e} - S_{11o}}{2} \tag{6.61}$$

$$S_{31} = \frac{S_{21e} - S_{21o}}{2} \tag{6.62}$$

$$S_{41} = \frac{S_{21e} + S_{21o}}{2} \tag{6.63}$$

In order to have perfect matching at all terminations and ideal isolation between output ports, it is required that $S_{11} = S_{22} = 0$ and $S_{41} = 0$ have to be satisfied. In this case, the following conditions can be derived:

$$S_{11e} = -S_{11o} \tag{6.64}$$

$$S_{21e} = -S_{21o} \tag{6.65}$$

With the transformation from S-parameters to ABCD-matrix and equations above, one can obtain the following relations regarded the electrical lengths and characteristic impedances [154]:

$$Z_2 \sin\theta_2 = Z_3 \sin\theta_3 \tag{6.66}$$

$$Z_2 = \sqrt{\frac{Z_1^2}{1 + \left(\frac{Z_1}{Z_o}\right)^2}} \tag{6.67}$$

$$\varphi = \tan^{-1}\left(-\frac{Z_2}{Z_o}\tan\theta_2\right) \tag{6.68}$$

To make the design compact and simple, the electrical length and characteristics impedance of θ_1 is set to be $\pi/2$, and meanwhile $Z_2 = Z_3$. Besides, the summation of θ_2 and θ_3 should meet $\theta_2 + \theta_3 = (2n-1)\pi$, where n is a positive integer.

From Equation (6.68) one can find that the differential phase is affected, and only affected by the electrical length of θ_2 when Z_2 is fixed. This indicates that a tunable coupler with reconfigurable differential phase can be realised by tuning the values of θ_2. To realise such kind of tunable phase of θ_2, a tunable phase shifting element is adopted to replace the original transmission lines of θ_2

and θ_3. It is noted that since the summation of θ_2 and θ_3 should be $(2n-1)\pi$, the summation of shifting phases of two tunable units should also satisfy the principle.

6.5.2 Tunable Differential Phase

The schematic diagram and calculation of ABCD-matrix of utilizing two tunable phase shifting units have been given in Section 6.4.2. Actually the tunable phase shifting unit is able to provide a wide phase tuning range and maintain magnitude with little change, which means it can work as a transmission line with variable phase and fixed impedance.

In this design, our focus is mainly on the differential phase range φ between 45˚ and 135˚, due to the limitation of unchangeable impedance of the phase shifting unit. Following the discussion in [154], when the desired differential phase is given, one can find the required values θ_2 and θ_3. In other words, the required shifting phase of two units can be found from the following formulas:

when $45° < \varphi < 90°$,

$$\theta_2 = \pi - \tan^{-1}(\frac{Z_o \tan\varphi}{Z_2}), \text{ and } \theta_3 = \pi - \tan^{-1}(\frac{Z_o \tan\varphi}{Z_2}) \tag{6.69}$$

when $90° < \varphi < 135°$,

$$\theta_2 = -\tan^{-1}(\frac{Z_o \tan\varphi}{Z_2}), \text{ and } \theta_3 = \pi + \tan^{-1}(\frac{Z_o \tan\varphi}{Z_2}) \tag{6.70}$$

The relation between differential phase and its required shifting phase under different values of Z_2 is displayed in Fig 6.20. It can be found that when Z_2 is chosen as different values, the required phase shifting range for the tunable phase shifting unit is also not the same. A larger phase shifting range ψ is required for a larger impedance ratio of Z_2/Z_o. On the other hand, to have a minimal deviation of the signal power at output terminations, the impedance of Z_1 should be chosen as equal to Z_o. Considering the Equation (6.67), the value of Z_2 can be determined as $Z_2/\sqrt{2}$. In this case, the phase shifting range is selected as the red line in Fig 6.20, which is from 55˚ to 125˚.

Table 6. 4 THE REQUIRED VALUES OF C_v FOR TWO TPSUS

	STATE 1	STATE 2	STATE 3	STATE 4
φ	45°	60°	75°	90°
C_{v1}	0.12 pF	0.35 pF	0.56 pF	0.78 pF
C_{v2}	1.64 pF	1.26 pF	0.98 pF	0.78 pF
	STATE 5	STATE 6	STATE 7	
φ	105°	120°	135°	
C_{v1}	0.98 pF	1.26 pF	1.64 pF	
C_{v2}	0.56 pF	0.35 pF	0.12 pF	

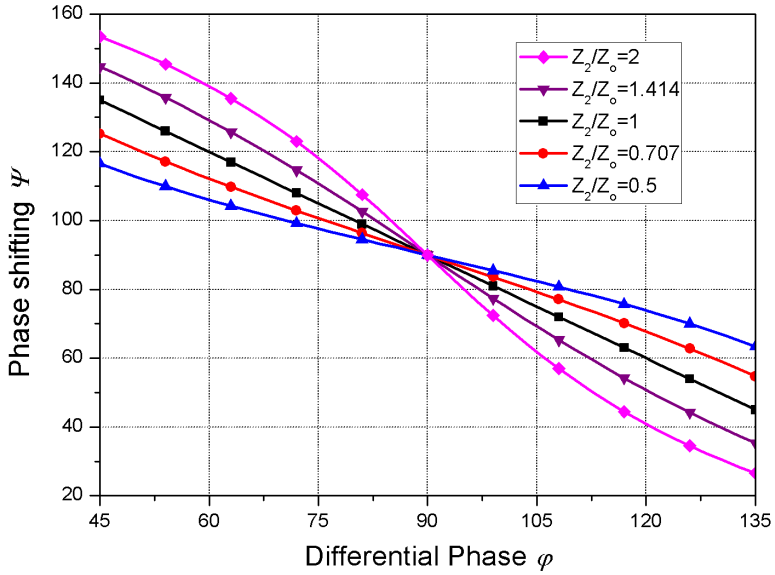

Fig 6. 20 Relations between the required phase shifting range against the targeted differential phase.

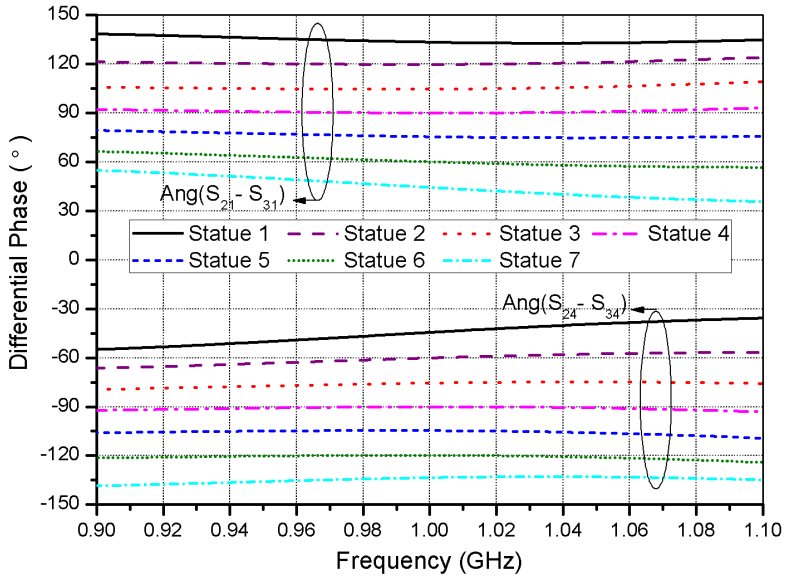

Fig 6. 21 Theoretical differential phase at Port 1 and Port 4 at seven statues.

Therefore, to realise a tunable differential phase at Port 1 from 45˚ to 135˚, two tunable phase shifting units should be able to tune the phase from 55˚ to 125˚ to replace the transmission lines of (Z_2, θ_2). Correspondingly, the transmission line (Z_3, θ_3) needs a tuning phase range from 125˚ to 55˚, since $\theta_2 + \theta_3 = (2n-1)\pi$ and suppose n = 1. To evaluate the possibility of using the tunable phase shifting unit to emulate a transmission line with variable length, the circuit is analysed using ABCD matrix. The method is to equate the ABCD matrix of the tunable phase shifting unit with that of a transmission line with characteristic impedance of Z_2 and electrical length of θ_2. By solving the equations, one can find that there might be multiple existing solutions that can cover the phase shifting range of 55˚ to 125˚. Following the design procedure presented in [156], the related

parameters of the tunable phase shifting unit are found to be: $Z_{oe} = 108\ \Omega$, $Z_{oo} = 32\ \Omega$, $\theta_s = 67°$, and $L_s = 2.2\ nH$.

Using the proposed tunable phase shifting units with loaded values of C_{v1} and C_{v2} to replace θ_2 and θ_3, it is now possible to predict the transmission property of the proposed design with tuning elements. Fig 6.21 depicts the theoretical response of the differential phase at Port 1 and Port 4. It is clearly seen that when φ (∠21-∠31) moves gradually from 45˚ to 135˚ at Port 1, the differential phase of -θ (∠21-∠31) at Port 4 also varies from -135˚ to -45˚. The adopted values for the tuning elements are given in Table 6.4. The operating bandwidth is around 20 percent. Within this range, the structure is able to have ideal matching at all terminations and isolation between output ports.

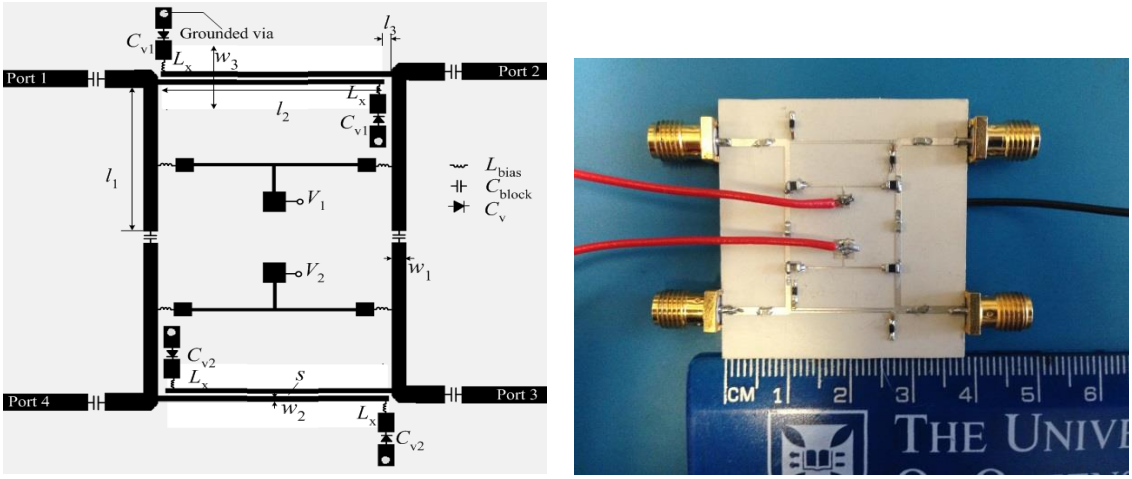

Fig 6. 22 Layout and photograph of the prototype.

6.5.3 Design and Results

To demonstrate the proposed design approach, full-wave simulation is done in Agilent's Advanced Design System by building an electromagnetic model and co-simulating with SPICE model of varactors. The tuning elements are selected as Skyworks SMV2019-219 (capacitance range from 0.16 pF to 2.25 pF, with parasitic resistance of 4.8 Ω). To provide a proper biasing voltage, a biasing circuit is built with DC blocking capacitors of 100 pF and RF chokes of 10 μH. Fig 6.22 shows the layout of the structure on the substrate of Rogers 3010 (dielectric constant of 10.2 and thickness of 1.27 mm) with biasing circuit. The optimized dimensions for the structure are: $w_1 = 0.85\ mm$, $w_2 = 0.26\ mm$, $w_3 = 5.2\ mm$, $l_1 = 12.2\ mm$, $l_2 = 15.1\ mm$, $l_3 = 0.4\ mm$, $s = 0.2\ mm$, and $L_x = 2.2\ nH$.

Fig 6.23 depicts the differential phase (∠21-∠31) from full-wave simulation and measurement when the signal is excited at Port 1. Different operating states are tested in which the biasing voltages are

found from the data sheet of the varactors according to the required capacitance in Table 6.4. It is clearly seen that a tunable differential phase is realised from 45˚ to 135˚ across a bandwidth of 20%. Ideal matching at all ports and isolation between Port 1 and Port 4 are realised in all the investigated cases, due to the transmission zeros generated at the centre frequency. The transmission and coupling coefficient at Port 2 and Port 3 are quite constant within the operating frequency range, though some small deviations existing in the tuning process. The proposed concept and design achieve the functions of hybrid couplers and tunable phase shifters, which reduce the circuit size and losses caused by connection of multiple devices.

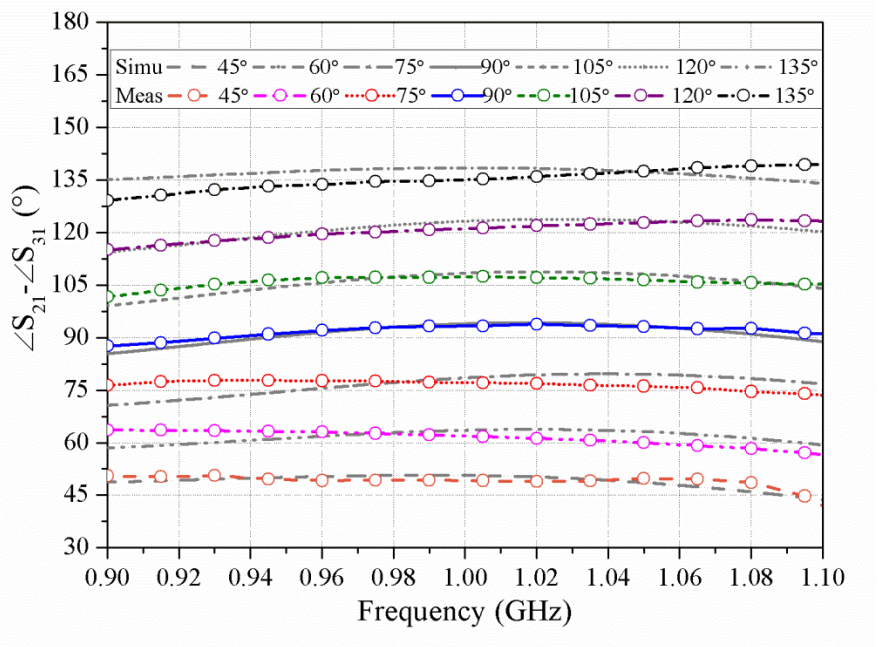

Fig 6. 23 Measured and simulated differential phase between Port 2 and Port 3 (Biasing voltages for V_1/V_2: 45˚-15V/1.2V, 60˚-8V/2V, 75˚-5.5V/2.5V, 90˚-3.6V/3.6V, 105˚-2.5V/5.5V, 120˚-2V/82V, and 135˚-1.2V/15V).

6.6 Summary

This chapter is aimed at developing multi-functional multi-port microwave devices, including tunable balun with tunable power division ratio, power divider with reconfigurable phase, tunable coupler with tunable coupling coefficient and tunable coupler with tunable differential phase. For the tunable balun and the tunable coupler with tunable coupling coefficient, the purpose of both designs is to have controllable signal power at two output ports. This concept is in line with the design of tunable power dividers with tunable power division ratio presented in the last chapter. The reconfigurable phase from the in-phase to out-of-phase state enables the switch of the differential phase between these two states. The propsed design realised this function by tuning the varactors within the structure. Compared with other reconfigurable power dividers designs using PIN diodes,

no extra matching circuits are loaded in the presented design. For the tunable hybrid coupler with tunable differential phase, the proposed concept and design have achieved the functions of both of hybrid couplers and tunable phase shifters, which reduce the circuit size and losses caused by connection of multiple devices.

Chapter 7: Reconfigurable Beam-forming Networks and their Applications on Phased Arrays

7.1 Introduction

Antenna arrays are essential parts of microwave systems since they can be working as transducers to convert guided waves to radiated waves so that signals can be transmitted or received. Feeding networks are critical sub-systems that can provide appropriate excitation or feeding power for antenna arrays. Usually when an array is installed, the radiation pattern will be fixed and unchangeable, including its beam direction, beamwidth, side-lobe level, nulls, and gains. However, to make the antenna arrays more flexible and adaptable, reconfigurable antenna arrays are investigated here. The purpose is to control the radiation pattern so as to adapt it to different scenarios. To that end, a kind of reconfigurable beam-forming network is demanded. Some techniques have been developed to provide the reconfigurability of the array's pattern including its spatial direction, the position of its nulls and its side-lobe levels [2], [157]-[158].

In most of the existing designs of beam-forming techniques, the main mechanism is to use a programmable chip to control the phase amplitude of each element. However, this method has many drawbacks, such as limited bandwidth and low power capacity. By using electrical control of the tunable beam-forming network, it is possible to have continuous, agile and flexible control of the array pattern. To build such a kind of reconfigurable sub-system, tunable microwave components are vitally important, especially tunable power dividers and tunable phase shifters. In Chapter 5, a novel concept of tunable power dividers with a tunable power division ratio was presented, which is favoured in building a tunable beam-forming network to control the power distribution at the output terminations.

In this research project, the objective is to have a tunable feeding network able to tune the signal amplitude at output terminations. The purpose of the design is to provide tunable or controllable feeding power to feed each element of the array, as depicted in Fig 7.1. When an antenna array is fed by unequal feeding power, the radiation pattern of the array, such as the side-lobe level and beamwidth, can be reconfigured and reshaped. Therefore, it is easy and quite feasible to achieve a desired beamwidth and side-lobe levels of antenna arrays by controlling the proposed tunable feeding network.

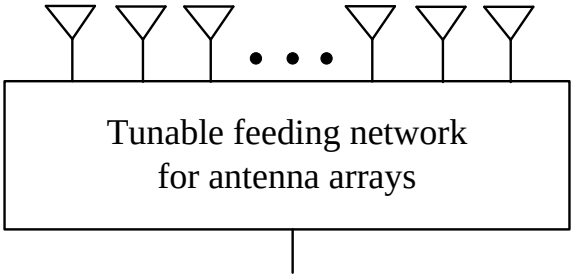

Fig 7. 1 Configuration of a subsystem composed of a tunable feeding network feeding a linear antenna array.

In some wireless systems, a steerable beam direction is very much required. To that end, traditional methods have been investigated like adding tuning elements or PIN diodes on radiators. These methods, however, have the major drawback that the tuning elements will deteriorate the radiation pattern and overall gain of arrays when the radiation angle is steered. Therefore, researchers started to focus on the controllability of the feeding network, which has been complemented by the work in this research. In this project, a new concept for a tunable feeding network with tunable phase shifters for beam steering has been proposed. As shown in Fig 7.2, tunable phase shifters are designed to be cascaded with the output terminations and each element of the antenna array. With controllability of beamwidth and side-lobe level, tunable phase shifters with certain differential phases can steer the beam direction.

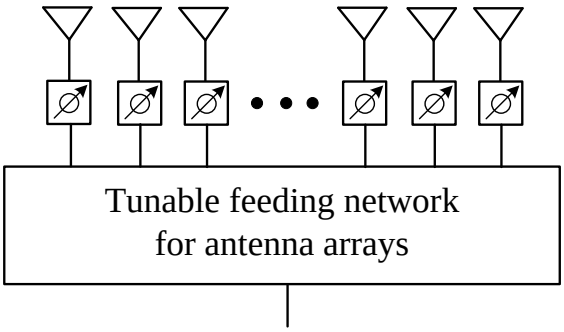

Fig 7. 2 Configuration of the tunable feeding network with tunable phase shifters for steerable beam.

In this chapter, a novel concept for tunable beam-forming networks is established using the proposed tunable power dividers with and without cascaded tunable phase shifters. Following this, a new kind of tunable phase shifter is presented. Finally, an antenna array is connected with the constructed feeding networks to verify the controllability of the array's radiation pattern and beam direction.

7.2 Design of Wideband Phase Shifters

Phase shifters are widely used in microwave systems, such as phased arrays, modulators, microwave instrumentation and measurement systems. For example, in a 4 × 4 Butler matrix, 45˚ phase shifters are needed to introduce a differential phase at output terminations. Similarly, in an 8 × 8 Butler matrix, 22.5˚ and 67.5˚ phase shifters are required. This section describes a wideband phase shifter with a wide range of phase shift using an open-ended parallel-coupled line. A novel L-shape network is adopted to improve the return loss at the input/output ports across a 100% fractional bandwidth. An 180˚ phase shifter across the band range of 1-3 GHz is built and then verified via theory, simulations, and measurements.

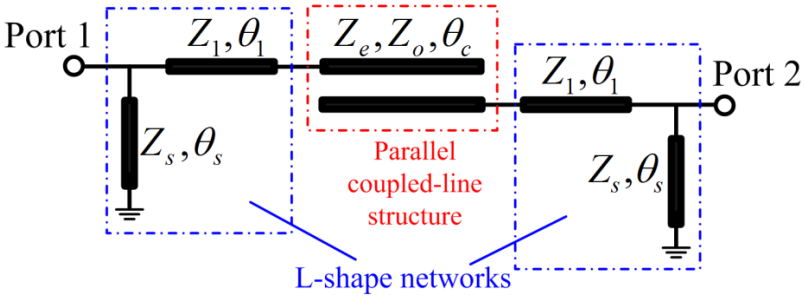

Fig 7. 3 Schematic diagram of the proposed phase shifter.

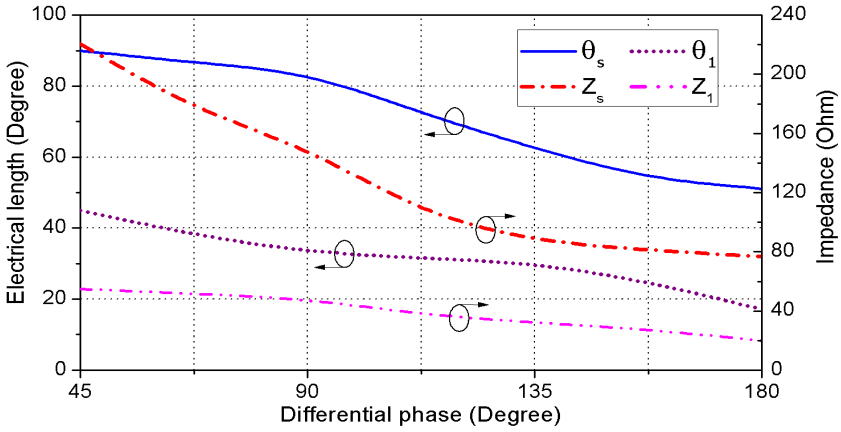

Fig 7. 4 Optimum values of $Z_1, Z_s, \theta_1, \theta_s$ for the required phase.

7.2.1 Parallel Coupled-line and L-shape Networks

The schematic diagram of the proposed device is shown in Fig 7.3. It is essentially a pair of L-shaped networks, which include a short-ended stub and a section of transmission line, and one section of quarter-wavelength ($\theta_c = \lambda/4$, where λ is the effective wavelength at the centre frequency) open-ended coupled line. It is well known that a single section of quarter-wavelength coupled line can provide a 30°~45° phase shift across a wide bandwidth. This coupled-line structure also has the potential to achieve a wide phase shift range at the cost of a low return loss at

the input/output ports. Therefore, two L-shaped networks are connected in the proposed design to the open-ended coupled line to improve the return loss, while the coupled-line section provides the required phase shift value.

The structure shown in Fig 7.4 can be analyzed using an ABCD matrix and S-parameters. The ABCD matrix of the L-shape network $[A]_L$ and the quarter-wavelength open-ended coupled line $[A]_{CL}$ are given as:

$$[A]_L = \begin{bmatrix} cos\theta_1 & jZ_1 sin\theta_1 \\ \dfrac{j(Z_s sin\theta_1 - Z_1 cot\theta_s cos\theta_1)}{Z_1 Z_s} & \dfrac{Z_1 sin\theta_1 cot\theta_s + Z_s cos\theta_1}{Z_s} \end{bmatrix} \tag{7.1}$$

$$[A]_{CL} = \begin{bmatrix} 0 & \dfrac{jb}{2} \\ \dfrac{2j}{b} & 0 \end{bmatrix} \tag{7.2}$$

Z_1, θ_1 and Z_s, θ_s are the characteristic impedance and electrical length of the L-shaped network transmission line and short-ended stub, respectively, $b = Z_{oe} - Z_{oo}$ where Z_{oe} and Z_{oo} are the even- and odd-mode impedances of the open-ended coupled line. For perfect matching at the input/output ports, two conditions should be satisfied:

$$|S_{11}| = |S_{22}| = 0 \tag{7.3}$$

$$|S_{21}| = |S_{12}| = 1 \tag{7.4}$$

Based on Equations (7.1)-(7.4) and using the ABCD parameters to S-parameters transfer functions, two conditions can be derived:

$$4jZ_1 \sin\theta_1 - \frac{jb^2(Z_s \sin\theta_1 - Z_1 \cot\theta_s \cos\theta_1)}{Z_1 Z_s} = 0 \tag{7.5}$$

$$b = \frac{4Z_1 \sin\theta_1 (Z_1 \sin\theta_1 \cot\theta_s + Z_s \cos\theta_1)}{Z_s} \tag{7.6}$$

7.2.2 Analysis of Wideband Phase Shifters

Using the cascaded structure of a coupled-line section and two L-shape networks, a wideband phase shifter with a wide phase shift range and operating bandwidth can be realised. In addition to the matching property for this phase shifter design, two other conditions with regard to the phase shift value and phase deviation also need to be satisfied:

$$\Delta\phi = \angle S_{21\_CL} + 2\angle S_{21\_L} + \theta_m$$

$$= 2\tan^{-1}\left(\frac{Z_o \cot\theta_s}{2Z_s}\right) - 2\tan^{-1}\left[\frac{(Z_1^2 + Z_o^2)\sin\theta_1}{2Z_1 Z_o \cos\theta_1}\right] - 90 + \theta_m \quad (7.7)$$

$$\frac{d\theta_m}{df} + \frac{d\angle S_{21\_CL}}{df} + 2\frac{d\angle S_{21\_L}}{df} = 0 \quad (7.8)$$

where Z_o is the characteristic impedance of the system port and θ_m is the electrical length of the reference line. Based on the required phase shift, the coupling coefficient *C* of the coupled-line and its characteristic impedances (Z_{oe} and Z_{oo}) are calculated as follows:

$$Z_{oe} = Z_o\sqrt{\frac{1+C}{1-C}} \qquad Z_{oo} = Z_o\sqrt{\frac{1-C}{1+C}} \quad (7.9)$$

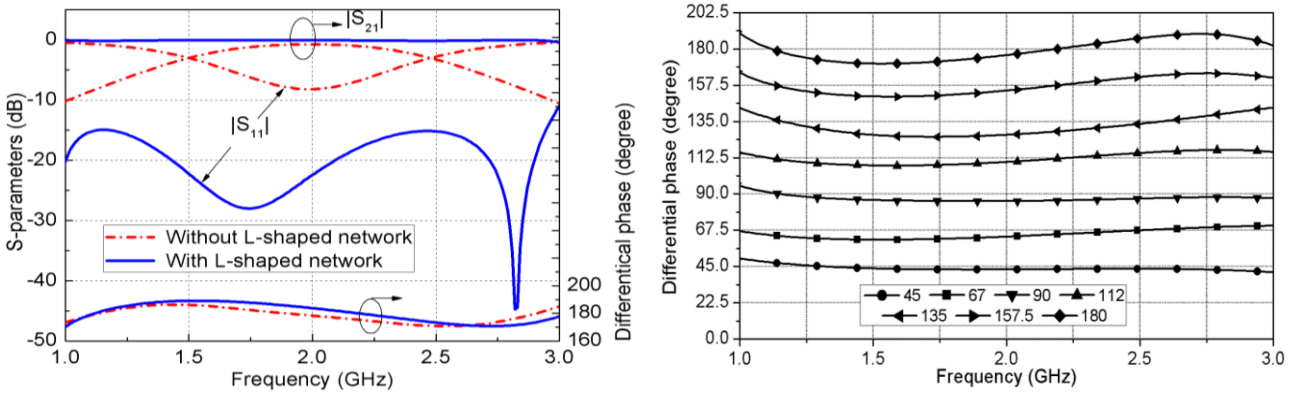

(a) (b)

Fig 7. 5 (a) The performance of 180° phase shifter using one section of quarter-wavelength open-ended coupled line with and without an L-shaped network; (b) The calculated reflection of the differential phases for seven phase shifters (45°~180°, with 22.5° intervals) using the proposed structure.

Based on the required phase shift, Z_1, θ_1, Z_s and θ_s are determined using Fig 7.4. The reference line is a 50 Ω microstrip line whose length l_m can be determined using Equation (7.7) with $\theta_m = -\beta_m l_m$ as:

$$l_m = -\lambda\left(\left|\angle S_{21_{CL}} + 2\angle S_{21_L} - \Delta\phi\right)/(2\pi)\right. \quad (7.10)$$

To verify the design principle concerning the effect of the L-shaped networks, a 180° phase shifter is initially designed here to have a centre frequency of 2.5 GHz and band 1-3 GHz. In this case, the calculated design parameters are Z_{oe}=106 Ω, Z_{oo}=26 Ω, Z_1=20 Ω, θ_1=17°, Z_s=77 Ω, and θ_s=51°. The performance is shown in Fig 7.5 (a) using the full-wave simulation tool HFSS.

It can be seen that when only the quarter-wavelength coupled line is used, the required phase is achieved but with a return loss that is less than 10 dB across the band of interest. When the L-

shaped networks are added to the structure, the phase shift performance is kept and the return loss is improved to be more than 10 dB across the whole band. Therefore, this approach enables increasing the achievable phase range while maintaining the wideband performance (at more than 100% fractional bandwidth).

The calculation results of the S-parameters and differential phase using the design procedure for the seven phase shifters covering the range from 45° to 180° are shown in Fig 7.5(b). It can be observed that the theoretical values of the differential phase possess the wide range of 45° to 180° and the phase deviations are within ±7° across the band 1-3 GHz.

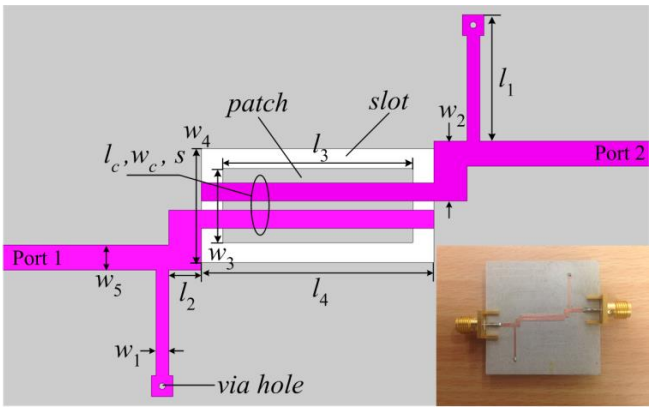

Fig 7. 6 Layout and photograph of the proposed phase shifter.

7.2.3 Simulation and Experimental Results

To validate the proposed method, one phase shifter with 180° differential phase shift is fabricated and tested. The layout and photo of the device are shown in Fig 7.6. The ground slot and patch at the ground layer shown in Fig 7.6 are used to realise the required mode impedances in the coupled structure. The substrate used in the design is Rogers RO6010 with a dielectric constant of 10.2 and thickness of 1.24 mm. The theoretical parameters are optimized using HFSS and the final design dimensions (mm) are: w_1=0.6, w_2=2.8, w_3=1.9, w_4=5.4, w_5=1.2, w_c=0.9, s=0.4, l_1=11.4, l_2=1.6, l_3=13.7, l_4=15.5, and l_c=15. The 180° phase shifter is manufactured based on these dimensions and then tested.

The simulated and measured S-parameters of the device are shown in Fig 7.7 (a). The reflection coefficient is below -10 dB and the transmission coefficient is above -1.3 dB over the chosen band of 1 GHz to 3 GHz, which is equivalent to 100% fractional bandwidth. Fig 7.7 (b) indicates that the achieved differential phases for the designed phase shifter is equal to the nominated value (180°) with a phase deviation of less than ±8° across the band 1-3 GHz.

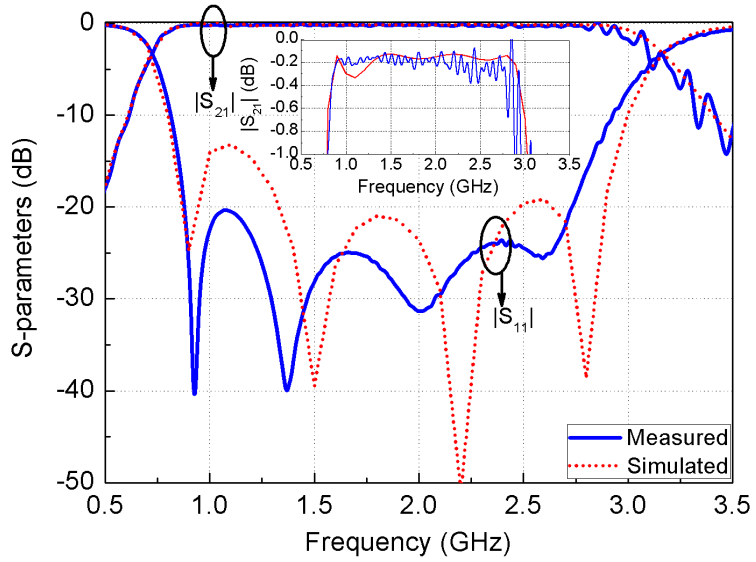

(a)

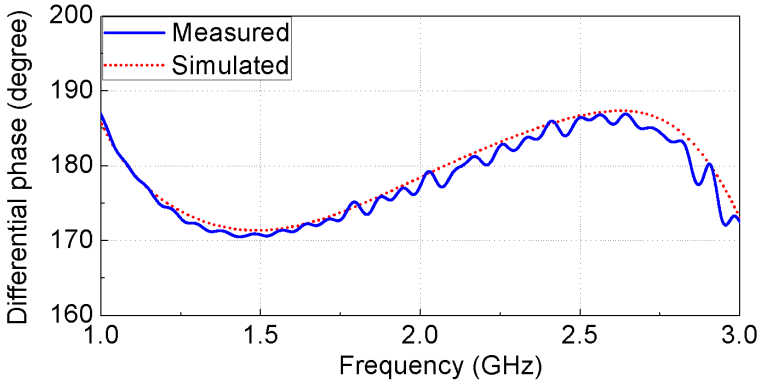

(b)

Fig 7. 7 Simulated and measured differential phase shift: (a) S-parameters; (b) Differential phase.

It can be seen that the simulation results agree well with the measured results. It is to be noted that due to the need for tight coupling for low phase shift designs, the gap between the coupled lines could be less than 0.1 mm, which requires using sophisticated manufacturing tools or other configurations, such as broad-side coupled structures. Compared with other existing works, the proposed design [159] possesses the widest phase range using a single layer structure with reasonable phase deviation and insertion loss across 100% bandwidth, which is extremely favorable in wideband microwave systems.

7.3 Design of Wideband Tunable Phase Shifters

Tunable phase shifters are critical in beam-forming sub-systems for the reason that they are able to change the phase of each signal so that the beam direction can be steered. As shown in Fig 7.2, after the division of power in the power divider, the input signal needs to be endued with a certain phase

to realise a steerable beam. Meanwhile, a wide bandwidth and a constantly variable phase are required for the tunable phase shifter design. After reviewing the state-of-the-art reported works, it was found that there is still a gap in designing tunable phase shifters with a wide operating band, full-360˚ phase shift, and low insertion loss.

In this section, a complete theoretical analysis of the four-port network and its effect on the phase shifter performance is firstly given, and then based on the design requirement for the desired performance, a new kind of four-port network is proposed, followed by a tunable phase shifter design with excellent matching properties and a wide operating bandwidth.

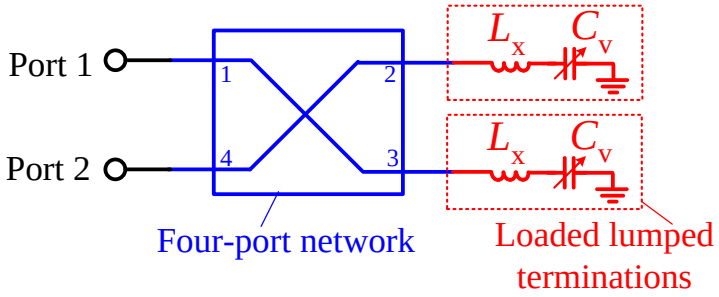

Fig 7. 8 Configuration of the proposed wideband tunable reflection-type phase shifter.

7.3.1 Analysis of Tunable Reflection-type Phase Shifters

Fig 7.8 displays the basic concept of the proposed wideband reflective phase shifter. It adopts the traditional method to build a reflection-type phase shifter (RTPS), which is composed of a four-port network (for example, directional couplers) and two reflective elements. Our target in undertaking this work includes exploring three aspects: (1) wideband performance; (2) full range of phase tuning; (3) low insertion loss. In order to make the differential phase stable and all ports matched across a wide band range, some specifications for the four-port network and reflective elements should be satisfied. This section is organised in the following order: firstly the relation between reflective phase shifters and four-port networks is introduced; a four-port coupler is proposed to fulfil the requirement of the specification for the phase shifter; finally a wideband tunable phase shifter is presented, and full-wave simulation and experimentation have been performed based on the proposed configuration, a discussion of which concludes this section.

The four-port network is set to be a directional coupler. The S-parameters of a directional coupler can be summarized with the following equations:

$$S_{11} = S_{22} = S_{33} = S_{44} = R \tag{7.11}$$

$$S_{12} = S_{21} = S_{34} = S_{43} = T \tag{7.12}$$

$$S_{13} = S_{31} = S_{42} = S_{24} = C \tag{7.13}$$

$$S_{14} = S_{41} = S_{32} = S_{23} = I \tag{7.14}$$

Here R, T, C, and I refer to the reflection, transmission, coupling and isolation coefficients of a directional coupler. If Port 2 and Port 3 are connected with some reflective elements, while Port 1 and Port 4 of the four-port network become the input and output of the phase shifter, it is possible to achieve consistent tuning of the differential phase. Suppose that the reflection coefficient of the reflective elements is Γ, the S-parameters of the phase shifter can be expressed using those of the directional couplers as below:

$$S_{11}^{ps} = S_{11} + \frac{S_{12}\Gamma \cdot (S_{21} + (S_{23}S_{31} - S_{21}S_{33})\Gamma)}{(1 - S_{22}\Gamma)(1 - S_{33}\Gamma) - S_{23}S_{32}\Gamma^2} + \frac{S_{13}\Gamma \cdot (S_{31} + (S_{32}S_{31} - S_{31}S_{22})\Gamma)}{(1 - S_{33}\Gamma)(1 - S_{22}\Gamma) - S_{32}S_{23}\Gamma^2} \tag{7.15}$$

$$S_{21}^{ps} = S_{41} + \frac{S_{42}\Gamma \cdot (S_{21} + (S_{23}S_{31} - S_{21}S_{33})\Gamma)}{(1 - S_{22}\Gamma)(1 - S_{33}\Gamma) - S_{23}S_{32}\Gamma^2} + \frac{S_{43}\Gamma \cdot (S_{31} + (S_{32}S_{31} - S_{31}S_{22})\Gamma)}{(1 - S_{33}\Gamma)(1 - S_{22}\Gamma) - S_{32}S_{23}\Gamma^2} \tag{7.16}$$

Combining (7.15) and (7.16) one can get simplified expressions:

$$S_{11}^{ps} = R + \frac{2ITC\Gamma^2 - T\Gamma(1 - R\Gamma)(T + C)}{(1 - R\Gamma)^2 - I^2\Gamma^2} \tag{7.17}$$

$$S_{21}^{ps} = I + \frac{2TC\Gamma(1 - R\Gamma) + IC\Gamma^2(T + C)}{(1 - R\Gamma)^2 - I^2\Gamma^2} \tag{7.18}$$

where

$$\Gamma = \frac{jX_l - Z_0}{jX_l + Z_0} \tag{7.19}$$

$$X_l = j\omega L_x + \frac{1}{j\omega C_v} \tag{7.20}$$

Γ and X_l represent the reflection coefficient and the reactance of the loaded lumped termination, which is composed of a fixed inductance and a variable capacitance. For design of phase shifters, the transmission of signals needs to satisfy the conditions of $S_{11}^{ps} = 0$ and $S_{21}^{ps} = 1$. Usually directional couplers are favoured for use as the four-port network due to their ideal isolation, matching and equal power splitting, and 90° differential phase at output ports. Meanwhile, the differential phase of the loaded elements and the RTPS can be expressed as:

$$\angle\phi_\Gamma = \tan^{-1}\left(\frac{2jX_lZ_0}{X_l^2 + Z_0^2}\right) \tag{7.21}$$

$$\Delta\angle S_{21}^{ps} = \angle\phi_{\Gamma 2} - \angle\phi_{\Gamma 1} = 2\tan^{-1}\left(\frac{\Delta X_l}{Z_0}\right) \tag{7.22}$$

In order to achieve the maximum differential phase of the RTPS, it is critical to get a larger value of $\angle\phi_\Gamma$, which is determined by the variation of the capacitance. Generally, the loaded lumped termination is able to realise more than a 360˚ phase shift tuning with typical values for narrowband range, since narrowband does not have high requirements in terms of phase deviation and transmission of signals.

For wideband purposes, problems will arise, including how to maintain satisfactory S_{11}^{ps} and S_{21}^{ps} at an acceptable level or how to make sure that $\frac{d\varphi}{d\omega}$ is equal to 0 for all ω. A fine design of the wideband four-port network can definitely lead to a wide operating bandwidth, large phase shift range and stable phase deviation.

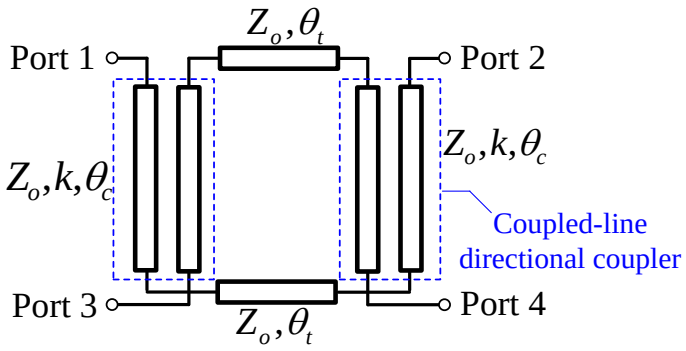

Fig 7. 9 Schematic diagram of the four-port network.

7.3.2 Proposed Four-port Network and its Application on the Tunable RTPS

To fulfil the requirement of high tunability of RTPS, a directional coupler with high directivity is needed; therefore, a directional coupler is proposed in this section. Fig 7.9 shows the schematic diagram of the proposed four-port network, which is composed of two traditional coupled-line directional couplers connected with two transmission lines. Key parameters of the structure include: Z_0 represents the characteristic impedance, k is the coupling factor of the coupled-line, and θ_c, θ_t are the electrical lengths for the coupled-lines and transmission lines. It is well-known that for a coupled-line directional coupler, the reflection and isolation is null, and the transmission coefficient and coupling coefficient are denoted as *t* and *c*, as indicated below:

$$c = \frac{jk \sin\theta_c}{\sqrt{1-k^2}\cos\theta_c + j\sin\theta_c} \tag{7.23}$$

$$t = \frac{\sqrt{1-k^2}}{\sqrt{1-k^2}\cos\theta_c + j\sin\theta_c} \tag{7.24}$$

In this design, 3-dB coupling is required, rendering $|c| = |t|$ and thus $k = 1/\sqrt{2}$. The electrical length of the coupled-line section is set to be equal to 90°. Besides, for the transmission lines the transmission coefficient is denoted as:

$$e = \cos\theta_t - j\sin\theta_t \tag{7.25}$$

The target is to link the transmission properties of the proposed four-port network with the tunable RTPS. Therefore, based on the analysis given in the last section, the overall transmission coefficient and coupling coefficient of the four-port network can be expressed with regards to the proposed directional coupler as:

$$T = S_{21}^{c} = 2cte \tag{7.26}$$

$$C = S_{31}^{c} = (c^2 + t^2)e \tag{7.27}$$

By substituting Equations (7.23)-(7.25) into (7.26) and (7.27), one can find the expression of *T* and *C* as:

$$T = \frac{2jk\sqrt{1-k^2}\sin\theta_c \cdot (\cos\theta_t - j\sin\theta_t)}{\left(\sqrt{1-k^2}\cos\theta_c + j\sin\theta_c\right)^2} \tag{7.28}$$

$$C = \frac{(1-k^2-k^2\sin^2\theta_c^2) \cdot (\cos\theta_t - j\sin\theta_t)}{\left(\sqrt{1-k^2}\cos\theta_c + j\sin\theta_c\right)^2} \tag{7.29}$$

Meanwhile, the reflection and isolation are ideal ($R = I = 0$) for the proposed four-port network. By substituting (7.28) and (7.29) into (7.17) and (7.18), it is easy to depict the S-parameters of the tunable RTPS with the proposed directional coupler. Figs 7.10(a) and (b) show the plotted S-parameters for the 1-stage and 2-stage structure. It can be observed from both results that the S_{11} is lower than -25 dB across more than 80% of the bandwidth from 0.8 GHz to 2.2 GHz.

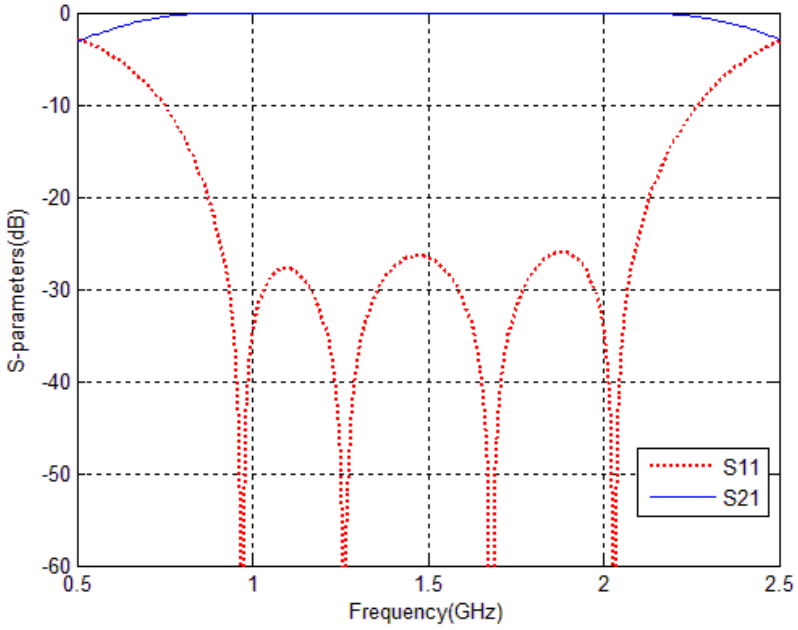

(a)

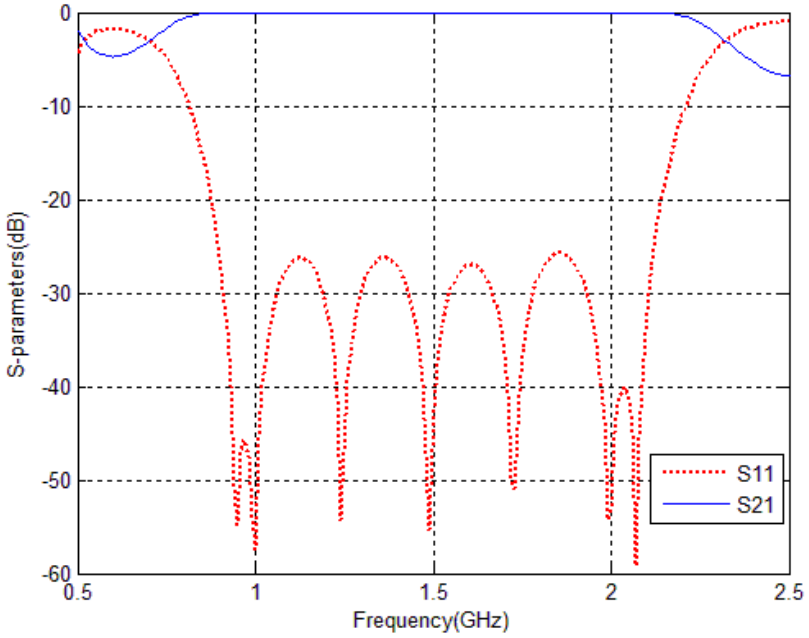

(b)

Fig 7. 10 Calculated S-parameters for (a) 1-stage and (b) 2-stage tunable RTPS.

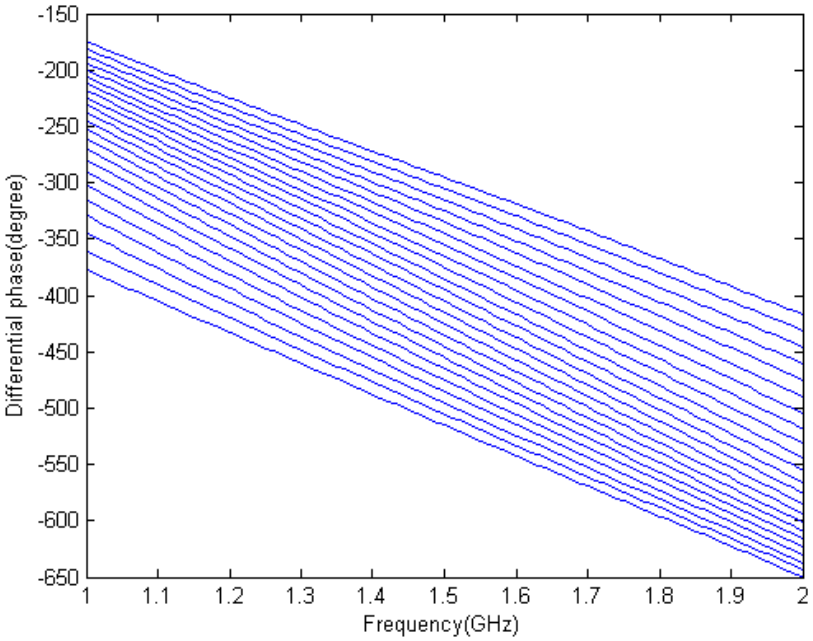

Fig 7. 11 Differential phase of the proposed RTPS by tuning C_v from 0.1 pF to 10 pF.

By changing the value of C_v which affects the reflection of the loaded lumped terminations, a tunable differential phase will be realised. The value of L_x also affects the tuning range of the differential phase ($\Delta\phi$) as well as the reflection of the phase shifter. As analysed in [156], when a larger L_x is adopted, a wider tuning range of $\Delta\phi$ may be achieved; however, it may lead to larger reflection within the operating range and decrease the useful bandwidth of the device. The appropriate value for L_x is set to be 2.2 nH. With the given values, the differential phase is calculated by deriving the phase of $|S_{21}^{ps}|$.

As shown in Fig 7.11, very steady and constant phases tuned by C_v from 0.2 pF to 15 pF are given. It can be found that the tuning range for the differential phase is more than 200˚ and the operating band range is from 1 to 2 GHz. For a two-stage structure, the achievable differential range is more than 360˚, which covers the full range of the shifting phase. These responses reveal the great potential of the proposed tunable phase shifter to be used in the development of a tunable feeding network for wideband phased arrays, which will be presented in the following sections.

7.3.3 Tested Result of the Tunable RTPS

Based on the analysis above, a prototype of tunable reflection-type phase shifter is fabricated. The prototype is based on a four-port network composed of two coupled-line sections and two connecting lines, as shown in Fig 7.9. The structure of the tunable phase shifter is shown in Fig 7.12. The inter-section of the coupled-line and connecting line is realised by via-hole transitions from

between the microstrip and a slotline on the ground. The lengths of the coupled-line sections and connecting lines are set as quarter wavelength and 10 degree at the centre frequency of 1.5 GHz. The Skyworks SMV1283-011LF (0.52-14.2 pF, 0-26 V, R_s=2.4 Ω) varactors are adopted as tuning elements. The biasing inductor and DC block capacitor are 10 μH and 100 pF, respectively. SPICE models of the aforementioned varactors as provided in [110] are used in the co-simulation within Advanced Design System (ADS).

Fig 7.13 depicts the performance of the fabricated prototype. When the biasing voltage is varied from 0 to 20 V, the phase of S_{21} can be gradually tuned within the band range from 0.8 GHz to 2.5 GHz. The phase tuning range is around 140˚ to 180˚. The phase tuning range can be extended if other types of varactors with smaller achievable capacitance are used. Moreover, since the tested prototype is one-stage tunable phase shifter, the phase tuning range is somehow limited. A widen tuning range of phase shift up to 360˚ can be achieved if a two-stage structure is used. The return loss and insertion loss are shown in Figs 13(b) and (c). High reflection between 1.5 GHz to 2 GHz is due to the fabrication error and soldering process, and some extra losses are caused by the tuning elements as well as the testing environment.

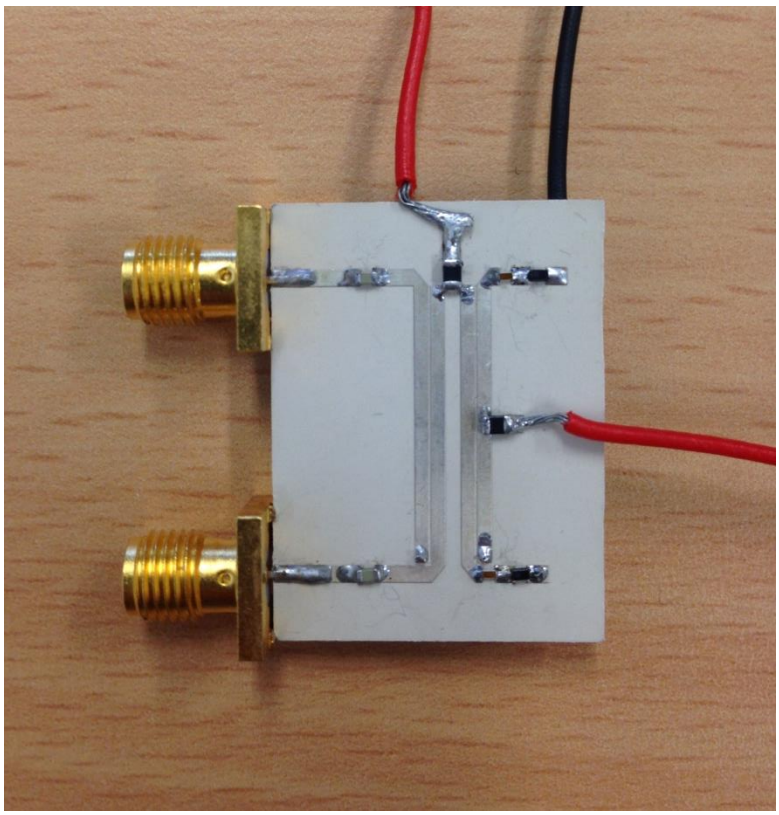

Fig 7. 12 Photograph of the fabricated prototype of the tunable RTPS.

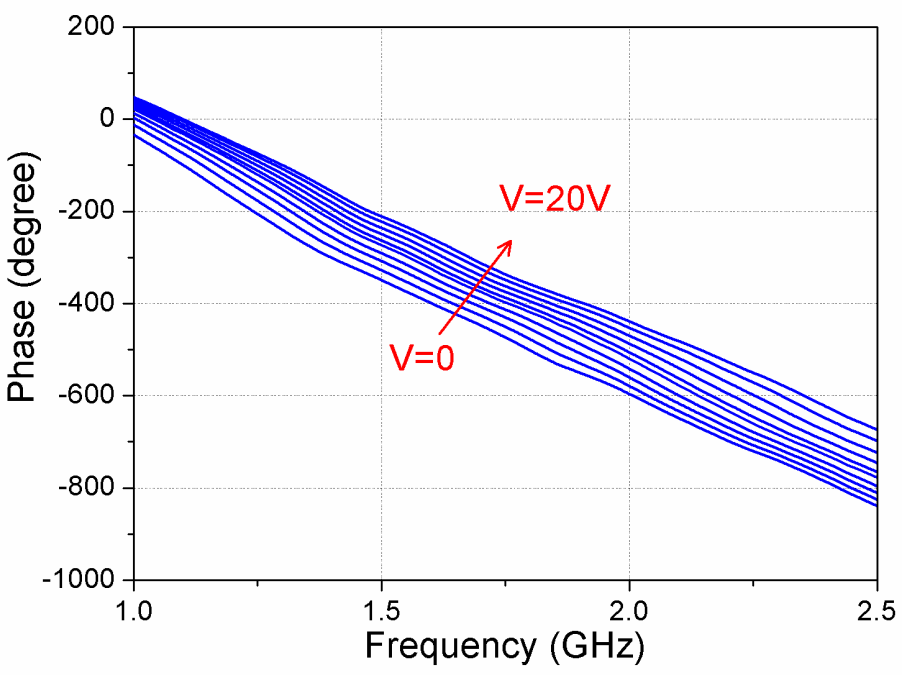

(a)

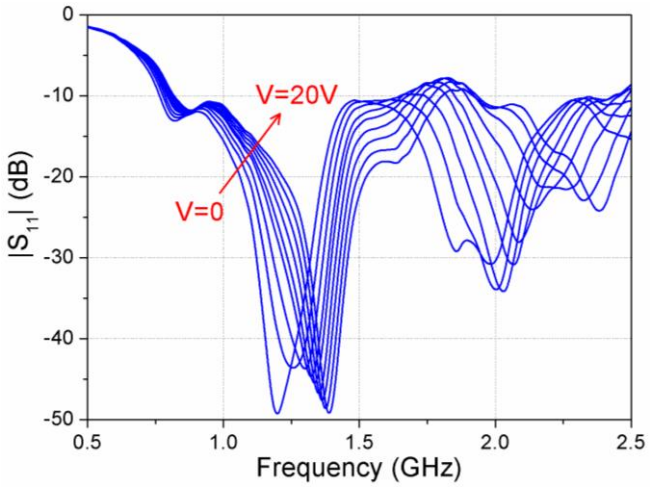

(b)

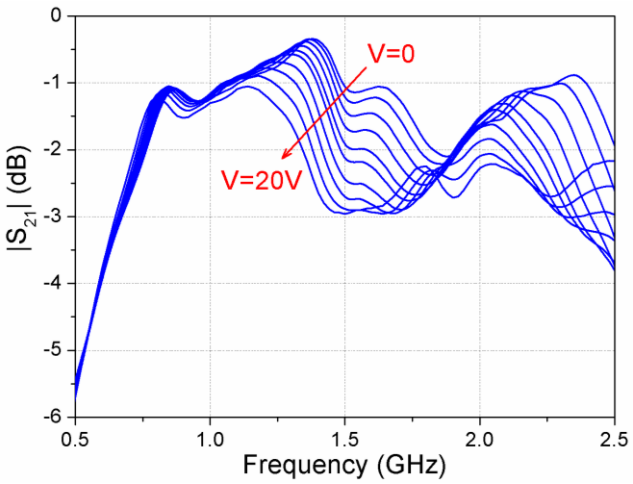

(c)

Fig 7. 13 Measured results of the fabricated prototype of the tunable RTPS: (a) phase; (b) $|S_{11}|$; (c) $|S_{21}|$.

7.4 Eight-way Tunable Feeding Network for Beam-forming

In this section, a new concept of tunable feeding network for eight-element antenna array will be presented. The configuration of the proposed tunable feeding network is firstly introduced, followed by verification of the feeding network to control the feeding excitation of a linear array to realise reconfigurable side-lobe suppression levels.

7.4.1 Construction and Transmission Properties of the Tunable Feeding Network

Fig 7.14 shows the configuration of the proposed tunable feeding network, which is an 8-way power divider with eight output ports. It can be seen that the proposed 8-way power divider consists of three sections: Section I is a traditional Wilkinson power divider, which is able to split the input signal into two identical parts. In this case, the output power at the eight terminations will be symmetrical. Sections II and III are composed of single-stage two-way tunable power dividers, which have been presented in Chapter 5. There are 12 tuning elements in total, controlled by six different voltages named V_1, V_2, V_3, V_4, V_5 and V_6. Among these voltages, V_1 and V_2 are in charge of the first stage of the two-port tunable power dividers, while the other four are related to the second stage. Since the voltage distribution is symmetrical along the central line for Ports 2~5 and Ports 6~9, one can predict that the scattering parameters at the output ports should follow these relations: $S_{21} = S_{91}$, $S_{31} = S_{81}$, $S_{41} = S_{71}$, and $S_{51} = S_{61}$. When all the voltages are set to be equal, the output signals at the eight output ports will be identical as well.

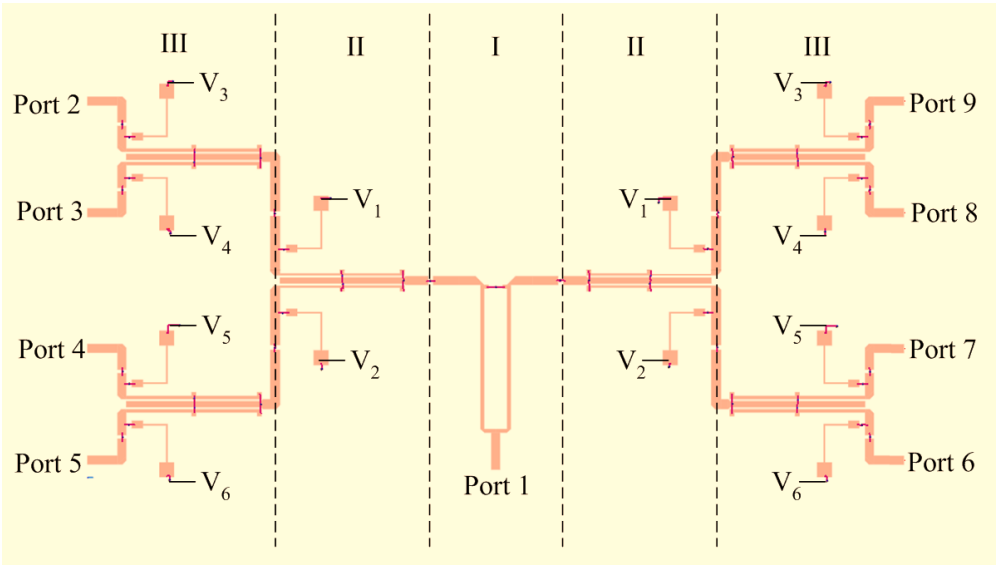

Fig 7. 14 Configuration of the proposed tunable feeding network

Table 7. 1 Power weights and S-parameters for 20-dB Taylor's SLL suppression

Port	Power weight	Power division	S-parameter (ideal)	S-parameter (full-wave)
Port 2 (Port 9)	0.36	0.14	11.57 dB	12.2 dB
Port 3 (Port 8)	0.46	0.17	10.61 dB	11.03 dB
Port 4 (Port 7)	0.77	0.3	8.25 dB	8.64 dB
Port 5 (Port 6)	1	0.39	7.13 dB	7.46 dB

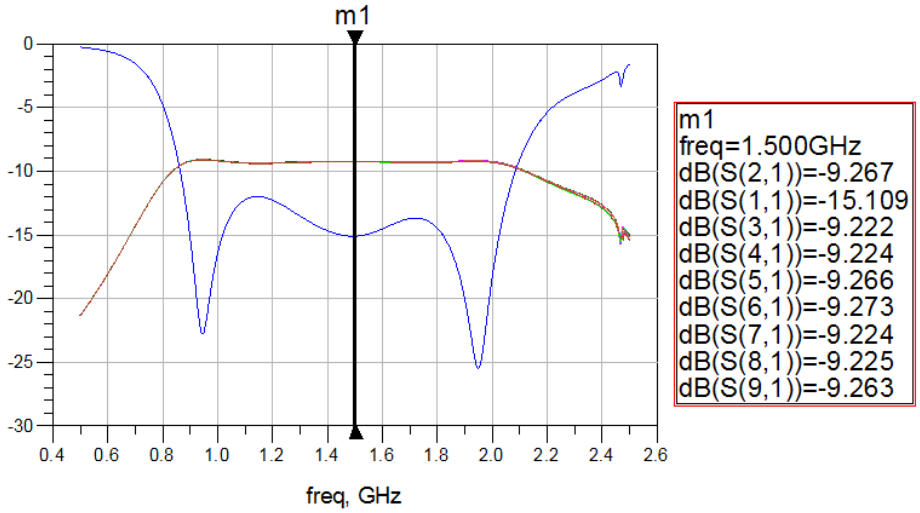

(a)

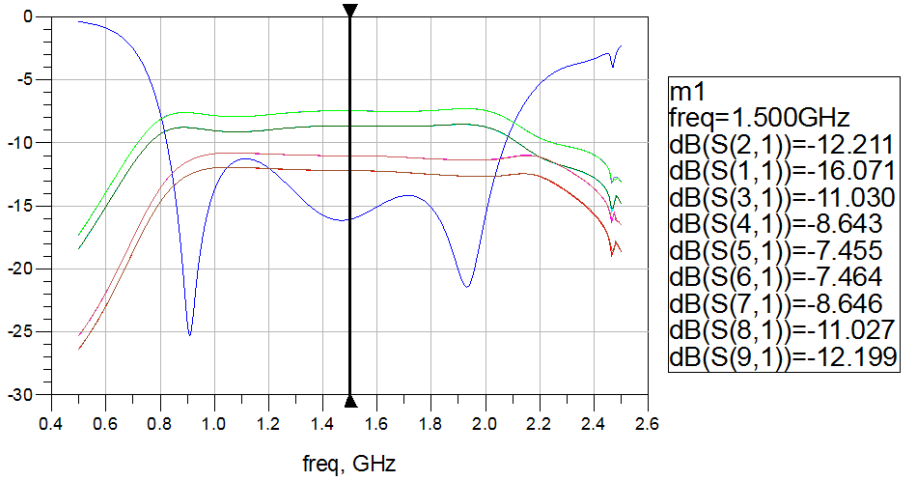

(b)

Fig 7. 15 Simulated S-parameters of the proposed feeding network with (a) equal output power; (b) unequal output power which follows the Taylor distribution for 20-dB side-lobe suppression.

When the proposed feeding network is connected with an antenna array, different kinds of power distribution at eight output terminations can be realised by controlling V_1~V_6. As an example, two different states of the feeding networks are investigated to provide equal and unequal feeding power for antenna arrays. When all the biasing voltages are set to be equal to 8V, the same amplitude (ideally -9 dB) can be found at each output port, as observed in Fig 7.15 (a). For the unequal excitation case, the target is to realise 20-dB side-lobe suppression when the feeding network is connected to an array. Therefore, the Taylor distribution for 20-dB side-lobe suppression is adopted to calculate the feeding power at each output port. To that end, the power weights at the eight output ports should be set at 1, 0.77, 0.46, and 0.36, from the centre of the array to the side.

Therefore, the target power levels at the eight-way power divider is set at -7.13 dB, -8.25 dB, -10.61 dB, and -11.57 dB, from the centre to side. By tuning V_1~V_6 to appropriate values ($V_1 = 22.8\,V$,

$V_2 = 4.4\,V, V_3 = 14.5\,V, V_4 = 9.6\,V, V_5 = 15.6\,V,$ and $V_1 = 8.2\,V$), unequal output power can be realised. Fig 7.15 (b) reveals that the output power at Port 2 (Port 9), Port 3 (Port 8), Port 4 (Port 7), and Port 5 (Port 6) are measured as -12.2 dB, -11.03 dB, -8.64 dB, and -7.46 dB, which are very close to the calculated values. It is also noted that in both equal power and unequal power cases, the return loss is better than 12 dB across the band range from 0.9 to 2.1 GHz. To verify the controllability of the tunable feeding network on antenna arrays, an eight-element array will be established and simulated together with the proposed feeding network, which will be elaborated on in the next section.

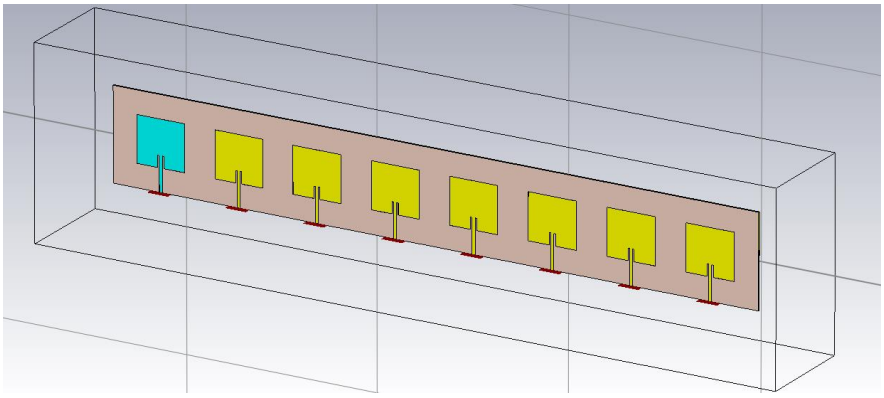

Fig 7. 16 Linear antenna array composed of eight elements.

7.4.2 Linear Antenna Array

To verify the controllability of antenna arrays of the proposed tunable feeding network, a linear antenna array which is composed of eight elements is built. Each element is adopted as a simple microstrip patch antenna, and the spacing between elements is set to be equal to half-wavelength, as shown in Fig 7.16. As displayed in Fig 7.17 (a), a single patch antenna is constructed with a length of L and a width of W based on a substrate with a dielectric constant of ε_r and height of h. To calculate the dimensions of a patch antenna, the following formulas are needed:

$$W = \frac{v_0}{2f}\sqrt{\frac{2}{\varepsilon_r + 1}} \tag{7.30}$$

$$L = \frac{1}{2f\sqrt{\varepsilon_e \varepsilon_0 \mu_0}} - 2\Delta L \tag{7.31}$$

where

$$\Delta L = 0.412\frac{(\varepsilon_e + 0.3)(W/h + 0.264)}{(\varepsilon_e - 0.258)(W/h + 0.8)}h \tag{7.32}$$

In Equations (7.30) – (7.32), ε_e refers to the effective dielectric constant of a microstrip patch which can be calculated using Equation (3.26) and v_0 and f represent the speed of light and resonant frequency, respectively. The resonant frequency in this design is set to be 1.5 GHz. An FR4 substrate with dielectric constant of 4.3 and thickness of 1.6 mm is adopted. After simulation and optimization is done in the full-wave simulation software of CST Microwave Studio, one can find the optimized dimensions of each element to be: $W = 50$ mm, $L = 47.3$ mm, and the optimal spacing between the two elements is 82 mm. The simulated S_{11} of each element is shown in Fig 7.17 (b). The displayed result here shows that the antenna element resonates at 1.5 GHz with about 2.5% bandwidth.

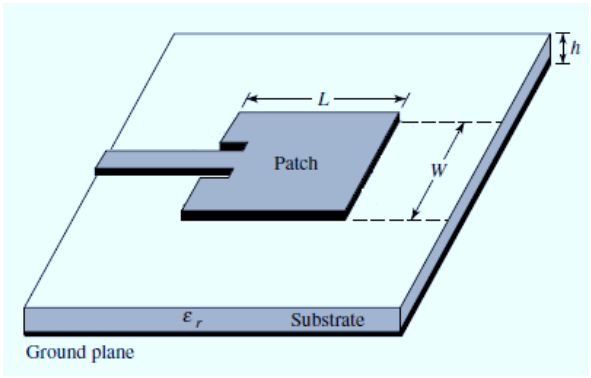

(a)

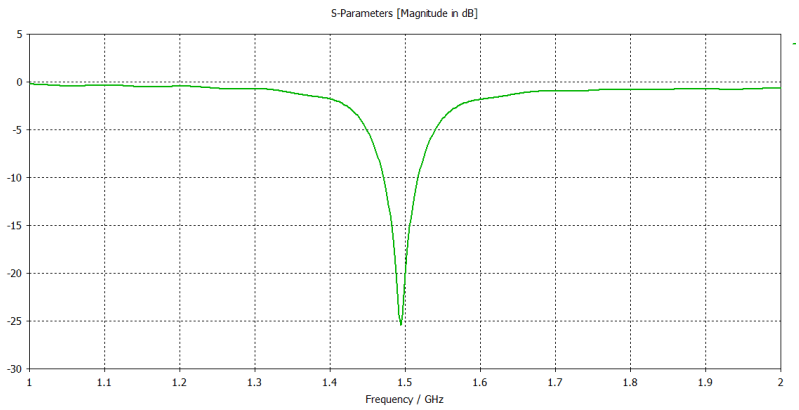

(b)

Fig 7. 17 (a) Layout and (b) $|S_{11}|$of single patch antenna element in the linear array.

7.3.3 Reconfigurable Radiation Pattern and Side-lobe Suppression

The side-lobe levels (SLLs) of antenna arrays are related to the spacing between elements and the feeding power for each element. Since it is difficult to change the spacing distance between elements, the only solution is to change the power distribution of feeding networks. When the power distribution follows certain rules, desired SLLs can be achieved. For example, there are

many types of power distribution that have been studied and applied in antenna arrays, such as Dolph-Chebyshev distribution, binomial distribution, Villeneuve distribution, Taylor distribution, etc. For different numbers of elements or different power weight, the SLLs are also varied. In this work, the Taylor distribution is adopted and used for SLL suppression. To achieve the objective of the 20-dB and 30-dB SLL of arrays, the power weight for each element should follow the distributions which are shown in Table II. In both cases, the spacing is equal to 0.68 λ_g.

Table 7. 2 Power weight for different SLLs

Power weight	Port 1	Port 2	Port 3	Port 4	Port 5	Port 6	Port 7	Port 8
No SLL	1	1	1	1	1	1	1	1
20-dB SLL	0.36	0.46	0.77	1	1	0.77	0.46	0.36
30-dB SLL	0.3	0.54	0.82	1	1	0.82	0.54	0.3

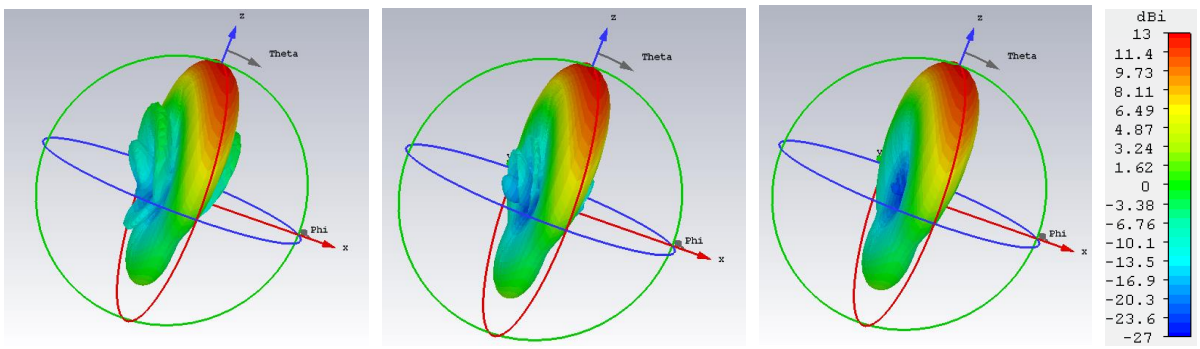

(a) (b) (c)

Fig 7. 18 3D radiation pattern for the linear array using different power distributions for (a) no SLL; (b) 20-dB SLL; and (c) 30-dB SLL.

To verify the objective of SLL suppression, the linear array shown in Fig 7.16 is fed with different power distributions. Ideal power sources are used in the EM environment of CST Microwave Studio. Firstly the feeding powers for eight elements are set to be identical. In this case, the SLL is relatively high without any suppression, as seen from the 3D radiation pattern displayed in Fig 7.18 (a). Then the power distributions of 20-dB and 30-dB SLLs are investigated, as shown in Figs 7.18 (b) and (c). It can be seen that the side-lobe levels in both cases are suppressed due to the unequal power distribution. This is clearer to see from Fig 7.19, where the E-plane radiation patterns ($\varphi = 90°$) for the three investigated cases are shown. The simulated SLLs are 13.5 dB, 21 dB, and 30.8 dB, respectively. These values are very close to the theoretical ones. Moreover, it is also found that the beamwidths of the main lobes are slightly changed. According to the antenna arrays theory,

a low SLL may lead to a wider main lobe beamwidth since more energy is concentrated in the central area.

After simulation of the ideal power sources is done, the co-simulation is required by connecting the proposed tunable feeding network with the linear antenna array. Only one source power is needed for Port 1 of the feeding network, while each output port of the feeding network is connected to each element of the array without changing the spacing distance between any two elements. This form of connection should follow the rules that Port 2 is connected with the first element, Port 3 is connected with the second one, and so on.

The S_{11} of the overall sub-system with a tunable feeding network with equal power division and a linear array is displayed in Fig 7.20. The bandwidth is about 5% which is close to the ideal case. Then, the unequal power for 20-dB SLL that is displayed in Fig 7.15 (b) is adopted to feed the array. In this case, the controlling voltages are set to $V_1 = 22.8\,V$, $V_2 = 4.4\,V$, $V_3 = 14.5\,V$, $V_4 = 9.6\,V$, $V_5 = 15.6\,V$, and $V_1 = 8.2\,V$. Fig 7.21 shows the comparison of the 3D radiation patterns between the full-wave simulation result using the proposed feeding network and ideal power sources.

It is clearly seen that two results agree with each other very well, which indicates that the proposed tunable feeding network is able to suppress the SLL from 13 dB to 23 dB. Moreover, the proposed tunable feeding network can tune the power distribution and SLL to any desired levels within the achievable range of power division ratio.

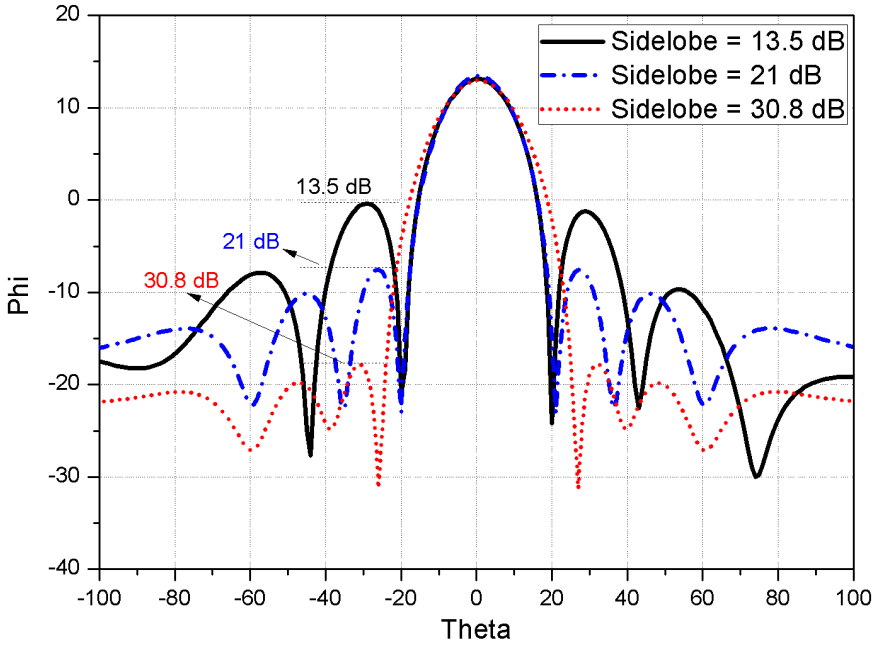

Fig 7. 19 E-plane radiation pattern for the investigated cases of different SLLs.

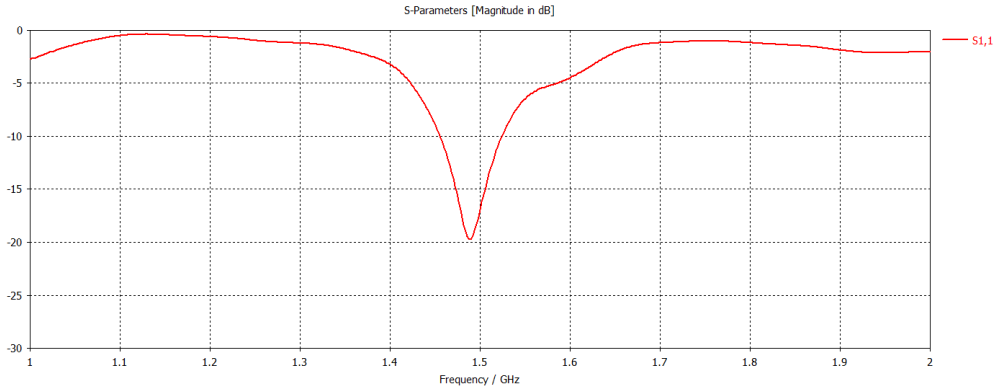

Fig 7. 20 S_{11} of the overall structure of the feeding network and linear array.

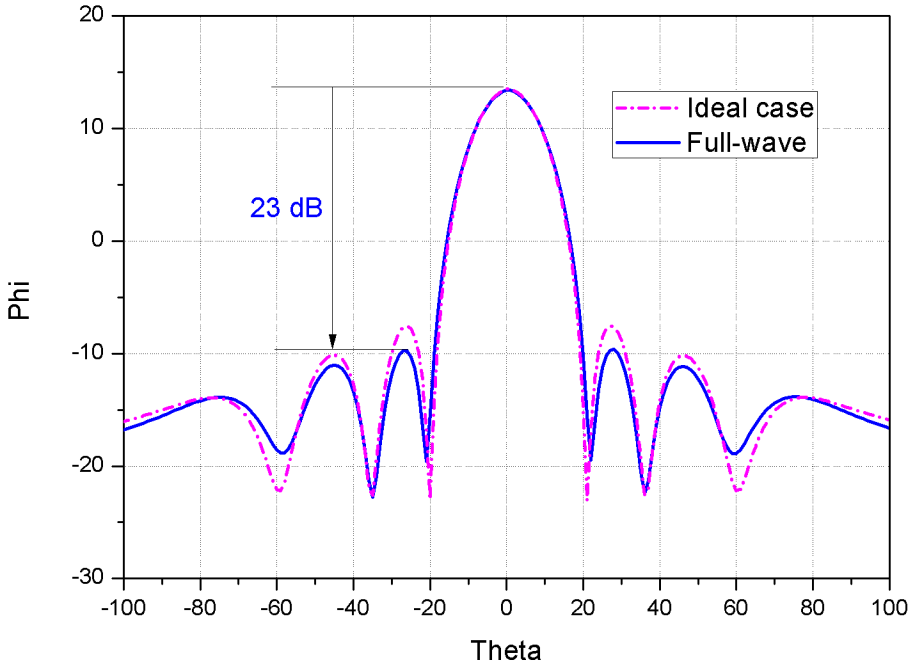

Fig 7. 21 Comparison of the 3D radiation patterns between the full-wave simulation result using the proposed feeding network and ideal power sources.

7.5 Tunable Feeding Network with Tunable Phase Shifters

The last section has presented a tunable feeding network which is connected to a linear antenna array for beam-forming purposes. The proposed structure managed to achieve arbitrary kinds of unequal power distributions that resulted in tuning the side-lobe level flexibly from 13 dB to more than 30 dB. In reality, it is also preferable that the beam direction is steerable. Combining the proposed tunable feeding network and tunable phase shifters with the linear antenna array, a steerable beam is realised and verified.

7.5.1 Configuration of the tunable feeding network for steerable beam

Based on the tunable feeding network presented in the last section, tunable phase shifters are cascaded with each output termination for beam steering to construct the beam-forming network in Fig 7.2. In this diagram, the tunable feeding network and antenna array are the same as the last section, and the eight tunable phase shifters presented previously in this chapter are cascaded between each output port of the network and corresponding array element.

As mentioned in Section 7.3, the proposed two-stage tunable phase shifter is able to achieve more than 360˚ (the full range) of phase shift, which is suitable and thus is adopted for the development of the tunable feeding network here. In this case, eight different voltage suppliers are required for controlling the tuning elements. Additionally, the differential phase interval for each antenna element is defined as ΔΦ, which means that the required differential phases for each element should be 0, ΔΦ, 2ΔΦ, …, 7ΔΦ. In this design, three different cases with 15˚, 30˚, and 45˚ are investigated. The required differential phases are listed in Table III.

Table 7. 3 Required ΔΦ at different output ports

ΔΦ	Output 1	Output 2	Output 3	Output 4	Output 5	Output 6	Output 7	Output 8
15˚	0˚	15˚	30˚	45˚	60˚	75˚	90˚	105˚
30˚	0˚	30˚	60˚	90˚	120˚	150˚	180˚	210˚
45˚	0˚	45˚	90˚	135˚	180˚	225˚	270˚	315˚

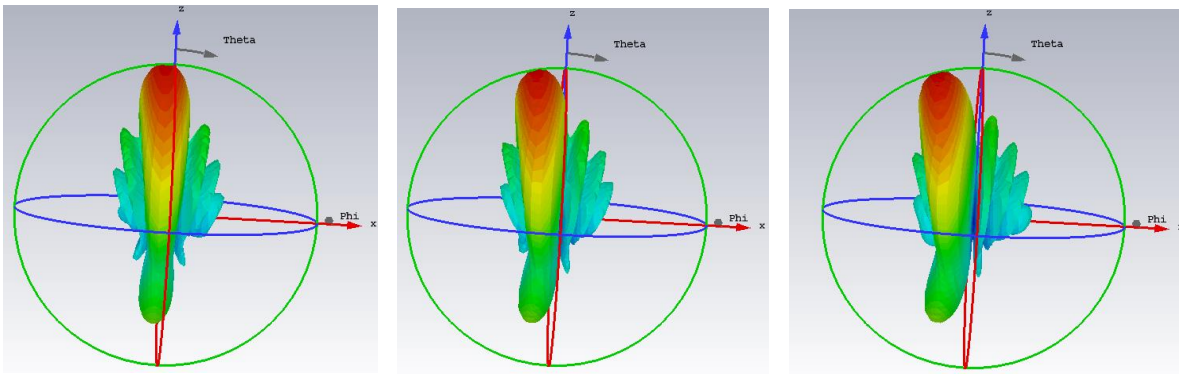

(a) (b) (c)

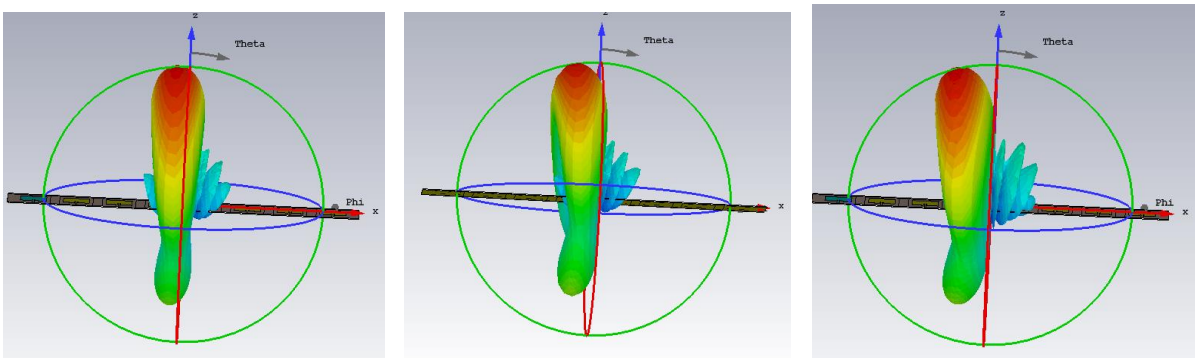

(d) (e) (f)

Fig 7. 22 3D radiation patterns for the tunable feeding network with equal power division and differential phase intervals of (a) 15˚; (b) 30˚; (c) 45˚; and 20-dB SLL and differential phase intervals of (d) 15˚; (e) 30˚; and (f) 45˚.

7.5.2 Steerable Beam with Side-lobe Suppression

After setting the differential phase for each phase shifter, co-simulation is done with the association of the eight-way tunable power divider (Fig 7.14), antenna array (Fig 7.16), and eight tunable phase shifters (introduced in Section 7.3). The function of the tunable power divider is to control the amplitude of output power at each output termination. In this simulation, two kinds of power distribution are used: equal power division and unequal power division of the 20-dB power distribution. The S-parameters of these two states of output signals are shown in Fig 7.15. On the other hand, phase shifters are tuned and endowed with specific values listed in Table III.

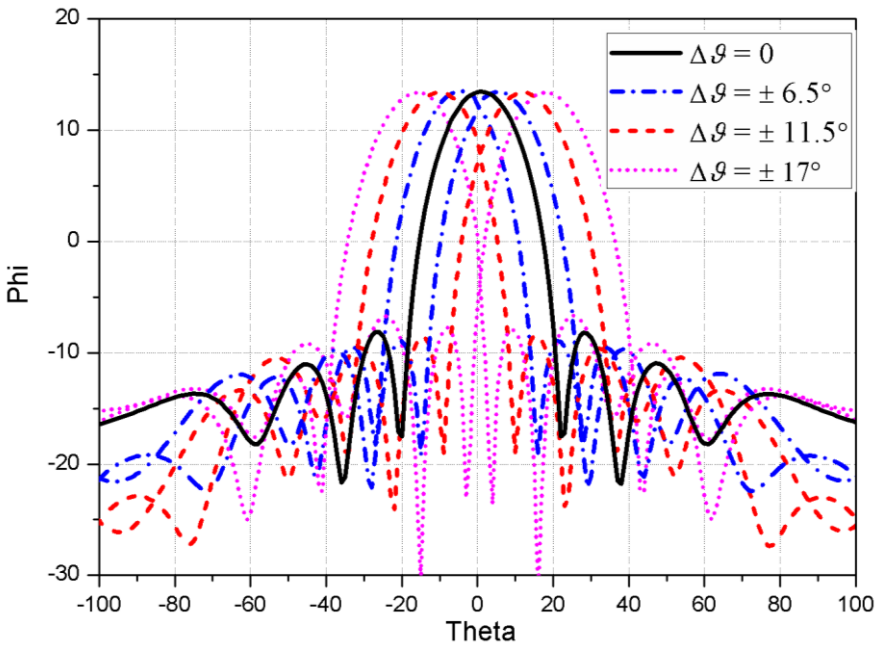

Fig 7. 23 E-field radiation pattern ($\varphi = 90°$) for 7 cases with differential phase intervals of 0˚, ±15˚, ±30˚ and ±45˚, with the realization of beam steering angles of 0, ±6.5˚, ±11.5, and ±17˚.

When the tunable feeding network is set to be equal power division and the differential phase ΔΦ is 15˚, the beam direction is tilted slightly (around 6.5˚ deviated away from z-axis) as shown in Fig 7.22 (a). When ΔΦ is increased to 30˚ and 45˚, the deviation angle is also increased to 11.5˚ and 17˚, as shown in Figs 7.22 (b) and (c). It is noted that the SLL is relatively high because no power distribution for SLL suppression is used. When the Taylor distribution for 20-dB SLL suppression (power weight is listed in Table II) is used to feed eight elements with differential phase intervals of

15˚, 30˚ and 45˚, great reduction of SLL suppression can be obtained as displayed in Figs 7.22 (d), (e) and (f).

Comparing Figs 7.22 (a) and (d), one can find that the SLL is suppressed as predicted in the last section. A similar phenomenon can be found in comparisons between Figs 7.22 (b) and (e), and Figs 7.22 (c) and (f). On the other hand, the steering angles for these three cases are also around 6.5˚, 11.5˚ and 17˚, which are the same as the equal power division cases without SLL suppression.

To display the SLL suppression more clearly, the in E-field radiation pattern is plotted in Fig 7.23. There are 7 states in total in Fig 7.23, for which the differential phase intervals are set to 0˚, ±15˚, ±30˚ and ±45˚, and the steering angles of the main beam are 0, ±6.5˚, ±11.5, and ±17˚, respectively. The side-lobe levels in all the investigated cases are around 21 dB, which is very close to the theoretical one.

7.5 Summary

In this chapter, tunable feeding networks for a reconfigurable array pattern have been proposed. Using the proposed two-way tunable power divider, an eight-way power divider with arbitrary amplitude of output power is realised and thus used as a tunable feeding network for antenna arrays. By connecting such a network with a linear array and tuning the output power to follow a certain kind of power distribution, it is possible to get the desired side-lobe levels for the array. In this design, the Taylor distribution for 20-dB SLL is adopted for verification of the concept. As a result, the SLL is suppressed from -13 dB to -21 dB.

To further achieve a steerable beam, tunable phase shifters have been designed and utilized in the feeding network. The proposed tunable phase shifter design is able to cover a full phase shifting range of 360˚ across a wide band range from 1 GHz to 2 GHz. After applying certain differential phases to each element of the array, the beam has been steered to 17˚ maximally. Besides, with the unequal power division for the Taylor distribution for 20-dB SLL, the side-lobe also can be suppressed with a steerable beam. These features indicate great application potential in the development of tunable feeding networks for antenna and phased arrays.

Chapter 8: Conclusions and Future Work

8.1 Conclusions

In modern society, microwave techniques are used in a variety of areas and microwave-based systems can be found everywhere in people's daily life. With the coming era of 5G, the connection between people and objects is becoming ever closer. Devices with a high-data rate, multiple functions and the controllability of objects are in demand. To realise these functions, microwave systems are the solution and thus have been focused on heavily. Overall performance and possible functions are determined by the composition of these systems, which involve microwave devices as such and their sub-systems. Though great efforts have been made to improve devices' capability and performance, huge drawbacks still exist with respect to issues like extensive losses, high cost, shortness of efficiency and flexibility, large circuit volumes, etc. Facing these problems and challenges, the innovation of new concept and design approaches as well as the development of high-performance devices and sub-systems has been the aim of this thesis, where a thorough study of tunable microwave components and sub-systems with multi-functional purposes for wideband applications has been provided. Notably, the main contributions of this thesis are:

1) Development of tunable microwave devices which can be controlled to realise multiple functions and become adapted to different microwave environments.
2) Proposal of new design approaches with multiple functions to reduce the number of devices used in building a system so that the volume and cost of systems are reduced.
3) Proposal, design, and verification of novel concepts of tunable devices with new functions that have never been investigated together with a miniaturized circuit size.
4) Construction of tunable beam-forming networks with a controllable power distribution and differential phase in feeding antenna arrays to get a steerable beam and reconfigurable pattern.

To achieve these targets, tunable microwave devices have been the main focus of this research project and several types of designs have been built and evaluated in Chapters 4, 5, 6, and 7. Chapter 4 discussed developing new types of tunable bandpass filters with both a high performance and miniaturized size. This included the tunability of the operating frequency range, bandwidth, and cut-off edge transmission zeros. Coupled-line structures with centre-loaded varactors were adopted for controlling bandwidth and cut-off transmission zeros.

Besides this aspect of flexibility, the sharp selectivity of the passband and upper-stopband harmonic suppression is also desired. To that end, a pair of varactor-ended short-circuit stubs was used to

control the position of a zero, which can be relocated from one side of the passband to another. The presented design was able to realise a maximum bandwidth tuning range from 55 MHz to more than 300 MHz, and a centre frequency shifting range from 0.52 GHz to 1.48 GHz. Apart from this improvement, the overall size of each design is smaller than 0.01 of the λ_g^2, which is extremely compact in size. All these merits exceed those in the existing state-of-the-art work in the literature reviewed. Last but not the least, based on the coupled-line structure, a compact design of a balanced tunable bandpass filter was proposed with a high suppression of common-mode signals.

Chapter 5 was devoted to the development of multi-functional power dividers, which include filtering power dividers, tunable power dividers, and a combination of both. Firstly, a kind of varactor-loaded three-line coupled structure was analysed with the result showing that this kind of structure is favourable as a design of a tunable power divider since the power division at its two sidelines can be varied by tuning the varactors loaded between the centreline and each sideline. In addition, the power division ratio is linked with the capacitance distribution of the structure, which is not related to the operating frequency. This means the power division ratio can be tuned across a wide frequency range, clearly a further improvement.

With the support of the three-line coupled structure, a tunable power divider was firstly built with loaded varactors. By controlling the biasing voltages, a tunable power division ratio from 1:1 to 3:1 working in the band range of 0.9 to 2.1 GHz has been achieved. To integrate the filtering characteristics with the proposed power divider, two kinds of stubs were shunted at the output ports. In the first case, a stepped-impedance stub was used to introduce two transmission zeros at the passband edges. In the second case, a pair of varactor-loaded coupled-line stubs was used to have a controllable passband.

The experimental result revealed that the proposed design is able to achieve a controllable filtering bandwidth from 48% to 71%, tunable centre frequency from 1.3 GHz to 1.48 GHz, sharp cut-off with transmission zeros, and upper-stopband harmonic suppressions up to more than 6 GHz. Though some work related to this topic has been done before, this research has achieved the first thorough study of tunable power dividers with power division and a controllable filtering response. Furthermore, a four-way filtering power divider was built. Compared with other existing designs, the proposed design has the widest bandwidth, sharpest cut-off selectivity and greatest upper-stopband suppression with excellent output matching and isolation.

Chapter 6 aimed to develop new functions in multi-port tunable microwave devices. In Chapter 5, power dividers with a tunable power division ratio have been realised. In Chapter 6, the tunability

of the power division ratio was applied in wideband balun and couplers, where tunable amplitude at output terminations can be obtained. A tunable balun with a wide tuning range of output power division across a wide band was presented and described. The utilized structure is based on a modified Marchand balun using multi-layer broadside-coupled structure. The proposed modification includes using a serially-connected varactor and resistor at the centre of the balun to achieve the required tunability in amplitude and stability in phase. The results showed that the power division can be tuned from 1:1 to 3.5:1 across the frequency range 1.2-2.8 GHz with a relatively stable differential phase of 180±9˚.

Similarly, a broadband quadrature coupler with a wide range of tunable coupling coefficients was presented. The device uses two sets of 45° coupled-line sections that are connected in a cross-shaped structure and loaded with two pairs of varactors. Based on a thorough analysis using the mixed-mode theory, a design procedure was given and a prototype was built and tested. The measured results indicated a full tuning range of coupling coefficients from 3 dB to 6 dB, 10 dB, 20 dB, and a non-coupling state.

On the other hand, in some cases, a differential phase is more critical in the design of microwave systems than the amplitude of signals. Therefore, this chapter also aimed to develop multi-port tunable devices with a constant amplitude and tunable differential phase. The first design was a phase-tuned power divider with reconfigurable in-phase and out-of-phase states. A novel concept, using a tunable phase shifting unit to approximate different lengths of transmission lines, was used. The concept was validated by theoretical analysis and, for further verifying the theory, followed by the construction and fabrication of a prototype to be tested. The measured results verify that the S-parameters under each of the states are desirable and the phase deviations of the phase difference between the two output ports for in-phase and out-phase states are satisfied. Using the same concept of the tunable phase shifting unit, a phase-tuned directional coupler was designed based on a modified branch-line coupler. Both simulation and experimentation were conducted to show a tunable differential phase is realised from 45˚ to 135˚ across a bandwidth of 20%. All these proposed design approaches are the first of their kind to be introduced in the literature.

Chapter 7 focused on the development of tunable feeding networks for the beam-forming function of antenna arrays. The goal was to achieve the tunability of the arrays' patterns in the aspects of beamwidth, side-lobe level, and beam directions. Instead of the traditional methods of adding PIN diodes or tuning elements on radiators, this work aimed to develop controllable feeding networks for antenna arrays. This kind of network is able to tune the power amplitude and phase at each

output port. To that end, a multi-port power divider with tunable power division and multiple tunable phase shifters are required.

For the multi-port power divider, the two-port tunable power divider which was presented in Chapter 5 is utilized to compose an eight-way power divider. The proposed eight-way power divider was able to allocate unequal power at each output port to follow a certain kind of power distribution, which can affect the connected arrays and change the side-lobe level. On the other hand, to realise arbitrary differential phases between any two elements of an antenna array, tunable phase shifters were designed. The proposed design was based on a directional coupler consisting of two coupled-line sections connected with two transmission lines. The proposed two-stage phase shifter was found to achieve a tunable differential phase range of more than 360˚ which covers the full range of the shifting phase. Notably, both the tunable eight-way power divider and the tunable phase shifter can operate at a band range from 1 to 2 GHz, which indicates wideband application potential for both designs.

Finally, a linear antenna array using eight patch antennas with equal spacing was adopted to verify the controllability of the proposed beam-forming network. The full-wave simulations revealed that by tuning the supplying voltages on the varactors, the feeding power to each element is tuned so that the array pattern can be reshaped. The side-lobe level can be greatly reduced from -13 dB to more than -23 dB. Moreover, the beam direction can be steered from 0˚ to 17˚. It is notable that the proposed beam-forming network is able to operate with wideband antenna arrays with 60% of bandwidth, which is quite favourable in wideband microwave systems.

8.2 Future Work

Although promising results have been reported in this thesis, there is still the potential for this line of research to be further improved. Therefore, the following work can be done in future:

1) Building the digital controlling systems of supplying voltages using software programming on chips in order to replace the analogue tuning with a digital tuning function.
2) Implementing the proposed multi-functional microwave components with other circuits to construct sub-systems for wideband applications, such as beam-forming networks, measurement systems, and RF transceivers.
3) Designing wideband antenna arrays with a bandwidth of more than 60%, and then applying the proposed tunable feeding network to steer the array pattern in experimentation.

References

[1] K. Chang, RF and Microwave Wireless Systems: *John Wiley & Sons*, Inc., New York, 2000.

[2] C. A. Balanis, in Antenna Theory: Analysis and Design, 3rd edition: *Wiley*, 2005.

[3] R. J. Cameron, C. M. Kudsia, and R. R. Mansour. Microwave Filters for Communication Systems: Fundamentals, Design and Applications. *Wiley*, 2007.

[4] J. S. Hong and M. J. Lancaster, "Microstrip Filters for RF/Microwave Applications," *John Wiley & Sons, Inc.*, New York, 2001.

[5] L. Zhu, S. Sun, and W. Menzel, "Ultra-wide (UWB) bandpass filter using multiple-mode resonator," *IEEE Microw. Wireless Compon. Lett*., vol. 15, no. 11, pp. 796–798, Nov. 2005.

[6] H. Zhu, and A. Abbosh, "Single- and dual-band bandpass filters using coupled stepped-impedance resonators with embedded coupled-lines", *IEEE Microw. Wireless Compon. Lett.*, vol. 26, no. 9, pp. 675-677, Sep. 2016.

[7] H. Zhu and Q. X. Chu, "Compact ultra-wideband (UWB) bandpass filter using dual-stub-loaded resonator (DSLR)", *IEEE Microw. Wireless Compon. Lett.*, vol. 23, no. 10, pp. 527-529, Oct. 2013.

[8] H. Zhu and Q. X. Chu, "Ultra-wideband bandpass filter with a notch-band using stub-loaded ring resonator", *IEEE Microw. Wireless Compon. Lett*., vol. 23, no. 7, pp. 309-311, Jul. 2013.

[9] H. Zhu, S. W. Wong, S. Wen and Q. X. Chu, "An ultra-wideband (UWB) bandpass filter with microstrip-to-CPW transition and a notch-band", *IEEE MTT-S International Wireless Symposium (IWS)*, Beijing, 2013.

[10] H. Zhu, Q. X. Chu, and X. K. Tian, "A UWB bandpass filter using slotline ring resonator with a notched band", International Conference on Microwave and Millimeter Wave Technology (ICMMT), Vol. 5, pp. 1777-1780, 2012.

[11] H. Zhu, E. Ahmed, and A. Abbosh, "Compact dual-band bandpass filters using multi-mode resonator of short-ended and open-ended coupled lines", Proceedings in *Asia-Pacific Microwave Conference (APMC)*, Nanjing, China, 2015.

[12] D. M. Pozar, Microwave Engineering: *Wiley*, 1997.

[13] E. Wilkinson, "An N-way hybrid power divider," *IRE Trans. Microw. Theory Tech*., vol. MTT-8, no. 1, pp. 116–118, Jan. 1960.

[14] U. H. Gysel, "A new N-way power divider/combiner suitable for high power applications," in *IEEE MTT-S Int. Microw. Symp. Dig*., May 1975, vol. 75, pp. 116–118.

[15] S. W. Wong, and L. Zhu, "Ultra-wideband power divider with good inband splitting and isolation performances," *IEEE Microw. Wireless Compon. Lett*., vol. 18, no. 8, pp. 518-520, Aug. 2008.

[16] H. Zhu, and A. Abbosh, "Compact ultra-wideband in-phase power divider using three-line coupled structure", *IEEE Antennas and Propagation Society International Symposium (APSURSI)*, 2014.

[17] L. Guo, A. Abbosh and H. Zhu, "Ultra-wideband in-phase power divider using stepped-impedance three-line coupled structure and microstrip-to-slotline transitions", *Electron. Lett.*, vol.50, no. 5, pp. 383–384, Feb. 2014.

[18] I. Sakagami, X. Wang, K. Takahashi, and S. Okamura, "Generalized two-way two-section dual-band Wilkinson power divider with two absorption resistors and its miniaturization," *IEEE Trans. Microw. Theory Tech*., vol. 59, no. 11, pp. 2833–2847, Nov. 2011.

[19] F. Lin, Q. X. Chu, Z. Gong, and Z. Lin, "Compact broadband Gysel power divider with arbitrary power-dividing ratio using microstrip/slotline phase inverter," *IEEE Trans. Microw. Theory Techn.*, vol. 60, no. 5, pp. 1226–1234, May 2012.

[20] A. M. Abbosh, "A compact UWB three-way power divider," *IEEE Microw. Wireless Compon. Lett.*, vol. 17, no. 8, pp. 598–600, Aug. 2007.

[21] H. Zhu, A. Abbosh and L. Guo, "Ultra-wideband unequal in-phase power divider using three-line coupled structure", Electron. Lett., vol.50, no. 17, pp. 1081–1082, Jul. 2014.

[22] H. Zhu, and A. Abbosh, "Directional coupler with two octaves band and high directivity using stepped-impedance coupled structure", Proceedings in *Asia-Pacific Microwave Conference (APMC)*, Nanjing, China, 2015.

[23] H. Zhu, Y. Wang, and A. Abbosh, "Broadband microwave crossover using parallel coupled microstrip lines and short-ended stubs", IET Microw. Antennas Prop., vol. 9, no. 1, pp. 79–85, 2015.

[24] A. Abbosh and M. Bialkowski, "Design of compact directional couplers for UWB applications," *IEEE Trans. Microw. Theory Tech*., vol. 55, no. 1, pp. 189–194, Jan. 2007.

[25] J. -L. Li, S. -W. Qu and Q. Xue, "Microstrip directional coupler with flat coupling and high isolation", *Electron. Lett.*, vol. 43, no. 4, pp. 228-229, Feb. 2007.

[26] S. Lee and Y. Lee, "An inductor-loaded microstrip directional coupler for directivity enhancement," *IEEE Microw. Wireless Compon. Lett*.,vol. 19, no. 6, pp. 362–364, Jun. 2009.

[27] Y. Wu, W. Sun, S.-W. Leung, Y. Diao, K.-H. Chan, and Y.-M. Siu, "Single-layer microstrip high-directivity coupled-line coupler with tight coupling," *IEEE Trans. Microw. Theory Techn.*, vol. 61, no. 2, pp. 746–753, Feb. 2013.

[28] S. Gruszczynski and K. Wincza, "Generalized methods for the design of quasi-ideal symmetric and asymmetric coupled-line sections and directional couplers," *IEEE Trans. Microw. Theory Tech.*, vol. 59, no. 7, pp. 1709–1718, Jul. 2011.

[29] Y. Guo, Z. Zhang, and L. Ong, "Improved wideband Schiffman phase shifter," *IEEE Trans. Microw. Theory Tech.*, vol. 54, no. 3, pp. 1196-1200, Mar. 2006.

[30] A. Abbosh, "Ultra-wideband phase shifter," *IEEE Trans. Microw. Theory Tech*., vol. 55, no. 9, pp. 1935-1941, Sep. 2007.

[31] L. Guo, H. Zhu, and A. Abbosh, "Planar UWB phase shifter using parallel coupled lines combined with short-ended stubs and impedance transformer," Proceeding in *Asia-Pacific Microwave Conference (APMC)*, Nanjing, China, 2015.

[32] A. Abbosh, "Compact tunable low-pass filter using variable mode impedance of coupled structure," *IET Microw. Antennas Propag.*, 2012, 6, (12), pp. 1306–1310.

[33] C. Kim, K. Chang, "Ring resonator bandpass filter with switchable bandwidth using stepped-impedance stubs," *IEEE Trans. Microw. Theory Tech.*, 2010, 58, (12), pp. 3936–3944.

[34] L. Athukorala, D. Budimir, "Open-loop tunable resonators and filters with constant bandwidth," *IET Microw. Antennas Propag.*, 2013, 7, (6), pp. 800–806.

[35] X. Luo, S. Sun, R. Staszewski, "Tunable bandpass filter with two adjustable transmission poles and compensable coupling', *IEEE Trans. Microw. Theory Tech.*, 2014, 62, (9), pp. 2003–2013.

[36] Y. Cho, G. Rebeiz, "Two- and four-pole tunable 0.7–1.1-GHz bandpass-to-bandstop filters with bandwidth control," *IEEE Trans. Microw. Theory Tech.*, 2014, 62, (3), pp. 457-463

[37] Y. –H. Cho and G. M. Rebeiz, "Tunable 4-Pole Noncontiguous 0.7– 2.1-GHz Bandpass Filters Based on Dual Zero-Value Couplings," *IEEE Trans. Microw. Theory Tech*., vol. 63, no. 5, pp. 1579–1586, May 2015.

[38] P. W. Wong and I. C. Hunter, "Parallel-coupled switched delay line (SDL) reconfigurable microwave filter," in IEEE MTT-S Int. Microwave Symp. Dig., June 2009, pp. 513–516

[39] W. Tu, "Compact low-loss reconfigurable bandpass filter with switchable bandwidth," *IEEE Microw. Wireless Components Lett*., 2010, 20, (4), pp. 208-210

[40] C. S. Tsai and G. Qiu, "Wideband microwave filters using ferromagnetic resonance tuning in flip-chip YIG-GaAs layer structures," *IEEE Trans. Magn.*, vol. 45, no. 2, pp. 656–660, Feb. 2009.

[41] A. Tombak, J. P. Maria, F. T. Ayguavives, J. Zhang, G. T. Stauf, A. Kingon and A. Mortazawi., "Voltage-controlled RF filters employing thin-film barium strontium-titanate

tunable capacitors," *IEEE Trans. Microwave Theory & Tech*., vol. 51, no. 2, pp. 462–467, Feb. 2003.

[42] S. Park, M. A. El-Tanani, I. Reines, and G. M. Rebeiz, "Low-loss 4-6 GHz tunable filter with 3-bit high-Q orthogonal bias RF-MEMS capacitance network," *IEEE Trans. Microwave Theory & Tech.*, vol. 56, no. 10, pp. 2348–2388, Oct. 2008.

[43] X. Huang, Q. Feng, Q. Xiang, "Bandpass filter with tunable bandwidth using quadruple-mode stub-loaded resonator," *IEEE Microw. Wireless Components Lett*., 2012, 22, (4), pp. 176-178

[44] H. Tsai, N. Chen, S. Jeng, "Reconfigurable bandpass filter with separately relocatable passband edge," *IEEE Microw. Wireless Components Lett.*, 2012, 22, (11), pp. 559-561

[45] A. Lacorte Caniato Serrano, F. Salete Correra, T. Vuong, and P. Ferrari, "Synthesis methodology applied to a tunable patch filter with independent frequency and bandwidth Control," *IEEE Trans. Microw. Theory Tech.*, 2012, 60, (3), pp. 484-493

[46] A. Miller, J.-S. Hong, "Wideband bandpass filter with reconfigurable bandwidth," *IEEE Micro. Wireless Compon. Lett*., vol. 20, no.1, pp. 28-30, Jan.2010.

[47] C. -W. Tang, C. -T. Tseng and S. -C. Chang, "A tunable bandpass filter with modified parallel-coupled line," *IEEE Micro. Wireless Compon. Lett*., vol. 23, no. 4, pp. 190-192, Apr.2013.

[48] C. -W. Tang, C. -T. Tseng, and S. -C. Chang, "Design of the compact tunable filter with modified coupled lines," *IEEE Trans. Compon. Packag. Manuf. Technol*., vol. 4, no. 11, pp. 1815-1821, Nov. 2014.

[49] P. W. Wong, and I.C. Hunter, "Electronically Reconfigurable Microwave Bandpass Filter," *IEEE Trans. Microw. Theory Tech*., vol. 57, no. 12, pp. 3070–3079, Jan. 2009.

[50] Y. Chiou and G. M. Rebeiz, "A tunable three-pole 1.5–2.2-GHz bandpass filter with bandwidth and transmission zero control," *IEEE Trans. Microw. Theory Techn.*, vol.59, no. 11, pp. 2872-2878, Nov. 2011.

[51] Y. Chiou and G. M. Rebeiz, "Tunable 1.55–2.1 GHz 4-pole elliptic bandpass filter with bandwidth control and rejection for wireless systems," *IEEE Trans. Microw. Theory Techn.*, vol. 61, no.1, pp. 17–124, Jan. 2013.

[52] J. Mao, W. Choi, K. Tam, W. Q. Che and Q. Xue, "Tunable bandpass filter design based on external quality factor tuning and multiple mode resonators for wideband applications," *IEEE Trans. Microw Theory Tech*., vol. 61, no. 7, pp. 2574-2584, Jul. 2013.

[53] H. Tsai, N. Chen, and S. Jeng, "Center frequency and bandwidth controllable microstrip bandpass filter design using loop-shaped dual-mode resonator," *IEEE Trans. Microw. Theory Techn.*, vol. 61, no. 10, pp. 3590-3600 , Oct. 2013.

[54] W. Tang and J. Hong, "Varactor-tuned dual-mode bandpass filters," *IEEE Trans. Microw. Theory Techn.*, vol.58, no. 8, pp. 2213-2219, Aug. 2010.

[55] J. Long, C. Li, W. Cui, J. Huangfu and L. Ran, "A tunable microstrip bandpass filter with two independently adjustable transmission zeros," *IEEE Micro. Wireless Compon. Lett.*, vol. 21, no.2, pp. 74-76, Feb.2011.

[56] H. Tsai, B. Huang and S. Jeng, "A Reconfigurable bandpass filter based on a varactor-perturbed, T-shaped dual-mode resonator," *IEEE Micro. Wireless Compon. Lett*., 2014.

[57] A. -L. Perrier, O. Exshaw, J. -M. Duchamp, and P. Ferrari, "A semi-lumped miniaturized spurious less frequency tunable three-port divider\combiner with 20 dB isolation between output ports," in *IEEE MTT-S Int. Microwave Symp. Dig*., pp. 1714-1717, 2006.

[58] L. Gao, X.Y. Zhang, and Q. Xue, "Compact Tunable Filtering Power Divider With Constant Absolute Bandwidth," *IEEE Trans. on Microw. Theory Tech.*, vol. 63, no. 10, Oct. 2015.

[59] C. F. Chen, C.-Y. Lin, B.-H. Tseng, and S.-F. Chang, "Compact microstrip electronically tunable power divider with Chebyshev bandpass response," in *Proc. Asia–Pacific Microw. Conf.*, Nov. 2014, pp. 1291–1293.

[60] P. –L. Chi, and T. Yang, "A 1.3-2.08 GHz filtering power divider with bandwidth control and high in-band isolation", *IEEE Microw. Wireless. Compon. Lett.*, vol. 23, no. 6, pp. 7–9, Jun. 2016.

[61] A. Abbosh and L. Guo, "Three-way signal divider with tunable ratio for adaptive transmitting antenna arrays," *IET Mirow. Antennas Propag.*, vol. 6, no. 12, pp. 1318-1324, 2012.

[62] E. Lourandakis, R. Weigel, H. Mextorf and R. Knoechel, "Circuit Agility," *IEEE Microwave Magazine*, pp. 111–121, Jan. 2012.

[63] E. A. Fardin, A. S. Holland, and K. Ghorbani, "Electronically tunable lumped element 90 hybrid coupler," *Electron. Lett*., vol. 42, no. 6, pp. 353–355, Mar. 2006.

[64] E. E. Djoumessi, E. Marsan, C. Caloz, M. Chaker, and K. Wu, "Varactor-tuned dual-band quadrature hybrid coupler," *IEEE Microw. Wireless Compon. Lett*., vol. 16, no. 11, pp. 603–605, Nov. 2006.

[65] H. Mextorf, T. Lehmann, and R. Knoechel, "Systematic design of reconfigurable quadrature directional couplers," in *IEEE MTT-S Int. Microw. Symp. Dig*., Jun. 2009, pp. 1009–1012.

[66] J. Sun, C. Li, Y. Geng, and P. Wang, "A highly reconfigurable low-power CMOS directional coupler," *IEEE Trans. Microw. Theory Techn.*, vol. 60, no. 9, pp. 2815–2822, Sep. 2012.

[67] O. D. Gurbuz, and G. M. Rebeiz, "A 1.6–2.3-GHz RF MEMS reconfigurable quadrature coupler and its application to a 360 reflective-type phase shifter," *IEEE Trans. Microw. Theory Tech.*, vol. 63, no. 2, pp. 414– 421, 2015.

[68] H. Zhu, Y. Wang, and A. Abbosh, "Compact tunable crossover with wide tuning range using coupled lines", Proceedings of *Asia-Pacific Microwave Conference (APMC)*, Sendai, Japan, 2014.

[69] M. A. Y. Abdalla, K. Phang, and G. V. Eleftheriades, "A compact highly reconfigurable COMS MMIC directional coupler," *IEEE Trans. Microw. Theory Techn.*, vol. 56, no. 2, pp. 305–319, Feb. 2008.

[70] L. K. Yeung, "A compact directional coupler with tunable coupling ratio using coupled-line sections", in *Proc. Asia–Pacific Microw. Conf.*, Dec. 2011, vol. 3, pp. 1730–1733.

[71] K. M. Cheng and S. Yeung, "A novel rat-race coupler with tunable power dividing ratio, ideal port isolation, and return loss performance," *IEEE Trans. Microw. Theory Techn.*, vol. 61, no. 1, pp. 55–60, Jan. 2013.

[72] K. M. Cheng and M. J. Chik, "A frequency-compensated rat-race coupler with wide bandwidth and tunable power dividing ratio," *IEEE Trans. Microw. Theory Tech.*, vol. 61, no. 8, pp. 2841–2847, Aug. 2013.

[73] S. Y. Zheng, W. S. Chan, and Y. S. Wong, "Reconfigurable RF quadrature patch hybrid coupler," *IEEE Trans. Ind. Electron.*, vol. 60, no. 8, pp. 3349–3359, Aug. 2013.

[74] U. Shah, M. Sterner, and J. Oberhammer, "High-directivity MEMS tunable directional couplers for 10–18-GHz broadband applications," *IEEE Trans. Microw. Theory Tech.*, vol. 61, no. 9, pp. 3236– 3246, 2013.

[75] M. Zhou, J. Shao, B. Arigong, H. Ren, R. Zhou, and H. Zhang, "A varactor based 90 directional coupler with tunable coupling ratios and reconfigurable responses," *IEEE Trans. Microw. Theory Tech.*, vol. 62, no. 3, pp. 416–421, Mar. 2014

[76] R. N. Hardin, E. J. Downey, and J. Munushian, "Electronically variable phase shifter utilizing variable capacitance diodes," *Proc. IRE*, vol. 48, pp. 944–945, May 1960.

[77] N. C. Karmakar and M. E. Bialkowski, "An L-band 90 hybrid coupled phase shifter using UHF band p-i-n diodes," *Microwave Opt. Technol. Lett.*, vol. 21, no. 1, pp. 51–54, Apr. 1999.

[78] F. Ellinger, R. Vogt, and W. Bachtold, "Compact reflective-type phaseshifter MMIC for C-band using a lumped-element coupler," *IEEE Trans. Microwave Theory Tech.*, vol. 49, pp. 913–917, May 2001.

[79] D. Kim, Y. Choi, M. Allen, J. Kenney, and D. Kiesling, “A wideband reflection-type phase shifter at S-band using BST coated substrate,” *IEEE Trans. Microw. Theory Tech*., vol. 50, no. 12, pp. 2903–2909, Dec. 2002.

[80] K. O. Sun, H. J. Kim, C. C. Yen, and D. Weide, “A scalable reflection type phase shifter with large phase variation,” *IEEE Microw. Wireless Compon. Lett.*, vol. 15, no. 10, pp. 647–648, Oct. 2005.

[81] C. Lin, S. Chang, and W. Hsiao, “A full-360 reflection-type phase shifter with constant insertion loss,” *IEEE Microw. Wireless Compon. Lett*, vol. 18, no. 2, pp. 106–108, Feb. 2008.

[82] R. J. Mailloux, Phased Array Antenna Handbook, 2nd Edition. *Artech House*, Boston, MA, 2005.

[83] J. Cha, Y. Kuga, A. Ishimaru, and S. Lee, "A 20 GHz Steerable Array Antenna Using 3-bit Dielectric Slab Phase Shifter on a Coplanar Waveguide", *IEEE Transactions on Antennas and Propagation*, Vol. 55, No. 2, pp. 290-297, February 2007.

[84] Y. Y. Bai, S. Q. Xiao, M. C. Tang, Z. F. Ding, and B. Z. Wang, "Wide-Angle Scanning Phased Array With Pattern Reconfigurable Elements," *IEEE Transactions on Antennas and Propagation*, vol. 59, pp. 4071-4076, Nov 2011.

[85] B. Babakhani, etc, “A Frequency Agile Microstrip Patch Phased Array Antenna with Polarization Reconfiguration," *IEEE Transactions on Antennas and Propagation*, vol. 64, pp. 43316-4327, Oct, 2016.

[86] S. Karimkashi and A. A. Kishk, “Focused microstrip array antenna using a Dolph-Chebyshev near-field design,” *IEEE Trans. Antennas propag*., vol. 57, no. 12, Dec. 2009, pp. 3813-3820.

[87] K. Hashimoto, J. Hirokawa, and M. Ando, “A post-wall waveguide center-feed parallel plate slot array antenna in the millimeter-wave band,” *IEEE Trans. Antennas Propag*., vol. 58, no. 11, pp. 3532-3538, Nov. 2010.

[88] B. Youzkatli, T. Djerafi, and K. Wu, "Three-dimensional architecture of substrate integrated waveguide feeder for Fermi tapered slot antenna array applications," *IEEE Trans. Antennas and Propagation*, vol. 60, pp. 4610-4618, Oct. 2012.

[89] D. -Y. Kim and S. Nam, “Excitation control method for a low sidelobe SIW series slot array antenna with 45˚ linear polarization,” *IEEE Trans. Antennas and Propag.*, vol. 61, no. 11, pp. 5807-5812, Nov, 2013.

[90] G. L. Huang, S. G. Zhou, T. H. Chio, H. T. Hui, and T. S. Yeo, “A low profile and low sidelobe wideband slot antenna array feb by an amplitude-tapering waveguide feed-network,” *IEEE Trans. Antennas Propag*., vol. 63, no. 1, pp. 419–423, 2015.

[91] T. –P. Kuo; T. –G. Ma, “Wideband operation of amplifying array using tunable phase shifters", *IEEE Antennas and Wireless Propagation Letters*, page(s): 995 - 998 Vol. 10, 2011

[92] Y. S. Jeong, and T. W. Kim, "Design and analysis of swapped port coupler and its application in a miniaturized Butler matrix", *IEEE Trans. Microw. Theory Techn.*, vol. 58, no. 4, pp.764 -770 2010

[93] A. A. M. Ali , N. J. G. Fonseca , F. Coccetti and H. Aubert, "Design and implementation of two-layer compact wideband Butler matrices in SIW technology for Ku-band applications", *IEEE Trans. Antennas Propag.*, vol. 59, no. 2, pp.503 -512 2011

[94] K. Wincza, S. Gruszczynski and K. Sachse "Broadband planar fully integrated 8×8 Butler matrix using coupled-linedirectional couplers", *IEEE Trans. Microw. Theory Techn.*, vol. 59, no. 10, pp.2441 -2446, Oct. 2011

[95] E. Gandini , M. Ettorre , R. Sauleau and A. Grbic, “A lumped-element unit cell for beam-formingnetworks and its application to a miniaturized Butler matrix”, *IEEE Trans. Microw. Theory Tech.*, vol. 61, no. 4, pp.1477 -1487, Apr. 2013

[96] J. -Y. Zou, C. H. Wu and T. -G. Ma, "Heterogeneous integrated beam-switching/retro-directive array using synthesized transmission lines", *IEEE Trans. Microw. Theory Techn.*, vol. 61, no. 8, pp.3128 -3139, Aug. 2013

[97] J. R. James, G. D. Evans, and A. Fray, “Beam scanning microstrip arrays using diodes,” *IEEE Trans. Antennas Propag*., vol. 140, no. 1, pp. 43–51, Feb. 1993.

[98] S. Lim, C. Carloz, and T. Itoh, “Electronically scanned composite right/left handed microstrip leaky-wave antenna,” *IEEE Microw. Wireless Compon. Lett.*, vol. 14, no. 6, pp. 277–279, Jun. 2004.

[99] Y. J. Guo, X. Huang, and V. Dyadyuk, “A hybrid adaptive antenna array for long-range mm-wave communications,” *IEEE Antennas and Propagation Magazine,* vol. 54 (2), pp. 271–282, April 2012.

[100] C. Ding, Y. J. Guo, P. Y. Qin, and Y. T. Yang, “A compact microstrip phase shifter employing reconfigurable defected mcrostrip structure (RDMS) for phased array antennas,” *IEEE Trans. Antennas Propag.*, vol. 63, no. 5, pp. 1985-1996, May 2015.

[101] C. -H. Lai, C. -Y. Shiau, and T.-G. Ma, "Tri-mode heterogeneous integrated beam-switching/Van Atta/phase-conjugating array using synthesized transmission lines," *IEEE Trans. Microw. Theory Techn.*, vol. 62, no. 9, pp. 2180-2192, Sep. 2014.

[102] E. O. Hammerstad, “Equations for Microstrip Circuit Design,” *Proceedings of the 5th European Microwave Conference,* pp. 268-272, 1975.

[103] T. C. Edwards, *Foundations of Interconnect and Microstrip Design*, 3rd ed. West Sussex, England: John Wiley & Sons Ltd. pp. 83-112, 2000.

[104] A. Abbosh, "Analytical closed-form solutions for different configurations of parallel-coupled microstrip lines," *IET Microw. Antennas Propa.*, vol. 3, no. 1, pp. 137-147, 2009.

[105] A. M. Abbosh, "Design of ultra-wideband three-way arbitrary power dividers", *IEEE Trans. Microw Tech.*, vol. 56, no. 1, pp. 194-201, Jan. 2008.

[106] H. Zhu, Q. X. Chu and X. K. Tian, "Compact UWB Bandpass Filter Using Folded-T-Shaped Resonator With a Notch-Band", Journal of Electromagnetic Waves and Applications, Vol. 26, No. 10, pp. 1366–1373, July 2012

[107] X. K. Tian, Q. X. Chu, H. Zhu, and X. H. Wu, "A UWB bandpass filter with wide stopband performance using cross-shaped coupled lines*", International Conference on Microwave and Millimeter Wave Technology (ICMMT),* Vol. 5, pp. 1777-1780, 2012.

[108] H. Zhu, and Q. X. Chu, "Ultra-wideband (UWB) bandpass filter with sharp selectivity and wide upper stopband", *IEEE International Conference on Ultra-Wideband*, pp.103-105, 2012.

[109] J. Ni, J. S. Hong, "Varactor-tuned microstrip bandpass filters with different passband characteristics', *IET Microw. Antennas Propag.*, 2014, **8**, (6), pp. 415–422

[110] "Skyworks SMV datasheets", Skyworks solutions, sunnyvale, CA, 2011.

[111] Sánchez-Renedo, M., Gómez-García, R., Alonso, J. I., and Briso-Rodríguez, C.: 'Tunable combline filter with continuous control of center frequency and bandwidth', *IEEE Trans. Microw. Theory Tech.*, 2005, 53, (1), pp. 191–199

[112] Wang, X., Cho, Y., and Yun, S.: 'A tunable combline bandpass filter loaded with series resonator', *IEEE Trans. Microw. Theory Tech.*, 2012, 60, (6), pp. 1569–1576

[113] Sun. J., Kaneda, N., Baeyens, Y., Itoh, T., and Chen, Y.: 'Multilayer planar tunable filter with very wide tuning bandwidth', *IEEE Trans. Microw. Theory Tech.*, 2011, 59, (11), pp. 2864–2871

[114] Long, J., Li, C., Cui, w., Huangfu, J., and Ran, L.: 'A tunable microstrip bandpass filter with two independently adjustable transmission zeros', *IEEE Microw. Wirel. Compon. Lett.*, 2011, 21, (2), pp. 74–76

[115] Zhao, B., He, Z., Wei, X., and Shi, X.: 'Compact tunable bandpass filter with wide tuning range and enhanced stopband characteristics', *Electron. Lett.*, 2013, 49, (16), pp. 1007-1008

[116] Chen, J., Zhu, X., Ge, C, and Cao, L.: 'Tunable bandpass filter with low-loss and enhanced selectivity based on controllable coupled negative resistance', *Electron. Lett.*, 2013, 49, (24), pp. 1544-1545

[117] Y. C. Li, and Q. Xue, "Tunable balanced bandpass filter with constant bandwidth and high common-mode suppression," *IEEE Trans. Microw. Theory Tech*., vol. 59, no. 10, pp. 2452–2460, Oct. 2011.

[118] J. Mao, Q. Che, Y. Ma, J. Chen, "Tunable differential-mode bandpass filters with wide tuning range and high common-mode suppression", *IET Microw. Antennas Prop*, vol. 8, no. 6, pp. 437-444, 2013.

[119] H. Oraizi and A.-R. Sharifi, "Design and optimization of broadband asymmetrical multisection Wilkinson power divider," *IEEE Trans. Microw. Theory Techn*., vol. 54, no. 5, pp. 2220–2231, May 2006

[120] X. Wang, I. Sakagami, K. Takahashi, and S. Okamura, "A generalized dual-band Wilkinson power divider with parallel L, C, and R components," *IEEE Trans. Microw. Theory Tech*., vol. 60, no. 4, pp. 952–964, Apr. 2012.

[121] F. Lin, Q. X. Chu, Z. Gong, and Z. Lin, "Compact broadband Gysel power divider with arbitrary power-dividing ratio using microstrip/slotline phase inverter," *IEEE Trans. Microw. Theory Techn.*, vol. 60, no. 5, pp. 1226–1234, May 2012.

[122] J. X. Chen and Q. Xue, "Novel 5:1 unequal Wilkinson power divider using offset duble-Sided parallel-strip lnes," *IEEE Microw. Wireless Compon. Lett.*, vol. 17, no. 3, pp. 175–177, Mar. 2007.

[123] K. K. M. Cheng and P. W. Li, "A novel power-divider design with unequal power-dividing ratio and simple layout," *IEEE Trans. Microw. Theory Techn*., vol. 57, no. 6, pp. 1589–1594, Jun. 2009.

[124] Y. C. Li, Q. Xue, and X. Y. Zhang, "Single- and dual-band power dividers integrated with bandpass filters," *IEEE Trans. Microw. Theory Techn*., vol. 61, no. 1, pp. 69–76, Jan. 2013.

[125] X. Y. Zhang, K.-X. Wang, and B.-J. Hu, "Compact filtering power divider with enhanced second-harmonic suppression," *IEEE Microw. Wireless. Compon. Lett*., vol. 23, no. 9, pp. 483–485, Sep. 2013.

[126] C. -F. Chen, C. -Y. Lin, B. -H. Tseng, and S. -F. Chang, "Microstrip bandpass power divider with high frequency selectivity and good in-band isolation," *IEEE MTT-S Int. Microw. Symp, Tampa*, USA, Jun. 2014.

[127] S. S. Gao, S. Sun, and S. Q. Xiao, "A novel wideband bandpass power divider with harmonic-suppressed ring resonator," *IEEE Microw. Wireless Compon. Lett*., vol. 23, no. 3, pp. 119–121, Mar. 2013.

[128] K. Song, Y. Mo, and Y. Fan, "Wideband four-way filtering-response power divider with improved output isolation based on coupled lines," *IEEE Microw. Wireless Compon. Lett*., vol. 24, no. 10, pp. 674–676, Oct. 2014.

[129] K. Wang, X. Zhang, and B.-J. Hu, “Gysel power divider with arbitrary power ratios and filtering responses using coupling structure,” *IEEE Trans. Microw. Theory Tech.*, vol. 62, no. 3, pp. 431–440, 2014.

[130] H. Zhu, and A. Abbosh, “Tunable balanced bandpass filter with wide tuning range of center frequency and bandwidth using compact coupled-line resonator”, IEEE Microw. Wireless Compon. Lett., vol. 26, no. 1, pp. 7-9, Jan. 2016.

[131] H. Zhu, and A. Abbosh, “Compact tunable bandpass filter with wide tuning range of centre frequency and bandwidth using coupled lines and short-ended stubs”, IET Microw. Antennas Prop., vol. 10, no. 8, pp. 863–870, 2016.

[132] H. Zhu, and A. Abbosh, “Tunable band-pass filter with wide stopband and high selectivity using centre-loaded coupled structure”, IET Microw. Antennas Prop., vol. 9, no. 13, pp. 1371–1375, 2015.

[133] H. Zhu, and A. Abbosh, “Compact tunable bandpass filter with wide tuning range using ring resonator and short ended coupled lines”, Electron. Lett., vol.51, no. 7, pp. 568–570, Apr. 2015.

[134] A. M. Abbosh, “Three-way parallel-coupled microstrip power divider with ultra-wideband performance and equal–power division”, *IEEE Microw. Wireless. Compon. Lett.*, vol. 21, no.12, pp.649–651, Dec. 2011.

[135] D. Pavlidis and H. L. Hartnagel, “The design and performance of threeline microstrip couplers,” *IEEE Trans. Microw Tech.*, vol. 24, no. 10, pp. 631-640, Oct. 1976.

[136] S. Yamamoto, T. Azakami, and K. Itakura, “Coupled strip transmission line with three center conductors,” *IEEE Trans. Microw Tech.*, vol. 14, no. 10, pp. 446-461, Oct. 1966.

[137] H. Zhu, A. Abbosh, and L. Guo, “Wideband four-way filtering power divider with sharp selectivity and wide stopband using looped coupled-line structures”, *IEEE Microw. Wireless Compon. Lett.*, vol. 26, no. 6, pp. 413-416, Jun. 2016.

[138] L. Guo, H. Zhu, and A. Abbosh, “Wideband tunable In-phase power divider using three-line coupled structre”, *IEEE Microw. Wireless Compon. Lett*., vol. 26, no. 6, pp. 404-406, Jan. 2016.

[139] K. S. Ang, I. D. Robertson, K. Elgaid, and I. G. Thayne, “40 to 90 GHz impedance-transforming CPW Marchand balun,” in *IEEE MTT-S Int. Dig.*, 2000, vol. 2, pp. 1141–1144.

[140] R. Michaelsen, T. Johansen, K. Tamborg, and V. Zhurbenko, “A modified Marchand balun configuration with tunable phase balance,” *IEEE Microwave and Wireless Components Letters*, vol. 23, no. 2, pp. 66–68, 2013.

[141] A. Abbosh and M. Bialkowski, “Design of compact directional couplers for UWB applications,” *IEEE Trans. Microw. Theory Tech.*, vol. 55, no. 1, pp. 189–194, Jan. 2007.

[142] E. A. Fardin, K. Ghorbani, and A. S. Holland, "A varactor tuned branch-line hybrid coupler," in *Proc. Asia–Pacific Microw. Conf.*, Dec. 2005, vol. 3, pp. 4–7.

[143] E. A. Fardin, A. S. Holland, and K. Ghorbani, "Electronically tunable lumped element 90 hybrid coupler," *Electron. Lett*., vol. 42, no. 6, pp. 353–355, Mar. 2006.

[144] E. E. Djoumessi, E. Marsan, C. Caloz, M. Chaker, and K. Wu, "Varactor-tuned dual-band quadrature hybrid coupler," *IEEE Microw. Wireless Compon. Lett*., vol. 16, no. 11, pp. 603–605, Nov. 2006.

[145] H. Mextorf, T. Lehmann, and R. Knoechel, "Systematic design of reconfigurable quadrature directional couplers," in *IEEE MTT-S Int. Microw. Symp. Dig*., Jun. 2009, pp. 1009–1012.

[146] J. Sun, C. Li, Y. Geng, and P. Wang, "A highly reconfigurable low-power CMOS directional coupler," *IEEE Trans. Microw. Theory Techn.*, vol. 60, no. 9, pp. 2815–2822, Sep. 2012.

[147] M. A. Y. Abdalla, K. Phang, and G. V. Eleftheriades, "A compact highly reconfigurable COMS MMIC directional coupler," *IEEE Trans. Microw. Theory Techn*., vol. 56, no. 2, pp. 305–319, Feb. 2008.

[148] L. K. Yeung, "A compact directional coupler with tunable coupling ratio using coupled-line sections", in *Proc. Asia–Pacific Microw. Conf*., Dec. 2011, vol. 3, pp. 1730–1733.

[149] H. Zhu, and A. Abbosh, "Modified wideband Marchand balun with tunable power division ratio and constant phase", *IEEE Microw. Wireless Compon. Lett*., vol. 26, no. 5, pp. 319-321, May. 2016.

[150] R. E. Collins, Foundations for Microwave Engineering, 2nd ed. NY, USA: *McGraw-Hill*, 1992.

[151] Y. S. Wong, S. Y. Zheng, and W. S. Chan, "Quasi-arbitrary phase difference hybrid coupler," *IEEE Trans. Microw. Theory Techn*., vol. 60, no. 6, pp. 1530–1539, Jun. 2012.

[152] S. Y. Zheng, J. H. Deng, Y. M. Pan, and W. S. Chan, "Circular sector patch hybrid coupler with an arbitrary coupling coefficient and phase difference," *IEEE Trans. Microw. Theory Techn.*, vol. 61, no. 5, pp. 1781–1792, May 2013.

[153] Y. Wu, J. Shen, Y. Liu, S.-W. Leung, and Q. Xue, "Miniaturized arbitrary phase-difference couplers for arbitrary coupling coefficients," *IEEE Trans. Microw. Theory Techn*., vol. 61, no. 6, pp. 2317–2324, Jun. 2013.

[154] P. -L. Chi and K.-L. Ho, "Design of dual-band coupler with arbitrary power division ratios and phase differences," *IEEE Trans. Microw. Theory Techn*., vol. 62, no. 12, pp. 2965-2974, Dec. 2014.

[155] R. Mongia, I. Bahl, and P. Bhartia, RF and Microwave Coupled-Line Circuits. Norwell, MA: *Artech House*, 1999.

[156] A. Abbosh, “Compact tunable reflection phase shifters using short section of coupled lines,” *IEEE Trans. Microw. Theory Tech.*, vol. 60, no. 8, pp. 2465-2472, Aug. 2012.

[157] M. A. Richards, in Fundamentals of Radar Signal Processing, 2nd Edition, *McGraw-Hill*, 2014, January.

[158] N. Fourikis, "Advanced Array Systems, Applications and RF Technologies," *Academic Press*, 2000.

[159] L. Guo, H. Zhu, and A. Abbosh, “Wideband phase shifter with wide phase range using parallel coupled lines and L-shaped networks”, IEEE Microw. Wireless Compon. Lett., vol. 26, no. 8, pp. 592-594, Aug. 2016.